



HAL
open science

Far-from-equilibrium dynamics and entanglement in long-range quantum systems

Jan Schneider

► **To cite this version:**

Jan Schneider. Far-from-equilibrium dynamics and entanglement in long-range quantum systems. Physics [physics]. Institut Polytechnique de Paris, 2022. English. NNT : 2022IPPAX087 . tel-04085151

HAL Id: tel-04085151

<https://theses.hal.science/tel-04085151v1>

Submitted on 28 Apr 2023

HAL is a multi-disciplinary open access archive for the deposit and dissemination of scientific research documents, whether they are published or not. The documents may come from teaching and research institutions in France or abroad, or from public or private research centers.

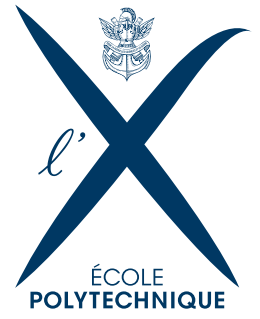
L'archive ouverte pluridisciplinaire **HAL**, est destinée au dépôt et à la diffusion de documents scientifiques de niveau recherche, publiés ou non, émanant des établissements d'enseignement et de recherche français ou étrangers, des laboratoires publics ou privés.



INSTITUT
POLYTECHNIQUE
DE PARIS

NNT : 2022IPPAX087

Thèse de doctorat



Far-from-equilibrium dynamics and entanglement in long-range quantum systems

Thèse de doctorat de l'Institut Polytechnique de Paris
préparée à l'École Polytechnique

École doctorale n°626 de l'Institut Polytechnique de Paris (EDIPP)
Spécialité de doctorat : Physique

Thèse présentée et soutenue à Palaiseau, le 30/09/2022, par

Jan Thorben Schneider

Composition du Jury :

Grégoire Misguich Directeur de Recherche, CEA Saclay (Institut de Physique Théorique)	President
Marco Schirò Principal Investigator, Collège de France (Institut de Physique)	Rapporteur
Karyn Le Hur Directrice de Recherche, École Polytechnique (Centre de Physique Théorique)	Examinatrice
Leonardo Mazza Maître de Conférences, Université Paris-Saclay	Examineur
Laurent Sanchez-Palencia Directeur de Recherche, École Polytechnique (Centre de Physique Théorique)	Directeur de thèse

Far-from-equilibrium dynamics and entanglement in long-range quantum systems

by

Jan Thorben Schneider



Thèse de doctorat de l'Institut Polytechnique de Paris
préparée au Centre de Physique Théorique
à
L'ÉCOLE POLYTECHNIQUE

Acknowledgements

This manuscript presents the research of my doctoral studies at the Centre for Theoretical Physics (CPHT) at École Polytechnique from October 2019 to September 2022. Although it bears a single author, the work detailed in this manuscript would have been impossible without the essential support of so many great people I owe my deep gratitude. First, I wish to thank the Jury of my PhD defence for accepting to take part; Karyn Le Hur, Leonardo Mazza, and especially Grégoire Misguich and Marco Schirò for accepting to carefully read and review my manuscript.

I am deeply grateful to my ‘doctor father’, as we say in German, Laurent Sanchez-Palencia for giving me the opportunity to work with him in his research group at CPHT. I treasure throughout all situations during these last three years. I truly appreciated the trust and the respect you showed me, the freedom I was allowed to explore new directions while you had always an open ear and mind about new perspectives while you also counselled excellently towards fruitful paths. It was more than a privilege to work with you, to learn from you about all aspects of working in academia.

I also owe a lot to my co-authors for the invaluable advice, patience, and trust. Most importantly, I thank Steven Thomson with whom I found a way to enjoy the collaborations during the pandemic. I am also grateful to Luca Tagliacozzo for his advice during our collaboration on our projects. Furthermore, I wish to thank Julien Despres for his kind introduction into the ongoing research, the methodology, and everything in and around CPHT.

This brings me to the immeasurable value of the lovely atmosphere during numerous discussions at CPHT fuelled by my heart-warming colleagues during lunch breaks, coffee breaks, and other great (dinner) situations; Louis, Hepeng, Steffen, Jakob, Sumanta, Alaska, Ronan, Benjamin B., Benjamin L., Anna, Marcello, Erik, Maria, Zhenya, Adrian, and Zhaoxuan. The fantastic team of secretaries, Florence, Malika, and Fadila, as well as the competent IT support around Danh, Yannick, and Vazoumana made life at CPHT really frictionless and provided essential support during my entire stay. I would also like to gladly thank Jean-René Chazottes for directing the CPHT and creating a very supportive and collaborative environment, especially having young researchers in mind. Heading the Physics Department, Silke Biermann deserves my thanks, too, for organising and coordinating not only the neighbouring condensed matter group but also providing us with useful information and widening my scope to the general physics and academic world.

Beyond the confines of the institute awaited me the beautiful world of living in Paris, in one of the most privileged housing conditions one can possibly dream of; Cité Universitaire de Paris. I wish to thank the Directors of the Maison Heinrich Heine as well as the Colegio de España for allowing me to stay in this marvellous park—a park one truly appreciates during a once-in-a-lifetime global pandemic. I enjoyed my three-year stay to the fullest during which I met so many great people, and had so many inspiring encounters. Beyond all, I am thankful for the old and new friends I made; Kai, Albert, Paolo, Claudia, Albert, Monica, Paula A., Paula G., Gabi, Manuel, Julian, Manu, Marta, Nico, Dani, Aïda, Raquel, Mendia, Stefan, Sophia, Eric, and Myriam and so many more I shamefully omit here. I also wish to thank my dear friends from Heidelberg and Lang-Göns which supported me throughout all those times.

Keineswegs am wenigstens, aber zu guter Letzt muss ich mich von ganzem Herzen bei meiner Familie bedanken, für ihren Halt, ihre Unterstützung, ihren Glauben an und Vertrauen in mich. Danke Papa, Timon, Claudia, Hans-André, Marie, und Madeleine!

Paris, October 2022

Contents

Abstract	1
Résumé en français	3
1 Introduction	5
1.1 The Many-Body Problem	5
1.2 One dimensional quantum systems	6
1.3 Equilibrium many-body physics	7
1.3.1 Quantum Phase Transitions	9
1.4 Out-of-equilibrium many-body physics	11
1.4.1 Quantum quenches	11
1.4.2 Lieb–Robinson bounds	12
1.5 Long-range interactions	13
1.6 Experimental realisation of quantum simulators	14
1.7 Quantum information in condensed matter physics	18
2 Tensor network simulations for long-range interacting quantum systems	23
2.1 Introduction	23
2.2 Area laws of entanglement	24
2.3 Matrix product states	25
2.3.1 Quantum states as tensor networks	26
2.3.2 Entanglement and geometry	30
2.3.3 Compression of a Matrix Product State	35
2.4 Matrix product operators	38
2.4.1 Single-site matrix product operator	39
2.4.2 Matrix product operators of Hamiltonians	40
2.5 Density matrix renormalisation group	45
2.6 Time-dependent variational principle	46
Appendices	49
2.A Some entanglement observables on an MPS	49
2.A.1 Computation of Geometric entanglement	49
2.A.2 Entanglement spectrum	49
2.B Long-range bulk MPO tensors for the LRXXZ model	51
2.C DMRG algorithm	52
2.D TDVP algorithm	54

3	Information and Correlation Spreading	59
3.1	Introduction	59
3.1.1	Extension of the Calabrese–Cardy Quasiparticle Picture	59
3.1.2	Outline of this chapter	63
3.2	Model and Approach	63
3.3	Results	64
3.3.1	Linear spin wave theory	64
3.3.2	Global quench dynamics	74
3.3.3	Local quench dynamics	75
3.4	Discussion	78
	Appendices	81
3.A	Determination of the edge	81
3.B	Rényi entropies after a local quench	82
3.C	Spreading of the G_x spin correlation function	82
3.C.1	Numerical TDVP results	85
4	Entanglement and quantum phase transitions	87
4.1	Introduction	87
4.2	Model and approach	89
4.3	Bosonisation and effective Luttinger liquid theory	89
4.3.1	Bosonisation dictionary of the free model	90
4.3.2	Perturbatively including interactions	93
4.3.3	Renormalisation group flow	95
4.4	Results	97
4.4.1	Geometric entanglement	97
4.4.2	Entanglement spectrum	99
4.4.3	Luttinger liquid parameters in XY phase	104
4.4.4	Entanglement Hamiltonian	110
4.5	Discussion	114
	Appendices	119
4.A	FM–phase ground state analysis	119
4.B	Derivation of the Renormalisation group flow equations	120
4.C	Finite-size scaling	122
4.D	Optimization of self-similar rescaling parameters	123
5	Conclusions and outlook	127
	Bibliography	131

Abstract

Long-range interacting quantum systems have attracted considerable attention in recent years both from an experimental and theoretical perspective. The class of long-range systems considers the all-to-all interaction of any two constituents whereas the interaction strength falls off algebraically with distance R between them as $R^{-\alpha}$. Latest experimental and technological progress made it possible to realise long-ranged systems on several quantum simulation platforms, including artificial ion crystals, dipolar quantum gases, and other systems where the Coulomb interaction is not completely screened. In the theoretical framework of quantum many-body systems, long-range interactions break various fundamental concepts and theorems with far-reaching consequences. Among those are Lieb–Robinson bounds which guarantee the emergence of causality in short-ranged non-relativistic lattice systems, as well as the Mermin–Wagner–Hohenberg theorem stating that continuous symmetries in short-ranged one dimensional quantum systems cannot be spontaneously broken by the ground state.

In this thesis, we study the effects of long-range interactions on out-of-equilibrium and equilibrium features of lattice spin models in one spatial dimension. To this end, we employ complementary analytical calculations based on linear spin-wave theory, and state-of-the-art tensor-network simulations while particularly focusing on the feature unique and central to many-body quantum systems: entanglement.

First, in the long-range transverse-field Ising model, we show the emergence of a weak form of causality characterised by non-universal dynamical exponents. On the one hand, local magnetisation and correlations have an emergent sub-ballistic causal cone while the marked features in the interior of it propagate super-ballistic or ballistic, respectively. On the other hand, the emergent causal cone for all entanglement entropies is shown to be ballistic irrespective of the interaction range and the interior is without marked features.

Second, we determine the equilibrium quantum phase diagram of the long-range XXZ model in terms of the anisotropic coupling and the long-range interaction exponent through studying a representation of the spectrum of the reduced density matrix following a half-chain bipartition, the so-called entanglement spectrum. We show it exhibits a remarkable self-similarity within the critical phase where the system is described by a Luttinger liquid while the self-similarity extends to the geometric entanglement and the Luttinger parameter. The transition away from a Luttinger liquid is consistent with the breakdown of self-similarity and a renormalisation group analysis. The combination of the two latter allows us to locate the corresponding phase transitions which we corroborate by numerical simulations. Furthermore, we show the Entanglement Hamiltonian, the Hermitian operator whose spectrum is the entanglement spectrum, follows the form of the Bisognano–Wichmann theorem in large regions of the phases which include the short-range limit, while such a form can be excluded in the phase where genuinely long-ranged effects are relevant. More precisely, this manuscript is organised as follows.

Chapter 1 introduces the basic concepts of many-body physics in one dimension (1D). We discuss equilibrium properties as well as out-of-equilibrium features of many-body systems, before covering long-range interacting systems. We then dedicate a section to the experimental realisation of such systems. The final section in this chapter briefly discusses the role of quantum information in condensed matter physics.

In Chapter 2, we introduce the necessary concepts to simulate 1D long-range interacting quantum systems with tensor-network techniques. We begin with introducing a graphical notation of tensors and their contractions, and continue explaining through the singular value decomposition how to construct Matrix Product States (MPS). Matrix Product Operators (MPO) are then introduced while particularly focusing on the construction of Hamiltonian operators in the form of sums of both local and long-range interacting operators. We then explain the density matrix renormalisation group algorithm for determining the ground state of a gapped Hamiltonian. Finally, we explain the central concepts to the time-dependent variational principle algorithm which takes an MPS and evolves it in time given some Hamiltonian.

In Chapter 3, we study the effects of long-range interactions on the spreading of information and correlation related to the emergence of causality in out-of-equilibrium dynamics in the long-range transverse Ising model (LRTI). We introduce and discuss relevant aspects in existing literature about short-range and long-range interacting systems. Then our main results are presented obtained by complementary analytical computations within linear spin-wave theory and numerical simulations through tensor-network methods. We conclude that a weak form of causality emerges in the quasi-local regime of the LRTI, contrarily to the short-range regime where all observables spread ballistically as in the short-range limit.

Chapter 4 is dedicated to the study of the quantum phase diagram of the long-range interacting XXZ model in terms of the anisotropic coupling in the spin-z direction and the long-range interaction exponent α . To this end, we study the entanglement spectrum defined as a representation of the eigenvalues of the half-chain bipartite reduced density matrix obtained through tensor-network simulations. We find it not only contains sufficient information to characterise the entire quantum phase diagram, but it also exhibits a remarkable self-similarity in the critical phase mapping its low-entanglement-energy part in the long-range model onto its short-range counterpart. Furthermore, we study the Entanglement Hamiltonian and show that it takes on a form compatible with the Bisognano–Wichmann theorem in large regions in the phase diagram including the short-range limit. Contrarily, such a form can be excluded in the phase with genuinely long-range interactions.

Finally, in Chapter 5, we draw our conclusions and give an outlook on further research directions.

Résumé

Les systèmes quantiques avec interaction à longue portée ont attiré une attention considérable ces dernières années, tant d'un point de vue expérimental que théorique. La classe des systèmes de longue portée considère l'interaction totale de deux constituants quelconques alors que l'amplitude d'interaction décroît algébriquement avec la distance relative R comme $R^{-\alpha}$. Les derniers progrès expérimentaux et technologiques ont permis de réaliser des systèmes de longue portée sur plusieurs plateformes de simulation quantique, dont les cristaux d'ions artificiels, les gaz quantiques dipolaires, et d'autres systèmes où l'interaction de Coulomb n'est pas complètement écrantée. D'un point de vue théorique, les interactions à longue portée rendent caduques certains concepts et théorèmes fondamentaux avec des conséquences considérables. Parmi ceux-ci figurent les bornes de Lieb–Robinson qui garantissent l'émergence de la causalité dans les systèmes non-relativistes de courte portée sur réseau, ainsi que le théorème de Mermin-Wagner-Hohenberg, selon lequel les symétries continues des systèmes quantiques unidimensionnels à courte portée ne peuvent pas être spontanément brisées par l'état fondamental.

Dans cette thèse, nous étudions les effets des interactions à longue portée sur les propriétés hors équilibre et à l'équilibre des modèles de spin sur réseau en une dimension spatiale. À cette fin, nous utilisons des calculs analytiques complémentaires basés sur la théorie linéaire des ondes de spin, et des simulations de réseaux tensoriels de pointe tout en nous concentrant particulièrement sur la caractéristique unique et centrale des systèmes quantiques à plusieurs corps : l'intrication.

Premièrement, dans le modèle d'Ising en champ transverse de longue portée, nous montrons l'émergence d'une forme faible de causalité caractérisée par des exposants dynamiques non universels. D'une part, la magnétisation et les corrélations locales présentent un cône causal émergent sub-balistique tandis que les structures marquées à l'intérieur de celui-ci se propagent de manière super-balistique ou balistique, selon l'observable considérée. D'autre part, le cône causal émergent pour toutes les entropies d'intrication s'avère être balistique indépendamment de la portée des interactions et l'intérieur est sans structures marquées.

Deuxièmement, nous déterminons le diagramme de phase quantique d'équilibre du modèle XXZ à longue portée en termes de couplage anisotrope et d'exposant d'interaction de longue portée en étudiant une représentation du spectre de la matrice de densité réduite suivant une bipartition à mi-chaine, appelée spectre d'intrication. Nous montrons qu'il présente une autosimilarité remarquable dans la phase critique où le système est décrit par un liquide de Luttinger, et que l'autosimilarité s'étend à l'intrication géométrique et au paramètre de Luttinger. La transition hors du liquide de Luttinger est cohérente avec la rupture de l'autosimilarité et une analyse par groupe de renormalisation. La combinaison de ces deux dernières nous permet de déterminer les transitions de phase correspondantes que nous corroborons à l'aide de simulations numériques. De plus, nous montrons que le Hamiltonien d'intrication, l'opérateur hermitien dont le spectre est le spectre d'intrication, suit la forme du théorème de Bisognano–Wichmann dans les grandes régions des phases incluant la limite à courte portée, tandis qu'une telle forme peut être exclue dans la phase où les effets à longue portée sont véritablement pertinents.

Plus précisément, le manuscrit est organisé comme suit.

Le chapitre 1 présente les concepts de base de la physique à plusieurs corps en une dimension (1D). Nous discutons des propriétés d'équilibre ainsi que des caractéristiques hors équilibre des systèmes à plusieurs corps, avant d'aborder les systèmes en interaction à longue portée. Nous consacrons ensuite une section à la réalisation expérimentale de tels systèmes. La dernière section de ce chapitre aborde brièvement le rôle de l'information quantique dans la physique de la matière condensée.

Dans le chapitre 2, nous introduisons les concepts nécessaires pour simuler des systèmes quantiques 1D en interaction à longue portée avec des techniques de réseaux tensoriels. Nous commençons par présenter une notation graphique des tenseurs et de leurs contractions, puis nous expliquons, par le biais de la décomposition en valeurs singulières, comment construire des états de produits matriciels (MPS). Nous présentons ensuite les opérateurs de produits matriciels (MPO) en nous concentrant particulièrement sur la construction d'opérateurs hamiltoniens sous la forme de sommes d'opérateurs interagissant à la fois localement et à longue portée. Nous expliquons ensuite l'algorithme du groupe de renormalisation de la matrice de densité pour déterminer l'état fondamental d'un hamiltonien gappé. Enfin, nous expliquons les concepts centraux de l'algorithme du principe variationnel dépendant du temps qui prend un MPS et le fait évoluer dans le temps étant donné un certain hamiltonien.

Dans le chapitre 3, nous étudions les effets des interactions à longue portée sur la propagation de l'information et la corrélation liée à l'émergence de la causalité dans la dynamique hors équilibre dans le modèle d'Ising transverse à longue portée (LRTI). Nous introduisons et discutons les aspects pertinents de la littérature existante sur les systèmes d'interaction à courte et longue portée. Nous présentons ensuite nos principaux résultats, obtenus par des calculs analytiques complémentaires dans le cadre de la théorie linéaire des ondes de spin et des simulations numériques par des méthodes de réseaux tensoriels. Nous concluons qu'une forme faible de causalité émerge dans le régime quasi-local de la LRTI, contrairement au régime à courte portée où toutes les observables se propagent de manière balistique comme dans la limite à courte portée.

Le chapitre 4 est dédié à l'étude du diagramme de phase quantique du modèle XXZ en interaction à longue portée en termes de couplage anisotrope dans la direction spin- z et de l'exposant d'interaction à longue portée α . À cette fin, nous étudions le spectre d'intrication défini comme une représentation des valeurs propres de la matrice de densité réduite bipartite de la demi-chaîne obtenue par des simulations de réseaux tensoriels. Nous constatons qu'il contient suffisamment d'information pour caractériser l'ensemble du diagramme de phase quantique. De plus, il présente une autosimilarité remarquable dans la phase critique qui fait correspondre sa partie à faible énergie d'intrication dans le modèle à longue portée avec sa contrepartie à courte portée. En outre, nous étudions l'hamiltonien d'intrication et montrons qu'il adopte une forme compatible avec théorème de Bisognano–Wichmann dans de larges régions du diagramme de phase, y compris dans la limite de courte portée. Par contre, une telle forme peut être exclue dans la phase avec des interactions véritablement à longue portée.

Enfin, dans le chapitre 5, nous résumons nos principaux résultats et tirons nos conclusions avant de donner une perspective sur les futures directions de recherche.

1 *Introduction*

“Sometimes science is more art than science. A lot of people don’t get that.”

— Rick Sanchez, in *Rick potion #9, Rick and Morty*

1.1 *The Many-Body Problem*

The many-body problem is a categorical term concerning the study of many—from three up to infinite—interacting quantum particles. With such a broad definition, it encompasses a plethora of different fields of modern physics, from the largest energy scales to the smallest. Although the recent past has witnessed an immense success of understanding the phenomena coming to play when considering many interacting quantum particles, exact analytical solutions are very rare, and in many cases they have been obtained through approximations. Arguably one of the most frequent and successful approximation techniques in the theory of many quantum particles are perturbation theory and mean-field approaches. A prime example of this success is Lev Landau’s Fermi liquid theory of interacting electrons inside a metal in three spatial dimensions. As its core idea, Fermi liquid theory adiabatically connects the free, i.e. non-interacting, fermion system to the fully interacting fermion system. Landau established a correspondence of the free single particle states to the fully interacting ones. Another example of a successful mean-field approximation is the theoretical explanation of low-temperature superconductivity, first discovered in solid mercury by H. K. Onnes in 1911, put forward by Bardeen, Cooper, and Schrieffer.

Many systems of interacting quantum particles are however not amenable to mean-field approximations, for some of which the predictions of the latter are entirely contradicting observation. Such systems exhibit quantum entanglement and are sufficiently correlated that the central idea of mean-field theory breaks down, and the physics of the ensemble of particles cannot be described by a single particle picture in which a particle interacts with a constant mean-field background. Entanglement is a property unique to quantum systems and present whenever a many-body state is not a product of the states of its constituents but rather in a superposition. Most of these correlated systems are at the heart of ongoing research in condensed matter physics, arguably the most consequential being high-temperature superconductors.

Recent years have witnessed unprecedented experimental progress in ultracold atomic physics which lead to new possibilities of pristine precision and extremely wide control of light–matter interactions. By virtue of these developments, almost perfectly isolated many-body quantum systems have been experimentally realised, i.e. they are very weakly coupled to the environment. These almost closed quantum systems are thus subject to very little decoherence and therefore evolve

under unitary time evolution following the Schrödinger equation. Furthermore, these devices are prime candidates for universal quantum simulators [1, 2], and their development has ushered in the era of Noisy Intermediate-Scale Quantum (NISQ) technologies [3]. Envisioned by Feynman in the 1980s, quantum simulation and more generally quantum information theory makes use of the laws of quantum mechanics at the very smallest scales technologically accessible to process information and perform computations more efficiently [1]. Nowadays, the burgeoning field of quantum information theory has profited as greatly from the experimental success of recent years as it has contributed to the theory of phases of matter and their understanding. Particularly, the field of topological quantum matter begot promising candidates for system that may be utilised for fault-tolerant quantum computing [4] thereby closing the mutually beneficial circle. Essential to the study of quantum information is the concept of entanglement, i.e. the fact that many-body quantum systems may be in a non-factorisable state.

Alongside the impressive experimental progress in recent years, novel numerical methods based on tensor networks have shed new light on the role of entanglement in phases of matter. Moreover, they reveal the pivotal role of quantum information and the holographic principle in the field of condensed matter, especially in 1D systems [5].

1.2 One dimensional quantum systems

Quantum systems in 1D are endowed with particular properties thanks to interactions between particles [6]. Clearly, in one dimensional many-body systems, a single electron cannot move through its neighbour without any effort in pushing it away since there is no dimension available to move around it. Moving a single electron therefore always excites neighbouring ones, and the elementary excitations (i.e. quasiparticles) of a 1D system become collective in nature, or they separate spin and charge of an electron [6]. Fermi liquid theory therefore fails in the one-dimensional quantum case albeit immensely successful in higher dimensions. Fermionic particles in one dimension are successfully described by so called Luttinger liquid theory introduced by Haldane [7, 8]. Hence, 1D many-body quantum systems most often provide examples where particles are sufficiently correlated such that they do not admit a mean-field solution. Our main focus within this thesis are spin-1/2 models. These spins may be transformed into spinless fermions by means of the Jordan-Wigner transform. However, the low energy collective excitations of a fermionic system in 1D may also be described by bosonic degrees of freedom. Indeed, the fermionic and bosonic degrees of freedom can be effectively translated into each other depending on the interaction regime as has been first shown by Coleman in the context of the fermionic Thirring model and the bosonic sine-Gordon model [9]. The fermionic theory can therefore be *bosonised* and the bosonic theory *fermionised*. In Chapter 4, we will discuss Luttinger liquid theory and the bosonisation technique in the context of a long-range interacting spin chain. There, we see the benefit of bosonisation lies in the fact that one can describe some interactions of fermions in terms of free bosons.

Providing an exact analytical solution to the problem of strongly interacting quantum systems is most often impossible with rare exceptions to this in 1D called integrable. Bethe published the first exact solution to the Heisenberg model with his elaborate ansatz for the eigenvectors of the

Hamiltonian endowing his name to the technique [10]. Today, Bethe's ansatz allows to solve the anisotropic generalisation of the Heisenberg model (the XXZ model), the Hubbard model, and several other interacting quantum models, both discrete and in the continuum. However, within the Bethe ansatz solution, the computation of observables like correlation functions involves a significant amount of effort [11]. On the other hand, a particularity of 1D quantum systems is that there are numerical methods at our disposal which efficiently tackle the quantum many-body problem and help unravel their properties. Exact diagonalisation approaches are regarded highly for their simulations up to machine precision, however they suffer strong finite-size effects as state-of-the-art implementations have only up to $\simeq 40$ sites since the exponential scaling of the Hilbert space prohibits further progress on modern high-performance computer architectures. The physics of systems in thermal equilibrium, i.e. a system which has no thermodynamic properties whose statistical average depends on time, may be simulated with a scalable numerical method in the form of Monte Carlo sampling of the Gibbs ensemble. In the quantum case, equilibrium properties are accessible through Monte Carlo sampling when the corresponding quantum version of the Gibbs ensemble does not suffer the so-called sign problem of rapidly oscillating integrals [5]. Fermionic and spin systems are particularly ill-suited for Monte Carlo methods since one encounters the sign problem which are formally NP-hard [12]. Within the framework of this thesis, we are interested in both the equilibrium and out-of-equilibrium properties of spin systems regarding entanglement and correlations. Contrarily, 1D systems may be numerically simulated efficiently, as well as tractably realised in state-of-the-art experiments. Indeed, the class of states of matter in which the system has a spectrum of energies with a gap between the ground state and the first excited state has an efficient representation as tensor networks (TN). They provide a representation of the wave function in real space coordinates in a variational class of states forming a low-dimensional manifold inside the exponentially large Hilbert space which is characterised by a finite amount of entanglement. TNs can be understood as a crucial tool linking a wide variety of theoretical and computational techniques to solve the many-body problem. To name a view [5], numerical algorithms on TNs have granted access to the ground states of gapped Hamiltonians via the density-matrix renormalisation group (DMRG), as well as time-dependent information (TDVP) by applying the time-dependent variational principle on the TN manifold. The physics of critical, i.e. gapless, systems has been inferred through finite-entanglement scaling. Theoretical insights have shed light on the coordinate and algebraic Bethe ansatz through respective reformulations in terms of TNs which allow then for a systematic exploration beyond integrable systems and 1D quantum systems. Furthermore, TNs allow for the complete classification of all possible symmetry protected topological phases of matter in one dimension. In Chapter 2, we will introduce a TN representation of a quantum wave function in 1D and discuss the algorithms to obtain the zero-temperature equilibrium ground state through DMRG, as well as a time-evolved wave function through TDVP.

1.3 Equilibrium many-body physics

Equilibrium many-body physics is characterised by the description of thermodynamic ensembles. An ensemble is an idealisation that consists of many (often infinite) virtual copies of the system of

interest each of which representing a possible state of the system one seeks to describe. Mathematically, an ensemble is the probability space of the random process that describes the state of the physical system at hand. One speaks of equilibrium when the ensemble is stationary and the time evolution of all its virtual copies does not affect any average macroscopic physical observable in the ensemble. Note that while any single physical system certainly evolves over time, equilibrium implies that the statistical properties of the ensemble do in fact not evolve over time. Gibbs introduced several thermodynamic ensembles in equilibrium characterised by different macroscopic variables and their constraints [13]; we shall introduce three prominent examples,

- *Microcanonical ensemble*—it is characterised by the conservation of energy and particle number. All virtual copies of the system have equal energy and particle number. To keep being in equilibrium, the system can neither exchange energy nor particle number. It therefore describes physical systems that are completely isolated.
- *Canonical ensemble*—it is characterised by a fixed number of particles and a fixed temperature. As such, it naturally describes a system in thermal contact with a heat bath with a stationary energy exchange without exchanging any particles.
- *Grand canonical ensemble*—characterised by fixed temperature and fixed chemical potential. As such, it describes an open system being in thermal contact with a heat bath.

In quantum many-body systems, the equilibrium state is described by the density matrix ρ . A density matrix is defined as a bounded linear, hermitian, positive semi-definite, trace-class operator (with trace normed to 1) acting on the Hilbert space given by the Hamiltonian H . Any statistical average of an observable X of the quantum system is then given by,

$$\langle X \rangle = \text{tr}(\rho X). \quad (1.1)$$

In the simple case of a pure state $|\psi\rangle$, the density matrix is given by,

$$\rho = |\psi\rangle\langle\psi|, \quad (1.2)$$

while the more general mixed state has a density matrix,

$$\rho = \sum_j p_j |\psi_j\rangle\langle\psi_j|, \quad (1.3)$$

where $\sum_j p_j = 1$, such that $\text{tr}(\rho) = 1$. In the case of a quantum canonical ensemble in thermal equilibrium at temperature T , the density matrix is given by,

$$\rho = \frac{1}{Z} e^{-\beta(T)H}, \quad (1.4)$$

where H is the Hamiltonian operator of the quantum model, $\beta = (k_B T)^{-1}$, k_B is the Boltzmann constant, and $Z = \text{tr}(\exp[-\beta H])$ the normalisation of the trace.

1.3.1 Quantum Phase Transitions

The lowest-energy physics of many-body systems has ever since the beginning of quantum physics attracted plenty of attention. Interesting phenomena in strongly correlated quantum systems can give rise to superconductivity, superfluidity, Bose–Einstein condensation, and many more phenomena which lack an intuitive counterpart in a classical realm. There are also more mundane transitions like the one from liquid to solid, or a transition of the magnetic susceptibility. The most prevalent and successful theoretical framework to explain above phase transitions is the one provided by Landau and Ginzburg [14, 15] based on spontaneous symmetry breaking. Landau postulated the microscopic equations of motion of the particles in a system respect the symmetries of it when crossing from one phase into another. However, the lowest energy configuration of the system transitions from respecting the very same symmetries as the equations of motion into breaking it. Such a change that occurs only in the lowest-energy configuration is said to ‘spontaneously break’ the symmetry of the system, i.e. equations of motion. The spontaneous-symmetry breaking occurs due to the nature of the interactions rendering the lowest-energy configuration not to obey the symmetries of the equations of motion. According to Landau’s theory, different orders of matter therefore correspond to different symmetries of its lowest-energy configuration. As an example, one may consider the transition from a liquid to a solid similar to the one from water to ice. The equations of motion are translational invariant; they are symmetric under any continuous translation in space. At large enough temperatures, the state of matter follows the same symmetry in that its description as a liquid is also symmetric under continuous translations in space. Generally it is considered to be disordered. However, below some critical temperature, the energetically most favourable state does not obey this symmetry any more but rather spontaneously breaks it as form a regular crystal. As such, it is only symmetric under discrete translations in space (multiples of the lattice spacing), and the state of matter is now in an ordered phase. The transition from liquid to crystal therefore breaks the continuous translation symmetry and reduces it to a discrete translation symmetry whereas the equations of motion are on both sides of the transition symmetric under continuous translations.

Within the framework of this thesis, we are interested in the phase transitions that occur at zero temperature where the system is always in its ground state, so-called quantum phase transitions. There, thermal fluctuations are zero and thus cannot account for a phase transition and instead quantum fluctuations due to the uncertainty principle drive the loss of order across a transition into a disordered state. Therefore, we are always discussing a transition where the ground state changes its type of order when one changes a physical microscopic parameter of the Hamiltonian $H = H(\lambda)$. Suppose we are inspecting discrete quantum many-body systems on finite regular lattices. We speak of a quantum phase transition when the ground state as a function of this physical parameter λ has a point where it is non-analytic, henceforth labelled λ_c . This nonanalyticity has as its origin either a true level-crossing on all finite lattice sizes and the infinite lattice limit, or an avoided level-crossing in the finite case which approaches a nonanalytic point in the thermodynamic, i.e. infinite volume, limit. It has been long thought that Landau’s theory of phase transitions also holds for all quantum phases of matter, i.e. the order in the ground state of physical systems. Within the recent past, new phases of matter have been discovered whose transitions

cannot be explained by a broken symmetry, most prominently topological phases. Landau theory covers so-called continuous (or second-order) phase transitions. These are transitions at which the characteristic energy scale of the spectrum of elementary excitations relative to the ground state approaches 0 and vanishes identically at the critical point λ_0 as,

$$\Delta \sim J|\lambda - \lambda_c|^{z\nu}, \quad (1.5)$$

where J is the microscopic coupling energy, and $z\nu$ is the critical exponent [16]. Furthermore, in continuous phase transitions, the characteristic length scale (e.g. correlation length) of the ground state diverges as,

$$\xi^{-1} \sim \Lambda|\lambda - \lambda_c|^\nu, \quad (1.6)$$

where Λ is the inverse length scale and momentum cutoff given by the lattice spacing a .

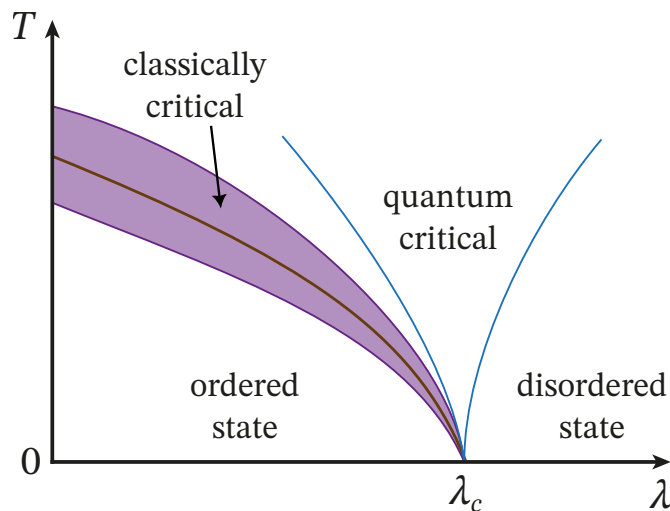


Figure 1.1: Phase diagram of temperature T and a Hamiltonian parameter λ where the quantum critical point ($\lambda = \lambda_c$) marks the quantum phase transition at zero temperature. The brown line marks a classical phase transition and the purple ribbon indicates the onset of features of criticality.

Above considerations are made only at absolute zero $T = 0$. Since reaching absolute zero is impermissible by the third law of thermodynamics, any experimental setup necessarily has a non-zero albeit possibly very small temperature $T > 0$. This begs the question if one can ever measure signals of quantum phase transitions. The answer is in the affirmative and the argument follows this logic: At any finite temperature $T > 0$, the characteristic energy scale of thermal fluctuations is $k_B T$. Quantum fluctuations however have a typical energy scale of $\hbar\omega \propto \hbar/\xi$ with ω a characteristic frequency and ξ a characteristic (correlation) length scale of the quantum oscillations. In a region where $\hbar\omega \gg k_B T$ (called quantum critical) one therefore expects to observe quantum critical behaviour even in the case of finite temperatures, as quantum fluctuations dominate over thermal fluctuations. Figure 1.1 is an illustration of these considerations. In a region around the thermal phase transition (solid brown line with purple region), one finds the onset of thermal or classical

critical behaviour. There, the correlation length diverges with temperature approaching the phase transition point as,

$$\xi \sim \frac{|T - T_c|^\nu}{T_c}, \quad (1.7)$$

analogously to the zero temperature case. This region decreases in size around the phase transition as thermal fluctuations decrease in energy when decreasing temperature. On the other hand, when one approaches $\lambda \rightarrow \lambda_c$ and the condition $\hbar\omega \gg k_B T$ is fulfilled, one expects quantum fluctuations to dominate over thermal ones. In this ‘quantum critical’ regime at finite temperatures, one expects to find signals of the quantum phase transition at zero temperature.

1.4 Out-of-equilibrium many-body physics

The problem of describing the dynamics of many particles of a generic quantum system is truly formidable, especially when the system is not in equilibrium. The history of studying out-of-equilibrium dynamics is rich as most physical phenomena in our ever-changing universe are not static but driven by dynamics. Particularly in recent years, they have been studied across different traditional fields. After all, out-of-equilibrium dynamics of quantum many-body systems describe, for example, the ultrarelativistic collisions of atomic nuclei in giant particle accelerators, as well as experiments with ultracold quantum gases far from equilibrium which typically fit on a table. Despite the vastly different energy scales of these systems, they can show very similar dynamical properties and are amenable to similar theoretical frameworks. Here, we will focus on the lower energy scales where relativistic effects can be safely ignored.

1.4.1 Quantum quenches

A quantum system can be thrown out of equilibrium by a sudden modification being realised on a negligible timescale compared to all relevant time scales of the system. We thus consider the quench to be instantaneous.

1.4.1.1 Global quenches

Global quenches, or sometimes also called homogeneous, are defined by a sudden change of a global system parameter in the Hamiltonian. We consider this change to occur at time $t = 0$ such that $H_i \rightarrow H_f$, while the state describing the system is unchanged. The initial state is therefore identical to the pre-quench state $|\psi_0\rangle = |\psi(t \leq 0)\rangle$, while the post-quench state—assuming an isolated quantum system with no further time dependence of the post-quench Hamiltonian—is given by the unitary time evolution according to the post-quench Hamiltonian H_f ,

$$|\psi(t > 0)\rangle = e^{-iH_f t} |\psi_0\rangle. \quad (1.8)$$

The conservation of energy $E_f = \langle \psi(t) | H_f | \psi(t) \rangle = \langle \psi_0 | H_f | \psi_0 \rangle$ immediately follows from said restrictions. Here, we consider such changes to the parameters of the Hamiltonian that the final

Hamiltonian does not have the initial many-body state as an eigenstate, yet the parameter change does not cross a first-order phase transition. The initial state is consequently a complex superposition of eigenstates over the entire energy spectrum. Henceforth, we consider only ground states of initial Hamiltonians as an initial state, $|\psi_0\rangle = |\psi_{GS}(H_i)\rangle$.

1.4.1.2 Local quenches

A local quench, sometimes referred to as inhomogeneous, are defined by the sudden application of a local linear operator at time $t = 0$ on the initial state. Contrarily to a global quench, the Hamiltonian within this protocol stays unchanged ($H_i = H_f$). Denoting the local operator applied at $t = 0$ as A , the dynamics of the initial state $|\psi_i\rangle$ is given by the unitary time evolution,

$$|\psi(t)\rangle = e^{-iHt}|\psi_i\rangle = e^{-iHt}A|\psi_{GS}\rangle. \quad (1.9)$$

We consider such local operators that the initial state $|\psi_i\rangle = A|\psi_{GS}\rangle$ is not an eigenstate of the Hamiltonian.

Immense technological and scientific progress in the experimental condensed matter communities in recent decades have made it possible that these types of protocols can be realised in state-of-the-art experiments, see Ref. [17] for a review. For a brief overview, see Section 1.6. Quantum quenches are being widely considered in theoretical works due to their straightforward and common experimental realisation. Moreover, there are some analytical results in conformal field theories in 1D [18] and integrable models like the Luttinger model [19, 20].

1.4.2 Lieb–Robinson bounds

In non-relativistic quantum models, causality is an emergent property. It manifests when the interaction range of the constituent particles is short-ranged, but also emerges in long-range interacting systems when the interaction range is not too long [21]. Lieb and Robinson showed in 1972 in their seminal work [22] that the spreading of any perturbation in a generic lattice quantum system with short-range interactions is bounded. Given a quantum model defined by a Hamiltonian H with degrees of freedom on a regular lattice Γ where each lattice point has a finite dimensional Hilbert space, and given two arbitrary local operators¹ $X_A(t)$ at time t and region of support $A \subset \Gamma$, as well as $Y_B(0)$ at time $t = 0$ with region of support $B \subset \Gamma$, then the following operator norms obey the inequality [22],

$$\|[X_A(t), Y_B(0)]\| \leq c \cdot e^{-\alpha(d(A,B) - v \cdot |t|)}, \quad (1.10)$$

for some constants α, c, v , and where we define the distance between the subsets A and B as $d(A, B)$, $\|\cdot\|$ indicates the operator norm, and $[A, B] = AB - BA$ is the commutator. It is particularly noteworthy that the inequality proven by Lieb and Robinson does not depend on a state but only on the Hamiltonian H governing the dynamics which must have short-ranged interactions. Moreover, the values of the constants α, c , and v is not predicted and rather challenging to obtain *ab initio* given a

¹Local operators are those whose supported region is finite and constant independent of the system size.

generic lattice model. Of particular interest is the constant v which has dimension of a velocity thus generally called Lieb–Robinson bound velocity. Equation (1.10) implies, among others, that the effect of any operator in one region A has negligible effect, i.e. exponentially small, on a separate and distant region B if $d(A, B) > v \cdot |t|$. Contrarily, a causal cone emerges when the time reaches values such that $d(A, B) \simeq v \cdot |t|$. This means all significant signals are travelling within a region whose boundary has a linear relation between its time and space coordinate, $t \propto R$, while any other signal outside this ‘light cone’ is decaying exponentially in distance to that boundary. These statements can be generalised to expectation values of correlation functions in gapped Hamiltonians [23]. Note that Lieb and Robinson provided merely a proof of upper bounds which are strictly not informative about the physical velocity with which information and correlations actually spread.

A physical explanation where this Lieb–Robinson velocity comes from, and more generally a comprehensive picture of this ballistic spreading of information was later proposed by Calabrese and Cardy [18]. They provided a quasiparticle picture explaining the bounded propagation of information in the case of conformal field theories (CFT) and suggested this picture is applicable in more general settings. The established interpretation of correlation and information spreading in short-range interacting quantum systems, which are accurately approximated by a quasi-particle picture, is to date provided by the Calabrese–Cardy quasiparticle picture. It concisely explains the bounded speed with which any information is at most propagating, as defined in Eq. (1.10) by the constant v , and it is given by the maximal group velocity of quasiparticles. Läuchli and Kollath corroborated the Calabrese–Cardy–quasiparticle picture in the Bose–Hubbard model with both Exact Diagonalisation (ED) and the time-dependent Density Matrix Renormalisation Group (t-DMRG) after using a strong quench, i.e. a global parameter change that crossed a phase boundary [24]. Furthermore, they found the general quasiparticle interpretation to hold even outside the critical phase space described by a CFT. The first experimental observations of emergent light cones was done in Ref. [25] in the Bose–Hubbard model inside the Mott insulating phase. Furthermore, Ref. [26] studied the isotropic Heisenberg model corroborating the Calabrese–Cardy picture, and in Bose gases described by a Luttinger liquid [27].

An emergent light cone was also numerically confirmed in spinless fermions at half-filling [28], in the Bose–Hubbard model both inside the Mott insulating phase [29] and inside the superfluid phase at unit filling [30], and both inside the superfluid and Mott-insulating phase of the Bose–Hubbard model in Ref. [31]. The latter employed additionally to numerical t-DMRG techniques also a generic analytic quasiparticle picture built on earlier works [32–34], which extends the Calabrese–Cardy quasiparticle picture beyond the conformal field theory framework.

1.5 Long-range interactions

Long-range interacting many-body systems, both classical and quantum, can be found throughout many disciplines of modern physics. The uniting paradigm is the all-to-all interaction of constituting particles whereas the amplitude decays as a power-law over the relative distance as $1/R^\alpha$ with α being the long-range interaction exponent. Systems with this type of interactions are found in anywhere Newtonian gravity plays the central role of interaction, or in systems with electrically

charged particles where the Coulomb interaction is not completely screened. Such systems are present in astrophysics, nuclear physics, plasma physics, ultracold atomic physics, and also hydrodynamics [35]. Since many fundamental concepts and theorems of many-body theory are based on the assumption of short-range interactions, long-range interactions can break them, often resulting in profound and far-reaching consequences. Among those dramatically altered behaviours are the equivalence of thermodynamic ensembles [36, 37], negative heat capacities, anomalous response functions [38], the dynamics of correlated systems [35]. Compared to standard approaches found throughout many-body physics, long-range interactions often necessitate fundamentally new approaches as profound theorems at the heart of many-body theory are sometimes rendered invalid.

In the framework of this thesis, we are interested in quantum systems whose microscopic interactions are described by so-called long-range interactions. To be more specific, we assume there are countably many degrees of freedom on a regular lattice, and they are all-to-all interacting with an amplitude that decays like a power law over distance as $\sim 1/R^\alpha$. In the context of condensed matter theory, long-range interactions render the Mermin–Wagner–Hohenberg theorem invalid [39–41], as well as the area law of entanglement entropy for large enough values of α [42–46].

The effects of long-range interactions on the *dynamics* of many-body quantum systems are dramatic. Thanks to the pristine precision and extremely wide control of light-matter interaction and the experimental progress thereof, the study of this field has dramatically accelerated and grown in recent years. Particularly whether and how a form of causality, reminiscent of the Lieb–Robinson bounds in short-range systems (cf. Section 1.4.2), emerges in long-range systems continues to be a central outstanding question. The emerging causal cone in short-range interacting systems has been demonstrated for various models in both experiments [25–27] and numerics [24, 28–31, 47, 48]. Moreover, it has been shown that sufficiently long-ranged interactions break causality, and information spreads arbitrarily fast [49, 50] in accordance with no known upper bounds in long-range systems analogous to those of Lieb and Robinson [21, 23, 51] and the vanishing characteristic dynamical timescale in the thermodynamic limit [33]. On the other hand, when the long-range interaction exponent is large enough and the interaction strength decays fast enough over space, one recovers the ballistic propagation of information [52–54]. Of particular interest, especially within the framework of this thesis, is the intermediate regime. Known upper bounds for long-range interacting systems allow, in principle, for super-ballistic propagation of information [21, 23, 51]. On the other hand, numerical simulations for various models and observables do not saturate those upper bounds, hinting at tighter bounds and slower propagation laws [32, 45, 49, 55–58].

1.6 Experimental realisation of quantum simulators

Above, we have discussed the relevance of long-range interacting models, in particular in the context of condensed matter physics. Here, we continue in this vein and discuss the relevance of quantum systems with long-range interactions in the study of condensed matter. First, long-range interactions occur naturally in systems such as artificial ion crystals [59–64], Rydberg gases [65–68], magnetic atoms [69–73], polar molecules [74–76], nonlinear optical media [77], and solid-state defects [78–80]. These systems are free of effects which completely screen the electrical charges

such that the Coulomb interaction is truly long-range. Secondly, long-range systems can now be emulated in quantum simulators [1, 2, 63, 81–92] with some of the very same systems thanks to the pristine precision and range of control of, among others, the interaction exponent α [59, 68].

Quantum simulators A quantum simulator is a technological device imitating quantum models which is equipped with precise and wide control of the relevant parameters, and with the means to prepare, manipulate, and detect the relevant quantum states of interest. Crucially relevant to a quantum simulator is the fact that any simulation on classical computers would constitute an unreasonable challenge in terms of memory and timescale at which the problem can currently be solved [93]. Currently, there are several experimental platforms at one’s disposal for implementing quantum simulator devices. They are broadly split in two categories: analogue quantum simulators, and digital quantum simulators. The former describe devices in which the physical degrees of freedom in a system are in one-to-one analogy to the physical degrees of freedom in the model of interest. These devices form a ‘miniature’ of the physical model one seeks to observe and understand. On the other hand, digital quantum simulators are devices that use the Lie–Trotter product formula, $e^{A+B} = \lim_{N \rightarrow \infty} (e^{A/N} e^{B/N})^N$, and factor the time evolution operator $U(t, t_0) = \exp\left(-i \int_{t_0}^t H(t') dt'\right)$ of the quantum system in a sequence of countably many steps, as was first proposed by Lloyd [94]. The countable steps to simulate the effect of the Hamiltonian which generates the time evolution is decomposed in quantum gates.

Trapped ion quantum simulators In the following, we briefly address the particularly fruitful platform trapped ions offer, cf. Ref. [63] for a review. In particular, we discuss the quantum gates necessary to simulate an n -body interaction [95, 96]. The wide and precise control in these platforms allows to variably change the long-range interaction exponent. The experimental progress and technological possibilities allow for very low temperatures at which these platforms offer high control over single and two-site control. Heavily paraphrased, cold ion experiments start by trapping ions with the attractive force of light–ion interaction of laser beams while the Coulomb repulsion competes such that a stable lattice is formed. Two internal electronic states are used as an effective qubit simulating a spin degree of freedom. Alkaline earth metals are typically used for these applications since their valance electron is naturally in a spin-1/2 state.

The relevant degrees of freedom for an ion chain are the spin-1/2 degrees of freedom on a regular 1D lattice, the relative motional, and the single motional degrees of freedom—the centre-of-mass mode [95]. The Hamiltonian thus reads as [95, 97],

$$H_{\text{int}} = \Omega \sum_{n=0}^{N-1} \left\{ \sigma_n^+ e^{-i(\Delta t - \phi)} + \sigma_n^- e^{i(\Delta t - \phi)} + i\eta (\sigma_n^+ e^{-i(\Delta t - \phi)} - \sigma_n^- e^{i(\Delta t - \phi)}) (a e^{-i\omega_t t} + a^\dagger e^{i\omega_t t}) \right\}, \quad (1.11)$$

where Ω is the Rabi frequency, σ^\pm the qubit raising and lowering operators, a and a^\dagger the phonon annihilation and creation operators, respectively. Furthermore, ϕ is the phase of the field with respect to the qubit polarisation, Δ is the laser-atom detuning, and ω_t is the laser frequency. Note that one applies several approximations including the rotating wave approximation which assumes

both laser detuning Δ and Rabi frequency Ω to be much smaller than any other optical relevant frequency.

Single-qubit gate Single site manipulations, i.e. single-qubit gates, are simple rotations of the spin on the Bloch sphere, and are realised by single-site applications of laser light. Theoretically, they are described by the rotation matrix,

$$R_i(\theta, \phi) = \exp\left\{i\frac{\theta}{2}(e^{i\phi}\sigma_i^+ + e^{-i\phi}\sigma_i^-)\right\} \quad (1.12)$$

$$= \mathbb{1}_i \cos\left(\frac{\theta}{2}\right) + i[\sigma_i^x \cos(\phi) - \sigma_i^y \sin(\phi)] \sin\left(\frac{\theta}{2}\right), \quad (1.13)$$

where ϕ specifies the azimuthal angle of the axis of rotation and θ describes the amount of rotation. Rotations around the z-axis are either decomposable in rotations around the x and y axis or it might be realised via far detuned laser beam which shifts the energies due to an AC-Stark effect [95].

2-qubit gate Finalising the qubit manipulation toolbox, we briefly discuss the two-qubit gate proposed by Mølmer and Sørensen (MS gate) [97] which uses a dichromatic laser field to irradiate all qubits at once. The two frequencies of the dichromatic laser are close and symmetrically detuned from the qubit transition frequency $\omega_0 \pm (\omega_{eg} + \Delta)$. The detuning is chosen such that an effective second-order coupling between pairs of ions is generated by off-resonantly coupling the blue-shifted and red-shifted phonon side bands [98]. The MS gate thus uses the collective motional degree of freedom and is particularly favourable as it does not require the ions to be in the motional ground state at ultracold temperatures [95, 97, 98]. Figure 1.2 shows an illustration of the energy level scheme in an MS gate. The blue and red detuned laser beams (blue and red arrows) drive the system via the virtual levels (marked by dashed lines) between the states $|n\rangle \otimes |gg\rangle$ and $|n\rangle \otimes |ee\rangle$. Note that $|n\rangle$ marks the state with phonon number n and $|g\rangle, |e\rangle$, the ground and excited state, respectively. This figure applies to cases where the detuning is much smaller than the Rabi frequency such that the latter is in fact independent of the phonon number n . This is because the effect of the phonon state destructively interferes due to the symmetric paths and the opposite sign of the detuning, allowing the application of the MS gate without cooling to the motional ground state. Consequently, by applying the MS gate to two qubits of one's liking, the transition they undergo reads as,

$$|gg\rangle \rightarrow \cos\left(\frac{\tilde{\Omega}t}{2}\right)|gg\rangle + i \sin\left(\frac{\tilde{\Omega}t}{2}\right)|ee\rangle, \quad (1.14)$$

$$|ee\rangle \rightarrow \cos\left(\frac{\tilde{\Omega}t}{2}\right)|ee\rangle + i \sin\left(\frac{\tilde{\Omega}t}{2}\right)|gg\rangle, \quad (1.15)$$

$$|ge\rangle \rightarrow \cos\left(\frac{\tilde{\Omega}t}{2}\right)|ge\rangle - i \sin\left(\frac{\tilde{\Omega}t}{2}\right)|eg\rangle, \quad (1.16)$$

$$|eg\rangle \rightarrow \cos\left(\frac{\tilde{\Omega}t}{2}\right)|eg\rangle - i \sin\left(\frac{\tilde{\Omega}t}{2}\right)|ge\rangle, \quad (1.17)$$

and as such forms the essential part of the digital quantum simulator toolkit.

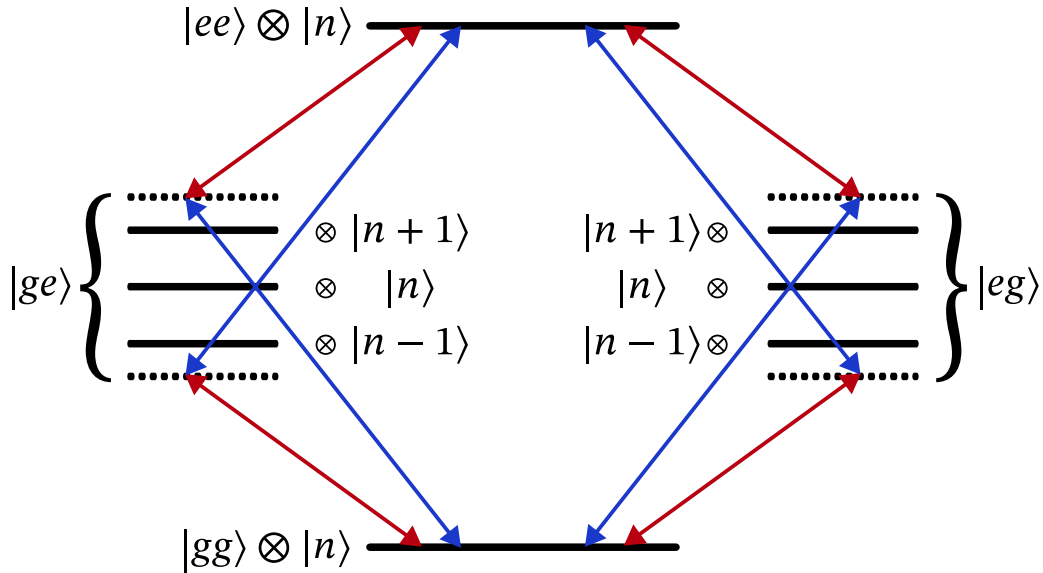


Figure 1.2: Illustration of the energy levels (horizontal bars) and optical wavelengths (arrows) involved in the two-qubit Mølmer-Sørensen (MS) gate. Note the two-qubit states are written as $|g\rangle$ (ground) and $|e\rangle$ (excited) while the phonon state is written as $|m\rangle$ with phonon number m . Energies of the state correspond to Hamiltonian (1.11).

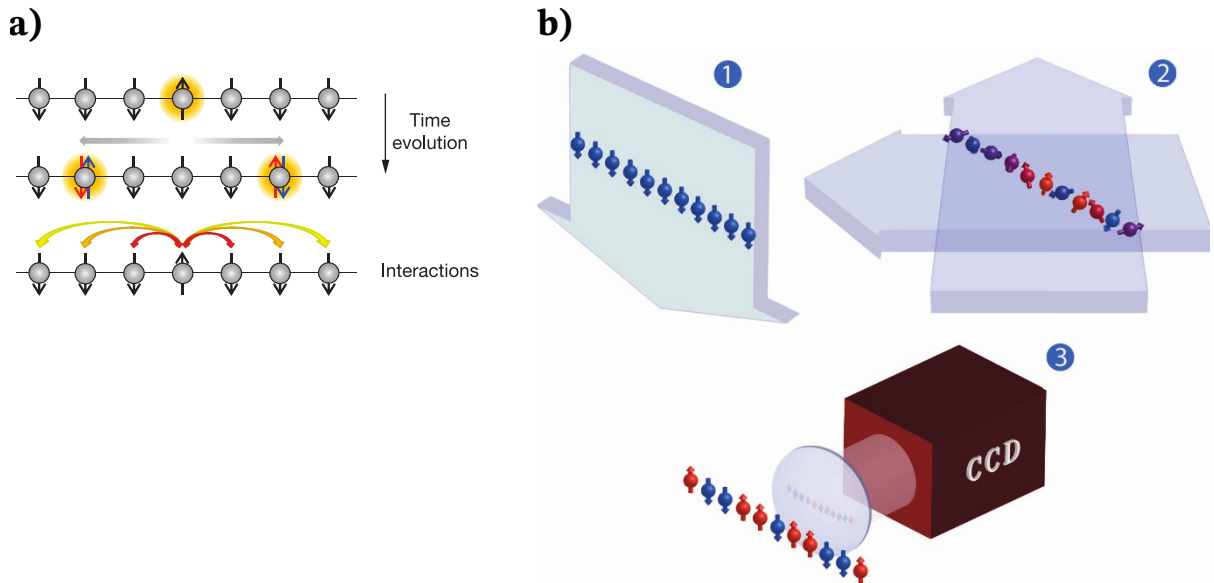


Figure 1.3: Illustration of digital quantum simulator of long-range interacting. **a)** Time evolution scheme of the long-range interacting Ising model. The initial state is locally quenched by flipping the centre spin (top row). Elementary excitations (spin waves) mediate the excitation and spread outwards (centre row) whereas some exemplary interactions in real space are shown in the bottom row. Figure from Ref. [99]. **b)** (1) sketches the initial state where all spins on the chain are optically pumped into the fully polarised state $|\downarrow_z\rangle$. (2) The system is then globally quenched by allowing it to freely evolve under a new Hamiltonian (both long-range interacting Ising model and XY model) via laser-induced ion-ion interactions. (3) The time-evolved state is measured with respect to the connected two-point correlation function in spin- z direction $C_{i,j}(t) = \langle S_i^z(t)S_j^z(t) \rangle - \langle S_i^z(t) \rangle \langle S_j^z(t) \rangle$. Figure from Ref. [100].

With single site resolution, the state can be read out by fluorescence measurements which couple one of the two internal states to a third, short-lived excited state. Above tools have been successfully used to experimentally realise usual long-range interacting spin chains, for instance the experiments on the long-range interacting Ising model by Jurcevic et al. [99] and Richerme et al. [100]. Figure 1.3 shows sketches of the experimental realisation of both experiments. Lastly, we wish to briefly mention that Rydberg atoms in optical tweezers nowadays offer a scalable and highly controllable quantum simulator platform [101–103].

1.7 Quantum information in condensed matter physics

In this section, we briefly introduce and discuss the new paradigm of entanglement entropy in condensed matter physics and the new insights that quantum information theory offers on the phases and states of matter in as well as out of equilibrium. Here, we mainly follow the lines of Refs. [4, 5, 104, 105].

The science of quantum information considers the understanding, processing, and possibly the transmission of information harnessing the effects and principles of quantum physics. Its fundamental entity of manipulation is the information content in a quantum-mechanical states which is measured by the family of Rényi entropies. Given a quantum state described by the density matrix ρ , the Rényi entropy of order n is defined as,

$$\mathcal{S}_n = \frac{1}{1-n} \log(\text{tr}(\rho^n)), \quad (1.18)$$

where $0 < n < \infty$. In the special case of $n \rightarrow 1$, the entropy of entanglement is called the von Neumann entropy which may also be written as $\mathcal{S}_{n=1} = -\text{tr}(\rho \log(\rho))$. When considering the reduced density matrix after tracing out some subsystem, Rényi entropies measure the amount of entanglement present in a quantum state given by its density matrix ρ , and allow to quantify the information content one may store inside the state. Otherwise, ρ may describe a thermal state in which case Rényi entropies also measure the *thermal* entropy present in the state. Entanglement originates in the principle that a quantum state can be in a non-factorisable superposition, in particular a many-body state, and as such it has no classical counterpart allowing for a conglomerate of classically unparalleled phenomena in the quantum realm.

In the context of condensed matter physics, of main interest is the *bipartite entanglement entropy* especially since one typically inspects pure states, such as ground states of Hamiltonians, which have no entanglement entropy on their own. It is constructed from the reduced density matrix of a subsystem after parting the entire system in two complementary subsystems, say A and B . The reduced density matrix ρ_A , which contains all information in subsystem A , is then given by the partial trace over all degrees of freedom in B of the density matrix of the entire system,

$$\rho_A = \text{tr}_B(\rho) = \sum_i \langle i_B | \rho | i_B \rangle, \quad (1.19)$$

where $\{|i_B\rangle\}$ is an orthonormal basis on B . The bipartite von Neumann entanglement entropy is hence given by $\mathcal{S}_A = -\text{tr}[\rho_A \log(\rho_A)]$. Noteworthy is that the entanglement entropy of subsystem

B is the same as that of A when the systems are complementary. Bipartite entanglement entropy in condensed matter systems has developed into a new paradigm to view, classify, and understand the behaviour of many-body states in an out of equilibrium [104]. We wish to emphasise that the bipartite entanglement entropy necessarily introduces a geometric interface by choosing a cut through the system, while this may also happen in momentum space. The latter is however not part of our focus within this thesis.

Equilibrium case In the case of equilibrium condensed matter physics, the systematic study of the bipartite entanglement entropy with a bipartition in real space such that the complementary subsystems are connected—arguably the most prevalent bipartition—has led to new profound insights in the representation of relevant degrees of freedom of ground states of gapped Hamiltonians through the celebrated area law of entanglement [5, 42], as we will further discuss below in Chapter 2. The proportionality constant of the area law, let that be a , has been shown to have critical behaviour when a quantum phase transition is approached [104, 106–110], with the prefactor behaving like $a(\lambda_c) - a(\lambda) \propto |\lambda - \lambda_c|^{\nu(d-1)}$ where ν is the critical exponent for the correlation length at that critical point. Reference [111] argues the singularity of that coefficient has been proposed to have a natural origin since the entanglement entropy of a bipartition may be interpreted as a dimensionless free energy. Moreover, we want to strongly emphasise that the scaling of bipartite entanglement entropy with system size including subleading corrections—to the area law if the system is gapped, and to the logarithmic scaling of a CFT if the system is gapless—have been successfully identified as unique signatures for different phases of matter, see review [104] for a detailed list.

Entanglement spectrum A natural generalisation of Rényi entropies is the so-called entanglement spectrum (ES) studied in the seminal work by Li and Haldane [112]. The ES is formed by the *set* of all entanglement energies ξ_j which are defined in terms of the eigenvalues of the (reduced) density matrix λ_j as $\xi_j = -\log(\lambda_j)$. Li and Haldane showed in their seminal work [112] that the ES signals topological order in the fractional quantum Hall state which cannot be observed by any local measurement [113, 114]. Given a topologically ordered ground state, the Li–Haldane conjecture states that the low-entanglement-energy ES is isomorphic to the low-energy spectrum of the conformal field theory (CFT) describing the critical states on the boundary of the topological state. Furthermore, the ES has been shown to signal quantum phase transition when it exhibits singular behaviour [115–117], as well as level-crossings [118]. In particular the latter has been shown for quantum spin chains in the short-range case. Below in Chapter 4 we will study how this paradigm of identifying phase transitions holds when long-range interactions are introduced.

Furthermore, the low-lying ES for the short-range interacting spin chain (XXZ model) as well as for the Bose–Hubbard chain, both in their respective critical regime and in open boundary conditions, and for subsystem length l_A have been shown to correspond to the energy spectrum of the Luttinger liquid as a function of magnetisation with the same Luttinger parameters as the full system [104, 119–121]. In 1D one expects to approximate the low-energy physics of a critical lattice model in terms of a Luttinger liquid—a quadratic CFT with central charge $c = 1$, as we will further detail in Chapter 4.

Entanglement Hamiltonian We may put the above-mentioned bulk–edge correspondence, meaning the ES is a feature of the edge described by the bipartition and the bulk is described by the effective CFT, in a wider context by briefly introducing the reader to the remarkable Bisognano–Wichmann (BW) theorem [122, 123]. It establishes a connection of the system Hamiltonian H with the Entanglement Hamiltonian (EH) \tilde{H}_A being defined in terms of the reduced density matrix ρ_A as,

$$\rho_A = \sum_j e^{-\xi_j} |\psi_j^A\rangle\langle\psi_j^A| =: e^{-\tilde{H}_A}. \quad (1.20)$$

The BW theorem states that the EH of a bipartite (in real space) ground state of a quantum field theory in d spatial dimensions with Lorentz invariance and local interactions is given by [122–124],

$$\tilde{H}_A = \int d^d x \beta_A(x) \mathcal{H}(x) + C, \quad (1.21)$$

where C is a constant fixing $\text{tr}(\rho_A) = 1$, $\mathcal{H}(x)$ is the Hamiltonian density, i.e. $H = \int d^d x \mathcal{H}(x)$, and $\beta_A(x) = 2\pi x$ may be interpreted as a local inverse temperature whereas x here measures the distance to the bipartition. The EH constitutes a generalisation of the ES in that the ES is the spectrum of the hermitian EH². The BW theorem thus connects the EH to the Hamiltonian of the system by weighting the Hamiltonian density $\mathcal{H}(x)$ with linear ‘local inverse temperature’. Note that the ‘linear inverse temperature’ $\beta_A(x) = 2\pi x = 1/(k_B T)$ implies a diverging ‘local temperature’ at the bipartition suggesting the degrees of freedom most relevant regarding entanglement are located on and close to the bipartition. We emphasise the BW theorem holds in any dimension, and for any type of degree of freedom, as it only requires Lorentz invariance and local interactions. Relativistic QFTs with conformal symmetry allow to extend the BW theorem to finite-volume subsystems and even finite-temperature, see review [124] and Refs. therein. Complementary to the BW theorem, CFT may be used to predict the EH in the case of finite volume and open boundary conditions [125, 126] to read as,

$$\tilde{H}_A = C \int_0^L \sin\left(\frac{\pi x}{2L}\right) \mathcal{H}(x), \quad (1.22)$$

where C is some constant fixing $\text{tr}(\rho_A) = 1$. One notices that the weighting of the Hamiltonian density is well-approximated by a linear function when considering position close to the bipartition site $x = 0$, as is the case in the BW theorem. Furthermore, in several integrable models (both gapped and gapless), the EH can be constructed in the thermodynamic limit through the corner transfer matrix (CTM) method [127–129]. Predicted by the CTM method, the EH reads [124],

$$\tilde{H}_A \propto \sum_{n=1}^{\infty} n h_n, \quad (1.23)$$

²Note that the EH always exists since the reduced density matrix is a hermitian and trace-class operator. However, in general one may not trivially infer that the EH is indeed a *local* operator intimately linked to the system Hamiltonian.

with h_n as the discrete version of the Hamiltonian density defined by $H = \sum_n h_n$. Thus, the EH, here too, follows the paradigm of the BW theorem although some of these integrable lattice models do not recover Lorentz invariance in the thermodynamic limit. Summarising, several lattice models, either gapless, gapped, integrable, or non-integrable, have been shown to host an EH that is well described by a discrete version of the BW theorem [105, 124, 130–135], although the lattice evidently breaks Lorentz invariance rendering the BW theorem formally inapplicable. Among those integrable models is the short-range XXZ model, for which the CTM predicts the EH in the gapped antiferromagnetic phase, while CFT predicts it in the gapless critical phase.

In Chapter 4, we study the EH and its operator form answering how long-range interactions alter the applicability of a discretised version of the BW theorem in the long-range XXZ model.

Out-of-equilibrium case Lastly, we wish to mention that entanglement and quantum information offer a new paradigm also in the study of out-of-equilibrium many-body systems as tools from quantum information theory found their way into this field.

The celebrated *eigenstate thermalisation hypothesis* (ETH) aims to explain when and how an isolated quantum system thermalises implying the physically well extended system acts as its own heat bath [104, 136]. The ETH states that the stationary, i.e. thermalised, reduced density matrix, following a bipartition into a local and connected region A and its complement B , is almost indistinguishable from a microcanonical thermal ensemble³ (cf. Section 1.3),

$$\lim_{t \rightarrow \infty} \lim_{N \rightarrow \infty} \rho_A(t) = \frac{1}{Z} \text{tr}_B(e^{-\beta H}), \quad (1.24)$$

where the order of the thermodynamic limit of the system size N to infinity comes before the long-time limit. If the ETH applies, one speaks of the ergodic regime. After a quantum quench as described in Section 1.4.1, the system's energy is determined as,

$$E = \begin{cases} \langle \psi_0 | H_f | \psi_0 \rangle & \text{for a global quench} \\ \langle \psi_i | H | \psi_i \rangle & \text{for a local quench} \end{cases}, \quad (1.25)$$

where in case of a global quench, $|\psi_0\rangle$ is the initial state of a global quench and H_f is the post-quench final Hamiltonian, and in case of a local quench ψ_i is the post-quench initial state and H is the (unchanged) Hamiltonian. After the stationary state is approached, and given the system conserved energy, it is according to ETH indistinguishable from a high energy eigenstate. The reduced density matrix of such a high energy eigenstate is thus expected to have an entanglement entropy very close to the thermodynamic entropy of the subsystem at the temperature corresponding to the energy of the system. The post-quench temperature is defined by

$$E = \text{tr} \left(H e^{-\frac{H}{k_B T}} \frac{1}{Z} \right), \quad (1.26)$$

³Indistinguishable here means that any generic operator with support only in the subsystem A has an expectation value that is given by $\langle O_A \rangle = \text{tr}(O_A \rho_A(t \rightarrow \infty))$. Almost here allows for small random fluctuations.

where E is given by Eq. (1.25), and H describes the post-quench Hamiltonian H_f in case of a global quench. Furthermore, the scaling of that entanglement entropy is expected to be extensive, i.e. volume law. Such scaling has successfully been verified to identify the ergodic phase of both disordered and non-disordered quantum spin chains, see e.g. Refs. [104, 137].

2 *Tensor network simulations*

for long-range interacting quantum systems

“All models are wrong, but some are useful”

— George E. P. Box

2.1 Introduction

This chapter is dedicated to introducing the reader to the basic notions and algorithms of tensor network techniques which we employ for the numerical computations throughout the rest of this thesis. This chapter is by no means an exhaustive introduction to all fields and applications of tensor networks. It is rather tailored to introduce all necessary notions and methods to simulate long-range interacting spin systems defined on a lattice. We will closely follow the notions and definitions of Refs. [5, 138–140].

The size of the Hilbert space of a quantum system consisting of N indistinguishable particles which have p degrees of freedom scales exponentially with the size like p^N implying it can grow spectacularly large. In particular, it renders the naive computation of such systems formidably challenging. Let us consider the simplest choice of N spin-1/2 particles on a chain for which the Hilbert space scales as 2^N . A chain of for example $N = 40$ is described by $2^{40} \simeq 10^{12}$ different complex numbers for which we typically need 64 bit each. We are thus immediately faced with the impracticability of saving the state of such a system on a hard drive since they tally to an incredible total of 8.8 TB of data. Things get totally out of hand when we reach scales of our every day life. Considering $N \simeq 10^{23}$ particles (order of magnitude of Avogadro’s number), we end up with a Hilbert space of dimension $\simeq 2^{10^{23}} \gg$ Number of atoms in the observable universe [141]. Simulating quantum systems is therefore notoriously difficult.

To our rescue comes a perhaps surprising fact that not all states in Hilbert space are created equal¹. Indeed, it is today known that all physically relevant states occupy a subspace being exponentially small compared to the size of the Hilbert space [142]. We will discuss in the following that a certain class of states has much more practical relevance when considering certain physical phenomena, namely the ground states of gapped Hamiltonians.

¹...neither do they have certain unalienable Rights.

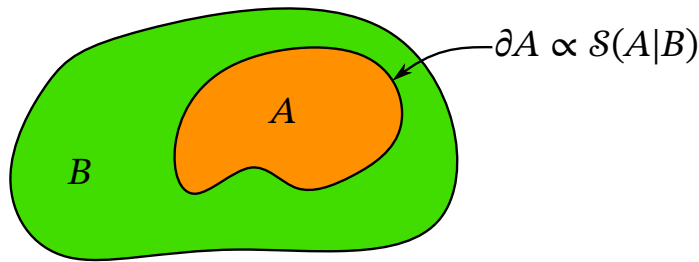


Figure 2.1: Area law of entanglement. A and B are complementary subsystems of a closed quantum system governed by a gapped Hamiltonian. When biparting the ground state in subsystem A and B , the bipartite entanglement entropy $S(A|B)$ grows with the boundary between them, $S \propto \partial A$.

2.2 Area laws of entanglement

In classical statistical mechanics, entropy quantifies an uncertainty or ignorance about the specific microstate that corresponds to an observed macrostate. It is larger in cases we need more information in order to identify the exact microstate of a system. In this classical context, the uncertainty of the exact microstate is generated by thermal fluctuations. Consequently, at zero temperature, where no thermal fluctuations occur, the entropy is identically zero and no uncertainty of the microstate arises. Furthermore, thermodynamic entropy constitutes an extensive quantity, i.e. it is proportional to the volume of the system, $S_{\text{therm}} \propto V$. In a stark contrast to this classical behaviour, quantum systems can display non-vanishing entropy even at zero temperature. This entropy of entanglement however does not arise in the pure, non-degenerate ground state $|\psi_0\rangle$ [42]. However, it only arises when considering two complementary subsystems, A and B . To see this, let us consider the entropy of entanglement quantified by the family of Rényi entropies,

$$S_n(\rho) = \frac{1}{1-n} \log(\text{tr}(\rho)^n), \quad (2.1)$$

with real positive order parameter $n \geq 0^2$. The closed quantum system at zero temperature is described by the density matrix of the ground state $\rho = |\psi_0\rangle\langle\psi_0|$. When consider two complementary subsystems, A and B , we describe the state of subsystem A by the reduced density matrix $\rho_A = \text{tr}_B(\rho) = \sum_{i_B} \langle i_B | \psi_0 \rangle \langle \psi_0 | i_B \rangle$ where $\{i_B\}$ is a basis of subsystem B . In general, the reduced density matrix ρ_A does not correspond to a pure state (unless the ground state is e.g. a product state), and the subsystem A will therefore have non-vanishing entropy of entanglement. In contrast to thermal entropy, this entropy does not arise from a lack of knowledge of the exact microstate [42]. Indeed, we just gave an example of a precise microstate and how it may have non-vanishing entropy. This non-zero entropy, and the accompanied uncertainty in the exact microstate given the measurement on subsystem A , arises due to the fundamental property of quantum systems; *entanglement* [42]. The question of how this non-vanishing entanglement entropy of a bipartite ground state scales with the system size has now been answered considering quantum Hamiltonians with an energy gap between the ground state and the first excited state, henceforth called ‘gapped’ Hamiltonians. In this context, we shall call it *the* area law of entanglement, and it states that the ground state of gapped Hamiltonians have a bipartite entanglement entropy which is proportional to the surface of

²For $n \rightarrow 1$ we obtain the von Neumann entanglement entropy $S_1 = -\text{tr}(\rho \log \rho)$.

the bipartition [5, 42, and Refs. therein]. This applies to both short-range interacting gapped Hamiltonians [143], and long-range interacting gapped Hamiltonians [46]. This principle of entropy being proportional to the surface of a region in space is in line with important results from other fields of physics where entropy has been shown to scale with the area rather than the volume [5, 42]. Examples include the seminal works by Bekenstein and Hawking on entropy of a black hole [144, 145]. More generally, they are part of the holographic principle [146], or bulk–boundary correspondence, which have profoundly influenced modern theoretical physics [5, 42]. Critical, i.e. gapless, spin Hamiltonians are described by Conformal Field Theories, e.g. a Luttinger liquid in the one dimensional case, and the entropy of entanglement of the ground state scales logarithmically with the system size, $S \propto \mathcal{O}(\log(N))$ [5].

In case of gapped systems in one spatial dimension, the area law straightforwardly implies that entanglement entropy is actually a constant as a function of system size. This has, together with the slow scaling of entanglement entropy in Luttinger liquids, important implications for the computability of spin models in one spatial dimension, as we will discuss in the following section.

2.3 Matrix product states

Previous discussion of the area law of entanglement entropy suggests that the degrees of freedom that characterise entanglement are located on the interface of the two bipartitions. In one dimensional systems with open boundary conditions, this is clearly a single point on the line and two points on the circle when considering periodic boundary conditions. We shall see that matrix product states (MPS) represent these degrees of freedom in their matrix product and thus form a natural representation of the entanglement description of a quantum state [139].

Tensors are the fundamental building blocks for those MPS. For the purpose of this thesis, a *tensor* of rank n is a multilinear function that maps n vectors onto the complex numbers \mathbb{C} . Therefore, a rank-0 tensor is a scalar number $z \in \mathbb{C}$, a rank-1 tensor is a vector x_a , and a rank-2 tensor is a matrix $A_{i,j}$. In the following, we employ a summation convention which implies that the repeated use of the same symbol as an index of a tensor is implicitly assumed to be contracted over,

$$C_{ij} = A_{is} B_{sj} = \sum_{s=1}^{D_s} A_{is} B_{sj}, \quad (2.2)$$

where we contracted over all possible values of $s \in \{1, \dots, D_s\}$. Furthermore, we adopt Penrose’s graphical notation for tensor networks and their contractions [147], which represents an n -rank tensor as a node with n open legs coming out of it, representing the n indices. For an illustration, see Fig. 2.2. The graphical notation allows for intuitive illustration of contractions and factorisation of tensors and matrices. For example, Fig. 2.3 shows the graphical equation of a singular value decomposition (SVD). The newly introduced index which is being contracted over between the diagonal matrix S and its two neighbours is generally called the *bond index*, or *link index* in the context of tensor networks.

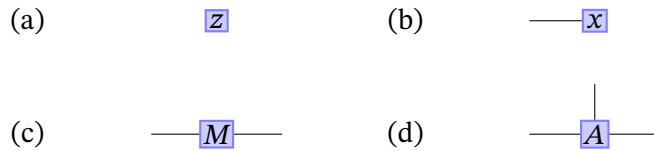


Figure 2.2: Penrose graphical tensor representation. (a) a scalar z , (b) a vector x , (c) a matrix M , and (d) a rank-3 tensor A .

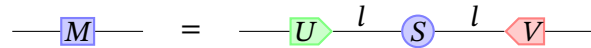


Figure 2.3: Graphical notation of the Singular Value Decomposition (SVD) theorem. Any matrix M can be factorised in the product of three matrices, $M = U \cdot S \cdot V$, whereas $U^\dagger U = \mathbb{1}$, $VV^\dagger = \mathbb{1}$, and $S = \text{diag}(\lambda_1, \lambda_2, \dots, \lambda_r)$, with r the matrix rank of M counting the non-zero singular values λ_n (not to be confused with the tensor rank). Note that U is right-orthogonal and highlighted in green, while V is left-orthogonal and highlighted in red. We labelled the internal contracted index l , which is called the *bond* or *link dimension* in the context of tensor networks, and display the diagonal matrix as a circle.

2.3.1 Quantum states as tensor networks

Let us now turn towards a graphical representation of a quantum state in a tensor network. To this end, we consider an arbitrary many-body pure state $|\psi\rangle$, defined on a lattice of local degrees of freedom (degrees of freedom) $\{\sigma_i\}$, with $\dim(\sigma_i) = d$, $i \in [1, \dots, N]$. Henceforth, we will restrict all considerations to the case of open boundary conditions (OBC). The local degrees of freedom may be spin-1/2 but indeed need not be specified for the purpose of this explanation. The full many-body wave function reads as,

$$|\psi\rangle = \sum_{\sigma_1, \dots, \sigma_N} c_{\sigma_1, \dots, \sigma_N} |\sigma_1\rangle \otimes \dots \otimes |\sigma_N\rangle, \quad (2.3)$$

where $c_{\sigma_1, \dots, \sigma_N}$ is a set of d^N complex numbers³—a direct consequence of the exponential growth of the size of the Hilbert space. Note now that $c_{\sigma_1, \dots, \sigma_N}$ fully describes the wave function in a chosen basis. Furthermore, it can be thought of as a tensor of rank N with indices $\{\sigma_i\}$ which take d different values, thus recovering d^N different entries.

As explained above, following this exponential growth and keeping track of all coefficients is an entirely un-resourceful way to describe a many-body state. The aim of MPS is to reduce the computational complexity efficiently to a scale which is computable on modern state-of-the-art computer systems. This goal is achieved by replacing this N -rank tensor with a product of lower ranked tensor, a product of rank-3 tensors, to be precise. To see how such a product of tensors is constructed, let us turn towards the SVD decomposition depicted in Fig. 2.3. As a necessary prerequisite for the SVD to work out, we must construct a matrix, or rank-2 tensor, to apply it to. For this, we start with $c_{\sigma_1, \dots, \sigma_N}$ and consider σ_1 to be the first index of the new matrix while taking $\sigma_2, \dots, \sigma_N$ as a super-index over all other degrees of freedom (note this matrix is not square). We

³Up to a normalisation constraint

consequently write $c_{\sigma_1, \dots, \sigma_N} = \Psi_{\sigma_1, (\sigma_2, \dots, \sigma_N)}$, and apply the SVD decomposition to Ψ , which yields both in an explicit tensor notation and a graphical notation,

$$c_{\sigma_1, \dots, \sigma_5} = \Psi_{\sigma_1, (\sigma_2, \dots, \sigma_N)} = A_{1l_1}^{\sigma_1} S_{l_1, l_2} V_{l_2, (\sigma_2, \dots, \sigma_N)} = A_{1l_1}^{\sigma_1} \Psi_{l_1, \sigma_2, \dots, \sigma_N} \quad (2.4)$$

$$\Leftrightarrow \begin{array}{c} \sigma_1 \quad \sigma_2 \quad \sigma_3 \quad \sigma_4 \quad \sigma_5 \\ \boxed{\Psi_{\sigma_1, (\sigma_2, \dots, \sigma_N)}} = \boxed{A_1} \text{---} \boxed{\Psi_{l_1, \sigma_2, \dots, \sigma_N}} \end{array} \quad (2.5)$$

Here, we use the SVD decomposition graphically depicted in Fig. 2.3 with the right-orthogonal tensor $A_{1l_1}^{\sigma_1}$ and the left-orthogonal tensor $V_{l_2, (\sigma_2, \dots, \sigma_N)}$ in Eq. (2.4). We then continue with contracting the diagonal matrix S into V to obtain the ‘remaining’ coefficients $\Psi_{l_1, \sigma_2, \dots, \sigma_N}$. Note that we use the shorthand notation $A_i = A_{i-1, l_i}^{\sigma_i}$ which hides all explicit indices of the rank-3 tensor (rank-2 at the boundaries) and only notes its spatial position i . Furthermore, note that we henceforth denote any left-orthogonal tensor A_i as a green arrow pointing right (cf. Eq. (2.15) for more details on the orthogonality properties), and that we do not differentiate between A_i and U_i when A_i is left-orthogonal. We continue with an SVD decomposition on the ‘remaining’ coefficient tensor by interpreting the indices (l_1, σ_2) as the left super-index and decompose $\Psi_{l_1, \sigma_2, \dots, \sigma_N}$ as,

$$A_{l_1}^{\sigma_1} \Psi_{l_1, \sigma_2, \dots, \sigma_L} = A_{1l_1}^{\sigma_1} A_{l_1, l_2}^{\sigma_1} S_{l_2, l_2'} V_{l_2', (\sigma_3, \dots, \sigma_N)} \quad (2.6)$$

$$= A_{1, l_1}^{\sigma_1} A_{l_1, l_2}^{\sigma_2} \Psi_{l_2, \sigma_3, \dots, \sigma_L} \quad (2.7)$$

$$\Leftrightarrow \begin{array}{c} \sigma_1 \quad \sigma_2 \quad \sigma_3 \quad \sigma_4 \quad \sigma_5 \\ \boxed{A_1} \text{---} \boxed{\Psi_{l_1, \sigma_2, \dots, \sigma_N}} = \boxed{A_1} \text{---} \boxed{A_2} \text{---} \boxed{\Psi_{l_2, \sigma_3, \dots, \sigma_L}} \end{array} \quad (2.8)$$

This procedure can be iterated over consecutive sites and one then ends up with,

$$A_{1, l_1}^{\sigma_1} A_{l_1, l_2}^{\sigma_2} \Psi_{l_2, \sigma_3, \dots, \sigma_5} = A_{1, l_1}^{\sigma_1} A_{l_1, l_2}^{\sigma_2} \dots A_{l_5, 1}^{\sigma_5} \quad (2.9)$$

$$\Leftrightarrow \begin{array}{c} \sigma_1 \quad \sigma_2 \quad \sigma_3 \quad \sigma_4 \quad \sigma_5 \\ \boxed{A_1} \text{---} \boxed{A_2} \text{---} \boxed{\Psi_{l_2, \sigma_3, \dots, \sigma_L}} = \boxed{A_1} \text{---} \boxed{A_2} \text{---} \boxed{A_3} \text{---} \boxed{A_4} \text{---} \boxed{A_5} \end{array} \quad (2.10)$$

Note that we abuse the symbol Ψ on both sides of the equation for different tensors which differ in rank and in composition. Above procedure, Eq. (2.4) to Eq. (2.10), has an asymmetric bias in that we started on the left end with our SVDs and proceeded rightwards with our *sweep*. Naturally, there is no reason why not to (also) start on the right end with an SVD. Considering the intermediate state of Eq. (2.8), also ‘sweeping’ with an SVD from the right yields,

$$A_{1, l_1}^{\sigma_1} A_{l_1, l_2}^{\sigma_2} \Psi_{l_2, \sigma_3, \dots, \sigma_L} = A_{1, l_1}^{\sigma_1} A_{l_1, l_2}^{\sigma_2} U_{l_2, \sigma_3, \sigma_4, l_4} S_{l_4, l_4'} V_{l_4', 1}^{\sigma_5} \quad (2.11)$$

$$= A_{1, l_1}^{\sigma_1} A_{l_1, l_2}^{\sigma_2} \Psi_{l_2, \sigma_3, \sigma_4, l_4} V_{l_4, 1}^{\sigma_5} \quad (2.12)$$

$$\Leftrightarrow \begin{array}{c} \sigma_1 \quad \sigma_2 \quad \sigma_3 \quad \sigma_4 \quad \sigma_5 \\ \boxed{A_1} \text{---} \boxed{A_2} \text{---} \boxed{\Psi_{l_2, \sigma_3, \dots, \sigma_L}} = \boxed{A_1} \text{---} \boxed{A_2} \text{---} \boxed{\Psi_{l_2, \sigma_3, \sigma_4, l_4}} \text{---} \boxed{A_5} \end{array} \quad (2.13)$$

where we again contracted the diagonal matrix into the ‘remaining’ coefficient tensor. Note also that we henceforth mark a **right-orthogonal** matrix A_i as a **red arrow pointing left** (cf. Eq. (2.16) for more details on the orthogonality properties), and note that we make no difference between A_5 and V_5 when A_5 is right-orthogonal. Similarly to above, we continue decomposing from the right via SVDs such that a single tensor somewhere in the bulk on site i remains without any well-defined orthogonality properties. This may be visualised as,

$$\begin{array}{ccccccccc}
 \sigma_1 & \sigma_2 & & \sigma_3 & \sigma_4 & & \sigma_5 & \sigma_1 & \sigma_2 & \sigma_3 & \sigma_4 & \sigma_5 \\
 \downarrow & \downarrow & & \downarrow & \downarrow & & \downarrow & \downarrow & \downarrow & \downarrow & \downarrow & \downarrow \\
 \boxed{A_1} & \boxed{A_2} & \rightarrow & \boxed{\Psi_{l_2, \sigma_3, \sigma_4, l_4}} & \leftarrow \boxed{A_5} & = & \boxed{A_1} & \boxed{A_2} & \boxed{A_3} & \leftarrow \boxed{A_4} & \leftarrow \boxed{A_5}, & (2.14)
 \end{array}$$

where we mark any tensor **without** special orthogonality features as a **blue box**. Furthermore, we denote the type of configuration as in Eq. (2.14) henceforth the mixed canonical form of an MPS, and we refer to A_3 as the ‘orthogonality centre’. By construction through the SVD, we have certain orthogonality features of the constituent left- and right-orthogonal tensors of the MPS, highlighted by the colour coding as well as their orientation, see e.g. Eq. (2.14). These orthogonality properties are defined by the singular value decomposition they originated from, cf. Fig. 2.3, and they can be graphically represented in the following relations,

$$\begin{array}{c}
 \boxed{A_1^\dagger} \leftarrow b \\
 \boxed{A_1} \leftarrow a
 \end{array}
 = \begin{array}{c}
 b \\
 a
 \end{array}
 = U_{1a}^{\sigma_1 \dagger} U_{1b}^{\sigma_1} = \delta_{ab} = (\mathbb{1})_{ab} = U_{lna}^{\sigma_n \dagger} U_{lnb}^{\sigma_n} = \begin{array}{c}
 \boxed{A_n^\dagger} \leftarrow b \\
 \boxed{A_n} \leftarrow a
 \end{array}, \quad (2.15)$$

$$\begin{array}{c}
 b \leftarrow \boxed{V_N^\dagger} \\
 a \leftarrow \boxed{V_N}
 \end{array}
 = \begin{array}{c}
 b \\
 a
 \end{array}
 = V_{a,1}^{\sigma_N} V_{b1}^{\sigma_N \dagger} = \delta_{ab} = (\mathbb{1})_{ab} = V_{aln}^{\sigma_n} V_{bn}^{\sigma_n \dagger} = \begin{array}{c}
 b \leftarrow \boxed{V_n^\dagger} \\
 a \leftarrow \boxed{V_n}
 \end{array}, \quad (2.16)$$

where a and b are the explicit labels of the indices of the corresponding tensor, and on the left-hand side of both equations we graphically represent the boundary tensors of an MPS, while the bulk tensors are depicted on the right-hand side. Furthermore, the solid line without any box representing a tensor is the symbol for the identity matrix $\mathbb{1}$, i.e. the Kronecker symbol δ_{ab} . Thus, the contractions of right- and left-orthogonal matrices, respectively, yields by definition the identity over the remaining indices. Keeping track of the orthogonality of all tensors constituting an MPS is highly advantageous as it allows one to compute significant parts of a tensor-network contraction trivially and analytically. Surely, any numerical simulation may then profit from the reduced numerical effort it has to perform. As an example, consider the norm of any MPS given by,

$$\langle \psi | \psi \rangle = \begin{array}{cccccc}
 \boxed{A_1^\dagger} & \boxed{A_2^\dagger} & \boxed{A_3^\dagger} & \boxed{A_4^\dagger} & \boxed{A_5^\dagger} \\
 \downarrow & \downarrow & \downarrow & \downarrow & \downarrow \\
 \boxed{A_1} & \boxed{A_2} & \boxed{A_3} & \boxed{A_4} & \boxed{A_5}
 \end{array}
 = \begin{array}{ccc}
 \boxed{A_2^\dagger} & \boxed{A_3^\dagger} & \boxed{A_4^\dagger} \\
 \downarrow & \downarrow & \downarrow \\
 \boxed{A_2} & \boxed{A_3} & \boxed{A_4}
 \end{array}
 = \begin{array}{c}
 \boxed{A_3^\dagger} \\
 \downarrow \\
 \boxed{A_3}
 \end{array}
 = 1, \quad (2.17)$$

which benefits greatly from the analytical contraction. We can immediately normalise the entire state by simply rescaling only a single tensor in the orthogonality centre without changing any of the other $N - 1$ tensors. This holds also should the orthogonality centre be comprised of n -tensors. One then encounters a higher computational cost for computing the norm but one still may rescale any tensor in the orthogonality centre.

Shifting the orthogonality centre Since the orthogonality centre plays an important role for the efficient computation of tensor-network contractions, we wish to briefly introduce the reader how to alter and shift it. One can swiftly move the orthogonality centre iteratively to the right or left with an SVD on the current orthogonality centre. To this end, the physical degree of freedom on the current orthogonality centre, σ_n , is considered as part of the *left* super index,

$$A_{l_{n-1} l_n}^{\sigma_n} = M_{(\sigma_n l_{n-1}), l_n} = U_{(\sigma_n l_{n-1}), l'_n} S_{l'_n l'_n} V'_{l'_n l_{n+1}} \quad (2.18)$$

$$\begin{array}{c} | \\ \text{---} A^n \text{---} \\ | \end{array} = \begin{array}{c} | \\ \text{---} U_n \text{---} S_n \text{---} V_n \text{---} \\ | \end{array} \quad (2.19)$$

to translate the orthogonality centre to the *right*. Note that we depict the diagonal tensors, e.g. S_n above, with a circle. Similarly, one interprets σ_n as part of the *right* super index,

$$A_{l_{n-1} l_n}^{\sigma_n} = M_{l_{n-1}, (\sigma_n l_n)} = U_{l_{n-1} l'_{n-1}} S'_{l'_{n-1} l'_{n-1}} V'_{l'_{n-1} (\sigma_n l_n)} \quad (2.20)$$

$$\begin{array}{c} | \\ \text{---} A^n \text{---} \\ | \end{array} = \begin{array}{c} | \\ \text{---} U_n \text{---} S_n \text{---} V_n \text{---} \\ | \end{array} \quad (2.21)$$

in order to shift the orthogonality centre to the *left*. In both cases the two matrices without physical index σ_n are contracted into the left or right tensor, respectively, to form the new orthogonality centre. Graphically, this shift of the orthogonality centre can be represented as follows. One shifts the orthogonality centre to the right as,

$$\begin{array}{c} \sigma_1 \quad \sigma_2 \quad \sigma_3 \quad \sigma_4 \quad \sigma_5 \\ \begin{array}{c} | \quad | \quad | \quad | \quad | \\ \text{---} A_1 \text{---} A_2 \text{---} A_3 \text{---} A_4 \text{---} A_5 \\ | \quad | \quad | \quad | \quad | \end{array} = \begin{array}{c} \sigma_1 \quad \sigma_2 \quad \sigma_3 \quad \sigma_4 \quad \sigma_5 \\ \begin{array}{c} | \quad | \quad | \quad | \quad | \\ \text{---} A_1 \text{---} A_2 \text{---} U_3 \text{---} S_3 \text{---} V_3 \text{---} A_4 \text{---} A_5 \\ | \quad | \quad | \quad | \quad | \end{array} \\ \\ \begin{array}{c} \sigma_1 \quad \sigma_2 \quad \sigma_3 \quad \sigma_4 \quad \sigma_5 \\ \begin{array}{c} | \quad | \quad | \quad | \quad | \\ \text{---} A_1 \text{---} A_2 \text{---} A_3 \text{---} A_4 \text{---} A_5 \\ | \quad | \quad | \quad | \quad | \end{array} \end{array} \end{array} \quad (2.22)$$

and similarly, one shifts it to the left as,

$$\begin{array}{c} \sigma_1 \quad \sigma_2 \quad \sigma_3 \quad \sigma_4 \quad \sigma_5 \\ \begin{array}{c} | \quad | \quad | \quad | \quad | \\ \text{---} A_1 \text{---} A_2 \text{---} A_3 \text{---} A_4 \text{---} A_5 \\ | \quad | \quad | \quad | \quad | \end{array} = \begin{array}{c} \sigma_1 \quad \sigma_2 \quad \sigma_3 \quad \sigma_4 \quad \sigma_5 \\ \begin{array}{c} | \quad | \quad | \quad | \quad | \\ \text{---} A_1 \text{---} A_2 \text{---} U_3 \text{---} S_3 \text{---} V_3 \text{---} A_4 \text{---} A_5 \\ | \quad | \quad | \quad | \quad | \end{array} \\ \\ \begin{array}{c} \sigma_1 \quad \sigma_2 \quad \sigma_3 \quad \sigma_4 \quad \sigma_5 \\ \begin{array}{c} | \quad | \quad | \quad | \quad | \\ \text{---} A_1 \text{---} A_2 \text{---} A_3 \text{---} A_4 \text{---} A_5 \\ | \quad | \quad | \quad | \quad | \end{array} \end{array} \end{array} \quad (2.23)$$

In the context of entanglement, one can make use of another form of mixed-canonical MPS where the orthogonality centre is located *on the link* j between two tensors with physical indices j

and $j + 1$. To this end and to nobodies surprise, we utilise the SVD on the orthogonality centre but follow a different contraction as in,

$$\begin{aligned}
 & \begin{array}{ccccccccc}
 \sigma_1 & \sigma_2 & \sigma_3 & \sigma_4 & \sigma_5 & \sigma_1 & \sigma_2 & & \sigma_3 & \sigma_4 & \sigma_5 \\
 \text{A}_1 & \text{A}_2 & \text{A}_3 & \text{A}_4 & \text{A}_5 & = & \text{A}_1 & \text{A}_2 & \text{U}_3 & \text{S}_3 & \text{V}_3 & \text{A}_4 & \text{A}_5 \\
 \end{array} \\
 & = \begin{array}{ccccccccc}
 \sigma_1 & \sigma_2 & & \sigma_3 & \sigma_4 & \sigma_5 & & & & & & & \\
 \text{A}_1 & \text{A}'_2 & \text{S}_3 & \text{A}_3 & \text{A}_4 & \text{A}_5 & & & & & & & \\
 \end{array}, \tag{2.24}
 \end{aligned}$$

where we have contracted the right-orthogonal tensors A_3 and U_3 into a single right-orthogonal tensor $A'_3 = A_3 \cdot U_3$. Similarly to above, one can shift the orthogonality centre on the link j , left and rightwards by contracting it into the respective neighbouring tensor and a subsequent SVD restores the orthogonality centre on a neighbouring link. We shall leave the graphical equations out for brevity.

2.3.2 Entanglement and geometry

In this subsection, we briefly introduce the reader to the concept that entanglement present in an MPS induces an effective lattice geometry in which the state has an efficient and effective representation [139, 148]. In the context of this work, we only consider MPS in open boundary conditions (OBC). Here, we examine how this presumption implies a geometric shape onto entanglement, and observe how an MPS is particularly suited for this geometry. There are other types of tensor networks whose geometry are better suited for different entanglement properties ($1D$, $2D$, critical systems, etc.). Figure 2.4 displays a non-exhaustive list of different tensor networks used in practice to represent quantum many-body wave functions. We briefly recite the descriptions of Ref. [148] for a rough overview of their properties and applications.

MPS, as depicted in Fig. 2.4(a), are $1D$ chains of tensors which generally represent the low-energy eigenstates of a gapped $1D$ Hamiltonian [143, 149]. They satisfy the $1D$ area law of entanglement. Moreover, expectation values of local operators can be efficiently computed albeit they can only represent states with finite correlation length [139]. Therefore, they are nominally not suited for representing quantum critical states. However, their comparatively high efficiency, and ease of use have lead to an extensive body of research including finite-size scaling and finite-entanglement scaling aiming to study $1D$ quantum critical phenomena through MPS [148].

PEPS, as in Fig. 2.4(c) for the particular case of a square lattice, are $2D$ arrays of tensors. They are known to capture the correct correlation structure of low-energy eigenstates of $2D$ local Hamiltonians satisfying the $2D$ area law, as well as of $2D$ thermal states[148]. Unlike MPS, PEPS can handle critical, i.e. diverging correlation lengths. However, since they cannot be contracted *both* efficiently and exactly, approximate methods have been developed for manipulating them. They can also represent topologically order states of matter, both chiral and non-chiral. However, they are still actively being researched and whether they support chiral topological order with gapped bulk excitations is an open question [148].

Multiscale entanglement renormalization ansatz (MERA) structures are tensor networks exemplary depicted in Fig. 2.4(d). They are tree-like structures of isometric and unitary tensors whereas

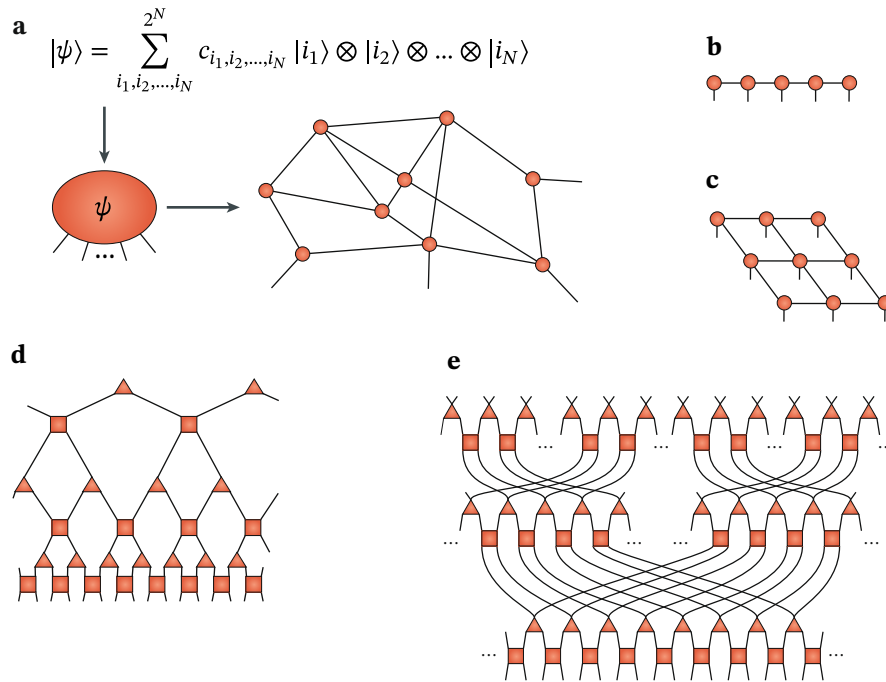


Figure 2.4: **a**: The coefficients c_{i_1, i_2, \dots, i_N} of a quantum many-body wave function with N sites, where each degree of freedom has local dimension of 2, can be thought of as a tensor with exponentially many coefficients in the system size N . One can account for the internal structure and the amount of entanglement by a suitable graph of interconnected tensors (a tensor network) with ancillary indices. The tensor network in **a** is supposed to be generic. **b–e**: concrete examples of tensor networks used in practice to represent quantum many-body states. **b**: Matrix product state (MPS), **c**: projected entangled pair state for a square lattice (PEPS), **d**: multiscale entanglement renormalization ansatz (MERA), **e**: branching MERA. Figure copied and adapted from Ref. [148].

the unitary operators account for entanglement between neighbouring sites, and have a number of remarkable properties. First, they can exhibit the entanglement entropy of critical 1D systems. Moreover, they are efficiently contractable for the purpose of expectation values. They have an extra holographic dimension that encodes a renormalization scale, related to the ‘entanglement renormalization’. Finally, MERA structures are believed to be linked to the AdS/CFT correspondence in quantum gravity [148, 150, 151].

A branching MERA (bMERA) is illustrated in Fig. 2.4(e). Being similar to MERAs with the addition that at every renormalisation scale a bMERA decouples into several copies. They therefore exhibit an arbitrary scaling of block entanglement entropy thus allowing the representation of the entanglement structure of systems that violate the area law. Physically speaking, this structure accounts for the decoupling of degrees of freedom at different renormalisation scales (e.g. spin-charge separation in electronic solid-state systems) [148]

Henceforth, we focus exclusively on 1D matrix product states with open boundary conditions. We have seen above in Section 2.3.1 how one can construct an MPS from any set of coefficients describing a many-body wave function. To understand how entropy is shaped by the geometry of such a tensor network, let us consider an exemplary quantum state $|\psi\rangle$, as well as a bipartition of the 1D chain into subsystem A and B . The state on the entire system and its two subsystems is then naturally described by the Schmidt decomposition of $|\psi\rangle$,

$$|\psi\rangle = \sum_{\sigma_1, \dots, \sigma_L} c_{\sigma_1, \dots, \sigma_N} |\sigma_1, \dots, \sigma_L\rangle = \sum_{l=1}^r \lambda_l |\psi_l^A\rangle \otimes |\psi_l^B\rangle, \quad (2.25)$$

where $\{|\psi_l^{A,B}\rangle\}$ is an orthonormal basis of subsystem A, B . The Schmidt decomposition of a quantum state can then be readily computed by its MPS representation when using SVDs to place the diagonal matrix of singular values on the link of the bipartition as in Eq. (2.24),

$$|\psi\rangle = \underbrace{\overset{\sigma_1}{A_1} \text{---} \overset{\sigma_2}{A_2} \text{---} \overset{\sigma_3}{A_3}}_{|\psi_{l_3}^A\rangle} \text{---} \overset{\sigma_3}{S_3} \text{---} \underbrace{\overset{\sigma_4}{A_4} \text{---} \overset{\sigma_5}{A_5}}_{|\psi_{l_4}^B\rangle}, \quad (2.26)$$

$\lambda_{l_3} \delta_{l_3, l_4}$

where we identify the elements of the Schmidt decomposition Eq. (2.25) by coloured braces below. Therefore, any mixed canonical form where the orthogonal centre is located on the link, one finds an associated Schmidt decomposition of the quantum state represented by the MPS. Note that the orthogonal centre on the link may be readily shifted following the instructions in Eqs. (2.22)

and (2.23) thereby moving the bipartition of the associated Schmidt decomposition. The reduced density matrix on subsystem A may then be written as,

$$\rho_A = \text{tr}_B(|\psi\rangle\langle\psi|) = \sum_{l=1}^r |\lambda_l|^2 |\psi_l^A\rangle\langle\psi_l^A| \quad (2.27)$$

$$= \text{tr}_B \begin{array}{c} \begin{array}{cccccc} | & & & & & | \\ \text{A}_1 & \text{A}_2 & \text{A}_3 & \text{S}_3 & \text{A}_4 & \text{A}_5 \\ | & & & & & | \end{array} \\ \begin{array}{cccccc} | & & & & & | \\ \text{A}_1^\dagger & \text{A}_2^\dagger & \text{A}_3^\dagger & \text{S}_3 & \text{A}_4^\dagger & \text{A}_5^\dagger \\ | & & & & & | \end{array} \end{array} \quad (2.28)$$

$$= \begin{array}{c} \begin{array}{cccccc} | & & & & & | \\ \text{A}_1 & \text{A}_2 & \text{A}_3 & \text{S}_3 & \text{A}_4 & \text{A}_5 \\ | & & & & & | \end{array} \\ \begin{array}{cccccc} | & & & & & | \\ \text{A}_1^\dagger & \text{A}_2^\dagger & \text{A}_3^\dagger & \text{S}_3 & \text{A}_4^\dagger & \text{A}_5^\dagger \\ | & & & & & | \end{array} \end{array} \quad (2.29)$$

$$= \begin{array}{c} \begin{array}{cccc} | & & & | \\ \text{A}_1 & \text{A}_2 & \text{A}_3 & \text{S}_3 \\ | & & & | \end{array} \\ \begin{array}{cccc} | & & & | \\ \text{A}_1^\dagger & \text{A}_2^\dagger & \text{A}_3^\dagger & \text{S}_3 \\ | & & & | \end{array} \end{array} \cdot (S_3)^2 \quad (2.30)$$

We hence find for the trace of ρ_A^n the expression,

$$\text{tr}(\rho_A^n) = \text{tr} \left(\left(\begin{array}{c} \begin{array}{cccc} | & & & | \\ \text{A}_1 & \text{A}_2 & \text{A}_3 & \text{S}_3 \\ | & & & | \end{array} \\ \begin{array}{cccc} | & & & | \\ \text{A}_1^\dagger & \text{A}_2^\dagger & \text{A}_3^\dagger & \text{S}_3 \\ | & & & | \end{array} \end{array} \right)^n \right) = \left(\begin{array}{c} \text{S}_3 \end{array} \right)^{2n} \quad (2.31)$$

$$= \text{tr} \left(\begin{array}{c} \text{S}_3 \end{array} \right)^{2n} = \sum_i ((S_3)_{i,i})^{2n}, \quad (2.32)$$

and thus conclude the entanglement entropy is given by,

$$\mathcal{S}_n = \frac{1}{1-n} \log(\text{tr} \rho_A^n), \quad (2.33)$$

$$= \frac{1}{1-n} \log \left(\begin{array}{c} \text{S}_3 \end{array} \right)^{2n}. \quad (2.34)$$

In above calculation, we made use of the orthogonality relations, Eqs. (2.15) and (2.16), to simplify the expression of the reduced density matrix. Our analytic computation elevates the numerical one as we can simply skip the contraction over the orthogonal matrices knowing the contractions over those tensors yields a trivial identity. This is of course equivalent to the tensor notation of Eq. (2.25) and Eq. (2.27). Furthermore, we can see in Eq. (2.30) the visual depiction of Eq. (2.27), showing

the entanglement in the state being encoded in the singular values S_j ‘living on’ the bipartition link j (in the graphic $j = 3$). In tensor notation, we may compute the Rényi entropy explicitly yielding,

$$\mathcal{S}_n = \frac{1}{1-n} \log(\text{tr}(\rho_A)^n) = \frac{1}{1-n} \log\left(\sum_{i=1}^r (S)_{ii}^{2n}\right), \quad (2.35)$$

from which we follow that $\max(\mathcal{S}) = \mathcal{O}(\log(r))$. Note that given the bipartition that defines A , the matrix rank r (not the tensor rank) determines the maximum amount of entropy the tensor network can represent. One can now see how the geometry of entanglement is induced through the geometry of the tensor network. Observe in Eq. (2.30) and subsequent calculation of the entanglement entropy that an MPS precisely relates any interface of different regions in space to a tensor product structure whose characteristics define the entanglement properties of the state at that interface. The fact that such an interface in an MPS is always of a dimension smaller than the original space is a manifestation of the area law for the entanglement entropy [5].

Let us now consider a quantum system in open boundary conditions and observe that an MPS are naturally suited for these types of systems. Since we impose open boundary conditions, the first, leftmost tensor has obviously no left neighbouring degree of freedom. The single degree of freedom on site 1 is described by a $d \times d$ reduced density matrix (d being the local dimension) when taking the partial trace over the remainder of the system. The dimension of the link from site 1 to 2 represents the number of non-zero eigenvalues of the reduced density matrix of the single, leftmost degree of freedom, cf. Eqs. (2.27) and (2.30). Therefore, the link l_1 has dimension at most the local dimension $l_1 \leq d$. Continuing and considering a bipartition on the second link, we find the two leftmost degrees of freedom left being described by a $d^2 \times d^2$ density matrix. Thus, the dimension of the link l_2 is at most d^2 , etc. Clearly, this argument applies due to reflection symmetry to the right end of the open chain as well. We therefore conclude that the local link dimension l_n is maximum in the centre of the chain and decreases towards the boundaries,

$$l_1 \leq d \leq l_2 \leq d^2 \leq \dots \leq l_{N/2} \leq d^{N/2}, \quad (2.36)$$

$$l_N \leq d \leq l_{N-1} \leq d^2 \leq \dots \leq l_{N/2} \leq d^{N/2} \quad (2.37)$$

$$\chi_m := \max_{n=1, \dots, N} \{l_n\} \quad (2.38)$$

In the following, we shall refer to $\chi_m = \max_n \{l_n\}$ as the maximum link dimension. Note the exponential increase in subsystem size of theoretically possible entanglement. The endeavour of describing a many-body wave function more efficiently as a tensor network therefore hinges on the relation between maximum entanglement in the state we want to describe as an MPS and the ‘reasonable’, i.e. not exponential, scaling of maximum link dimension χ_m with system size. As described above in Section 2.2, to our rescue comes the area law of entanglement. Ground states of gapped Hamiltonians actually do not fill out above bounds Eq. (2.36), and their entanglement entropy does not scale exponentially with system size. Furthermore, note that periodic boundary conditions (PBC) would not allow for above consideration and instead naturally induce more entanglement since there is a second interface (in 1D) such that entanglement entropy in PBC is for all interfaces of the order $\mathcal{O}(d^{N/2})$.

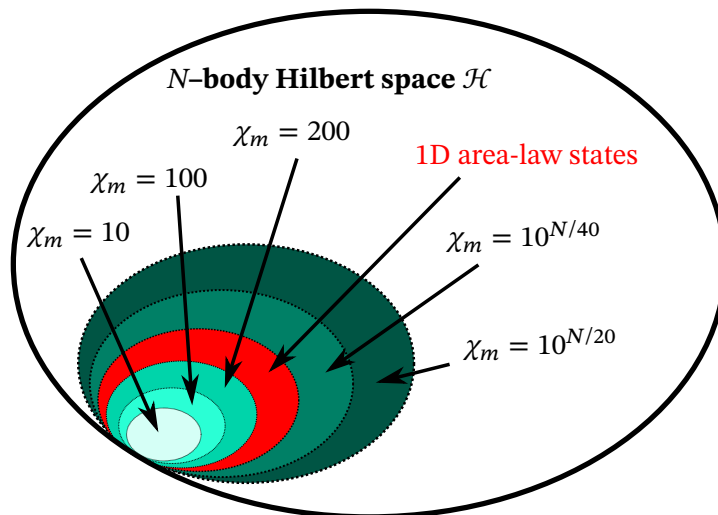


Figure 2.5: Onion-like growth of the submanifold of MPS with link dimension χ_m inside an N -particle many-body Hilbert space \mathcal{H} in 1 spatial dimension. With larger link dimension, the MPS submanifold covers more of the many-body Hilbert space, including the area-law states in 1D, and when χ_m scales exponentially also the entire Hilbert space eventually. Note the concrete numbers are exemplary, and the corresponding areas are not to scale. Adapted from [139].

In the following, we denote it as χ_m and view it as a numerical parameter characterising the size of the submanifold of Hilbert space we approximate with the given tensor network, as well as a quantitative estimate of our numerical effort. Figure 2.5 is a sketch of this growth of the submanifold with maximum link dimension χ_m . Crucially, the entanglement entropy of a gapped Hamiltonian is a constant not diverging with system size. Thus, we may not only represent the ground state of a finite system with finite link dimension (i.e. computational effort) but instead may represent the ground state of an infinite system in 1D with finite but sufficiently large link dimension!

2.3.3 Compression of a Matrix Product State

In this subsection, we detail the two approaches for an approximate compression of an MPS following Ref. [138]. Either, we compress an MPS via SVD or we use a variational approach. In the following, we are advertising for the subsequent order of first compression via SVD and then taking this result as the initial starting point for a variational optimisation. Later, we will discuss how to use this method to measure the entanglement witness called geometric entanglement (cf. Section 2.A.1). Compressing an MPS to obtain an approximate yet more resourceful MPS is an essential technique when using tensor network methods. It is particularly useful after adding two MPS since the bond dimension of their sum is the product of each bond dimension [138]. More importantly for the study that follows, we will use these techniques to construct the observable of geometric entanglement [152, 153], a novel entanglement witness that measures the geometric distance in Hilbert

space of a given state to its closest product state. To this end, we consider for both approaches an MPS in the Schmidt decomposition with the bipartition on link p ,

$$|\psi\rangle = \begin{array}{c} \sigma_1 \quad \quad \quad \sigma_p \quad \quad \quad \sigma_{p+1} \quad \quad \quad \sigma_N \\ \text{---} \langle A_1 | \text{---} \dots \text{---} \langle A_p | \text{---} S^p \text{---} \langle A_{p+1} | \text{---} \dots \text{---} \langle A_N | \end{array} \quad (2.39)$$

$$= A_{1,l_1}^{\sigma_1} \dots A_{l_{p-1},l_p}^{\sigma_p} S_{l_p,l'_p}^p A_{l'_p,l_{p-1}}^{\sigma_{p+1}} \dots A_{l_N,1}^{\sigma_N} \quad (2.40)$$

$$= \sum_{l_p}^{\chi_m} s_{l_p} |\psi_{l_p}^A\rangle \otimes |\psi_{l_p}^B\rangle, \quad (2.41)$$

where $s_i = (S)_{i,i}$ and the $\{l_n\}$ have a maximum link dimension χ_m . We now seek to find the best approximate MPS $|\tilde{\psi}\rangle$ of the given MPS $|\psi\rangle$ whereas $|\tilde{\psi}\rangle$ has maximum link dimension $\tilde{\chi}_m < \chi_m$.

2.3.3.1 Compressing an MPS via SVD

Here, we wish to detail the algorithm how to compress an MPS through repeated application of an SVD. The singular values of this bipartition Eq. (2.41) can be readily read off to be the diagonal (and only) entries of S^p (labelled s_{l_p}) of which there are χ_m many. This prescription lends itself to a natural truncation method: simply retaining only $\tilde{\chi}_m < \chi_m$ of all stored singular values and discarding the corresponding orthonormal basis states $|\psi_{l_p}^{A,B}\rangle$ of subsystem A and B . In the language of tensor networks, this corresponds to discarding the $\chi_m - \tilde{\chi}_m$ last rows and columns of the corresponding tensors left and right tensors, respectively. To see this, consider the transformation following the compression detailed above,

$$\dots \text{---} \langle A_p | \text{---} l_p \text{---} S^p \text{---} l'_p \text{---} \langle A_{p+1} | \text{---} \dots \rightarrow \dots \text{---} \langle \tilde{A}_p | \text{---} l_p \text{---} \tilde{S}^p \text{---} l'_p \text{---} \langle \tilde{A}_{p+1} | \text{---} \dots \quad (2.42)$$

$$\sum_{l_p, l'_p=1}^{\chi_m} A_{l_{p-1}, l_p}^{\sigma_p} S_{l_p, l'_p}^p A_{l'_p, l_{p-1}}^{\sigma_{p+1}} \rightarrow \sum_{l_p, l'_p=1}^{\tilde{\chi}_m} \tilde{A}_{l_{p-1}, l_p}^{\sigma_p} \tilde{S}_{l_p, l'_p}^p \tilde{A}_{l'_p, l_{p-1}}^{\sigma_{p+1}}, \quad (2.43)$$

where we indicated the larger link dimension as a wider line between the diagonal matrix of singular values and its two neighbouring tensors. Note that we collect the uncompressed tensors (A_1, \dots, A_N) in the vector $\mathbf{A} = (A_1, \dots, A_N)$ while we denote the compressed versions with a tilde as $\tilde{\mathbf{A}} = (\tilde{A}_1, \dots, \tilde{A}_N)$. Once the information is discarded, one has to rescale the remaining singular values such that the state is normalised to unity again. This procedure rests on a single Schmidt decomposition with orthogonality centre on site p (or $p - 1$); we therefore reduce the link dimension on all sites by starting say on the left at link $p = 1$ and shift the orthogonality centre to the right as described above (cf. Eq. (2.22)) while reducing the link dimension. A notable disadvantage of this method is that the compression is not symmetric with respect to parity. When shifting the orthogonality centre the new orthogonality centre is constructed with an already compressed \tilde{U} (\tilde{V}), i.e. $\tilde{U}(\tilde{V})$ with fewer rows (columns), when shifting to the left (right), cf. Eqs. (2.22) and (2.23). Therefore, the sweep from left to right generally yields a different result for the compressed MPS as the sweep from right to left considering the same constituent matrix A^{σ_n} .

2.3.3.2 Compressing an MPS via iterative variation

As a variational approach, the optimal iterative compression happens when one starts with a good guess on what a close MPS with lower link dimension might look like. Then, one varies each of the constituent matrices A^{σ_n} in the MPS iteratively to approach the best approximation in the lower link dimension manifold. The weight function to be minimised is naturally the two norm of the difference vector in Hilbert space $W = \|\psi\rangle - |\tilde{\psi}\rangle\|^2$. This implies the minimisation of

$$W(\tilde{\mathbf{A}}, \tilde{\mathbf{A}}^\dagger) = \langle \psi(\mathbf{A}^\dagger) | \psi(\mathbf{A}) \rangle - \langle \tilde{\psi}(\tilde{\mathbf{A}}^\dagger) | \psi(\mathbf{A}) \rangle - \langle \psi(\mathbf{A}^\dagger) | \tilde{\psi}(\tilde{\mathbf{A}}) \rangle + \langle \tilde{\psi}(\tilde{\mathbf{A}}^\dagger) | \tilde{\psi}(\tilde{\mathbf{A}}) \rangle, \quad (2.44)$$

with respect to $|\tilde{\psi}\rangle$. Again, we note the uncompressed original tensors as $(A^{\sigma_1}, \dots, A^{\sigma_N})$ while we mark its compressed counterpart with a tilde as, $(\tilde{A}^{\sigma_1}, \dots, \tilde{A}^{\sigma_N})$. Note that as we have seen above in the SVD compression approach in Section 2.3.3.1, varying the matrices $(\tilde{A}^{\sigma_1}, \dots, \tilde{A}^{\sigma_N}) = \tilde{\mathbf{A}}$ that make up the MPS of $|\tilde{\psi}\rangle$ will break its normalisation. Thus, it is indeed meaningful to include the respective norms in the minimisation process. Considering the constituent matrices \tilde{A}^{σ_n} , the minimisation of Eq. (2.44) is a highly non-linear optimisation problem which we are tackling iteratively site by site from left to right or vice versa. This one-sided sweep is then repeated an even number of times until desired convergence of the Hilbert-space distance is reached. The updated $\tilde{A}_{l_{n-1}, l_n}^{\sigma_n}$ is given by the point where $W(\tilde{\psi})$ is minimal with respect to a change in $\tilde{A}_{l_{n-1}, l_n}^{\sigma_n \dagger}$ since we consider $|\psi\rangle = |\psi(\mathbf{A})\rangle$ and $\langle \psi| = \langle \psi(\mathbf{A}^\dagger)|$ independently. Obviously, only two terms in Eq. (2.44) contain A^\dagger explicitly, implying

$$0 \stackrel{!}{=} \frac{\partial}{\partial \tilde{A}_{l_{n-1}, l_n}^{\sigma_n \dagger}} W(\psi) = \frac{\partial}{\partial \tilde{A}_{l_{n-1}, l_n}^{\sigma_n \dagger}} (\langle \tilde{\psi}(\tilde{\mathbf{A}}^\dagger) | \tilde{\psi}(\tilde{\mathbf{A}}) \rangle - \langle \tilde{\psi}(\tilde{\mathbf{A}}^\dagger) | \psi(\mathbf{A}) \rangle), \quad (2.45)$$

$$\Leftrightarrow \frac{\partial}{\partial \tilde{A}_{l_{n-1}, l_n}^{\sigma_n \dagger}} \langle \tilde{\psi}(\tilde{\mathbf{A}}^\dagger) | \tilde{\psi}(\tilde{\mathbf{A}}) \rangle = \frac{\partial}{\partial \tilde{A}_{l_{n-1}, l_n}^{\sigma_n \dagger}} \langle \tilde{\psi}(\tilde{\mathbf{A}}^\dagger) | \psi(\mathbf{A}) \rangle \quad (2.46)$$

We therefore find after performing the derivative,

$$\begin{aligned} & \tilde{A}_{l'_1}^{\sigma_1 \dagger} \tilde{A}_{l_1}^{\sigma_1} \cdots \tilde{A}_{l'_{n-2}, l'_{n-1}}^{\sigma_{n-1} \dagger} \tilde{A}_{l_{n-2}, l_{n-1}}^{\sigma_{n-1}} \cdot \tilde{A}_{l_{n-1}, l_n}^{\sigma_n} \cdot \tilde{A}_{l'_n, l'_{n+1}}^{\sigma_{n+1} \dagger} \tilde{A}_{l_n, l_{n+1}}^{\sigma_{n+1}} \cdots \tilde{A}_{l'_N}^{\sigma_N \dagger} \tilde{A}_{l_N}^{\sigma_N} \\ &= \tilde{A}_{l'_1}^{\sigma_1 \dagger} \tilde{A}_{l_1}^{\sigma_1} \cdots \tilde{A}_{l'_{n-2}, l'_{n-1}}^{\sigma_{n-1} \dagger} \tilde{A}_{l_{n-2}, l_{n-1}}^{\sigma_{n-1}} \cdot A_{l_{n-1}, l_n}^{\sigma_n} \cdot \tilde{A}_{l'_n, l'_{n+1}}^{\sigma_{n+1} \dagger} \tilde{A}_{l_n, l_{n+1}}^{\sigma_{n+1}} \cdots \tilde{A}_{l'_N}^{\sigma_N \dagger} \tilde{A}_{l_N}^{\sigma_N}. \end{aligned} \quad (2.47)$$

In case of mixed canonical orthogonality where the centre is located on site n , we may immediately and trivially contract the left $(\tilde{A}_{1, \dots, n-1}^\dagger \tilde{A}_{1, \dots, n-1})$ and right-orthogonal matrices $(\tilde{A}_{n+1, \dots, N} \tilde{A}_{n+1, \dots, N}^\dagger)$ on the left-hand side of Eq. (2.47) yielding,

$$\tilde{A}_{l_{n-1}, l_n}^{\sigma_n} = L_{l_{n-1}, l'_{n-1}} \cdot A_{l'_{n-1}, l'_n}^{\sigma_n} \cdot R_{l'_n, l_n}, \quad (2.48)$$

where we introduced the contracted tensors $L_{l_{n-1}, l'_{n-1}} = \tilde{A}_{l'_1}^{\sigma_1 \dagger} A_{l_1}^{\sigma_1} \dots \tilde{A}_{l'_{n-2}, l'_{n-1}}^{\sigma_{n-1} \dagger} A_{l_{n-2}, l_{n-1}}^{\sigma_{n-1}}$ and $R_{l_n, l_n} = \tilde{A}_{l'_n, l'_{n+1}}^{\sigma_{n+1} \dagger} A_{l_n, l_{n+1}}^{\sigma_{n+1}} \dots \tilde{A}_{l'_N}^{\sigma_N \dagger} A_{l_N}^{\sigma_N}$. We may represent these equations graphically as,

$$\frac{\partial}{\partial \tilde{A}_{l_{n-1}, l_n}^{\sigma_n \dagger}} \langle \tilde{\psi}(\tilde{\mathbf{A}}^\dagger) | \tilde{\psi}(\tilde{\mathbf{A}}) \rangle = \frac{\partial}{\partial \tilde{A}_{l_{n-1}, l_n}^{\sigma_n \dagger}} \langle \tilde{\psi}(\tilde{\mathbf{A}}^\dagger) | \psi(\mathbf{A}) \rangle \quad (2.49)$$

$$\Leftrightarrow \begin{array}{c} \begin{array}{ccccccccc} \tilde{A}_1^\dagger & \tilde{A}_2^\dagger & & \tilde{A}_4^\dagger & \tilde{A}_5^\dagger & \tilde{A}_1^\dagger & \tilde{A}_2^\dagger & & \tilde{A}_4^\dagger & \tilde{A}_5^\dagger \\ \tilde{A}_1 & \tilde{A}_2 & \tilde{A}_3 & \tilde{A}_4 & \tilde{A}_5 & \tilde{A}_1 & \tilde{A}_2 & \tilde{A}_3 & \tilde{A}_4 & \tilde{A}_5 \end{array} \\ \Leftrightarrow \end{array} \quad (2.50)$$

$$\Leftrightarrow \begin{array}{c} \tilde{A}_3 \\ \Leftrightarrow \end{array} = \begin{array}{c} \text{---} L \text{---} \\ \text{---} A_3 \text{---} \\ \text{---} R \text{---} \end{array}, \quad (2.51)$$

where the compressed unknown matrix \tilde{A}_n is highlighted as yellow, and the higher uncompressed link dimension is marked with a wider line. Note that when the orthogonality centre is located on site n while we take the partial derivate $\partial / \partial \tilde{A}_{l_{n-1}, l_n}^{\sigma_n \dagger}$, the computation simplifies dramatically due to the convenient orthogonality conditions on the left-hand side of the equation. Contrarily, on the right-hand side we obtain the expressions for the contracted tensors L and R , which are nothing but the first part of the overlap $\langle \tilde{\psi} | \psi \rangle$ starting from the left and right, respectively:

$$L_{l_{n-1}, l'_{n-1}} = \tilde{A}_{l'_1}^{\sigma_1 \dagger} A_{l_1}^{\sigma_1} \dots \tilde{A}_{l'_{n-2}, l'_{n-1}}^{\sigma_{n-1} \dagger} A_{l_{n-2}, l_{n-1}}^{\sigma_{n-1}}, \quad (2.52)$$

$$L = \begin{array}{c} \tilde{A}_1^\dagger \dots \tilde{A}_{n-1}^\dagger \\ | \\ A_1 \dots A_{n-1} \end{array}, \quad (2.53)$$

and respectively for R ,

$$R_{l_n, l_n} = \tilde{A}_{l'_n, l'_{n+1}}^{\sigma_{n+1} \dagger} A_{l_n, l_{n+1}}^{\sigma_{n+1}} \dots \tilde{A}_{l'_N}^{\sigma_N \dagger} A_{l_N}^{\sigma_N} \quad (2.54)$$

$$R = \begin{array}{c} \tilde{A}_{n+1}^\dagger \dots \tilde{A}_N^\dagger \\ | \\ A_{n+1} \dots A_N \end{array}. \quad (2.55)$$

This equips us with all details to update the tensor \tilde{A}_n for arbitrary n inside the chain according to Eqs. (2.48) and (2.51). This update procedure is now repeated from say left end $n = 1$ to the right end $n = N$ and backwards until a satisfactory convergence is achieved. To this end, one assesses the convergence by inspecting the weight function $W(\tilde{\psi})$ (2.44) and monitor its convergence. While updating, one must not forget to rescale the new compressed matrix to unit norm.

2.4 Matrix product operators

Matrix product operators (MPO) relate to operators defined on vectors in Hilbert space analogously to how MPSs relate to pure quantum states. An MPO is a tensor network that when contracted with

an MPS has another MPS as its output. In the following section, we lay out the foundations of an MPO looks like both in tensor notation and graphical representation. We particularly emphasise the construction of the MPO representing the Hamiltonian of a long-range power law interacting operator, which we shall make use of later.

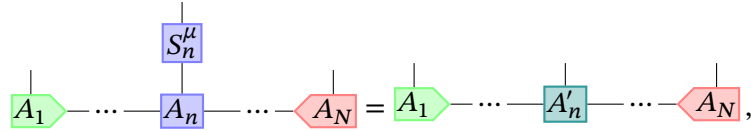
2.4.1 Single-site matrix product operator

Arguably, the simplest version of an MPO is a single-site operator. In the context of spin-1/2 chains, we may think of the Pauli matrices $\sigma_{x,y,z}$, which read as,

$$\sigma_x = \begin{pmatrix} 0 & 1 \\ 1 & 0 \end{pmatrix}, \quad \sigma_y = \begin{pmatrix} 0 & -i \\ i & 0 \end{pmatrix}, \quad \sigma_z = \begin{pmatrix} 1 & 0 \\ 0 & -1 \end{pmatrix}, \quad \sigma_0 = \mathbb{1} = \begin{pmatrix} 1 & 0 \\ 0 & 1 \end{pmatrix}, \quad (2.56)$$

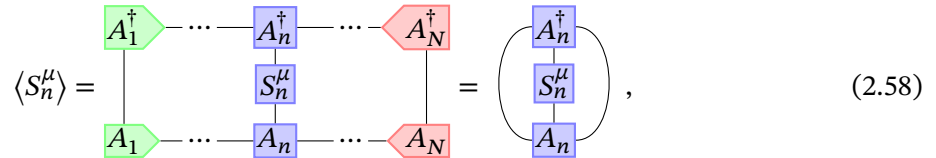
as the basis of any single site operator, in particular of the spin operators $S^{x,y,z} = \sigma^{x,y,z}/2$.

Graphically, an application of a single site MPO can be represented,



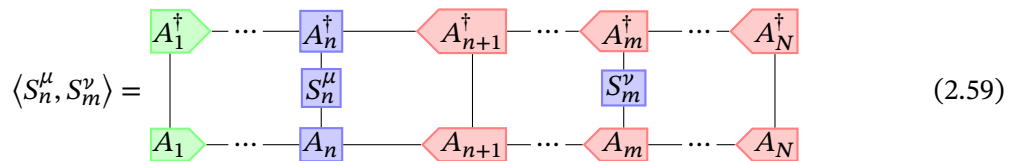
$$\begin{array}{c} | \\ \boxed{S_n^\mu} \\ | \\ \text{---} \boxed{A_n} \text{---} \dots \text{---} \boxed{A_N} \end{array} = \begin{array}{c} | \\ \text{---} \boxed{A'_n} \text{---} \dots \text{---} \boxed{A_N} \end{array}, \quad (2.57)$$

where $S_n^\mu = S_n^{x,y,z}$ acting on site n . Note that the mixed canonical form of an MPS is particularly useful when evaluating an n -point function, e.g. the two-point correlation function $\langle S_n^\mu S_m^\nu \rangle$, when the orthogonality centre is located at site j and $n \leq j \leq m$ assuming without loss of generality that $n \leq m$. To see this, let us first consider the graphical representation of the expectation value of a one-point function which reads as,

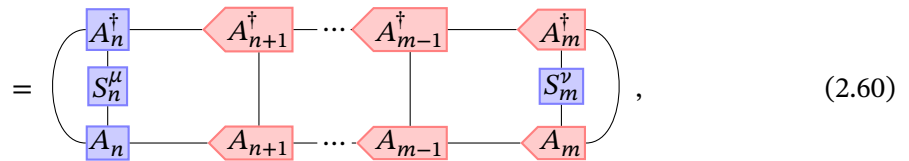


$$\langle S_n^\mu \rangle = \begin{array}{c} \text{---} \boxed{A_1^\dagger} \text{---} \dots \text{---} \boxed{A_n^\dagger} \text{---} \dots \text{---} \boxed{A_N^\dagger} \\ | \\ \boxed{S_n^\mu} \\ | \\ \text{---} \boxed{A_1} \text{---} \dots \text{---} \boxed{A_n} \text{---} \dots \text{---} \boxed{A_N} \end{array} = \begin{array}{c} \boxed{A_n^\dagger} \\ | \\ \boxed{S_n^\mu} \\ | \\ \boxed{A_n} \end{array}, \quad (2.58)$$

which trivially equates due to orthogonality to only the contractions on the spatial site n in the sense depicted above. This evidently saves a dramatic amount of necessary contractions. Similarly, the two-point function reads as,



$$\langle S_n^\mu, S_m^\nu \rangle = \begin{array}{c} \text{---} \boxed{A_1^\dagger} \text{---} \dots \text{---} \boxed{A_n^\dagger} \text{---} \dots \text{---} \boxed{A_{n+1}^\dagger} \text{---} \dots \text{---} \boxed{A_m^\dagger} \text{---} \dots \text{---} \boxed{A_N^\dagger} \\ | \\ \boxed{S_n^\mu} \\ | \\ \text{---} \boxed{A_1} \text{---} \dots \text{---} \boxed{A_n} \text{---} \dots \text{---} \boxed{A_{n+1}} \text{---} \dots \text{---} \boxed{A_m} \text{---} \dots \text{---} \boxed{A_N} \\ | \\ \boxed{S_m^\nu} \\ | \\ \text{---} \boxed{A_{n+1}^\dagger} \text{---} \dots \text{---} \boxed{A_m^\dagger} \end{array} \quad (2.59)$$



$$= \begin{array}{c} \boxed{A_n^\dagger} \text{---} \boxed{A_{n+1}^\dagger} \text{---} \dots \text{---} \boxed{A_{m-1}^\dagger} \text{---} \boxed{A_m^\dagger} \\ | \\ \boxed{S_n^\mu} \\ | \\ \boxed{A_n} \text{---} \boxed{A_{n+1}} \text{---} \dots \text{---} \boxed{A_{m-1}} \text{---} \boxed{A_m} \\ | \\ \boxed{S_m^\nu} \end{array}, \quad (2.60)$$

where you can see that it naturally includes the contraction of all tensors in between the two points n and m . Note that this has profound implications on the scaling of the two-point correlation function as the correlation length is always finite, and they decay exponentially over long distances $m \gg n$ [139].

2.4.2 Matrix product operators of Hamiltonians

In this section, we introduce and discuss the construction of matrix product operators (MPO) given a many-body Hamiltonian. Firstly, we will discuss the short-range interacting case before translating it to the long-range case.

Having previously discusses single site MPOs, we now turn towards many-body operators possibly acting on all sites. Analogously to how we argued that one may write any quantum state as,

$$|\psi\rangle = \sum_{\sigma_1 \dots \sigma_N} c_{\sigma_1 \dots \sigma_N} |\sigma_1 \dots \sigma_N\rangle \quad (2.61)$$

$$= \sum_{\sigma_1 \dots \sigma_N} A^{\sigma_1} A^{\sigma_2} \dots A^{\sigma_{N-1}} A^{\sigma_N} |\sigma_1 \dots \sigma_N\rangle, \quad (2.62)$$

we may write *any* linear operator on Hilbert space as,

$$\hat{O} = \sum_{\sigma_1 \dots \sigma_N \sigma'_1 \dots \sigma'_N} c_{\sigma_1 \dots \sigma_N, \sigma'_1 \dots \sigma'_N} |\sigma'_1 \dots \sigma'_N\rangle \langle \sigma_1 \dots \sigma_N| \quad (2.63)$$

$$= \sum_{\sigma_1 \dots \sigma_N \sigma'_1 \dots \sigma'_N} W^{\sigma_1, \sigma'_1} W^{\sigma_2, \sigma'_2} \dots W^{\sigma_{N-1}, \sigma'_{N-1}} W^{\sigma_N, \sigma'_N} |\sigma'_1 \dots \sigma'_N\rangle \langle \sigma_1 \dots \sigma_N|, \quad (2.64)$$

where the W_n in the bulk are rank-4 tensors (and rank-3 at the boundary). Graphically we may represent an MPO analogously to an MPS as,

$$\hat{O} = \begin{array}{c} | \\ \boxed{W_1} \\ | \end{array} \dots \begin{array}{c} | \\ \boxed{W_n} \\ | \end{array} \dots \begin{array}{c} | \\ \boxed{W_N} \\ | \end{array} \quad (2.65)$$

2.4.2.1 MPOs of short-range interacting Hamiltonians

Although formally existing, one might naively expect the quest of constructing an explicit MPO from a given Hamiltonian to be a hopeless endeavour since the latter is usually given in terms of sums of local few-body interaction operators while the former is a product of tensors. Consider for example the short-range XXZ spin-1/2 model, defined by the Hamiltonian,

$$H_{XXZ} = -J \sum_{n=1}^{N-1} \frac{1}{2} (S_n^+ S_{n+1}^- + S_n^- S_{n+1}^+) + \Delta S_n^z S_{n+1}^z - h \sum_{n=1}^N S_n^z \quad (2.66)$$

where the sum is of course shorthand notation for the addition of large tensor product operators acting on the full many-body Hilbert space,

$$\begin{aligned}
 H_{XXZ} = & -hS_1^z \otimes \mathbb{1}_2 \otimes \mathbb{1}_3 \otimes \mathbb{1}_4 \otimes \dots \mathbb{1}_N \\
 & + \frac{J}{2}S_1^+ \otimes S_2^- \otimes \mathbb{1}_3 \otimes \mathbb{1}_4 \otimes \dots \mathbb{1}_N \\
 & + \frac{J}{2}S_1^- \otimes S_2^+ \otimes \mathbb{1}_3 \otimes \mathbb{1}_4 \otimes \dots \mathbb{1}_N \\
 & + J\Delta S_1^z \otimes S_2^z \otimes \mathbb{1}_3 \otimes \mathbb{1}_4 \otimes \dots \mathbb{1}_N \\
 & + \mathbb{1}_1 \otimes -hS_2^z \otimes \mathbb{1}_3 \otimes \mathbb{1}_4 \otimes \dots \mathbb{1}_N \\
 & + \mathbb{1}_1 \otimes \frac{J}{2}S_2^+ \otimes S_3^- \otimes \mathbb{1}_4 \otimes \dots \mathbb{1}_N \\
 & + \dots
 \end{aligned} \tag{2.67}$$

However, McCulloch introduced an efficient way of constructing an MPO corresponding to a given Hamiltonian with low link dimension and only upper or lower triangular form [154]. The construction recipe may be best explained as follows; consider only lines of single field operators in Eq. (2.67), i.e. consider the Hamiltonian $H = h \sum_{n=1}^N S_n^z$. Such a Hamiltonian can be constructed as a product of tensors when the bulk MPO tensor reads,

$$W_n = \begin{pmatrix} \mathbb{1} & 0 \\ hS^z & \mathbb{1} \end{pmatrix}, \tag{2.68}$$

where the entries of this 2×2 matrix are operator valued, i.e. itself $d \times d$ matrices. For the first and last sites the MPO tensor reads as the row and column, respectively,

$$W_1 = (hS^z \quad \mathbb{1}), \quad W_N = \begin{pmatrix} \mathbb{1} \\ hS^z \end{pmatrix}, \tag{2.69}$$

which can be confirmed by multiplying everything out. This procedure can be readily generalised to two-body terms of the nearest neighbouring interacting Hamiltonian (2.66) by introducing more link dimensions for each operator term. This yields for the bulk MPO tensor,

$$W_n = \begin{pmatrix} \mathbb{1}_n & 0 & 0 & 0 & 0 \\ S_n^+ & 0 & 0 & 0 & 0 \\ S_n^- & 0 & 0 & 0 & 0 \\ S_n^z & 0 & 0 & 0 & 0 \\ -hS_n^z & JS_n^-/2 & JS_n^+/2 & J\Delta S_n^z & \mathbb{1}_n \end{pmatrix}, \tag{2.70}$$

and for the boundary tensors,

$$W_1^{XXZ} = \begin{pmatrix} -hS_1^z & JS_1^-/2 & JS_1^+/2 & J\Delta S_1^z & \mathbb{1}_1 \end{pmatrix}, \quad W_N^{XXZ} = \begin{pmatrix} \mathbb{1}_N \\ S_N^+ \\ S_N^- \\ S_N^z \\ -hS_N^z \end{pmatrix}, \quad (2.71)$$

As mentioned above, any non-nearest neighbour interaction term requires the introduction of a new MPO link dimension as well as an intermediate identity operator $\mathbb{1}$ as can be seen for example when including next-nearest neighbour interactions,

$$H = H_{XXZ} + J_2 \sum_n S_n^z S_{n+2}^z, \quad (2.72)$$

whose MPO bulk tensor is given by,

$$W_n = \begin{pmatrix} \mathbb{1}_n & 0 & 0 & 0 & 0 & 0 \\ S_n^+ & 0 & 0 & 0 & 0 & 0 \\ S_n^- & 0 & 0 & 0 & 0 & 0 \\ S_n^z & 0 & 0 & 0 & 0 & 0 \\ 0 & 0 & 0 & \mathbb{1}_n & 0 & 0 \\ -hS_n^z & JS_n^-/2 & JS_n^+/2 & J\Delta S_n^z & J_2 S_n^z & \mathbb{1}_n \end{pmatrix} \quad (2.73)$$

2.4.2.2 MPOs of exponentially decaying long-range interacting Hamiltonians

Before turning towards the desired power-law long-range interacting Hamiltonians, at least in the context of this thesis, let us first discuss how to construct an MPO corresponding to Hamiltonians with interactions that decay exponentially in space. To this end, consider the exponentially decaying interacting Hamiltonian

$$H = J \sum_{n=1}^{N-1} \sum_{d \neq 1} \lambda^d S_n^z S_{n+d}^z, \quad (2.74)$$

and note that between any pair of S_n^z and S_{n+d}^z there are implicitly identity matrices also in between the two positions n and $n+d$ compared to the sum in Eq. (2.67). That goes to say we have operators additionally operators of the form,

$$J\lambda^d S_1^z \otimes \mathbb{1}_2 \otimes \cdots \otimes \mathbb{1}_{d-1} \otimes S_d^z \otimes \mathbb{1}_{d+1} \otimes \cdots \otimes \mathbb{1}_N. \quad (2.75)$$

These operators are then ingeniously incorporated without the need of any extra link dimension by using the MPO,

$$W_n = \begin{pmatrix} \mathbb{1}_n & 0 & 0 \\ S_n^z & \lambda \mathbb{1}_n & 0 \\ 0 & J\lambda S_n^z & \mathbb{1}_n \end{pmatrix}, \quad (2.76)$$

as can be verified by multiplying out all constituent tensors of this MPO. Again, the first and last MPO are given by the row and column vector, respectively.

With this technique at hand, we may consider the exponentially interacting XXZ model,

$$H = -J \sum_{n=1}^{N-1} \sum_{d \neq 1} J\lambda^d \left[\frac{1}{2} (S_n^+ S_{n+d}^- + S_n^- S_{n+d}^+) + \Delta S_n^z S_{n+d}^z \right] - h \sum_{n=1}^N S_n^z, \quad (2.77)$$

and find it described by the bulk MPO tensor,

$$W_n = \begin{pmatrix} \mathbb{1}_n & 0 & 0 & 0 & 0 \\ S_n^+ & \lambda \mathbb{1}_n & 0 & 0 & 0 \\ S_n^- & 0 & \lambda \mathbb{1}_n & 0 & 0 \\ S_n^z & 0 & 0 & \lambda \mathbb{1}_n & 0 \\ -h S_n^z & J\lambda S_n^-/2 & J\lambda S_n^+/2 & J\Delta \lambda S_n^z & \mathbb{1}_n \end{pmatrix}, \quad (2.78)$$

and the standard row and column vectors corresponding to the first and last MPO tensor. This indeed reproduces the exponentially decaying all-to-all interaction when multiplied out. We wish to stress again that the link dimension does not increase through this type of interaction.

2.4.2.3 MPOs of long-range power-law interacting Hamiltonians

In this subsection, we are constructing the MPO of a power-law interacting Hamiltonian. As we have seen above, the MPO link dimension increases by one for each interaction term in the Hamiltonian, in particular for each two-body interaction on different sites. Naively, one expects that the MPO link dimension corresponding to a Hamiltonian with power-law all-to-all interaction as,

$$H = J \sum_{n \neq m}^N \frac{S_n^z S_m^z}{|n - m|^\alpha}, \quad (2.79)$$

scales with system size. This is obviously impractical as we want to ideally scale the system size large enough to extrapolate results in the infinite volume. To our rescue come two tricks. Firstly, we approximate the power-law decay $f(x) = x^{-\alpha}$ as a sum of decaying exponentials $f(x) \approx \sum_{\mu=1}^M a_\mu b_\mu^{-x}$ [155, 156]. Secondly, we use a surprising fact that exponentially decaying interactions of the form $J(r) = J\lambda^r$ with $r > 0$ may be realised at the same MPO link dimension as the short-range nearest neighbour interacting system [138, 156].

The approximation of the interaction potential $R^{-\alpha}$ in terms of sums of exponential has already been explored including in the context of MPOs [138, 155–157] The prescription is straightforward; one uses numerical methods to approximate $f(x) = x^{-\alpha}$ for $x \geq 1$ —which means no UV divergence—

where only non-vanishing entries are written explicitly. See Eq. (2.93) for a more detailed and larger bulk MPO tensor. The boundary terms are as per usual given by the projections onto the row and column vectors $W_{l_2}^{n=1} = \delta_{2,l_1} W_{l_1,l_2}^n$ and $W_{l_1}^{n=N} = W_{l_1,l_2}^n \delta_{l_2,1}$, respectively. We have furthermore permuted the last row vector in Eq. (2.78) with the second row, and we permute the last and second to last column vectors with the second and third column, and then iterated over the exponential interaction terms. Note that this permutation is entirely equivalent to the previous triangular shape of the bulk MPO tensor. However, this form is suitable for implementation in the software package `ITensors.jl` [158] for the Julia programming language [159] in case one wants to use the *conserved quantum number* functionality. This functionality rests on the fact that the Hamiltonian H_{LRXXZ} (2.82) conserves the total quantum number $S^Z = \sum_n S_n^Z$. Therefore, the Hamiltonian can be written as a block-sparse matrix with unique local quantum number *flux* (local change of globally conserved quantum number). Note that H_{LRXXZ} (2.82) contains terms that translate in three different groups of operators with different quantum number flux in the bulk MPO tensor. Firstly, $S_n^Z S_m^Z$ does not change the conserved quantum number locally on n and m . Secondly, $S_n^+ S_m^-$ has a net flux of +2 by convention of `ITensors.jl` (counting change of half-integer spin), while thirdly $S_n^- S_m^+$ has a net flux of -2. Due to our rearrangement, notice that all entry tensors in blue are diagonal in the local physical spin degrees of freedom and do therefore not change the local magnetisation. Contrarily, the red terms change the local spin degrees by net -1 while green terms change it by net +1. Taking advantage of this functionality greatly improves the numerical runtime as the software can make use of modern multithreaded CPU architectures and run code in parallel for each of the respective blocks.

2.5 Density matrix renormalisation group

The density matrix renormalisation group (DMRG) algorithm was devised by Steve White in his seminal work in 1992 [160, 161], and has since profoundly changed the field of condensed matter physics. It is considered the most established algorithm in the numerical study of one-dimensional quantum systems [138, 139, 162, 163] and its intimate relation to tensor networks—which form the natural language of the algorithm—have lead to new theoretical understandings and the complete classification of all phases of matter in 1D [5]. In its essence, the DMRG algorithm is a real-space variational renormalisation scheme in the space of matrix product states [5, 162], that searches the MPS with the lowest energy (eigenvalue) of a hermitian Hamiltonian operator.

This objective naturally corresponds to minimising the energy function E ,

$$E(\psi) = \frac{\langle \psi | H | \psi \rangle}{\langle \psi | \psi \rangle}. \quad (2.84)$$

As it turns out, a ground state search algorithm can be made more efficient than an imaginary time evolution starting with some random initial guess [138]. Let us first discuss the approach in prose. Firstly, we introduce a Lagrangian multiplier λ , and minimise the cost function,

$$E(\psi, \lambda) = \langle \psi | H | \psi \rangle - \lambda \langle \psi | \psi \rangle \quad (2.85)$$

$$= \begin{array}{c} \begin{array}{c} \color{green}{A_1^\dagger} \dots \color{blue}{A_n^\dagger} \dots \color{red}{A_N^\dagger} \\ \color{blue}{W_1} \dots \color{blue}{W_n} \dots \color{blue}{W_N} \\ \color{green}{A_1} \dots \color{blue}{A_n} \dots \color{red}{A_N} \end{array} - \lambda \cdot \begin{array}{c} \color{green}{A_1^\dagger} \dots \color{blue}{A_n^\dagger} \dots \color{red}{A_N^\dagger} \\ \color{green}{A_1} \dots \color{blue}{A_n} \dots \color{red}{A_N} \end{array} \end{array} \quad (2.86)$$

which yields ψ as the minimised ground state and λ as its ground state energy [162]. The minimisation has to be performed over all variables, being all elements of all tensors $A_{l_{n-1}, l_n}^{\sigma_n}$, which in turn appear in Eq. (2.86) in many products, rendering the optimisation an extremely non-linear problem. The crucial step to taming the minimisation problem is analogous to our variational minimisation approach; we shall take only the tensor $A_{l_{n-1}, l_n}^{\sigma_n}$ for given n as variable while considering all others fixed. Consequently, the highly non-linear problem turns into a favourable linear algebra problem where the degrees of freedom appear in quadratic form. The optimisation then yields an improved local tensor of the MPS, which slightly decreases the energy but will obviously not yield the optimal state. The same step is then simply repeated on the next local site $n+1$ iterating through the entire MPS multiple times until the total energy is sufficiently converged to a minimal value. For all details and necessary steps in the DMRG algorithm acting on an MPS, we refer the reader to Appendix 2.C.

2.6 Time-dependent variational principle

This section introduces the time-dependent variational principle (TDVP) as a means to compute the time-evolution of a quantum state, and it is based on the excellent review of Ref. [164].

TDVP [165, 166] is a method to approximately solve the initial value problem of the time-dependent Schrödinger equation,

$$\frac{\partial |\psi\rangle}{\partial t} = -iH|\psi\rangle, \quad (2.87)$$

given an initial quantum state $|\psi\rangle$ as an MPS and the Hamiltonian operator H as an MPO.

The approach TDVP takes may be phrased as follows: Central to the ideas of the algorithm is a specific manifold of matrix product states characterised by a given bond dimension. To see why this manifold plays a crucial role, consider the state $H|\psi\rangle$ in terms of an MPO H and an MPS $|\psi\rangle$. It is lying in a different MPS manifold than the original $|\psi\rangle$ since the application of an MPO to an MPS generically increases the link dimension. The Schrödinger evolution is therefore not closed inside a single MPS manifold. To remedy this, the TDVP algorithm introduces the pull-back projector which takes an arbitrary state and projects it onto a given tangent space to the MPS manifold. Con-

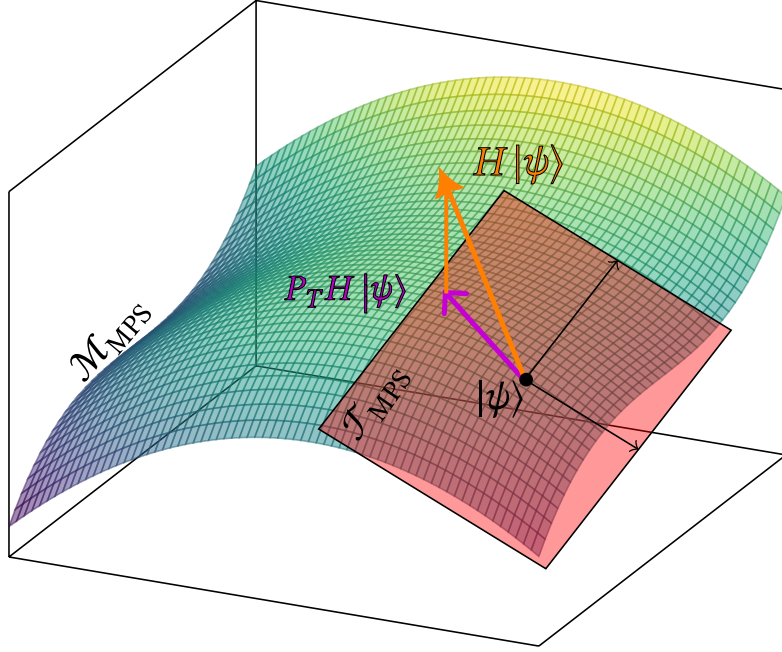


Figure 2.6: Illustration of TDVP and the relations between the MPS manifold \mathcal{M}_{MPS} (coloured surface) embedded in the entire Hilbert (enclosing box), and the tangent space \mathcal{J}_{MPS} (flat red plane) anchored on the tangent point given by $|\psi\rangle$. One finds $H|\psi\rangle$ outside the MPS manifold as indicated by the orange arrow, while the projector associated to the state $|\psi\rangle$ projects it onto the tangent space \mathcal{J}_{MPS} . The purple arrow is then the projected tangent vector indicating the optimal direction of time evolution.

sequently, we write the time-dependent Schrödinger equation in a form projected into this manifold as,

$$\frac{\partial}{\partial t}|\psi\rangle = -iP_T(\psi)H|\psi\rangle, \quad (2.88)$$

where we have introduced the *single-site* projection operator $P_T(\psi)$ which projects a state—in the case of the Schrödinger equation the state $H|\psi\rangle$ —onto the tangent space of the manifold at the point (tangential to) $|\psi\rangle$. The TDVP algorithm transforms the Schrödinger equation from a linear differential equation defined on the full Hilbert space into a set of nonlinear symplectic differential equations in the parameter space of the variational MPS manifold [167]. The challenge of solving the many-body Schrödinger equation is therefore reposed in this set of nonlinear equations. If one could solve these equations exactly, the only source of error would be the variational MPS approximation of the many-body quantum state. TDVP then prescribes the optimal direction in which the quantum state has to evolve given the restriction to the manifold [140]. Figure 2.6 gives an illustration of these relations and ideas in a simplified graphical representation. For the detailed steps and equations necessary to perform the TDVP algorithm, we refer the reader to the Appendix 2.D.

A salient feature of the TDVP algorithm is that it arrives at the Lie-Trotter decomposition (Trotterisation) of the time-evolution operator $U(t)$,

$$U(t) = e^{iHt} \xrightarrow{\text{Lie-Trotter}} U(t) \simeq \lim_{N \rightarrow \infty} (U(\delta t))^{Nt} \quad \text{with } \delta t = t/N_t \quad (2.89)$$

with a single approximation, namely the projection onto the tangent space as opposed to most other time evolution algorithms for MPS. Then, one applies repeatedly the time evolution operator with a small time step $U(\delta t)$ such that one may evaluate the state at any desirably late time considering the error per time step of order $\mathcal{O}(\delta t^3)$ [164]. TDVP is agnostic to the form of interactions of the Hamiltonian, and in particular, therefore one of the few algorithms suitable for the time-evolution of systems with long-range interactions [164, 168].

Appendix

2.A Some entanglement observables on an MPS

In this appendix, we wish to briefly discuss two entanglement witnesses which are observables on a quantum many-body state readily accessible by the means explained above; the geometric entanglement (GE) and the entanglement spectrum (ES).

2.A.1 Computation of Geometric entanglement

The above compression procedures explained in Section 2.3.3 can be readily adapted to measure the geometric entanglement $E_g(\psi)$. Measuring the geometric distance in Hilbert space between a given state $|\psi\rangle$ and its closest product state $|\phi\rangle$, it is defined as [152, 153],

$$E_g(\psi) = -\log_2\left(\max_{\phi: \text{prod. state}} |\langle\phi|\psi\rangle|^2\right). \quad (2.90)$$

Note that a product state as a tensor network is simply an MPS with constant link dimension $l_n = 1$ on every link; then and only then can it be written as a product $|\phi\rangle = \bigotimes_{j=1}^N |\varphi_j\rangle$ and is therefore not entangled anywhere.

Consequently, we are aiming at finding the closest MPS $(\tilde{A}_1, \dots, \tilde{A}_N)$ with fixed link dimension $\tilde{l}_n = 1$ to a given MPS (A_1, \dots, A_N) . The previous two algorithms—compression via SDV and compression via variation—naturally lend themselves to perform this task. Firstly, we take a copy of the input state (A_1, \dots, A_N) and decimate the link dimension of the copy to only 1 according to the compression via SVD detailed in Section 2.3.3.1. This compressed copy of the input state is now considered as the initial guess for the compression algorithm via variation explained in Section 2.3.3.2. The resulting compressed state is considered the closest product state when the geometric distance converged sufficiently. In practice for the results in Section 4.4.1, we consider a difference of 10^{-9} before and after a complete sweep from the left end to the right end as sufficient.

2.A.2 Entanglement spectrum

Since the seminal work by Li and Haldane [112], recent years have seen an increasing interest in the so-called *entanglement spectrum*, which has been proven useful in distinguishing topological order [104, 112, 124]. The entanglement spectrum is given by the distribution of singular values associated to a given bipartition of a quantum state. Entanglement entropy contains a lot of information about the bipartite state, as well as the distribution of singular values, especially when considering many Rényi entropies. These hold information on the typical width of the distribution of singular values. Surely though, each Rényi entropy does not contain the entire distribution.

The fundamental idea to the entanglement spectrum is therefore to contain this information and simply map all singular values s_i onto entanglement energies ξ_i as $\xi_i = -\log(s_i)$. Note that they are related to the eigenvalues λ_i of the reduced density matrix ρ_A (2.30) by squaring, $s_i^2 = \lambda_i$. Indeed, Li and Haldane conjecture that for topologically ordered ground states $|0\rangle$ —describing for example a quantum Hall state—have an entanglement spectrum whose low-lying excitations are in one-to-one correspondence with the low-lying spectrum of critical edge modes described by an effective conformal field theory (CFT) [104, 112, 124, 169, 170]. We follow their convention and define the entanglement spectrum $\{\xi_j\}$ from the Schmidt values, i.e. the singular values, $s_j = (S)_{j,j}$ of the mixed canonical orthogonality in Eq. (2.26) as,

$$\xi_j = -\log(s_j^2) = -\log(\lambda_j), \quad (2.91)$$

where we call ξ_j the *entanglement energy* since it takes values $\xi_j \in [0, +\infty)$, and it is the j -th spectral value of the *entanglement Hamiltonian* \tilde{H}_A ,

$$\rho_A =: \frac{1}{Z_A} \exp(-\tilde{H}_A), \quad (2.92)$$

where \tilde{H}_A is a hermitian operator, and $Z_A = \text{Tr}(\exp(-\tilde{H}_A))$ is the normalisation.

2.B Long-range bulk MPO tensors for the LRXXZ model

In this appendix, we shall display the bulk MPO operator for the long-range interacting XXZ model in landscape such that it fits on an A4 page. We nevertheless have to choose an abbreviated form in which we indicate the sum of exponentially decaying interactions over terms $j = 1, \dots, M$ by the ellipses ‘...’. Furthermore, we sort and label all interaction terms in their corresponding flux of the conserved quantity $S_{\text{tot}}^z = \sum_n S_n^z$, $\Phi(S_{\text{tot}}^z) = 0, +2, -2$, such that the bulk MPO operator may be written as a block sparse operator for the ITensors software library.

$$W_n^{LRXXZ} = \left[\begin{array}{c} \left. \begin{array}{l} \Phi(S_{\text{tot}}^z) = 0, \\ \text{out} \end{array} \right\} \left[\begin{array}{c} \mathbb{1}_n \\ -hS_n^z \\ S_n^z \\ S_n^z \\ \vdots \\ S_n^z \\ S_n^- \\ \vdots \\ S_n^- \\ S_n^+ \\ \vdots \\ S_n^+ \end{array} \right] \\ \left. \begin{array}{l} \Phi(S_{\text{tot}}^z) = \\ +2, \text{out} \end{array} \right\} \left[\begin{array}{c} S_n^- \\ \vdots \\ S_n^- \\ S_n^+ \\ \vdots \\ S_n^+ \end{array} \right] \\ \left. \begin{array}{l} \Phi(S_{\text{tot}}^z) = \\ -2, \text{out} \end{array} \right\} \left[\begin{array}{c} S_n^+ \\ \vdots \\ S_n^+ \end{array} \right] \end{array} \right] \begin{array}{c} \text{link indices in block with } S_{\text{tot}}^z \text{ flux } \Phi(S_{\text{tot}}^z) = 0, \text{ in} \\ \Phi(S_{\text{tot}}^z) = +2, \text{ in} \\ \Phi(S_{\text{tot}}^z) = -2, \text{ in} \end{array} \left[\begin{array}{ccccccc} \mathbb{1}_n & & & & & & \\ \mathbb{1}_n & J\Delta a_1 b_1 S_n^z & J a_2 \Delta b_2 S_n^z & \dots & J\Delta a_M b_M S_n^z & J a_1 b_1 S_n^+ / 2 & \dots & J a_M b_M S_n^+ / 2 & J a_1 b_1 S_n^- / 2 & \dots & J a_M b_M S_n^- / 2 \\ & b_1 \mathbb{1}_n & & & & & & & & & \\ & & b_2 \mathbb{1}_n & & & & & & & & \\ & & & \ddots & & & & & & & \\ & & & & b_M \mathbb{1}_n & & & & & & \\ & & & & & b_1 \mathbb{1}_n & & & & & \\ & & & & & & \ddots & & & & \\ & & & & & & & b_M \mathbb{1}_n & & & \\ & & & & & & & & b_1 \mathbb{1}_n & & \ddots \\ & & & & & & & & & & b_M \mathbb{1}_n \end{array} \right] \quad (2.93)$$

2.C DMRG algorithm

In this appendix, we detail the steps necessary to follow the DMRG algorithm which is only paraphrase in Section 2.5. Central to the efficiency of the entire computation is the orthogonal centre being at the same spot as the optimisation, as can be seen in Eq. (2.86) where the computation of the second term, the overlap, is simplified to the single orthogonal centre site. This yields the simplification for the second term in Eq. (2.86) as,

$$\langle \psi | \psi \rangle = \begin{array}{c} \text{---} A_1^\dagger \text{---} \dots \text{---} A_n^\dagger \text{---} \dots \text{---} A_N^\dagger \text{---} \\ | \\ \text{---} A_1 \text{---} \dots \text{---} A_n \text{---} \dots \text{---} A_N \text{---} \end{array} = \begin{array}{c} A_n^\dagger \\ | \\ A_n \end{array}. \quad (2.94)$$

On the other hand, the first term in the energy function can be evaluated efficiently by a similar approach as discussed in the section of expectation values of MPOs;

$$\langle \psi | H | \psi \rangle = \begin{array}{c} \text{---} A_1^\dagger \text{---} \dots \text{---} A_n^\dagger \text{---} \dots \text{---} A_N^\dagger \text{---} \\ | \\ W_1 \text{---} \dots \text{---} W_n \text{---} \dots \text{---} W_N \text{---} \\ | \\ \text{---} A_1 \text{---} \dots \text{---} A_n \text{---} \dots \text{---} A_N \text{---} \end{array} = \begin{array}{c} L^W \text{---} A_n^\dagger \text{---} R^W \\ | \\ W_n \\ | \\ A_n \end{array}, \quad (2.95)$$

where we define L^W and R^W simply as the entire contraction left or right of the orthogonality centre at site n , respectively.

We may now find the optimising tensors with the extremal condition of Eq. (2.86) that is, $\partial E(\psi, \lambda) / \partial A_{l_{n-1}, l_n}^{\sigma_n^\dagger} = 0$ while keeping all other tensors $A_{l_{m-1}, l_m}^{\sigma_m^\dagger}$ ($m \neq n$) fixed. This yields in case of mixed canonical orthogonality,

$$0 = \frac{\partial E(\psi, \lambda)}{\partial A_{l_{n-1}, l_n}^{\sigma_n^\dagger}} \quad (2.96)$$

$$= \begin{array}{c} \text{---} A_1^\dagger \text{---} \dots \text{---} A_n^\dagger \text{---} \dots \text{---} A_N^\dagger \text{---} \\ | \\ W_1 \text{---} \dots \text{---} W_n \text{---} \dots \text{---} W_N \text{---} \\ | \\ \text{---} A_1 \text{---} \dots \text{---} A_n \text{---} \dots \text{---} A_N \text{---} \end{array} - \lambda \cdot \begin{array}{c} \text{---} A_1^\dagger \text{---} \dots \text{---} A_n^\dagger \text{---} \dots \text{---} A_N^\dagger \text{---} \\ | \\ \text{---} A_1 \text{---} \dots \text{---} A_n \text{---} \dots \text{---} A_N \text{---} \end{array} \quad (2.97)$$

$$= \begin{array}{c} L^W \text{---} W_n \text{---} R^W \\ | \\ A_n \end{array} - \lambda \cdot \text{---} A_n \text{---}, \quad (2.98)$$

where we highlighted the tensor to be optimised as yellow, and again shorten the entire contraction to the left (right) of the centre site n by the rank-3 tensor L^W (R^W). Above equation is clearly an eigenvalue equation of the form

$$H^n v = \lambda v, \quad (2.99)$$

if we define H^n and v in Eq. (2.99) by means of the entities in Eq. (2.98) as,

$$H_{\sigma'_n l'_{n-1} l'_n, \sigma_n l_{n-1} l_n}^n = L_{l_{n-1}, l'_{n-1}, p_{n-1}}^W W_{p_{n-1}, p_n}^{\sigma_n, \sigma'_n} R_{l_n, l'_n, p_n}^W = \begin{array}{c} \text{---} \text{---} \text{---} \\ | \quad | \quad | \\ \boxed{L^W} \quad \boxed{W_n} \quad \boxed{R^W} \\ | \quad | \quad | \\ \text{---} \text{---} \text{---} \end{array}, \quad (2.100)$$

$$v_{\sigma_n l_{n-1} l_n} = A_{l_{n-1}, l_n}^{\sigma_n} = \text{---} \boxed{A_n} \text{---}. \quad (2.101)$$

The ‘vector’ v has $d \cdot \chi_m^2$ degrees of freedom corresponding to all entries is $A_{l_{n-1}, l_n}^{\sigma_n}$, and the ‘matrix’ H^n crucially is hermitian as can be checked through its definition. This allows for approximate diagonalisation algorithms which find the lowest eigenvalues and eigenvectors since $d \cdot \chi_m^2$ is generally too large to be diagonalised exactly. A typical and established approximate algorithm is the Lanczos eigensolvers for large sparse matrices. As a result, we find the minimal $A_{l_{n-1}, l_n}^{\sigma_n}$, while keeping all other $A_{l_{m-1}, l_m}^{\sigma_m}$ fixed. Surely, the energy of the entire state is not minimal after a single optimisation of a single site, instead one incrementally minimises the energy variationally. This minimisation step is then repeated starting from say $n = 1$ and moving rightwards while also changing the orthogonality centre as described in Eq. (2.23) until $n = N$ where we repeat the iteration leftwards until we find ourselves back at $n = 1$ (again changing the orthogonality centre after each local optimisation). This procedure going from one end to the other and back again is generally called a (symmetric) *DMRG sweep*. We shall repeat sweeping over the updated MPS until convergence of the energy is reached. To this end, one may also verify that the variance of the energy $\text{var}(E) = \langle \psi | H^2 | \psi \rangle - (\langle \psi | H | \psi \rangle)^2$ approaches zero sufficiently close since $|\psi\rangle$ should be an eigenvector of H .

Here, it should be mentioned that the above detailed algorithm is generally called the *single-site* DMRG algorithm since the optimisation condition $\partial E(\psi, \lambda) / \partial A_{l_{n-1}, l_n}^{\sigma_n \dagger} = 0$ is given with respect to the degrees of freedom on a single physical site. As explained above, this has the immense advantage of rendering the problem an eigenvalue problem from linear algebra. Alternatively, one may define the minimisation problem with respect to the degrees of freedom on *two* physical sites, defined as,

$$0 \stackrel{!}{=} \frac{\partial E(\psi, \lambda)}{\partial (A_{l_{n-1}, l_n}^{\sigma_n \dagger} A_{l_n, l_{n+1}}^{\sigma_{n+1} \dagger})}. \quad (2.102)$$

As you can see in Eq. (2.102), the link dimension between site n and $n + 1$ (l_n) is itself now variable and subject to the eigensolver result of the generalised linear algebra problem with $d^2 \chi_m^2$ degrees of freedom. We then split the two-site optimal result with an SVD and move the orthogonality centre further. Compared to the single-site algorithm, the two-site algorithm may increase the link dimension given some maximum cutoff criteria. Assuming both algorithms act on MPS with the same maximum link dimension, the difference between the two is that the two-site algorithm necessarily needs to perform a truncation in the SVD since there are more degrees of freedom in the two-site algorithm ($d^2 \chi_m^2$) compared to $d \chi_m^2$ in the single site algorithm. This may ‘mix’ degrees of freedom corresponding to different conserved quantum numbers since they are being

ordered and then possibly omitted simply on the basis of their singular value. Consequently, the two-site algorithm may be more practical since the initial ansatz for the ground state does not matter as much and one may get less often stuck in a local minimum in a given conserved quantum number sector than the (possibly random) initial state occupies [138]. Nevertheless, Steve White proposed in Ref [171] a single-site algorithm that further advances the protection against the problem of ‘getting stuck’ in a local minimum of the energy landscape.

2.D TDVP algorithm

In this appendix, we turn towards explicit equations and detail the paraphrased TDVP algorithm mentioned in Section 2.6. As mentioned above, one has to introduce the concept of the single-site tangent space of $|\psi\rangle$ which is defined by the space spanned by all MPS that vary from $|\psi\rangle$ *only on a single site* n [140, 164]. The projector into this tangent space reads in mixed canonical orthogonality as [164–166],

$$P_T(\psi) = \sum_{n=1}^N P_{n-1}^L(\psi) \otimes \mathbb{1}_n \otimes P_{n+1}^R(\psi) - \sum_{n=1}^{N-1} P_n^L(\psi) \otimes P_{n+1}^R(\psi), \quad (2.103)$$

where we have defined the left (right) projectors $P_n^{L(R)}$ that project onto the left (right) part of the state up to (from) and including site n ,

$$(P_n^L(\psi))_{\sigma'_1, \dots, \sigma'_n, \sigma_1, \dots, \sigma_n} = A_{l'_1}^{\sigma_1 \dagger} A_{l'_1, l'_2}^{\sigma_2 \dagger} \cdots A_{l'_{n-1}, l_n}^{\sigma_n \dagger} \cdot A_{l_{n-1}, l_n}^{\sigma'_n} A_{l_{n-2}, l_{n-1}}^{\sigma'_{n-1}} \cdots A_{l_1}^{\sigma'_1} \quad (2.104)$$

$$= \begin{array}{c} \sigma_1 \qquad \qquad \sigma_n \\ \color{green}{\boxed{A_1}} \cdots \color{green}{\boxed{A_n}} \\ \color{green}{\boxed{A_1^\dagger}} \cdots \color{green}{\boxed{A_n^\dagger}} \\ \sigma'_1 \qquad \qquad \sigma'_n \end{array}, \quad (2.105)$$

$$(P_n^R(\psi))_{\sigma'_n, \dots, \sigma'_N, \sigma_n, \dots, \sigma_N} = A_{l'_{N-1}}^{\sigma_N \dagger} A_{l'_{N-2}, l'_{N-1}}^{\sigma_{N-1} \dagger} \cdots A_{l_{n-1}, l'_n}^{\sigma_n \dagger} \cdot A_{l_{n-1}, l_n}^{\sigma'_n} A_{l_n, l_{n+1}}^{\sigma'_{n+1}} \cdots A_{l_N}^{\sigma'_N} \quad (2.106)$$

$$= \begin{array}{c} \sigma_n \qquad \qquad \sigma_N \\ \color{red}{\boxed{A_n}} \cdots \color{red}{\boxed{A_N}} \\ \color{red}{\boxed{A_n^\dagger}} \cdots \color{red}{\boxed{A_N^\dagger}} \\ \sigma'_n \qquad \qquad \sigma'_N \end{array} \quad (2.107)$$

We can write the projector Eq. (2.103) by the following graphical representation,

$$P_T(\psi) = \sum_{n=1}^N \begin{array}{c} \sigma_1 \quad \dots \quad \sigma_{n-1} \quad \sigma_n \quad \sigma_{n+1} \quad \dots \quad \sigma_N \\ \text{A}_1 \text{---} \dots \text{---} \text{A}_{n-1} \quad \text{A}_{n+1} \text{---} \dots \text{---} \text{A}_N \\ \text{A}_1^\dagger \text{---} \dots \text{---} \text{A}_{n-1}^\dagger \quad \text{A}_{n+1}^\dagger \text{---} \dots \text{---} \text{A}_N^\dagger \\ \sigma'_1 \quad \dots \quad \sigma'_{n-1} \quad \sigma'_n \quad \sigma'_{n+1} \quad \dots \quad \sigma'_N \end{array} \quad (2.108)$$

$$+ \sum_{n=1}^{N-1} \begin{array}{c} \sigma_1 \quad \dots \quad \sigma_n \quad \sigma_{n+1} \quad \dots \quad \sigma_N \\ \text{A}_1 \text{---} \dots \text{---} \text{A}_n \quad \text{A}_{n+1} \text{---} \dots \text{---} \text{A}_N \\ \text{A}_1^\dagger \text{---} \dots \text{---} \text{A}_n^\dagger \quad \text{A}_{n+1}^\dagger \text{---} \dots \text{---} \text{A}_N^\dagger \\ \sigma'_1 \quad \dots \quad \sigma'_n \quad \sigma'_{n+1} \quad \dots \quad \sigma'_N \end{array}, \quad (2.109)$$

where the free, uncontracted indices are highlighted in blue. We shall call the projector in Eq. (2.108) the single-site map since it maps into the single site n in the context of the given state $|\psi\rangle$ (hence N different terms in the sum) while the projector in Eq. (2.109) maps into the link (hence $N - 1$ different terms) and we shall call it the centre link map. Let us now plug Eq. (2.103) into Eq. (2.88) and obtain an explicit Schrödinger evolution equation inside the MPS manifold,

$$\frac{\partial}{\partial t} |\psi\rangle = -i P_T(\psi) H |\psi\rangle \quad (2.110)$$

$$= -i \sum_{n=1}^N P_{n-1}^L(\psi) \otimes \mathbb{1}_n \otimes P_{n+1}^R(\psi) H |\psi\rangle + i \sum_{n=1}^{N-1} P_n^L(\psi) \otimes P_{n+1}^R(\psi) H |\psi\rangle. \quad (2.111)$$

Note that Eq. (2.111) contains two sums with opposite sign which we consequently interpret as forward time evolution and backwards time evolution, respectively. Moreover, Eq. (2.111) is still not solvable and needs to be approximated further by solving each term in the respective sum individually and iteratively. To this end, we may consider each term in the sum individually while keeping all others fixed similarly to the approach in the DMRG algorithm. To this end, we consider the forward-evolving differential equations for N different n ,

$$\frac{\partial}{\partial t} |\psi\rangle = -i P_{n-1}^L(\psi) \otimes \mathbb{1}_n \otimes P_{n+1}^R(\psi) H |\psi\rangle, \quad (2.112)$$

and analogously the $N - 1$ backward-evolving equations,

$$\frac{\partial}{\partial t} |\psi\rangle = +i P_n^L(\psi) \otimes P_{n+1}^R(\psi) H |\psi\rangle, \quad (2.113)$$

The algorithm is then (twice) symmetrically iterated over all sites from say right to left end and vice versa with a time step of $\delta t/2$ for each direction such that the total time step after a symmetric sweep is δt .

Noteworthy about the single-site TDVP algorithm is that projection into the MPS manifold happens before the time-evolution equations are solved. Therefore, the norm and the energy, as well as all conserved quantum numbers that commute with the Hamiltonian and with the projection operator are identically conserved during the time evolution.

Furthermore, we emphasise that the TDVP algorithm explained above can be readily generalised to the two-site problem analogously to the generalisation of the DMRG algorithm to the two-site version. The two-site TDVP then contains a tensor $A_{n,n+1}$ which needs to be split by an SVD into two physical sites. At this point a truncation occurs adapting the current link dimension. Advantage of this method is that it adapts the link dimension on the fly, disadvantages are that the norm and the energy of the state are not necessarily exactly conserved but subject to the truncation. In fact, the analogy of the TDVP algorithm and the DMRG algorithm are much more profound than we mentioned so far. The TDVP algorithm can be formulated also with imaginary time steps such that one may converge towards a ground state. Taking the imaginary time step to infinity, one recovers the dominating eigenvectors that the DMRG algorithm for an MPS finds [5, 140, 164, 166].

3 Information and Correlation Spreading

This chapter is based on our publication, J. T. Schneider et al., “Spreading of correlations and entanglement in the long-range transverse Ising chain”, *Phys. Rev. Research* **3**:1, L012022 (2021) [172].

3.1 Introduction

Here, we build on our discussion of Lieb–Robinson bounds in Section 1.4.2. We mentioned above that the quasiparticle picture originally proposed by Calabrese and Cardy in the context of conformal field theories is indeed applicable to other cases outside the strict requirement of conformally symmetric Hamiltonians. In the following, we introduce the extension of this quasiparticle picture put forward by Cevolani et al. [34].

3.1.1 Extension of the Calabrese–Cardy Quasiparticle Picture

Cevolani et al. [34] propose a generic form of a two-point correlation function

$$G(\mathbf{r}, t) = G_0(\mathbf{r}, t) - G_0(\mathbf{r}, 0), \quad (3.1)$$

$$G_0(\mathbf{r}, t) = \langle A_X(t) B_Y(t) \rangle - \langle A_X(t) \rangle \langle B_Y(t) \rangle, \quad (3.2)$$

for systems in D spatial dimensions, with translation invariance, and (possibly non-local) two-site interactions as,

$$G(\mathbf{r}, t) = g(\mathbf{r}) - \int_{-\pi}^{\pi} \frac{d\mathbf{k}}{(2\pi)^D} \mathcal{F}(\mathbf{k}) \frac{1}{2} \left(e^{i\mathbf{k}\cdot\mathbf{r} + 2i\epsilon^f(\mathbf{k})t} + e^{i\mathbf{k}\cdot\mathbf{r} - 2i\epsilon^f(\mathbf{k})t} \right) \quad (3.3)$$

where $A_X(t)$, $B_Y(t)$ are local operators with support in region X , Y at time t and X and Y are spatially separated by \mathbf{r} . Equation (3.3) is derived in a microscopic mean-field model and interprets the spreading correlations as a weighted superposition—with $\mathcal{F}(\mathbf{k})$ as weight—of two waves with energy $\epsilon^f(\mathbf{k})$ depending only on the final state after quenching, and travelling in opposite direction with wave vector $\pm\mathbf{k}$. Here, we wish to emphasise that the dispersion relation $\epsilon(\mathbf{k})$ plays the central role in the quasiparticle picture which approximates the Hamiltonian of the many-body system in diagonal form as $H = \sum_{\mathbf{k} \in \text{BZ}} \epsilon(\mathbf{k}) b_{\mathbf{k}}^{\dagger} b_{\mathbf{k}}$, where $b_{\mathbf{k}}^{\dagger}$ is the creation operator for a quasiparticle occupying mode \mathbf{k} in the Brillouin zone (BZ). We call this type of approximation scheme linear spin-wave theory (LSWT). Let us now discuss the physical interpretation of Eq. (3.3) in the quasiparticle picture for which Fig. 3.1.1 serves as an illustration. A global quench introduces energy into the system by creating quasiparticles everywhere. Any correlation of the form Eq. (3.1) vanishes identically by

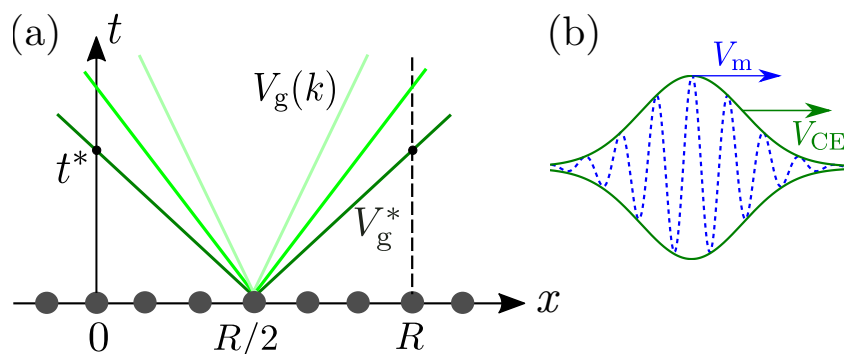


Figure 3.1.1: Quasiparticle interpretation of two-point correlation spreading following a global quench. (a) The earliest correlation between $x = 0$ and $x = R$ is due to a pair of counter-propagating quasiparticles with the fastest group velocity V_g^* originating at half-distance $R/2$. (b) Quasiparticles around the correlation edge are in a coherent superposition forming a wave packet. The correlation edge (CE) propagates with V_{CE} related to the quasiparticles moving with the fastest group velocity $V_{CE} = 2V_g^*$. Conversely, the maxima close to the front (m) propagate with V_m related to the quasiparticles with the fastest phase velocity as $V_m = 2V_\phi^*$. Figure adapted from [31].

definition at time $t = 0$. Correlations at any later time are then mediated through pairs of counter-propagating quasiparticles originating at the midway point between the two locations probed by the correlation function. Suppose we are interested in the correlation between site 0 and site R . The earliest correlation between the two sites is t^* when the pair of counter-propagating quasiparticles with the fastest *group velocity* $V_g^* = \max_k V_g(k) = \max_k \partial_k \varepsilon(k)$ arrive from the centre site $R/2$, see Fig. 3.1.1(a). This means that the correlation edge (CE), i.e. the correlation signal front, propagates with $V_{CE} = 2V_g^*$. On the other hand, all local extrema (maxima and minima) immediately behind the correlation edge are formed by the pair of counter-propagating quasiparticle travelling with the fastest *phase velocity* $V_\phi^* = \max_k V_\phi(k) = \max_k \varepsilon(k)/k$ and originating from the centre site. The local extrema therefore propagate with velocity $V_m = 2V_\phi^*$. Note however that the maxima can never exceed the CE, albeit they may have a greater velocity, because the quasiparticle close to the CE form a coherent superposition, i.e. a wave packet, see also Fig. 3.1.1(b). The CE thus encloses all signals while local maxima may propagate faster but decay beyond the former.

Thus, the expression for the correlation function Eq. (3.3) at asymptotically large R and t but constant R/t may be expressed in terms of the group velocity $V_g = \partial_k \varepsilon(k)$ and the phase velocity $V_\phi = \varepsilon(k)/k$ of quasiparticle. The weight function $\mathcal{F}(\mathbf{k})$ depends on the specific observable as well as the model therefore hiding the non-universal behaviour of out-of-equilibrium dynamics. For certain models and suitable observables, $\mathcal{F}(\mathbf{k})$ can be analytically approximated. An example of such an analytic treatment in the short-range interacting Bose-Hubbard model is given in Ref. [34]. Figure 3.1.2 shows the numerical behaviour of Eq. (3.3) as time (vertical) versus space (horizontal) plotted in linear scales for the short-range interacting Bose-Hubbard model. We observe an intricate interference pattern in both the (a) weakly interacting regime (super phase) and (b) in the strongly interacting regime (Mott insulator). We distinguish two *independent* marked features regarding the spreading of signals. Firstly, there is a signal edge that encloses all significant signals beyond which only rapidly vanishing contributions can be observed. This signal is associated with the Lieb-Robinson bounds and marks the spreading of information in this model. We mark the signal edge as a solid green line in both subplots of Fig. 3.1.2. Secondly, we observe local maxima

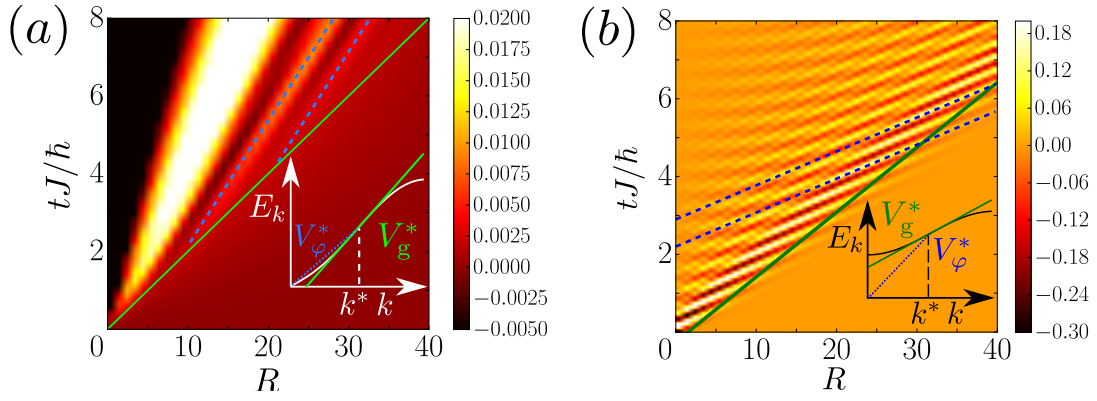


Figure 3.1.2: Computation of Eq. (3.3) with $G(R, t) = \langle a_R^\dagger(t)a_0(t) \rangle - \langle a_R^\dagger(0) \rangle \langle a_0(0) \rangle$ in the short-range interacting Bose-Hubbard model (a) $G(R, t)$ after a global quench in the superfluid phase from $(U\bar{n}/J)_i = 1$ to $(U\bar{n}/J)_f = 0.5$, and (b) $G(R, t)$ in the strongly interacting Mott Insulator phase after a global quench from $(U/J)_i = \infty$ to $(U/J)_f = 18$ at $\bar{n} = 1$. Figure from [34].

propagating *independently* with respect to the velocity of the signal edge. Local maxima may have a faster or slower propagation velocity than the signal front. They are however always contained in the light-cone-like signal edge and decay rapidly beyond the latter.

In accordance with Lieb–Robinson bounds, a causal cone, similar to the intrinsic light-cone of theories obeying Lorentz invariance, i.e. relativistic theories, is hence an emergent feature of the dynamics of non-relativistic short-range interacting lattice models.

Contrarily, for systems with long-range interactions, where the interaction strength is decaying like $1/R^\alpha$ with R the distance between two particles and α the long-range interaction exponent, the breakdown of this emergent causality is theoretically permitted [21, 23, 51]. Accordingly, the breakdown and the accompanying arbitrarily fast information spreading has been numerically observed when interactions are sufficiently long-ranged [49, 50]. On the other hand, when the interaction exponent is large enough, the interaction strength decays fast enough rendering the interaction effectively short-ranged, and one recovers ballistic propagation of information as theoretically predicted by Refs. [52–54].

However, the intermediate regime, where the interaction exponent is neither too small to cause instantaneous propagation of correlations nor too large to recover ballistic propagation as in the short-range case, is strongly debated. Whether a form of causality emerges there remains an open question and is the subject of this investigation. Theoretically known bounds permit super-ballistic ($t \propto R^\beta$, $\beta < 1$) propagation of correlations [21, 23, 51]. Yet several numerical studies have not filled out those bounds thereby challenging them and pointing towards significantly slower propagation [32, 45, 49, 55–58]. These simulations, however, reported different propagation scaling laws. Experiments performed with trapped ions have reported bounded propagation [99, 100], but they are limited to very small system sizes which impedes the extraction of scaling laws leaving the contradictions unsettled.

Cevolani et al. [34] attribute these apparent contradictions to the coexistence of above described two-fold dynamical scaling laws where a signal front bounds all correlations, but local signal maxima close to the edge propagate independently within the signal front. Furthermore, they extend the quasiparticle picture to the long-range interaction case and distinguish three different generic

but non-universal dynamical regimes. Firstly, the local regime is defined by the range of $\alpha > \alpha_c$ in which the quasiparticle dispersion relation $\varepsilon(k)$ is once differentiable. Here, all observables behave qualitatively like in the short-range limit $\alpha \rightarrow \infty$. Secondly, the quasi-local regime is defined by the range of $\alpha_c > \alpha > \alpha'_c$ in which the quasiparticle dispersion relation $\varepsilon(k)$ is finite but not differentiable everywhere in the thermodynamic limit. Thirdly, when the quasiparticle dispersion relation itself has some divergence and is not differentiable everywhere in the thermodynamic limit, we enter the instantaneous regime marked by the breakdown of causality and arbitrarily fast propagation of information. In Ref. [34], the authors also inspect the non-universal form of $\mathcal{F}(\mathbf{k})$ in the one dimensional long-range XXZ (LRXXZ) model as well as the long-range transverse Ising (LRTI) model within their generic analytical mean-field approach, and confirm the two-fold correlation spreading for the intermediate case. Figure 3.1.3 displays the quantitative behaviour of Eq. (3.3) with $G^\mu(R, t) = G_0(R, t) - G_0(R, t = 0)$, $G_0(R, t) = \langle S_R^\mu(t) S_0^\mu(t) \rangle - \langle S_R^\mu(t) \rangle \langle S_0^\mu(t) \rangle$ ($\mu = x, y, z$) in the above-mentioned long-range spin models. Note the logarithmic scale for both the time (vertical) and space (horizontal) axis. We observe a complex interference pattern whose main feature is again the qualitatively same twofold structure close to the propagation edge; the propagation of the signal front (marked as a green solid line) as well as local maxima (marked as blue dashed lines). Both features trace out straight lines in the log-log plot which means that the signals propagate with a power law $t \propto R^\beta$.

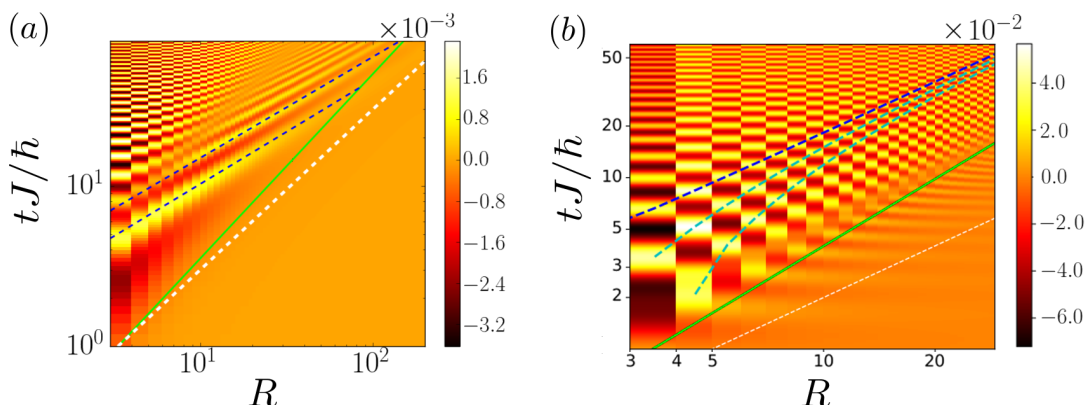


Figure 3.1.3: Computation of Eq. (3.3) displayed in a log-log-plot of time and space. We take $G^\mu(R, t) = G_0(R, t) - G_0(R, t = 0)$, $G_0(R, t) = \langle S_R^\mu(t) S_0^\mu(t) \rangle - \langle S_R^\mu(t) \rangle \langle S_0^\mu(t) \rangle$ with S_n^μ ($\mu = x, y, z$) the spin-1/2 operator. (a) $G^z(R, t)$ in the LRXXZ model with $\alpha = 2.3$ after a global quench from Δ_i to $\Delta_f = 0$, and (b) $G_x(R, t)$ in the LRTI model with $\alpha = 1.7$ connected correlation. Figure adapted from [34].

This analytical framework, however, has a generic but non-universal form, i.e. the dynamical regimes differ for different models, and it does not capture interactions beyond quadratic terms in the Hamiltonian. Nevertheless, the consistency and excellent agreement of these linear spin-wave theory (LSWT) predictions with numerics including beyond mean-field effects has been shown in Ref. [31] in the case of short-range interactions for the Bose-Hubbard chain utilising state-of-the-art tensor network simulations.

Here, we extend this research to systems with long-range interactions and study their dynamical propagation laws beyond mean-field theory by means of numerical, state-of-the-art tensor network techniques. Moreover, we extend the analytic approach to not only cover the far-from-equilibrium

dynamics induced by quenching a global parameter in the Hamiltonian but also inducing dynamics via a local quench on the ground state of the respective system.

Lastly, we wish to mention complementary studies following Cevolani et al. [34]. There, the two-fold structure close to the propagation front—consisting in a signal edge and local maxima—is explained by virtue of the model-dependent group velocity $\partial\varepsilon(k)/\partial k$ and phase velocity $\varepsilon(k)/k$, respectively, with quasiparticle dispersion relation $\varepsilon(k)$. It is therefore natural to ask whether this framework can be extended and more information about the dispersion may be extracted. The answer is affirmative as the authors Villa et al. showed in their Quench Spectroscopy framework as it is possible to extract the entire dispersion relation from equal time correlation functions [47, 48].

3.1.2 Outline of this chapter

In this chapter, we aim to characterise the spreading of quantum information and correlations in the intermediate (quasi-local) regime of a long-range interacting spin model in one spatial dimension by applying the aforementioned state-of-the-art numerical techniques, and furthermore extend the analytical framework of Refs. [31, 33, 34], which indicate an emergence of causality bound in time and space by a generic algebraic scaling $t \propto R^\beta$, to the spreading of local magnetisation and Rényi entropies when the out-of-equilibrium dynamics is induced by a local quench. Specifically, we determine the scaling laws for the propagation of a variety of observables in the long-range transverse Ising (LRTI) chain using matrix product state simulations. We find that a form of weak causality emerges, characterised by generic algebraic scaling laws $t \sim R^\beta$, where the specific value of the exponent β depends on the observable and the quench protocol. This warrants us to ascribe to this form of causality the attribute weak.

3.2 Model and Approach

The LRTI is defined by the Hamiltonian,

$$H_{\text{LRTI}} = \sum_{R \neq R'} \frac{J}{|R - R'|^\alpha} S_R^x S_{R'}^x - 2h \sum_R S_R^z, \quad (3.4)$$

where S_R^j ($j = x, y, z$) are the spin-1/2 operators on lattice site $R \in [0, N - 1]$, N is the system size, $J > 0$ is the coupling energy, and h is the transverse field.

At equilibrium, the phase diagram of the LRTI chain comprises two gapped phases separated by a second-order quantum phase transition, see Fig. 3.2.1 and Ref. [43]. For low fields h and rather short-range couplings (high values of α), the nearest-neighbour anti-ferromagnetic coupling dominates, and the system forms an ordered phase along the x direction (called x -Néel in Fig. 3.2.1) whereas the one-point function $\langle S_i^x \rangle \propto (-1)^i$ is alternating (staggered). For a large field h and long-range couplings (low values of α), the spin-field interaction is favoured, and an ordered phase is formed (called z -polarized phase in Fig. 3.2.1) where the state is polarized and the one-point function in z -direction is $\langle S_i^z \rangle \propto 1$.

Out of equilibrium, LSWT predicts, as mentioned above, three dynamical regimes (shaded by different colours in Fig. 3.2.1) [32, 49] which are characterised by non-analytic features of the quasi-

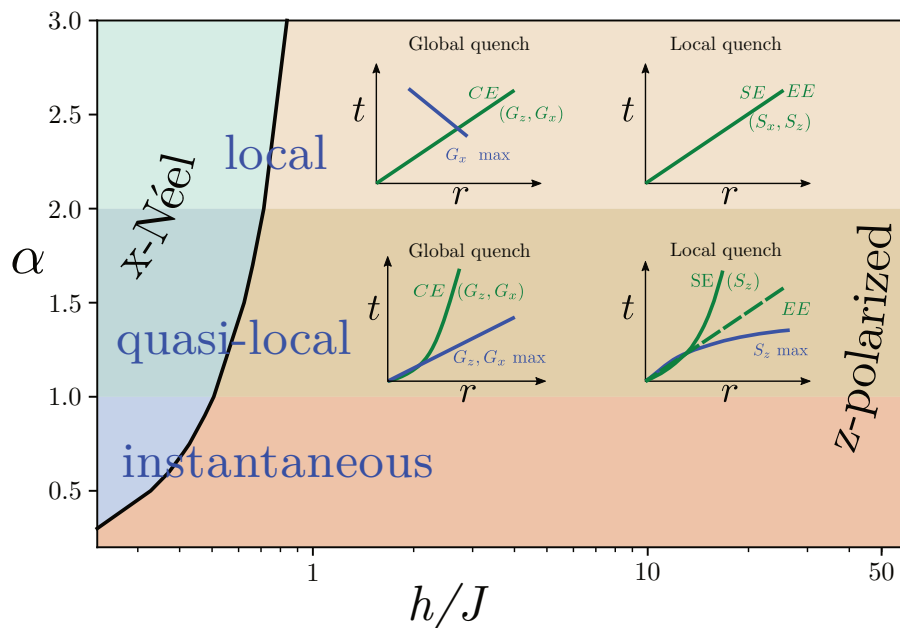


Figure 3.2.1: Phase diagram and dynamical properties of the LRTI chain in the $(h/J, \alpha)$ plane. The x -Néel phase (shades of blue) is separated from the z -polarized phase (shades of orange) by a critical line in black. The three dynamical regimes are shaded differently. As shown in the insets, the local and quasi-local regimes are characterised by distinct algebraic scaling laws for the correlation and spin edges (CE and SE, respectively), their maxima in space-time (max), and the entanglement edge (EE) after a global or local quench. Figure from [172].

particle (spin-waves) dispersion relation. For $\alpha \geq 2$ (local regime), the spin-wave dispersion relation (i.e. excitation spectrum) $\varepsilon(k)$ is bounded and differentiable thus the group velocities $V_g(k) = \partial_k \varepsilon_k$ (k is the momentum) exists and is finite for all k . This regime is qualitatively the same as the short-range case where the energy of the quasiparticle Hamiltonian is an analytic function of the quasiparticle momentum. In the local regime, correlations spread at a finite speed, giving rise to a linear causal cone [22, 23]. For $\alpha < 1$ (instantaneous regime), ε_k features an algebraic, infrared (thermodynamic limit $N_{\text{sys}} \rightarrow \infty$) divergence. This divergence is accompanied by the breakdown of causality, the lack of a characteristic timescale, and correlations spread arbitrarily fast. Lastly, for $1 < \alpha < 2$ (quasi-local regime), ε_k is finite in the thermodynamic limit but not differentiable, i.e. $V_g(k)$ diverges as $V_g(k) \sim 1/k^{2-\alpha}$.

3.3 Results

3.3.1 Linear spin wave theory

In this subsection we discuss the analytical approach to the out-of-equilibrium dynamics of the LRTI via linear spin wave theory working along the lines of Refs. [33, 34], and elaborate its implications on the dynamics of spin-spin correlation functions after a global quench (Section 3.3.1.1). We then extend this analytic framework to the out-of-equilibrium dynamics following a local quench predicting the scaling of local magnetisation (Section 3.3.1.2) and all Rényi entropies (Section 3.3.1.3). Subsequently, we compare these predictions with the findings via tensor network simulations in Section 3.3.2 and Section 3.3.3, respectively. There, our approach always starts by preparing the

ground state of the Hamiltonian (3.4) through the density matrix renormalisation group (DMRG) algorithm, which yields a faithful representation as a matrix product state (MPS). We then use the TDVP algorithm to evolve the MPS in time, see also Chapter 2.

The Hamiltonian (3.4) in the z-polarised phase (generally for $h/J \gg 1$) is amenable to an approximate diagonalisation. Firstly, a Holstein–Primakoff transformation [173],

$$S_R^x \simeq \frac{1}{2}(a_R^\dagger + a_R), \quad (3.5)$$

$$S_R^y \simeq -\frac{1}{2i}(a_R^\dagger - a_R), \quad (3.6)$$

$$S_R^z \simeq \frac{1}{2} - a_R^\dagger a_R, \quad (3.7)$$

where a_R is the annihilation operator of a boson on site R , approximates the Hamiltonian (3.4) as a bosonic quadratic one [33, 49]. This approximation is formally exact in the limit of very high transverse field strength $h/J \rightarrow \infty$. We subsequently apply a Fourier transform, which we define here as

$$\tilde{f}_k = \sum_{R=0}^{N-1} e^{iRk} f_R, \quad f_R = \frac{1}{N} \sum_{k=0}^{2\pi(N-1)/N} e^{-iRk} \tilde{f}_k, \quad (3.8)$$

with $k \in [0, 2\pi/N, \dots, 2\pi(N-1)/N]$. Note that we assume periodic boundary conditions such that H obeys translation invariance on the lattice. The Hamiltonian then reads in terms Holstein–Primakoff bosons as [33],

$$H \simeq \frac{1}{2} \sum_k \left[\mathcal{A}_k (a_k^\dagger a_k + a_{-k} a_{-k}^\dagger) + \mathcal{B}_k (a_{-k} a_k + a_k^\dagger a_{-k}^\dagger) \right], \quad (3.9)$$

with $\mathcal{A}_k = JP_\alpha(k) + 2h$, $\mathcal{B}_k = JP_\alpha(k)$, and $P_\alpha(k) = \sum_{R=1}^{N-1} \frac{\cos(Rk)}{R^\alpha}$ the Fourier transform of the long-range interaction potential $|R - R'|^{-\alpha}$. Applying a Bogolyubov transformation [174], where we define the quasiparticle creation and annihilation operators b^\dagger , b , as

$$\begin{pmatrix} b_k \\ b_{-k}^\dagger \end{pmatrix} = \begin{pmatrix} u_k & -v_k \\ -v_k & u_k \end{pmatrix} \begin{pmatrix} a_k \\ a_{-k}^\dagger \end{pmatrix}, \quad (3.10)$$

we find that the transformation diagonalises the Hamiltonian (3.9) if and only if

$$u_k = \text{sign}(\mathcal{A}_k) \sqrt{\frac{1}{2} \left(\frac{|\mathcal{A}_k|}{\varepsilon_k} + 1 \right)}, \quad v_k = \text{sign}(\mathcal{B}_k) \sqrt{\frac{1}{2} \left(\frac{|\mathcal{A}_k|}{\varepsilon_k} - 1 \right)}, \quad (3.11)$$

The Hamiltonian is then cast into diagonal form in terms of quasiparticle spin wave excitations (magnons) as,

$$H = \sum_k \varepsilon_k b_k^\dagger b_k, \quad \varepsilon_k = \sqrt{\mathcal{A}_k^2 - \mathcal{B}_k^2} = 2\sqrt{h[h + JP_\alpha(k)]}. \quad (3.12)$$

3.3.1.1 Spin–Spin correlations after a global quench

In the following, we consider the sudden change of a global parameter of the Hamiltonian (3.4) within the z -polarised phase, cf. Fig. 3.2.1. In such a case, the correlation function $G_x(R, t)$ as defined in Eq. (3.1) takes the form [34],

$$G(r, t) = g(r) - \int_{-\pi}^{\pi} \frac{dk}{(2\pi)^D} \mathcal{F}(k) \frac{1}{2} \left(e^{ik \cdot r + 2i\varepsilon(k)t} + e^{ik \cdot r - 2i\varepsilon(k)t} \right), \quad (3.13)$$

$$\text{with } \mathcal{F}(k) = \frac{\hbar(J_i - J_f)P_\alpha(k)}{8[h + J_f P_\alpha(k)]\sqrt{\hbar[h + J_i P_\alpha(k)]}}. \quad (3.14)$$

We recover the generic form for the two-point correlation function as discussed above while the non-generic weight function $\mathcal{F}(k)$ depends on the observable and the quench protocol. We aim to extract the asymptotic scaling behaviour of Eq. (3.13) in the sense of $R \rightarrow \infty$, $t \rightarrow \infty$, and $R/t = \text{const}$. To this end, we employ the stationary phase approximation which yields,

$$G_x(R, t) \sim \frac{\mathcal{F}(k_{\text{sp}})}{\sqrt{|\partial_k^2 \varepsilon_{k_{\text{sp}}}|t}} \cos(k_{\text{sp}}R - 2\varepsilon_{k_{\text{sp}}}t + \phi), \quad (3.15)$$

where ϕ is a for us irrelevant constant, k_{sp} is the quasi-momentum at which the complex phase of Eq. (3.13) is stationary. It is defined by the solution to

$$2 \left. \frac{\partial \varepsilon_k}{\partial k} \right|_{k=k_{\text{sp}}} = 2V_g(k_{\text{sp}}) = R/t > 0, \quad (3.16)$$

for given $R/t = \text{const}$.

Quasi-local regime $1 < \alpha < 2$ In the quasi-local regime, ε_k is bounded over the entire Brillouin zone but not differentiable everywhere implying an IR divergence of the group velocity $V_g(k \rightarrow 0) \rightarrow \infty$. Hence, for *any* given ratio R/t , the signal is dominated by the quasiparticles propagating with momentum k_{sp} such that $V_g(k_{\text{sp}}) = R/t$. Since the group velocity has an IR divergence, only the low momentum limit of ε_k and $V_g(k)$ for $k \rightarrow 0$ are relevant to their behaviour for asymptotically large R and t . We hence expand those in terms of k keeping only the zero and first order terms to extract the asymptotic behaviour of Eq. (3.15). The long-range interaction potential reads as $P_\alpha(k) \simeq P_\alpha(0) + P'_\alpha |k|^{\alpha-1}$, with $P_\alpha(0) > 0$ and $P'_\alpha < 0$ as the expansion coefficients. The excitation energy expands as $\varepsilon_k \simeq \Delta - c|k|^z$, with $\Delta = 2\sqrt{\hbar[h + JP_\alpha(0)]} > 0$ is the gap, $z = \alpha - 1 \geq 0$ is the dynamical exponent, and $c = \sqrt{\hbar/[h + JP_\alpha(0)]} |P'_\alpha| > 0$ is a prefactor. For given R/t , we obtain

$k_{\text{sp}} = (2czt/R)^{\frac{1}{1-z}}$ through Eq. (3.16) and insert it in Eq. (3.15) to obtain the IR limit of the $G_x(R, t)$ correlation function. It yields,

$$G_x(R, t) \propto \frac{t^\gamma}{R^\chi} \cos\left(A_z \left(\frac{t}{R^z}\right)^{\frac{1}{1-z}} - 2\Delta t + \phi\right), \quad (3.17)$$

$$A_z = 2c(2cz)^{z/(1-z)}(1-z), \quad (3.18)$$

$$\gamma = \frac{\nu + 1/2}{1-z}, \quad (3.19)$$

$$\chi = \frac{\nu + (2-z)/2}{1-z}, \quad (3.20)$$

where we defined $\nu \geq 0$ as the scaling exponent of the weight function $\mathcal{F}(k)$ in the infrared limit $\mathcal{F}(k \rightarrow 0) \sim |k|^\nu$. From its definition (3.14) and from the expansion of $P_\alpha(k)$ in the IR limit follows that $\nu = 0$ for the $G_x(R, t)$ correlation function. The spin correlation signal edge (CE) is now found by imposing that the amplitude of the oscillations in Eq. (3.17) shall be constant thereby defining a curve in spacetime $t \propto R^\beta$ given by,

$$\text{const.} = \frac{t^\gamma}{R^\chi} \quad \Rightarrow \quad t \propto R^{\beta_{\text{CE}}}, \quad \beta_{\text{CE}} = \chi/\gamma = 3 - \alpha. \quad (3.21)$$

On the other hand, the spreading of local extrema (in particular maxima) is dictated by a constant phase of the oscillations in Eq. (3.17),

$$\text{const.} = A_z \left(\frac{t}{R^z}\right)^{\frac{1}{1-z}} - 2\Delta t + \phi \quad \Rightarrow \quad A_z \left(\frac{t}{R^z}\right)^{\frac{z}{1-z}} - 2\Delta = \frac{\text{const.}}{t} \xrightarrow{t \rightarrow \infty} 0 \quad \Rightarrow \quad t \propto R, \quad (3.22)$$

thus local extrema propagate ballistically $t \propto R^{\beta_m}$ with $\beta_m = 1$. Note that this applies when the system has a gap $\Delta \neq 0$. Otherwise, one finds for a gapless system $\Delta = 0$ in the quasi-local regime, $t \propto R^{\beta_m}$ with $\beta_m = z = \alpha - 1 < 1$. In such a case, local maxima of the correction function propagate super-ballistically.

Local regime $\alpha > 2$ Contrarily to the quasi-local regime, in the local regime the quasiparticle energy ε_k as well as the quasiparticle group velocity are bounded over the entire Brillouin zone, i.e. there exists a finite maximum group velocity $V_g(k^*) = \max_{k \in \text{BZ}} V_g(k)$ even in the thermodynamic limit. Therefore, the stationary phase condition Eq. (3.16) has only a solution for $R/t \leq 2V_g(k^*)$, as opposed to *any* ratio R/t as it is the case in the quasi-local regime. Consequently, the CE—given by the fastest moving quasiparticles—is determined by the spreading of quasiparticles with and close to the stationary quasi-momentum $k_{\text{sp}} \simeq k^*$. The CE thus spreads ballistically with velocity $V_{\text{CE}} = 2V_g(k^*)$. Moreover, the spacetime curve of local maxima close to the edge is determined by the condition that the phase of the oscillations in Eq. (3.15) with $k = k^*$ shall be constant. Hence, the local maxima, too, spread ballistically in the local regime with velocity $V_m = 2V_\phi(k^*)$ where $V_\phi(k) = \varepsilon_k/k$ is the quasiparticle phase velocity.

3.3.1.2 Local magnetisation after a local quench

In the following, we consider the sudden change of the ground state of the Hamiltonian (3.4) deep in the z -polarised phase by applying a spin flip to the centre site of the spin chain; $|\psi_0\rangle \propto S_{N/2}^- |\psi_{GS}\rangle$. The resulting state breaks translation invariance and is therefore suitable for studying the propagation of local one-point functions (magnetisation in the LRTI) as well as the bipartite entanglement entropies with variable bipartition location. Since we inspect the ground state deep in the z -polarised phase, $h \gg J$, we can very well approximate it as the fully polarized product state $|\uparrow \dots \uparrow\rangle$. Following the diagonalisation in Section 3.3.1 we therefore obtain the time dependence of the initial state in Heisenberg picture as,

$$|\Psi_0(t)\rangle = \tilde{\mathcal{N}} S_0^-(t) |\Psi_{GS}\rangle = \tilde{\mathcal{N}} a_0^\dagger(t) |0_b\rangle = \tilde{\mathcal{N}} \sum_{k=0}^{2\pi(N-1)/N} u_k e^{i\varepsilon_k t} b_k^\dagger(t=0) |0_b\rangle, \quad (3.23)$$

where $S_0^- = S_0^x - iS_0^y$ is the spin lowering operator at the central site (labelled by $j = 0$), a_0^\dagger is the bosonic Holstein–Primakoff creation operator (cf. Eq. (3.5)), $b_k(0)$ is the quasiparticle annihilation operator, u_k is defined in Eq. (3.11), $|0_b\rangle$ is the quasi-particle vacuum, and $\tilde{\mathcal{N}} = (\sum_k u_k^2)^{-1/2}$ is the normalisation of the state.

To compute the one-point function $M^z(R, t) = 1/2 - \langle S_R^z(t) \rangle$, we use Eq. (3.23) as well as Eq. (3.5). This yields,

$$M^z(R, t) := \frac{1}{2} - \langle S_R^z(t) \rangle \simeq \left| \int_{-\pi}^{\pi} \frac{dk}{2\pi} \frac{\mathcal{F}_1(k)}{2} (e^{i(kR+\varepsilon_k t)} + e^{-i(kR-\varepsilon_k t)}) \right|^2 + \left| \int_{-\pi}^{\pi} \frac{dk}{2\pi} \frac{\mathcal{F}_2(k)}{2} (e^{i(kR+\varepsilon_k t)} + e^{-i(kR-\varepsilon_k t)}) \right|^2. \quad (3.24)$$

Here, $\mathcal{F}_1(k)$ and $\mathcal{F}_2(k)$ are weight functions which read as,

$$\mathcal{F}_1(k) = \frac{1}{2} \left(\frac{\mathcal{A}_k}{\varepsilon_k} + 1 \right) = \frac{1}{2} \left(\frac{2h + JP_\alpha(k)}{2\sqrt{h[h + JP_\alpha(k)]}} + 1 \right), \quad \mathcal{F}_2(k) = -\frac{\mathcal{B}_k}{2\varepsilon_k} = -\frac{JP_\alpha(k)}{4\sqrt{h[h + JP_\alpha(k)]}}. \quad (3.25)$$

For large transverse fields, $h \gg J$, we find $\mathcal{F}_1(k) \simeq 1 \gg \mathcal{F}_2(k) \sim J/h$. Thus, we neglect the term proportional to $\mathcal{F}_2(k)$ in Eq. (3.24) in the following.

Quasi-local regime $1 < \alpha < 2$ Paralleling the discussion of the global quench dynamics, the spreading of $M^z(R, t)$ in the quasi-local regime is dominated by the IR behaviour $k \rightarrow 0$ of its constituting functions as the quasiparticle group velocity diverges in the thermodynamic limit, yet the energy is bounded everywhere in the Brillouin zone. We expand the long-range interaction

potential in powers of k as $P_\alpha(k) \simeq P_\alpha(0) + P'_\alpha|k|^{\alpha-1}$, and the quasiparticle energy as $\varepsilon_k \simeq \Delta - c|k|^z$, cf. Section 3.3.1.1 for the expansion coefficients. Inserting these into Eq. (3.24) yields,

$$\frac{1}{2} - \langle S_R^z(t) \rangle \simeq \left| e^{i\Delta t} \int_{-\pi}^{\pi} \frac{dk}{2\pi} \frac{\mathcal{F}_1(k)}{2} \left(e^{i(kR - c|k|^z t)} + e^{-i(kR + c|k|^z t)} \right) \right|^2 \quad (3.26)$$

$$= \left| \int_{-\pi}^{\pi} \frac{dk}{2\pi} \frac{\mathcal{F}_1(k)}{2} \left(e^{i(kR - c|k|^z t)} + e^{-i(kR + c|k|^z t)} \right) \right|^2. \quad (3.27)$$

The gap is therefore irrelevant to the local magnetisation since it is in the exponential contributing as an oscillating prefactor of the integral which is thus identically unity in the absolute value squared. This is in direct contrast to the behaviour of the spin-spin correlation function Eq. (3.17). There, the gap plays a crucial role regarding the scaling laws for the local maxima. This is equivalent to our earlier observation that the initial state after the local quench Eq. (3.23) is a state in the first excited submanifold of the bosonic quasiparticle Hilbert space. Similarly to above, we employ the stationary phase approximation to Eq. (3.27) whose stationary phase quasi-momentum is given by the solution of the equation $V_g(k_{\text{sp}}) = R/t > 0$. This yields,

$$\frac{1}{2} - \langle S_R^z(t) \rangle \sim \frac{t^\lambda}{R^\mu} \cos\left(B_z \frac{t^{2\lambda}}{R^\xi} + \phi \right), \quad (3.28)$$

where $\lambda = \frac{1}{2(1-z)}$, $\mu = \frac{2-z}{2(1-z)}$, $\xi = \frac{z}{1-z}$, and $B_z = c(cz)^{\alpha'} - (cz)^{2\lambda}$. Consequently, the spin magnetisation edge (SE) is determined by lines of constant amplitude of the oscillations of Eq. (3.28) yielding $t \propto R^{\beta_{\text{SE}}}$ with $\beta_{\text{SE}} = 3 - \alpha$, while the magnetisation maxima trace out the curve of constant phase yielding $t \propto R^{\beta_{\text{m}}}$ with $\beta_{\text{m}} = \alpha - 1$. Thus, the SE propagates sub-ballistically while the local maxima contained inside propagate super-ballistically in the quasi-local regime.

Local regime $\alpha > 2$ In the local regime, both quasiparticle energy ε_k and group velocity are finite over the entire Brillouin zone in the thermodynamic limit. Analogously to the CE, the SE is thus determined by the maximum group velocity $V_g(k^*)$, and the stationary phase approximation has a solution only for $V_g(k^*) \geq R/t > 0$ as opposed to *any* ratio R/t . Note that for the magnetisation a factor of 2 is absent compared to the CE. Consequently, the spin edge propagates ballistically with velocity $V_{\text{SE}} = V_g(k^*)$ as opposed to the correlation edge's velocity $V_{\text{CE}} = 2V_g(k^*)$. To estimate the propagation of local maxima, we employ the stationary phase approximation to Eq. (3.24) yielding,

$$1/2 - \langle S_R^z(t) \rangle \sim \left| \frac{\mathcal{F}_1(k^*)}{\sqrt{|\partial_k^2 \varepsilon_{k^*}| t}} [\cos(k^* R - \varepsilon_{k^*} t + \phi) - i \sin(k^* R - \varepsilon_{k^*} t + \phi)] \right|^2, \quad (3.29)$$

with ϕ a constant phase. We thus obtain in absolute value squared a sum of two terms proportional to the sin and cos, respectively. These two terms have evidently a relative phase of $\pi/2$, which mutually cancels the local maxima under the absolute value squared. Therefore, no oscillations with local maxima inside the SE are expected in the local regime as opposed to the quasi-local regime.

3.3.1.3 Density matrix and Rényi entanglement entropy dynamics after a local quench

In this subsection, we aim at computing the bipartite Rényi entanglement entropies defined as,

$$\mathcal{S}_n(R, t) = \frac{1}{1-n} \log(\text{tr}[\rho^n(R, t)]), \quad (3.30)$$

with $n > 0$ the Rényi entropy order and $\rho(R, t) = \rho_A = \text{tr}_B(|\Psi(t)\rangle\langle\Psi(t)|)$ the reduced density matrix at time t of the subsystem $A = [R, R + 1, \dots, N/2]$. The position R is measured from the flipped central spin and B denotes the complementary subsystem. We employ the exact knowledge of the quadratic quasiparticle excitation spectrum and its relation to the microscopic Hamiltonian (3.4) through the Holstein–Primakoff (Eq. (3.5)) and Bogolyubov transformations (Eq. (3.10)) to infer the time dependence of the density matrix of the entire system. Crucially, the initial state for $h/J \gg 1$ after a local spin flip, Eq. (3.23), is a superposition of single-quasiparticle excitations allowing us to proceed analytically. Defining S as the entire system and A and B as complementary subsystems, we may decompose the initial state Eq. (3.23) into the cases where the excitation is in either subsystem A or B and decompose any single excitation state $|1\rangle$ as,

$$\sum_{m \in S} |1_m\rangle = \sum_{m \in A} |1_m\rangle \otimes |0_B\rangle + \sum_{m \in B} |0_A\rangle \otimes |1_m\rangle, \quad (3.31)$$

where $|0_{A,B}\rangle$ is the unique vacuum of the subsystems A and B , respectively. The state of the entire system thus reads as

$$|\Psi_0(t)\rangle = \tilde{\mathcal{N}} \sum_{m \in B} \sum_{k=-\pi}^{\pi} u_k e^{i(\varepsilon_k t + mk)} |0_A\rangle \otimes |1_m\rangle + \tilde{\mathcal{N}} \sum_{m \in A} \sum_{k=-\pi}^{\pi} u_k e^{i(\varepsilon_k t + mk)} |1_m\rangle \otimes |0_B\rangle \quad (3.32)$$

$$:= \sqrt{\lambda_1} e^{i\theta_1} |0_A\rangle \otimes |\chi_B\rangle + \sqrt{\lambda_2} e^{i\theta_2} |\chi_A\rangle \otimes |0_B\rangle, \quad (3.33)$$

where λ_1 and λ_2 are real-valued functions,

$$\lambda_2(R, t) := \tilde{\mathcal{N}}^2 \sum_{m \in A} \left| \sum_{k=-\pi}^{\pi} e^{i(\varepsilon_k t + mk)} \right|^2 \quad (3.34)$$

such that $\lambda_1 + \lambda_2 = 1$, θ_1 and θ_2 are some phases, and $|\chi_{A,B}\rangle$ is the complex single-particle state in subsystem A , B the first excited submanifold of the Hilbert space. The density matrix of the entire system thus contains four terms,

$$\begin{aligned} \rho(t) = & \lambda_1 |0_A\rangle\langle 0_A| \otimes |\chi_B\rangle\langle \chi_B| + \lambda_2 |\chi_A\rangle\langle \chi_A| \otimes |0_B\rangle\langle 0_B| \\ & + \sqrt{\lambda_1 \lambda_2} e^{i(\theta_1 - \theta_2)} |0_A\rangle\langle \chi_A| \otimes |\chi_B\rangle\langle 0_B| + \sqrt{\lambda_1 \lambda_2} e^{i(\theta_2 - \theta_1)} |\chi_A\rangle\langle 0_A| \otimes |0_B\rangle\langle \chi_B|, \end{aligned} \quad (3.35)$$

while the reduced density matrix of subsystem A contains two terms,

$$\rho_A(t) = \text{tr}_B(\rho(t)) = \lambda_1(t) |0_A\rangle\langle 0_A| + \lambda_2(t) |\chi_A\rangle\langle \chi_A|, \quad (3.36)$$

whereas λ_1 and λ_2 are its two eigenvalues.

At this stage it is worthwhile to discuss Eq. (3.34). Since the two eigenvalues are constrained to add to unity and have the same functional form, we may without loss of generality restrict our analysis to one of them. The eigenvalue $\lambda_2 = \lambda_2(R, t)$ is a function of R through the boundary of the subsystem A and a function of time through the coherent superposition of quasiparticles forming the spin-lowering operator. Moreover, it is a non-local quantity since it contains contributions from all space coordinates inside the subsystem A . The reduced density matrix Eq. (3.36) is a diagonal 2×2 matrix. This has the noteworthy consequence that any entropy of entanglement is bounded from above by the maximally entangled state $\lambda_1 = \lambda_2 = 1/2$, implying all Rényi entropies are bounded by $\mathcal{S}_n = \log(2) \approx 0.693$. We will later see, cf. Fig. 3.3.3 and Appendix 3.B, that this bound is indeed confirmed by our simulation of the out-of-equilibrium dynamics of the exact microscopic Hamiltonian (3.4) thereby *a posteriori* confirming our approximations made within LSWT. Furthermore, Eq. (3.34) constitutes an explicit solution of one of the two eigenvalues of the reduced density matrix in a finite system and within LSWT approximations. In particular, it contains two sums each proportional to the size of the system since the subsystem A evidently scales with the system size $N \propto \|A\|$, as does the sum over the Brillouin zone $N = \|BZ\|$. The complexity of Eq. (3.34) and thus Eq. (3.36) is therefore only N^2 instead of the naive exponential scaling 2^N . This is a direct consequence of the fact that the initial state Eq. (3.23), within the Holstein–Primakoff approximation, is a superposition of first-excited states implying that it can be decomposed in the case of the excitation being in subsystem A or B , respectively. This can also be read off the expression of the density matrix of the entire state, Eq. (3.35). The advantageous scaling of the complexity of λ_2 renders the numerical computation of it in a very large system size, here e.g. $N = 512$, entirely feasible without the need of a High-performance Computing Clusters. We therefore proceed in a double approach. Firstly, we proceed to approximate Eq. (3.34) in an analytic form allowing us to extract the asymptotic scaling behaviour of the eigenvalue λ_2 and therefore of all Rényi entropies. Secondly, we shall numerically compute Eq. (3.34) in a large system size. We hence may verify our approximations made *a posteriori* within LSWT, as well as with the beyond mean field theory numerics discussed in the following section.

In the limit of $h/J \gg 1$ the Bogolyubov coefficient approaches unity, $u_k \simeq 1$. The $t \rightarrow \infty$, $R \rightarrow \infty$, $R/t = \text{const.}$ behaviour of the second eigenvalue of the reduced density matrix in the infinite volume limit using the stationary phase approximation is given by

$$\lambda_2 \simeq \tilde{\mathcal{N}}^2 \sum_{m \in A} \left| \sum_{k=-\pi}^{\pi} e^{i(\varepsilon_k t + mk)} \right|^2 \stackrel{N \rightarrow \infty}{\propto} \tilde{\mathcal{N}}^2 \sum_{m \in A} \frac{1}{t |\partial_k^2 \varepsilon_{k_{\text{sp}}}|} \cos^2[\varepsilon(k_{\text{sp}})t - k_{\text{sp}}m + \phi] \quad (3.37)$$

where k_{sp} is defined by the stationary phase condition $V_g(k_{\text{sp}}) = m/t$ with $V_g(k) = \partial \varepsilon_k / \partial k$. We obtain an expression of the reduced density matrix which is the superposition of stationary phase approximations—each with their own stationary phase condition—summed over all spatial coordinates m in subsystem A . While in principle arbitrary, in the following we consider the bipartitions $A = \{R, R+1, \dots, N/2\}$ and $B = \{-N/2, -N/2+1, \dots, R-1\}$ and compute an analytic expression for Rényi entropies \mathcal{S}_n .

Quasi-local regime $1 < \alpha < 2$ The quasiparticle energy spectrum in the quasi-local regime is bounded but its first derivative $V_g(k)$ diverges in the infrared limit ($k_{sp} \rightarrow 0$) as $V_g(k) \sim 1/k^{2-\alpha}$ dominating the eigenvalues of the reduced density matrix Eq. (3.37). Inserting the stationary phase quasi-momentum for each term in the sum yields,

$$\lambda_2 \propto \tilde{\mathcal{N}}^2 t^{\frac{1}{1-z}} \sum_{m=0}^{\infty} \frac{1}{(m+R)^{\frac{2-z}{1-z}}} \cos^2 \left[C_z \left(\frac{t}{(m+R)^z} \right)^{\frac{1}{1-z}} + \phi \right], \quad (3.38)$$

with $C_z = (cz)^{\frac{1}{1-z}} (1 + c^{z+1} z^z)$ and $\phi = \text{const}$. Owing to the superposition of all contributions from all sites m in the subsystem A , the scaling behaviour cannot be extracted for each term individually, and we instead have to consider all terms in the sum. This means that we cannot *a priori* simply inspect the scaling of the coefficient without taking into account the oscillatory cosine term. However, in both our TDVP and LSWT numerical results, cf. Fig. 3.3.3, we find no significant internal oscillations of the Rényi entanglement entropies, implying that the oscillatory term does not contribute significantly to the observed behaviour of the entanglement edge. Additionally, we find the frequency C_z to be very large such that the cosine term varies rapidly compared to the algebraically decaying amplitude. We therefore argue *a posteriori* to substitute the oscillating cosine term with its average value of $1/2$ in the sum. We subsequently find,

$$\lambda_2 \propto \tilde{\mathcal{N}}^2 \frac{2\pi(cz)^\kappa}{|cz(z-1)|} t^{\frac{\kappa}{2-z}} \zeta(\kappa, R), \quad (3.39)$$

where $\zeta(s, q) = \sum_{m=0}^{\infty} (m+q)^{-s}$ is the Hurwitz zeta function [175, 176] and $\kappa = \frac{z-2}{z-1} = \frac{\alpha-3}{\alpha-2}$. Using the series representation of the Hurwitz zeta function in the limit of large R and positive κ , this may be written as

$$\lambda_2 = \tilde{\mathcal{N}}^2 \frac{2\pi(cz)^\kappa}{|cz(z-1)|} t^{\frac{\kappa}{2-z}} \left[\frac{R^{1-\kappa}}{\kappa-1} + \frac{R^{-\kappa}}{2} + \sum_{j=1}^{\infty} \frac{B_{2j}}{(2j)!} \frac{\Gamma(\kappa+2j-1)}{\Gamma(\kappa)} R^{1-\kappa-2j} \right], \quad (3.40)$$

where B_n are the Bernoulli numbers, and $\Gamma(s) = \int_0^\infty e^{-u} u^{s-1} du$ is the gamma function [176]. In the quasi-local regime, we have $\kappa > 2$ and so in the limit of large R we may neglect the second and third terms which contain contributions of the order equal to $R^{-\kappa}$ and higher, and only consider the leading term of order $R^{1-\kappa}$. It yields

$$\lambda_2 \approx \tilde{\mathcal{N}}^2 \frac{2\pi(cz)^\kappa}{|cz(z-1)|} \frac{1}{\kappa-1} \left(\frac{t}{R} \right)^{\frac{1}{1-z}} \quad (3.41)$$

which scales in R and t with the same power. Note that the stationary phase approximation is not valid when taking $t \rightarrow \infty$ alone, and the above equation does not hold in this limit. Consequently, any analytic function of λ_2 , particularly Rényi entropies, will scale in R and t with the same power, such that

$$\mathcal{S}_n(R, t) \simeq \frac{1}{1-n} \log[(\lambda_1(R/t))^n + (\lambda_2(R/t))^n] = \frac{1}{1-n} \log[(1 - \lambda_2(R/t))^n + (\lambda_2(R/t))^n]. \quad (3.42)$$

This yields a dynamical exponent of the entanglement entropy edge (EE) of unity, $\beta_{EE}^n = 1 \forall n$, in close agreement with our numerical results using both TDVP and LSWT (i.e. Eq. (3.34)). Additionally, the finite-size corrections neglected in the step from Eq. (3.40) to Eq. (3.41) are likely responsible for the deviation from ballistic behaviour seen in our simulations on small system sizes.

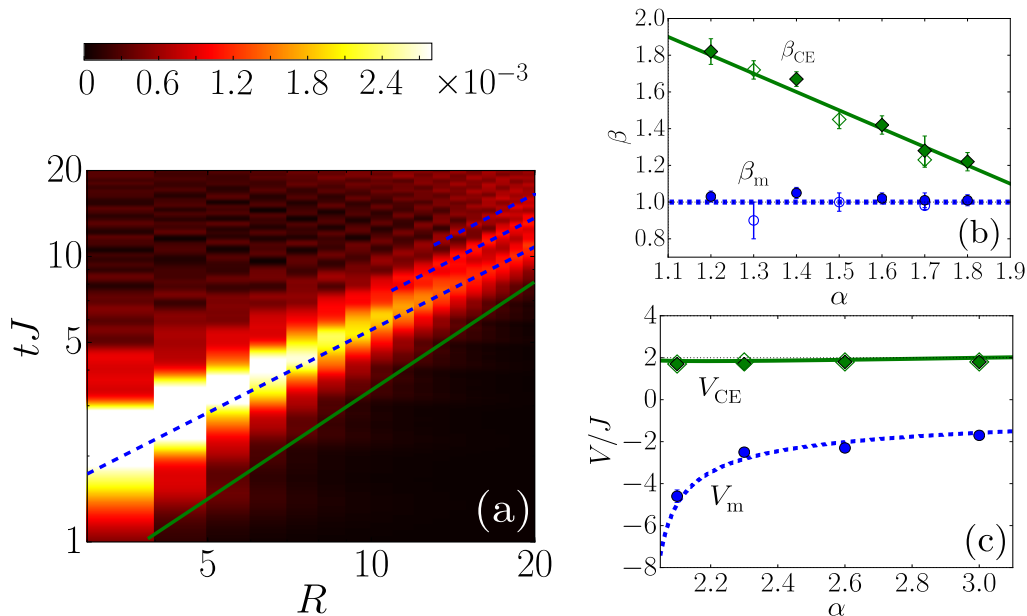


Figure 3.3.1: Spreading of spin correlations in a global quench, with system size $N = 48$. (a) TDVP results for G_z and a quench from $(h/J)_i = 50$ to $(h/J)_f = 1$ in the quasi-local regime at $\alpha = 1.7$. The solid green and dashed blue lines are fits of the CE and the extrema, respectively. (b) Dynamical exponents β_{CE} (green diamonds) and β_{m} (blue disks), fitted from results as in panel (a) for G_z (empty symbol) and G_x (full symbol), and comparison to the LSWT predictions (solid green and dashed blue lines). (c) Spreading velocities V_{CE} (green diamonds) and V_{m} (blue disks), in the local regime and comparison to the LSWT predictions (solid green and dashed blue lines). Figure from [172].

3.3.2 Global quench dynamics

In this subsection, we present the numerical results by means of the time-dependent variational principle (TDVP) of the out-of-equilibrium dynamics of the LRTI induced by a global quench. We start with an initial ground state of Hamiltonian (3.4) at $(h/J)_i = 50$. The state is then thrown out of equilibrium by a sudden change of a global transverse field parameter h of the Hamiltonian (3.4) to a lower value by evolving it in time with the Hamiltonian at $(h/J)_f = 1$, both in the z -polarised phase. This global quench produces out-of-equilibrium dynamics as the timescale of this change is shorter than any timescale in the system, and the previous ground state is in general not an eigenstate of the new, post-quench Hamiltonian. We consider the resulting dynamics of the two-point spin correlation function,

$$G_j(R, t) = G_j^0(R, t) - G_j^0(R, 0), \quad (3.43)$$

$$G_j^0(R, t) = \langle S_R^j(t) S_{N/2}^j(t) \rangle - \langle S_R^j(t) \rangle \langle S_{N/2}^j(t) \rangle, \quad (3.44)$$

where t marks the time, R the distance to the central lattice site $N/2$, and we focus along the spin-direction $j = x$. Subsequently, we are interested in the scaling of those observables with different values of α in the quasi-local ($1 < \alpha < 2$) and local regime ($\alpha > 2$). The numerical result of $G_z(R, t)$ after a global quench in the quasi-local regime ($\alpha = 1.7$) is displayed in Fig. 3.3.1(a) (note the log-log plot). The asymptotic long time and space behaviour of $G_z(R, t)$ can be well fitted by the scaling law $t \propto R^\beta$. Here, it is important to distinguish the scaling of the marked maxima (dashed blue lines in

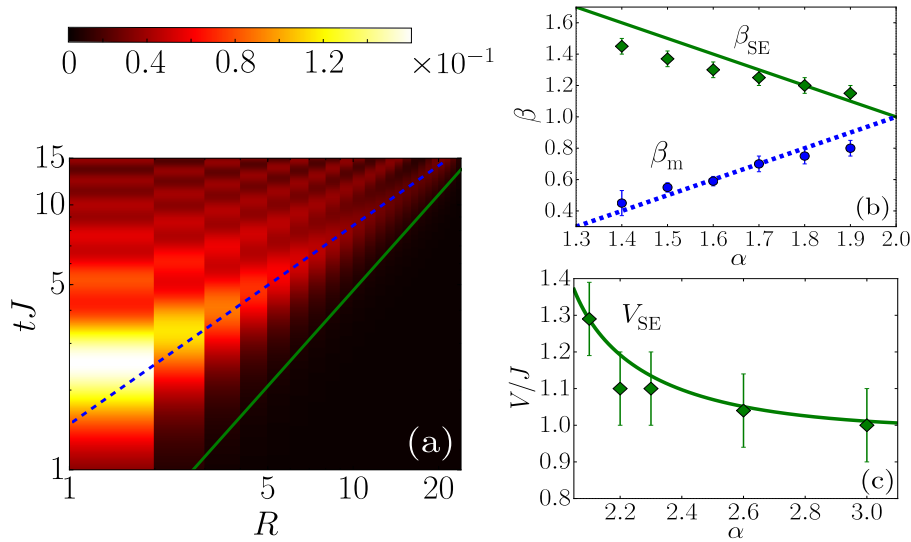


Figure 3.3.2: Spreading of the local magnetisation for a local quench, with system size $N = 48$. (a) Log-log spacetime plot of TDVP results for $M^z(R, t)$ (3.24) versus the time and the distance from the flipped spin for $h/J = 50$ and $\alpha = 1.8$. (b) Dynamical exponents β_{SE} (green diamonds) and β_m (blue disks), fitted form results as in panel (a) and comparison to the LSWT predictions (solid green and dashed blue lines). (c) Spreading velocity V_{SE} (green diamonds) and comparison to the LSWT prediction in the local regime (solid green line). Figure from our paper [172].

Fig. 3.3.1(a)), and the envelope or edge of all correlations (CE) beyond which the signal falls below a constant threshold (solid green line). Correspondingly, we show the fitted dynamical exponents β_m and β_{CE} for the quasi-local regime in Fig. 3.3.1(b). There, the LSWT prediction of the dynamical exponents in the asymptotic space and time limit for the CE is plotted by the solid green line, and the dynamical exponents for the maxima is plotted by the dashed blue line, respectively. We find a good agreement between the numerical fits and the LSWT prediction confirming the characteristic two-fold spreading scenario of the latter with sub-ballistic spreading of the correlation edge and super-ballistic spreading of local maxima.

In the local regime ($\alpha > 2$), we find that the correlation edge and the maxima in the correlation function spread ballistically $\beta_m \simeq 1 \simeq \beta_{CE}$. The two velocities are however different from each other, which is characteristic of a non-linear dispersion relationship $\varepsilon(k)$. The velocity of the CE is $V_{CE} = 2V_g(k^*)$, that is twice the maximum group velocity $V_g(k) = \partial\varepsilon/\partial k$ of the spin-waves. Furthermore, the maxima are spreading with $V_m = 2V_\phi(k^*)$, that is twice the phase velocity $V_\phi(k) = \varepsilon/k$ at quasi-momentum k^* where the group velocity is maximum. Note that in the LRTI, $k^* < 0$ and $V_m = 2V_\phi(k^*) = 2\varepsilon_{k^*}/k^* < 0$. In Fig. 3.3.1(c), we find the LSWT predictions for the two spreading velocities match the numerical fits with good agreement confirming the twofold spreading behaviour also in the local regime.

3.3.3 Local quench dynamics

We now consider inducing out-of-equilibrium dynamics by a local quench on the ground state of Hamiltonian (3.4) at large values of $h/J = 50$ deep in the z -polarised phase by applying a sudden flip to the central spin at site $N/2$. Consequently, the initial state is not an eigenstate of the Hamiltonian, and the resulting dynamics are far from equilibrium. The ground state at such large field values is

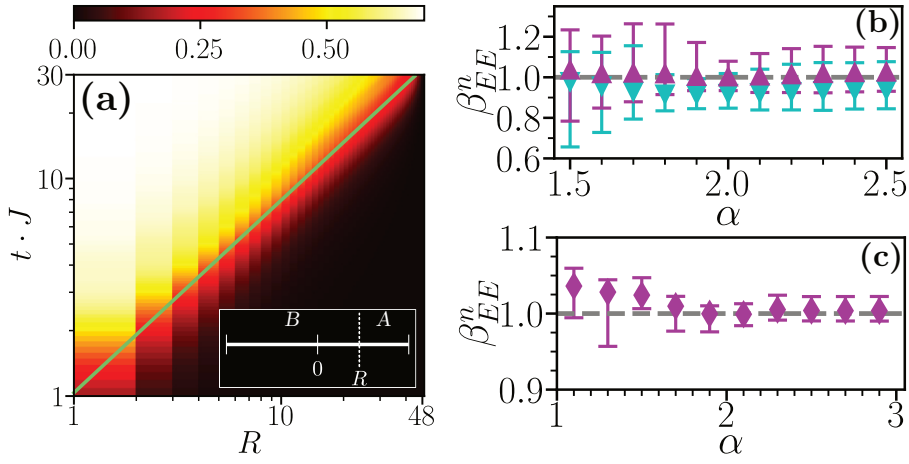


Figure 3.3.3: Spreading of the von Neumann entanglement entropy $\mathcal{S}_{n=1}(R, t)$ for the same quench as in Fig. 3.3.2(a). (a) TDVP results for $h/J = 50$, $\alpha = 1.8$, and a system size $N = 96$. The solid green line marks a power law fit to the EE with $\epsilon = 0.5$, yielding $\beta_{EE}^n = 0.899 \pm 0.005$. (b) Dynamical exponents for the EE obtained via TDVP (cyan downwards triangles) and LSWT (magenta upwards triangles, Eq. (3.34)), with error bars corresponding to the variations concerning the threshold ϵ . (c) Dynamical exponents obtained via LSWT Eq. (3.34) for a larger system, $N = 512$. Figure from [172].

well approximated by $\Psi_{\text{GS}} \simeq |\uparrow \dots \uparrow\rangle$. The initial state can thus be written as $\Psi_0 \simeq |\uparrow \dots \uparrow \downarrow \uparrow \dots \uparrow\rangle$. It is consequently orthogonal to the ground state and lives in the first excited manifold.

The dynamics induced by this local quench is examined in two observables. Firstly, we inspect the local magnetisation, $M^z(R, t) = 1/2 - \langle S_R^z(t) \rangle$ as defined in Eq. (3.24), where R is the distance from the centre flipped spin. Secondly, we inspect the dynamics of the Rényi entropies, Eq. (3.30), and we choose the bipartition of the system in subsystem A and B at time t such that $A = [R, R + 1, \dots, N/2]$ (B denotes the respective complementary subsystem). In the following paragraph, we focus on the local magnetisation (3.24) before we turn to the Rényi entropies (3.30) below.

Local magnetisation Figure 3.3.2(a) shows a typical TDVP result for the quantity $M^z(R, t)$ (3.24) versus time t and distance R from the flipped spin, in the quasi-local regime. The result again displays an algebraic twofold structure. Fitting the maxima (dashed blue line) and the spin edge (SE, solid green line), we extract the dynamical exponents β_m and β_{SE} plotted in Fig. 3.3.2(b) (blue disks and green diamonds, respectively). The SE follows the sub-ballistic scaling law $\beta_{\text{SE}} \simeq 3 - \alpha$ (solid green line) obtained from LSWT closely [34]. In contrast, the maxima of the local magnetisation spread faster than the SE, and here we find $\beta_m < 1$ corresponding to a super-ballistic propagation. Quantitatively, the local maxima match the LSWT prediction ($\beta_m = \alpha - 1$) [34], see Fig. 3.3.2(b). In the local regime ($\alpha > 2$), not displayed in the figure, we find that M^z (3.24) propagates ballistically. Both this property and the SE velocity extracted from the TDVP calculations are in good agreement with the LSWT analysis, see Fig. 3.3.2(c). Note that in this regime, we do not observe maxima propagating at a different velocity. This is also consistent with the LSWT analysis as the local magnetisation $\langle S_R^z(t) \rangle$ is the sum of contributions, each with their internal twofold structure. However, those terms have a relative phase ($\pi/2$) such that they are in quadrature and cancel out any internal maxima, cf. end of Section 3.3.1.2.

Entanglement entropies Finally, we study the spreading of quantum information via the Rényi entropies Eq. (3.30) of the reduced density matrix of a block A of the total chain, see inset in Fig. 3.3.3 (a). The main part of Figure 3.3.3(a) shows a typical TDVP result for the von Neumann entropy, $n \rightarrow 1^1$, and the same local quench as in Fig. 3.3.2 (a). We find $\mathcal{S}_n(R, t)$ to be a monotonic function of both position and time, and no local maxima such as those found previously for the correlation function and the magnetisation are observed. The entanglement edge (EE) is clearly visible in Fig. 3.3.3(a) and fitting the algebraic scaling law $t \sim R^{\beta_{EE}^n}$ allows us to extract the dynamical exponent. We find $\beta_{EE}^n \approx 1$ within error bars, regardless of the interaction range, see cyan points in Fig. 3.3.3(b). This implies the propagation of entanglement is close to ballistic in both the local and quasi-local regimes. The error bars correspond to the variation of β_{EE}^n with threshold ϵ , which is due to finite-size effects. We conclude this from our analytical computation of the entanglement entropy within LSWT, cf. Eq. (3.34). As discussed in Section 3.3.1.3, LSWT allows to solve the eigenvalues of the reduced density matrix following the local quench described above. This equation is numerically solvable in a finite but very large system size due to its favourable scaling of complexity as $\sim N^2$. Furthermore, its only approximation is made in the linearised Holstein–Primakoff transformation. Equation (3.34) constitutes an integral equation that is valid beyond the asymptotic behaviour found through the stationary phase approximation. The fitted EE to the simulation of Rényi entropies through Eq. (3.34) (EE through LSWT) is shown in Fig. 3.3.3(c)–(b) in purple diamonds. The LSWT results are in good agreement with those extracted via TDVP for the same system sizes, see Fig. 3.3.3(b) and even for larger systems, see Fig. 3.3.3(c).

The bipartite entanglement entropy is a highly non-local quantity, which takes into account all pairs of entangled particles separated by the bipartition R [18, 177–179]. As a direct consequence of this non-locality, the quasiparticle contributions to the Rényi entropy from either side of the bipartition neither regard the quasiparticle’s origination nor its velocity. Furthermore, we show that the sum of those contributions adds up to a ballistic propagation, cf. Section 3.3.1.3, in the asymptotic limit in both the local and quasi-local regimes. We have found by analytic computation that the reduced density matrix $\rho_A(R, t)$ has only two non-vanishing eigenvalues, $\lambda_1(R, t)$ and $\lambda_2(R, t) = 1 - \lambda_1(R, t)$, cf. Eq. (3.36). This is consistent with our TDVP results at all times and the observation that entanglement entropies saturate at $\mathcal{S}_n(R, t \rightarrow \infty) \simeq \log(2) \simeq 0.69$, see Fig. 3.3.3(c). We demonstrated in the asymptotic limit of R and t , $R/t = \text{const}$, and not too small values of R/t , cf. Section 3.3.1.3,

$$\lambda_2(R, t) \sim (t/R)^{\frac{1}{2-\alpha}}. \quad (3.45)$$

Crucially, the n -order Rényi entropy is a function of the ratio R/t only,

$$\mathcal{S}_n(R, t) \simeq \frac{1}{1-n} \log[(\lambda_1(R/t))^n + (\lambda_2(R/t))^n], \quad (3.46)$$

which confirms the ballistic propagation of the entanglement entropy ($\beta_{EE}^n = 1$) consistent with the results of Fig. 3.3.3 for $n = 1$ and other Rényi orders n , cf. Appendix 3.B.

Determining the EE emerges as a challenge due to the absence of a sharply defined edge in the quasi-local regime. In practice, we chose a large range and average over it to find a value for $\beta_{EE,n}$ in

¹The von Neumann entropy also reads as $\mathcal{S}_{vN} = \mathcal{S}_{n \rightarrow 1}(R, t) = -\text{Tr}\{\rho(R, t) \log(\rho(R, t))\}$

Fig. 3.3.3(b) and (c). For all Rényi entropies \mathcal{S}_n obtained from TDVP and LSWT in all system sizes, the threshold range is $\epsilon \in [20\%, 80\%]$. The associated error is taken to be the difference between the maximal and minimal value for the dynamical exponent within this range of thresholds. Although we find ballistic spreading of all entanglement entropies, we do not find consistent spreading velocities associated to the entanglement edge independently of the threshold chosen. Instead, the fitted velocity depend greatly on the chosen threshold. We therefore not consider these fitted velocities.

3.4 Discussion

In this chapter, we have investigated the spreading behaviour of spin–spin correlation functions, local magnetisation, and Rényi entropies in the long-range interacting transverse Ising chain in both the local and quasi-local regime. The dynamics is induced by a global quench during which we inspect the correlation functions. The spreading behaviour of local magnetisation and Rényi entropies is studied in the dynamics following a local quench. This investigation is performed in a complementary approach of analytic approximations within linear spin wave theory (LSWT) and state-of-the-art tensor network simulations.

By virtue of state-of-the-art numerics we find that in the quasi-local regime, the causal edges of spin–correlations and the local magnetisation are both sub-ballistic, with the same dynamical exponent ($\beta_{\text{CE}} = \beta_{\text{SE}} > 1$). In the vicinity of the edge, however, the local maxima propagate differently, *i.e.* ballistically ($\beta_{\text{m}} = 1$) for spin–spin correlations and super-ballistically ($\beta_{\text{m}} < 1$) for local magnetisation. On the other hand, Rényi entanglement entropies always propagate ballistically, irrespective of the range of interactions, in both the local and quasi-local regimes. In the local regime, all signals propagate ballistically recovering the same qualitative behaviour as in the short-range limit. The analytic quasiparticle picture, based on linear spin-wave theory, accurately reproduces the numerical predictions and provides a clear interpretation of its results. The different algebraic space-time patterns of correlation functions and local magnetisation provide a unique fingerprint of the dynamical regimes of the LRTI model suggesting the emergence of a *dynamical phase-diagram*. These correlation patterns can be directly measured in state-of-the-art experiments.

Our results show the emergence of a weak form of causality in the intermediate regime of the long-range Ising model, characterised by algebraic propagation laws with exponents that depend on the observables and the range of interactions. While local spins and spin correlations both have a sub-ballistic propagation edge, $t \propto R^\beta$, with $\beta > 1$, the causal region is characterised by local maxima propagating super-ballistically and ballistically, respectively. The distinction between the causal edge and the local maxima, which can show drastically different dynamical behaviours, is thus pivotal in the characterization of causality in long-range quantum systems. In contrast, the propagation of entanglement is ballistic in both the local and quasi-local regimes, and the causal region is featureless.

These results call for future experimental and theoretical work. On the one hand, our predictions are directly relevant to quantum simulators using for instance trapped ions, where the interaction range can be controlled. While analysis of spin and correlation spreading in first experiments [99,

100] have been limited by finite-size effects due to system sizes of $N = 15$ and $N = 11$, respectively, systems with more than 50 ions, comparable to the system size used in our simulations, are now accessible [96] and Rényi entanglement entropies can now be measured in trapped ion platforms [180, 181] and noisy intermediate-scale quantum devices [182]. On the other hand, it would be interesting to further test the robustness of the observed algebraic scaling laws by quantitatively investigating the dependence (if any) of the exponents on the strength of the quenches, the phases of the model and their values in different models, such as the long-range XY [34, 45], Heisenberg [183, 184], and Hubbard [28, 32] models, as well as in dimensions higher than one. This extended analysis could allow the identification of *dynamical universality classes*, i.e. models which share the same algebraic laws for correlations out-of-equilibrium.

Appendix

3.A Determination of the edge

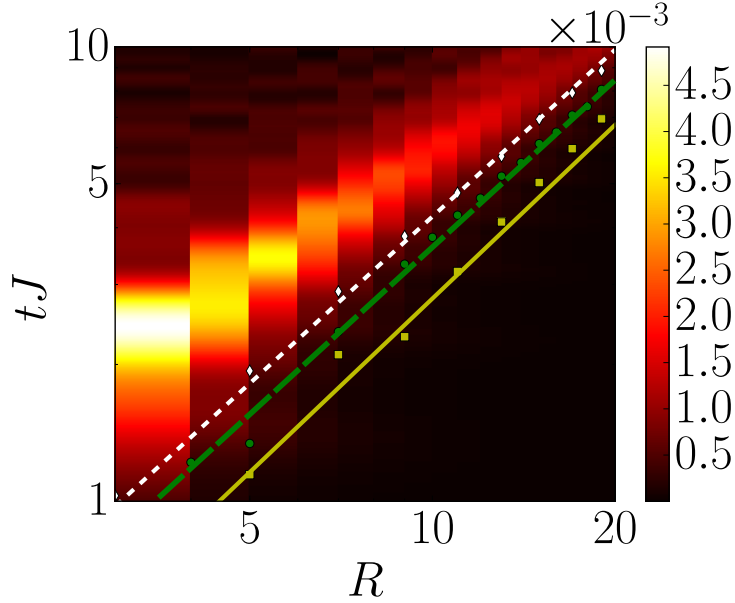


Figure 3.A.1: Spreading of the G_z spin correlation function in the quasi-local regime ($\alpha = 1.7 < 2$), for a global quench from $(h/J)_i = 50$ to $(h/J)_f = 1$, both in the z polarized phase [same data as in Fig. 3.3.1(a)]. The squares, disks, and diamonds indicate points where $G_z(R, t)$ reaches a fraction ϵ of its maximum value for various values of ϵ . The corresponding lines are linear fits to these points in log-log scale, consistently with Eq. (3.47). The brown squares correspond to $\epsilon = 2.6\%$ for which we find $\beta_{\text{CE}} \simeq 1.27$, the green disks to $\epsilon = 6.5\%$ for which we find $\beta_{\text{CE}} \simeq 1.23$, and the white diamonds to $\epsilon = 11.2\%$ for which we find $\beta_{\text{CE}} \simeq 1.22$. Figure from [172].

For all the data reported in the main text, we have determined the spin-correlation, local magnetisation, and entanglement edges by tracking the ensemble of points in the R - t plane where the signal reaches a fraction ϵ of its maximal value. Since this threshold line depends on the value of ϵ , we have systematically scanned ϵ , e.g. from 0.01 to 0.12 for $G_z(R, t)$ and from 0.20 to 0.80 for $S_n(R, t)$. In all the cases considered in this work, we find that the edge is well-fitted by the algebraic law

$$t = a \cdot R^\beta. \quad (3.47)$$

While the coefficient a fundamentally depends on ϵ , the scaling law exponent β is nearly independent of ϵ . An example of such an analysis, plotted in log-log scale, is shown in Fig. 3.A.1 where the various lines correspond to different values of ϵ . The fact that they are parallel straight lines validates the scaling law $t \sim \times R^{\beta_{\text{CE}}}$ with an exponent β_{CE} nearly independent of ϵ .

3.B Rényi entropies after a local quench

In this appendix we present complementary numerical results for different Rényi entropies in the local and quasi-local regimes obtained via TDVP simulations and LSWT calculations.

In Fig. 3.B.1(a) and (b), the counterparts of Fig. 3.3.3(b) and (c), dynamical exponents β_{EE}^n are shown for the different values of the Rényi parameter considered ($n = 1/2, n = 1, n = 2$) obtained via TDVP and LSWT with system size $N = 96$ and $N = 512$, respectively. The dynamical exponent of the EE remains close to unity almost independently of the order of the Rényi entropy, both in TDVP and LSWT. Each of the $S_n(R, t)$ considered displays a linear causal structure fully characterised by an entanglement edge (EE) and its behaviour is very similar to Fig. 3.3.3(a).

We have also computed the entanglement entropy on much larger system sizes using LSWT. This allows us to obtain a better estimate of the spreading exponent β_{EE}^n in the thermodynamic limit. The results are shown in Fig. 3.B.1(c)–(h) for three values of the Rényi order $n = 1/2, 1$, and 2 and two values of α for a chain of length $N = 512$. The results of the fits to the EE are shown in Fig. 3.B.1(b), where we see that the error bars of the von Neumann entanglement entropy are much smaller and give a more precise indication of ballistic spreading of the EE.

The determination of the EE emerges as a challenge, due to the absence of a sharply defined edge in the quasi-local regime. In practice, we chose a large range and average over it to find a value for $\beta_{EE,n}$ in Fig. 3.3.3(b) and (c). The threshold ranges for all Rényi entropies S_n obtained from TDVP and LSWT in all system sizes is $\epsilon \in [20\%, 80\%]$. The associated error is taken to be the difference between the maximal and minimal value for the dynamical exponent within this range of thresholds.

3.C Spreading of the G_x spin correlation function

In this Appendix, we discuss analytic and numerical results of the spreading of spin correlations along the spin- x direction, measured by the correlation function

$$G_x(R, t) = G_x^0(R, t) - G_x^0(R, 0) \quad \text{with} \quad G_x^0(R, t) = \langle S_R^x(t) S_0^x(t) \rangle - \langle S_R^x(t) \rangle \langle S_0^x(t) \rangle, \quad (3.48)$$

where $S_R^x(t)$ is the spin operator along x at position R and time t .

To this end, we quench the hopping amplitude J from J_i to J_f , after which the $G_x(R, t)$ correlation function can be cast in the form [34],

$$G_x(R, t) \simeq g(R) - \int_{-\pi}^{\pi} \frac{dk}{2\pi} \mathcal{F}(k) \left\{ \frac{e^{i(kR+2\varepsilon_k^f t)} + e^{i(kR-2\varepsilon_k^f t)}}{2} \right\}, \quad (3.49)$$

$$\text{with} \quad \mathcal{F}(k) = \frac{h(J_i - J_f) P_\alpha(k)}{8[h + J_f P_\alpha(k)] \sqrt{h[h + J_i P_\alpha(k)]}}, \quad (3.50)$$

where the index i refers to the pre-quench (initial) Hamiltonian and the index f to the post-quench (final) Hamiltonian. The function $\mathcal{F}(k)$ weights each quasi-particle according to their mode k . Note that it depends on the observable and the quench.

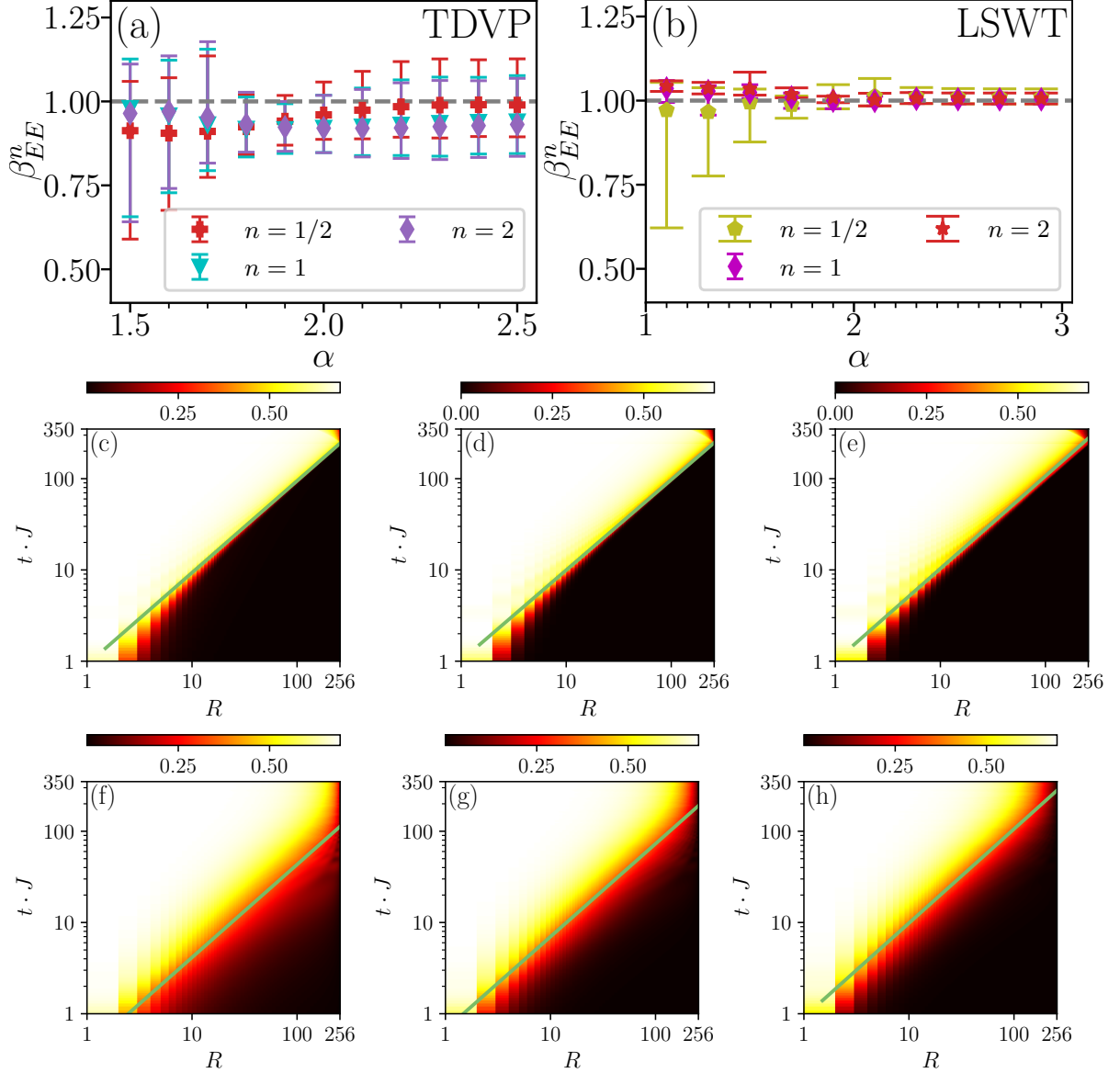


Figure 3.B.1: EE after a local quench in the z -polarized phase ($h/J = 50$). (a) TDVP ($N = 96$): dynamical exponent β_{EE}^n of the three Rényi entropies over different values of α . (b) LSWT ($N = 512$): dynamical exponent β_{EE}^n of the three Rényi entropies over different values of α . (c)–(h) LSWT ($N = 512$): Space-time behaviour of the three Rényi entropies $\mathcal{S}_n(R, t)$ considered in the local regime at $\alpha = 2.5$ (top row (c)–(e)) and in the quasi-local regime at $\alpha = 1.5$ (bottom row (f)–(h)). (c) $\alpha = 2.5$ and $n = 1/2$, (d) $\alpha = 2.5$ and $n = 1$, (e) $\alpha = 2.5$ and $n = 2$. (f) $\alpha = 1.5$ and $n = 1/2$, (g) $\alpha = 1.5$ and $n = 1$, (h) $\alpha = 1.5$ and $n = 2$. The solid green lines represent power law fits to the entropy edges with dynamical exponents, (c) $\beta_{EE}^{n=1/2} = 1.006 \pm 0.001$, (d) $\beta_{EE}^{n=1} = 0.9907 \pm 0.0002$, (e) $\beta_{EE}^{n=2} = 1.014 \pm 0.002$, and (f) $\beta_{EE}^{n=1/2} = 1.018 \pm 0.003$, (g) $\beta_{EE}^{n=1} = 1.018 \pm 0.001$, (h) $\beta_{EE}^{n=2} = 1.031 \pm 0.002$. Figure from [172].

To characterise the asymptotic behaviour $R, t \rightarrow +\infty$ along a constant line R/t , we employ the stationary-phase approximation, applied to Eq. (3.49), yielding,

$$G_x(R, t) \sim \frac{\mathcal{F}(k_{\text{sp}})}{(|\partial_k^2 \varepsilon_{k_{\text{sp}}}|t)^{1/2}} \cos(k_{\text{sp}}R - 2\varepsilon_{k_{\text{sp}}}t + \phi), \quad (3.51)$$

where ϕ is a constant phase irrelevant to our study, k_{sp} is the stationary-phase quasi-momentum, given by the solution of the equation $2V_g(k_{\text{sp}}) = 2\partial_k \varepsilon_{k_{\text{sp}}} = R/t > 0$ with V_g the group velocity associated to spin-wave excitations.

Quasi-local regime The quasi-local regime corresponds to the case where the quasi-particle energy ε_k is finite over the whole first Brillouin zone but the group velocity $V_g(k)$ presents a divergence. The space-time behaviour of G_x in the vicinity of the CE (correlation edge) is dominated by the quasi-particles propagating with the fastest group velocities. Due to the infrared divergence, only the limiting behaviour in $k \rightarrow 0$ is relevant. There the long-range interaction potential reads as $P_\alpha(k) \approx P_\alpha(0) + P'_\alpha|k|^{\alpha-1}$, with $P_\alpha(0) > 0$, $P'_\alpha < 0$, and the excitation energy is $\varepsilon_k \simeq \Delta - c|k|^z$, where $\Delta = 2\sqrt{h[h + JP_\alpha(0)]} > 0$ is the gap, $z = \alpha - 1 \geq 0$ is the dynamical exponent, and $c = \sqrt{h/[h + JP_\alpha(0)]J|P'_\alpha|} > 0$ is a prefactor. Then, computing k_{sp} and injecting it into Eq. (3.51), we find

$$G_x(R, t) \sim \frac{t^\gamma}{R^\chi} \cos \left[A_z \left(\frac{t}{R^z} \right)^{\frac{1}{1-z}} - 2\Delta t + \phi \right], \quad (3.52)$$

with

$$A_z = 2c(2cz)^{z/(1-z)}(1-z) \quad , \quad \gamma = \frac{\nu + 1/2}{1-z} \quad , \quad \text{and} \quad \chi = \frac{\nu + (2-z)/2}{1-z}, \quad (3.53)$$

where $\nu \geq 0$ is the scaling exponent of the amplitude function in the infrared limit, $\mathcal{F}(k) \sim |k|^\nu$. It follows from Eq. (3.49) and the approximation of P_α in the infrared limit that $\nu = 0$ for the G_x spin correlation function. On the one hand, the CE is found by imposing the condition that the prefactor is constant. The latter leads to the algebraic form $t \propto R^{\beta_{\text{CE}}}$ with $\beta_{\text{CE}} = \chi/\gamma = 3 - \alpha$. Since $1 \leq \alpha < 2$ in the quasi-local, the CE is always sub-ballistic, i.e. $\beta_{\text{CE}} > 1$. On the other hand, the spreading law of the local extrema is determined by the equation

$$A_z \left(\frac{t}{R^z} \right)^{\frac{1}{1-z}} - 2\Delta t + \phi = \text{cst} \quad \text{leading to} \quad A_z \left(\frac{t}{R} \right)^{\frac{z}{1-z}} - 2\Delta \rightarrow 0. \quad (3.54)$$

The maxima are thus ballistic, i.e. $t \sim R_m^\beta$ with $\beta_m = 1$.

Local regime In the local regime, corresponding to the case where both the quasi-particle energy ε_k and the group velocity $V_g(k)$ are finite over the whole first Brillouin zone, there exists a quasi-momentum k^* such that the group velocity is maximum, $V_g(k^*) = \max_k(V_g(k))$. Hence, the stationary-phase condition $2V_g(k_{\text{sp}}) = R/t$ has a solution only for $R/t \leq 2V_g(k^*)$. The CE is determined by the spreading of the quasi-particles with a quasi-momentum $k_{\text{sp}} \simeq k^*$. It is thus ballistic, with the CE velocity $V_{\text{CE}} = 2V_g(k^*)$. Moreover, in the vicinity of the CE, the motion of the local maxima is determined by the phase factor in Eq. (3.51) with $k_{\text{sp}} = k^*$. It follows that the local ex-

trema propagate ballistically at the velocity $V_m = 2V_\varphi(k^*)$ where $V_\varphi(k) = \varepsilon_k/k$ is the quasi-particle phase velocity. Note that here, $k^* < 0$ and $V_m = 2V_\varphi(k^*) = 2\varepsilon_{k^*}/k^* < 0$.

3.C.1 Numerical TDVP results

We have performed numerical TDVP calculations for the spreading of the spin correlation function along x for the same parameters as for its counterpart in the z direction, discussed in the text.

The left panel of Fig. 3.C.1 shows a typical result, plotted in log-log scale, in the quasi-local regime. The underlying chequered structure is characteristic of the G_x function and was similarly found using mean-field calculations in Ref. [34]. In spite of this complex structure, we can identify a CE, using the same ϵ method used for the G_z correlation function, as well as propagating local maxima. The green solid and dashed blue lines correspond to algebraic fits to the CE and the local extrema, respectively. The associated scaling law exponents β_{CE} and β_m are in very good agreement with the theoretical ones discussed in Sec. 3.C, see filled marks in Fig. 3.3.1(b) of the main text.

The right panel of Fig. 3.C.1 shows a typical result in the local regime, now plotted in linear scale. The solid green and dashed blue lines are linear fits to the CE and local extrema, respectively. The corresponding numerical velocities V_{CE} and V_m are in good agreement with the theoretical ones, see filled marks in Fig. 3.3.1(c) of the main text.

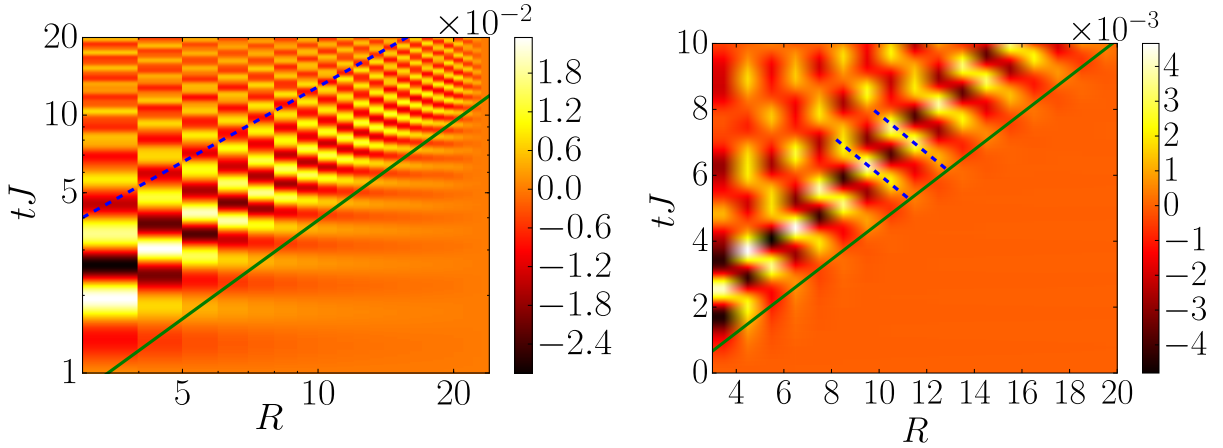


Figure 3.C.1: Spreading of the G_x spin correlations. Left panel (log-log scale): Quasi-local regime with $\alpha = 1.7 < 2$ for a global quench from $(h/J)_i = 50$ to $(h/J)_f = 1$, both in the z polarized phase of the LRTI model. Right panel (linear scale): Local regime with $\alpha = 3 < 2$ for a global quench starting from $(h/J)_i = 0.9$ to $(h/J)_f = 1$. The solid green and dashed blue lines are algebraic (for $\alpha < 2$) or linear (for $\alpha > 2$) fits to the CE and the extrema, respectively.

4 *Entanglement and quantum phase transitions*

This chapter is mainly based on our publication, J. T. Schneider, et al., “Entanglement Spectrum and Quantum Phase Diagram of the Long-Range XXZ Chain”, [Physical Review B 106:1, 014306 \(2022\)](#) [185].

4.1 *Introduction*

Macroscopic physical properties of the equilibrium state of a quantum system are determined by the complex interplay of microscopic interactions, and competing symmetries leading to a variety of critical phenomena. As we have introduced in Section 1.7, In Landau’s paradigm of second order phase transitions one identifies an order parameter characterising the ground state’s breaking of a symmetry. Typically, above a certain critical point, the order parameter vanishes identically while below it is non-zero signalling that the ground state spontaneously breaks a symmetry [16]. Traditionally, these order parameters are local observables on the ground state [105]. However, recent years have witnessed the development of new understanding of phases of matter that do not fall inside Landau’s paradigm [186]. Therefore, such an approach is inoperant for several quantum phase transitions including infinite-order and topological phase transitions which are only signalled in global observables [187]. The former do not display an order parameter that spontaneously breaks a symmetry, arguably the most famous is the Berezinskii–Kosterlitz–Thouless transition in the 2D XY model [188–190]. At the same time it has been noted that quantum entanglement constitutes a fruitful alternative to the characterization of quantum phases and quantum phase transitions [104, 191, 192]. For instance, the von Neumann entropy has been shown to display characteristic logarithmic divergence at critical points [143, 187, 193–196]. In systems described by gapped Hamiltonians, the von Neumann entanglement entropy follows an area law and subleading corrections can be used to identify topological order or spontaneous symmetry breaking, see e.g. [104] and Refs. therein. Moreover, other entanglement witnesses, such as the geometric entanglement [152, 197–200] have been shown to be instrumental for the detection of elusive quantum phase transitions [153, 201, 202]. Nevertheless, both the entanglement entropy [203, 204] and the geometric entanglement [205] have been shown to not exhibit any singular behaviour at the respective critical point and thus more refined entanglement properties are required.

Following the seminal work of Li and Haldane [112], entanglement spectroscopy as an extension to entanglement entropy emerged as a research direction. The complete set of Schmidt weights $\{s_j\}$ associated to the ground-state wave function following a bipartition is mapped onto $\{\xi_j\}$ as,

$$\xi_j = -\log(s_j^2), \quad (4.1)$$

where $\{\xi_j\}$ is known as the entanglement spectrum (ES) and ξ_j is the j -th entanglement energy. The ES contains a wealth of information beyond traditional entanglement witnesses [104, 105, 112] and proves instrumental for detecting quantum phase transitions [115, 121, 206–208] and topological order [105, 112, 209, 210]. In spin models for instance, quantum phase transitions have been signalled by a singular behaviour of the Schmidt gap [115, 116], the difference between the lowest and second-lowest entanglement energy, and by degeneracy lifts of higher entanglement spectral lines [118]. Entanglement properties of prototypical (short-range) spin models have been extensively studied in connection with many-body physics [187, 211–215].

In this chapter, we study the entanglement spectrum (cf. Appendix 2.A.2) of the long-range, spin-1/2 XXZ chain and show that it contains sufficient information to determine the phase diagram as a function of the anisotropy parameter and the interaction range exponent. The anti-ferromagnetic-XY and XY-ferromagnetic phase transitions are, respectively, characterised by degeneracy lifts and the divergence of the Schmidt gap, similarly to the short-range XXZ model. Analysis of the entanglement spectrum is also instrumental in identifying a remarkable self-similar property of the XY phase. Its breakdown signals the onset of genuine long-range effects and the spontaneous breaking of a continuous symmetry, consistent with renormalisation group theory. Our results are confirmed by numerical calculations using tensor-network techniques. Moreover, we show that the self-similarity observed in the entanglement spectrum extends to other quantities, including the geometrical entanglement and the Luttinger parameter in the critical phase.

In Section 4.2, we introduce the model and lay out our approach. Section 4.3 discusses the bosonisation technique to formulate an effective bosonic field theory model of the low-energy LRXXZ Hamiltonian. After discussing the basic principles (Section 4.3.1), we include the interaction terms (Section 4.3.2) and study the renormalisation group flow of the coupling constants to determine a phase diagram of the effective field theory model (Section 4.3.3). We continue with the study of the quantum phase diagram of the LRXXZ model in Section 4.4.1 via measuring geometric entanglement. In Section 4.4.2, we discuss entanglement-spectrum signatures of quantum phase transitions in the same phase diagram, and we reveal its self-similarity upon rescaling the anisotropic coupling parameter. Furthermore, we combine this remarkable feature with the results of RG theory for the critical Luttinger parameter to locate the phase transition into the continuous symmetry breaking phase. In Section 4.4.3, we verify Luttinger liquid behaviour, in particular the self-similarity feature for the Luttinger parameter. Finally, we draw our conclusion and give an outlook in Section 4.5.

4.2 Model and approach

We study the long-range, anisotropic XXZ Heisenberg (LRXXZ) chain, governed by the Hamiltonian,

$$H = -J \sum_{R \neq R'} \frac{S_R^x S_{R'}^x + S_R^y S_{R'}^y + \Delta S_R^z S_{R'}^z}{|R - R'|^\alpha}, \quad (4.2)$$

where S_R^j ($j = x, y, z$) are the spin-1/2 operators on lattice site $R \in [0, N - 1]$, N is the system size, $J > 0$ is the coupling energy, and Δ is the anisotropy parameter. As an archetype of an interacting spin chain, the short-range XXZ model has been extensively studied in various contexts such as a textbook example for theoretical techniques like bosonisation [6, 16, 216], the Bethe ansatz [6, 16, 217, 218], many-body localization [219], as well as out-of-equilibrium dynamics in the context of integrable systems [220, 221]. The short-range anisotropic XXZ chain ($\alpha \rightarrow \infty$, *i.e.* $\alpha^{-1} = 0$) is integrable and can be exactly solved via Bethe ansatz [16, 217, 218]. At equilibrium, it encompasses three phases: One finds a trivial, fully polarized, gapped ferromagnetic (FM) phase for $\Delta > 1$, a gapless paramagnetic XY phase for $-1 < \Delta < 1$, and a gapped antiferromagnetic (AFM) phase for $\Delta < -1$. While the phase transition from XY to FM is of first order, the transition from AFM to XY is conversely an infinite-order phase transition of the Berezinskii–Kosterlitz–Thouless (BKT) type and no local correlation measure signals this phase transition [187, 217] highlighting the need for a global measure. Moreover, the low-energy physics in the paramagnetic phase is well described by a Luttinger liquid. The latter is characterised by a massless, quadratic, conformally-invariant field theory with central charge $c = 1$, described by the Hamiltonian

$$H_{\text{LL}} = \frac{u}{2} \int dx \left[K (\partial_x \theta(x))^2 + \frac{1}{K} (\partial_x \phi(x))^2 \right], \quad (4.3)$$

where $\phi(x)$ is a scalar field, $\Pi(x) = \partial_x \theta(x)$ is the canonical conjugate momentum with $[\Pi(x), \phi(y)] = i\delta(x - y)$, such that $\theta(x)$ is the dual field to $\phi(x)$, K is the Luttinger parameter, and u is the speed of sound. For more details on the Luttinger liquid description, see Section 4.3. Hereafter, we study the entanglement properties of the LRXXZ model (4.2) for $\alpha^{-1} \geq 0$ via density matrix renormalisation group (DMRG) simulations [138] as well as the renormalisation group flow of the effective field theory description to combine the two into a comprehensive prediction for the quantum phase diagram of the LRXXZ model. To this end, we discuss the effective bosonic field theory and its RG flow in Section 4.3. We then inspect the geometric entanglement and study the entanglement spectrum in Section 4.4.

4.3 Bosonisation and effective Luttinger liquid theory

In this section, we discuss the bosonisation technique to describe fermionic degrees of freedom in terms of effective bosonic degrees of freedom while taking the example of the long-range, anisotropically interacting spin chain (LRXXZ). In one dimension, such an effective bosonic model is generally called a Luttinger liquid. It is the most prevalent description of fermionic one-dimensional

systems replacing Fermi liquid theory which is only valid in higher dimensions [6]. The bosonisation technique allows us to describe (parts of) the interacting fermionic theory in terms of a free bosonic theory thereby (partly) solving the many-body problem. Here, we will discuss in which sense the solution of the free bosonic theory is actually the full solution of the fermionic model. Moreover, we study when the fermionic interactions become too strong to be amenable to a free bosonic description, and study these phase transition, driven by these microscopic interactions, by means of the renormalisation group (RG). Paraphrasing below considerations in the context of the LRXXZ chain, we build a ‘bosonisation dictionary’ by translating those microscopic spins on the lattice which represent free fermions on the lattice. We continue by defining effective fermionic continuum fields by only considering the linear part of the lattice dispersion at half-filling, and subsequently translate these into bosonic fields according to standard bosonisation formulas. Finally, we translate the remaining interaction terms into bosonic field variables and consider the renormalisation of the introduced interaction terms to study when the free bosonic theory fails to be the fixed point of the RG flow and a phase transition occurs. We wish to note that the linearisation of the lattice dispersion around the Fermi momentum is not restrictive to fermionic systems and may also apply to bosonic lattice systems, e.g. the integer spin Heisenberg model at large external fields. This is an example of a ‘Luttinger liquid’ which is a conformally invariant (with central charge $c = 1$), effective bosonic field theory of the low-energy physics of some 1D lattice model. In general, it is obtained when the 1D lattice dispersion admits a linear approximation and the low-energy excitations are bosonic.

In the context of one dimensional free fermions on the lattice, Lorentz invariance is an emergent property in the low-energy limit where the lattice dispersion relation may be approximated by a linear one. There, the Fermi velocity acts as the speed of light as the only characteristic velocity in the free model. Furthermore, the free fermion and boson model are invariant under *conformal transformations*, i.e. rotations, translations, and changes of length scale, and in the case we exhibit here, with the associated conserved charge to the conformal transformation, the central charge, is identically unity.

4.3.1 Bosonisation dictionary of the free model

The bosonisation technique hinges on the observation that in one dimension particle–hole excitations are bosonic in nature which is based on the quasiparticle picture defined at the point of the free quadratic theory. We consider the LRXXZ Hamiltonian,

$$H = - \sum_{n,m=1; n \neq m}^{N-1} J_{n,m} (S_n^x S_m^x + S_n^y S_m^y + \Delta S_n^z S_m^z) \quad (4.4)$$

$$= - \sum_{n \neq m} J_{n,m} \left(\frac{1}{2} [S_n^+ S_m^- + S_n^- S_m^+] + \Delta S_n^z S_m^z \right), \quad (4.5)$$

where S_n^t ($t = x, y, z$) are the spin-1/2 operators on lattice site $n \in [0, N - 1]$, N is the system size, $S_n^\pm = S_n^x \pm iS_n^y$ are the spin raising and lowering operators, and Δ is the anisotropic coupling parameter. In the following, we only focus on the short-range case of $J_{n,m} = J\delta_{m,n+1}$ ($J > 0$ the coupling energy), and come back to the long-range case $J_{n,m}(\alpha) = J/|n - m|^\alpha$ after bosonisation.

We are therefore following textbook approaches for the bosonisation of the short-range interacting XXZ model [6, 16, 216, 218] in considering the free fermion point $\Delta = 0$, $\alpha = \infty$ as the basis of the bosonisation technique. Furthermore, we consider periodic boundary conditions within this analytic framework of the bosonisation. Expressing the free spins on the lattice as free fermions on the lattice using the Jordan–Wigner transform,

$$S_n^- = \Phi(n)c_n, \quad S_n^+ = \Phi(n)c_n^\dagger, \quad S_n^z = c_n^\dagger c_n - \frac{1}{2}, \quad (4.6)$$

where $\{c_n^\dagger, c_m\} = \delta_{n,m}$ are spinless fermionic creation and annihilation operators, and

$$\Phi(n) = \frac{1}{2} \exp\left(-i\pi \sum_{m<n} c_m^\dagger c_m\right) + \text{H.c.} \quad (4.7)$$

is the hermitian ‘fermionic phase factor’, we obtain the fermionic Hamiltonian,

$$H_0 = -\frac{J}{2} \sum_n c_n^\dagger c_{n+1} + \text{H.c.} = -J \int_{-\frac{\pi}{a}}^{\frac{\pi}{a}} \frac{dk}{2\pi} \cos(ka) \tilde{c}_k^\dagger \tilde{c}_k. \quad (4.8)$$

Having used the Fourier transform defined as,

$$f_n = \frac{1}{\sqrt{N}} \sum_{k=0}^{N-1} \tilde{f}_k e^{+i\frac{2\pi}{N}kn}, \quad \tilde{f}_k = \frac{1}{\sqrt{N}} \sum_{n=0}^{N-1} f_n e^{-i\frac{2\pi}{N}kn}, \quad (4.9)$$

we thus identify the dispersion relation $\varepsilon(k) = -J \cos(ka)$ for free fermions. In one dimension, the free fermions have two Fermi points at $\pm k_F$ with $k_F = \pi/(2a)$ in case of a half-filled lattice, see also Fig. 4.3.1(a). In general, k_F may differ when one considers an external field h coupling as $-h \sum_n S_n^z$ to the spins and the lattice is not at half-filling. Until explicitly mentioned otherwise, we continue only considering the model at half-filling, i.e. $k_F = \pi/(2a)$. The low energy modes up to a cutoff $1/a_c$ around either Fermi point are then approximated by a linear dispersion relation $\omega(k)|_{\pm k_F} \simeq \pm J a (k \mp k_F)$, cf. Fig. 4.3.1(b). It gives rise to the Fourier mode decomposition of a fermionic quantum field with two species,

$$\psi_\pm(x_n) = \lim_{a \rightarrow 0} \frac{1}{\sqrt{a}} c_n \exp(\pm i k_F x_n), \quad (4.10)$$

with $x_n = an$ and the exponential serving as the translation in the Brillouin zone to the respective Fermi point. We can then formulate H_0 to read in the low energy limit as,

$$H_0 = \int \frac{dk}{2\pi} [\tilde{\psi}_+^\dagger(k) k \tilde{\psi}_+(k) - \tilde{\psi}_-^\dagger(k) k \tilde{\psi}_-(k)]. \quad (4.11)$$

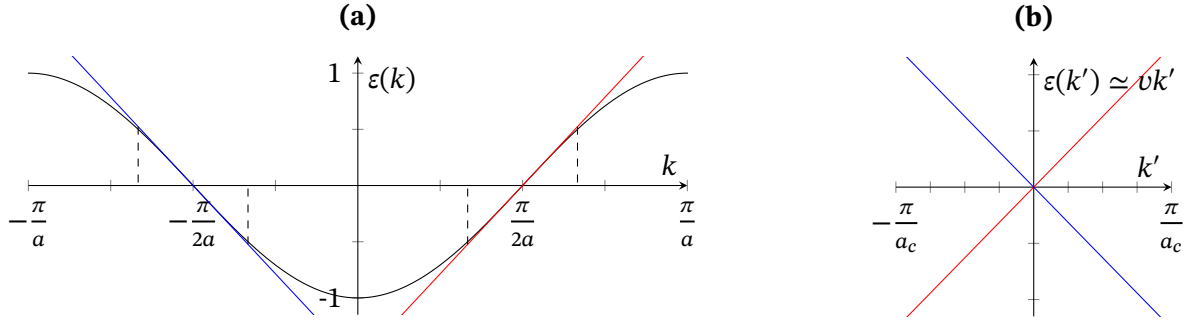


Figure 4.3.1: **(a)** Dispersion relation of the free Hamiltonian $H_0 = -\frac{J}{2} \sum_n S_n^+ S_{n+1}^- + S_{n+1}^+ S_n^- = \int_{-\pi/a}^{\pi/a} \frac{dk}{2\pi} \varepsilon(k) \tilde{c}_k^\dagger \tilde{c}_k$, with $\varepsilon(k) = -J \cos(ka)$ plotted as black solid line. Linearisation of the low energy modes around the two Fermi momenta $k_F = \pm\pi/(2a)$ is plotted as solid red and blue lines for the left and right moving modes, respectively. While the discrete lattice introduces a UV cutoff through its finite lattice spacing a , the range of accuracy of the linearisation is controlled by the UV cutoff $a_c > a$ (range between vertical dashed lines). **(b)** Linearised dispersion relation is combined to the free dispersion of relativistic Dirac fermions by shifting the momentum for the left (right) moving modes to $k' = k + k_F$ ($k' = k - k_F$).

We may combine these two species to define a single (spinful) spinor Dirac fermion field $\Psi(x) := (\psi_R(x), \psi_L(x))$, with the Hamiltonian,

$$H_0 = \int \frac{dp}{2\pi} \tilde{\Psi}^\dagger(p) \gamma^5 p \tilde{\Psi}(p) \quad (4.12)$$

$$= \int dx \Psi^\dagger(x) \gamma^5 \partial_x \Psi(x), \quad (4.13)$$

where in 1 + 1 dimension the Clifford algebra $\{\gamma^\mu, \gamma^\nu\} = 2\eta^{\mu,\nu} \mathbb{1}$ ($\eta^{\mu,\nu} = \text{diag}(1, -1)$) is spanned by the Pauli matrices $\gamma^0 = \sigma^y$, $\gamma^1 = \sigma^x$, $\gamma^5 = i\gamma^0\gamma^1 = \sigma^z$. Figure 4.3.1 illustrates the origin of the two fermion species, namely the two Fermi points $\pm k_F$.

By means of the bosonisation formula,

$$\psi_\pm(x) \equiv \frac{1}{\sqrt{2\pi a_c}} \exp\left[\mp i\sqrt{4\pi}\phi_\pm(x)\right], \quad (4.14)$$

and the definitions $\phi(x) = \phi_+(x) + \phi_-(x)$, $\theta(x) = \phi_+(x) - \phi_-(x)$, we obtain the free bosonic field Hamiltonian,

$$H_0 = \frac{u}{2} \int dx \left[K(\Pi(x))^2 + \frac{1}{K}(\partial_x \phi(x))^2 \right], \quad (4.15)$$

where $\Pi(x) = \partial_x \theta(x)$ is the canonical conjugate of ϕ , $[\Pi(x), \phi(y)] = i\delta(x - y)$. Furthermore, we have abbreviated in the free theory $K = 1$ and $u = J$, which is nothing but the Fermi velocity. The action associated to H_0 reads as

$$S_0[\phi] = \frac{1}{2K} \int d^2\mathbf{r} (\partial_\mu \phi(\mathbf{x}))^2 \quad (4.16)$$

$$= \frac{1}{2K} \int \frac{d^2\mathbf{p}}{(2\pi)^2} (p^\mu \phi(\mathbf{p}))^2 \quad (4.17)$$

$$\equiv \frac{1}{2} \int \frac{d^2\mathbf{p}}{(2\pi)^2} \phi(p) D_\phi^{-1}(p) \phi(p) \quad (4.18)$$

with $\mathbf{r} = r^\mu = (u \cdot t, x)$ the spacetime vector (with Euclidean norm), $\mathbf{p} = p^\mu = (\omega/u, k)$ the spacetime Fourier vector, and $D_\phi(p) = K/p^2$ the (free) Feynman propagator for field ϕ . Note the symmetry of S_0 under the duality transformation $\phi \rightarrow \theta$, $K \rightarrow 1/K$, $D_\phi(p) \rightarrow D_\theta(p) = K^{-1}p^{-2}$. Subsequently, we relate the microscopic spin degrees of freedom on the lattice to their bosonic counterpart in the continuum as [6, 216, 218],

$$S_n^\pm(x) = \frac{S_n^\pm}{\sqrt{a}} = \frac{(-1)^{x/a}}{\sqrt{2\pi a_c}} \exp(\pm i\sqrt{\pi}\theta(x)), \quad (4.19)$$

$$S_n^z(x) = \frac{S_n^z}{a_c} = \frac{1}{\sqrt{\pi}} \partial_x \phi(x) - \frac{(-1)^{x/a_c}}{\pi a_c} \sin(\sqrt{4\pi}\phi(x)), \quad (4.20)$$

where the Jordan–Wigner phase factor $\Phi(x)$ is taken to be the Hermitian version

$$\Phi(x) = \frac{1}{2} \exp\left(-i\pi \sum_{y < x} c_y^\dagger c_y\right) + \text{H.c.} = \cos(\phi(x) - k_F x). \quad (4.21)$$

4.3.2 Perturbatively including interactions

In the following, we use the definitions Eqs. (4.19) and (4.20) to include the microscopic interaction terms contained in Eq. (4.4) in our bosonic model. Since the link between spins on the lattice to bosonic field operators hinges on the free model, we are thus adding these interaction terms as a perturbation to our free model. Ultimately, our aim is to study the renormalisation group flow to inspect when the interaction terms become strong enough to drive the system away from the free Gaussian fixed point with conformal symmetry. To this end, we consider in principle three interaction potentials. First, we consider the translation of the bosonised interaction of the short-range nearest neighbour interaction $-\Delta S_n^z S_{n+1}^z$, which we write following textbook examples [6,

216, 218]. Second, we consider the long-range interaction in XY-direction. And third, we consider the long-range interaction of the $S_n^z S_m^z$ term. Using Eqs. (4.19) and (4.20) they translate as,

$$J\Delta S_n^z S_{n+1}^z \rightarrow J\Delta(\partial_x \phi(x))^2 + \frac{J\Delta}{(\pi a_c)^2} \cos(\sqrt{16\pi}\phi), \quad (4.22)$$

$$J \frac{S_n^+ S_m^- + \text{H.c.}}{|n-m|^\alpha} \rightarrow \frac{J}{2\pi a_c} \frac{\cos(\sqrt{\pi}(\theta(x) - \theta(y)))}{|x-y|^\alpha}, \quad (4.23)$$

$$\Delta \frac{S_n^z S_m^z}{|n-m|^\alpha} \rightarrow \frac{\Delta}{\pi} \frac{\partial_x \phi(x) \partial_y \phi(y)}{|x-y|^\alpha}, \quad (4.24)$$

where we define $x = an$, $y = am$. Note the bosonised version of the interaction $\Delta S_n^z S_{n+1}^z$ contains a term quadratic in the boson field. This term is generally absorbed in the free quadratic part of the Hamiltonian (4.15), at the cost of perturbative renormalising the Luttinger parameters with microscopic parameters according to,

$$uK = v_F, \quad (4.25)$$

$$\frac{u}{K} = J \left(1 + \frac{4\Delta}{\pi}\right). \quad (4.26)$$

Furthermore, the long-range interaction term $S_n^z S_m^z / |n-m|^\alpha$ is highly irrelevant for $\alpha^{-1} < 1$ [222], as it contains two derivatives and two field operators. We therefore omit it in our following RG analysis. Furthermore, we rename the coupling g_{LRXY} to g_{LR} henceforth.

Consequently, we add the following interaction potentials to our action,

$$V_{ZZ}[\phi] = \frac{g_{ZZ}}{(\pi a_c)^2} \int dx \cos(\sqrt{16\pi}\phi(x)), \quad (4.27)$$

$$V_{LR}[\theta] = \frac{g_{LR}}{2\pi a_c} \int_{|x-y| \gg a} \frac{\cos(\sqrt{\pi}[\theta(x) - \theta(y)])}{|x-y|^\alpha} dx dy, \quad (4.28)$$

such that we have the fully interacting model defined by,

$$\begin{aligned} S[\phi, \theta] = & \frac{1}{2K} \int d^2\mathbf{r} (\partial_\mu \phi(\mathbf{x}))^2 \\ & - \frac{g_{ZZ}}{(\pi a_c)^2} \cos(\sqrt{16\pi}\phi(x)) \\ & - \frac{g_{LR}}{2\pi a_c} \int_{|x-y| \gg a} \frac{\cos(\sqrt{\pi}[\theta(x) - \theta(y)])}{|x-y|^\alpha} dx dy. \end{aligned} \quad (4.29)$$

Equations (4.25) and (4.26) are perturbative relations of the microscopic parameter Δ and the Luttinger parameters K and u . In the short-range case, $\alpha \rightarrow \infty$, can be improved and extended over the entire paramagnetic phase in which the model is gapless and amenable to the linearisation of the dispersion relation [6]. The Bethe ansatz allows for two predictions—in the case of the XXZ model

this is the magnetic susceptibility linked to u/K and the spin stiffness linked to uK —such that we may extend above relations [6, 217, 218],

$$K(\Delta, \alpha = \infty) = \frac{\pi}{2 \arccos(\Delta)}, \quad (4.30)$$

$$u(\Delta, \alpha = \infty) = \frac{\pi \sqrt{1 - \Delta^2}}{2 \arccos(-\Delta)}, \quad (4.31)$$

which are valid for $\alpha \rightarrow \infty$ and $|\Delta| \leq 1$ over the entire critical phase of the (short-range) XXZ model. Note the linearised versions of Eqs. (4.30) and (4.31) yield up identical relations to Eqs. (4.25) and (4.26) for $|\Delta| \ll 1$. However, upon including the interaction terms $V_{ZZ}[\phi]$ and $V_{LRXY}[\theta]$, the value of the Luttinger parameter K and the speed of sound u are generally a function of the microscopic parameters Δ and α , i.e. $K = K(\Delta, \alpha)$, $u = u(\Delta, \alpha)$.

4.3.3 Renormalisation group flow

Taking the path integral approach to renormalisation, we consider the microscopic generating functional $Z_0 = \int D\phi D\theta \exp(-S[\phi, \theta])$ with action $S[\phi, \theta] = S_0[\phi] - V_{ZZ}[\phi] - V_{LRXY}[\theta]$ in Euclidean spacetime. As per usual, one splits the spacetime Fourier modes of both fields in slow and fast moving ones according to,

$$\phi(k) = \begin{cases} \phi_s(k) & \text{if } 0 \leq k \leq \Lambda(1 - d\ell) \\ \phi_f(k) & \text{if } \Lambda(1 - d\ell) < k \leq \Lambda \end{cases}, \quad (4.32)$$

$$\phi(k) = \phi_s(k) + \phi_f(k), \quad (4.33)$$

with k being the norm of the Fourier spacetime vector, and $d\ell$ the width of the spacetime momentum shell being integrated out. The analogous splitting applies to the field $\theta(k) = \theta_s(k) + \theta_f(k)$. In integrating out the fast moving modes, the fully interacting quantum theory generates a mixing of Fourier modes that changes the effective values of the coupling ‘constants’. Such an integration leaves the new theory with a lower momentum cutoff. To compare the two theories, before and after integrating out fast fluctuating modes, one only considers an infinitesimal shell at the old cutoff as the integration interval and then rescales the newly obtained theory such that both theories have the same momentum cutoff. This infinitesimal change of the coupling constants is generally referred to as the renormalisation group (RG) flow. They generically constitute differential equations, and in the context of the Luttinger liquid with the interaction terms coming from the LRXXZ model, Eqs. (4.27) and (4.28), they read [216, 223],

$$\frac{dg_{ZZ}}{d\ell} = (2 - 4K)g_{ZZ}, \quad (4.34)$$

$$\frac{dg_{LR}}{d\ell} = \left(3 - \alpha - \frac{1}{2K}\right)g_{LR}, \quad (4.35)$$

where $d\ell$ is the width of the spacetime momentum shell at momentum cutoff Λ , integrated out in one RG step. For more details and a derivation, see Appendix 4.B. Note that the flow equations (4.34) and (4.35) are uncoupled. To first-order perturbative RG, the renormalisation of g_{ZZ} is thus

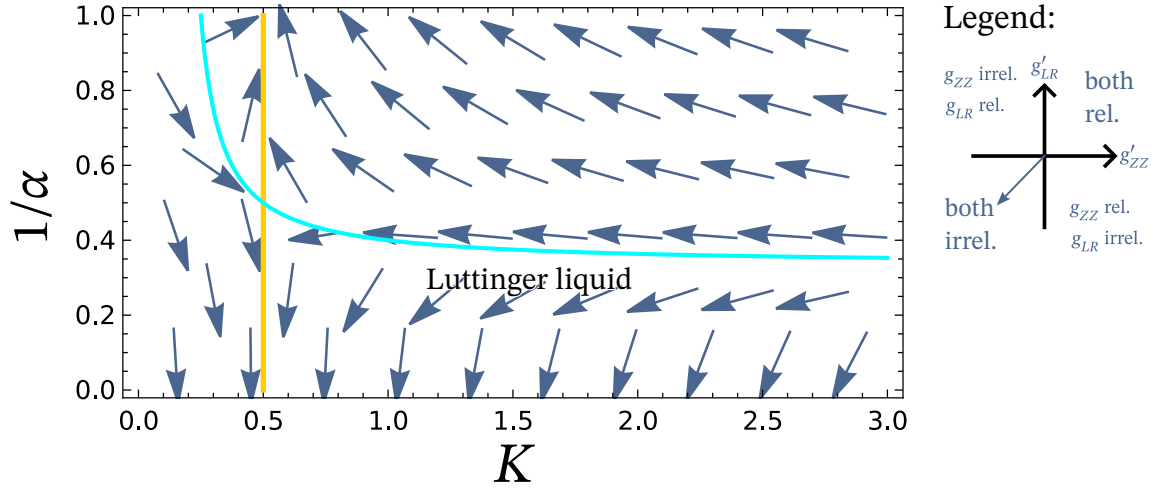


Figure 4.3.2: A projection of the RG flow based on the flow Eqs. (4.34) and (4.35) of the effective bosonic field theory (EFT) model of the LRXXZ defined by the action in Eq. (4.29). The curves for K_c (4.36) and K'_c (4.37) are shown as the solid yellow and cyan lines, respectively. The vector field visualises in the x -direction the derivative g'_{ZZ} while the y -direction shows the derivative g'_{LR} . The coupling g_{ZZ} is thus irrelevant when the vector field points into the left half plane, while the coupling g_{LR} is irrelevant when the vector field is pointing into the lower half plane. Therefore, only when pointing into the lower left quadrant are both couplings irrelevant, and we obtain a Luttinger liquid.

completely controlled by the Luttinger parameter K [6, 216], while that of g_{LR} is controlled by both K and the long-range exponent α [223].

Equation (4.34) governs the AFM-XY transition: The ZZ interaction term is relevant for $K < 1/2$ (AFM phase) and irrelevant for $K > 1/2$ (XY phase), indicating a transition characterised by the critical Luttinger parameter

$$K_c(\Delta, \alpha) = 1/2, \quad (4.36)$$

which defines a curve in the parameter space (Δ, α) of the LRXXZ model. As mentioned above in Eqs. (4.30) and (4.31), the Bethe ansatz provides a non-perturbative solution of the effective field theory parameters K and u in terms of the microscopic anisotropy parameter Δ in case of short-range interactions ($\alpha \rightarrow \infty$). Therefore, the AFM to Luttinger liquid (LL) phase transition in the short-range case occurs at $K_c(\Delta, 1/\alpha = 0) = 1/2 \Leftrightarrow \Delta_c = -1$. This prediction of the critical value of $K_c = 1/2$ is confirmed by numerical calculations all along this transition line, see Sec. 4.4.3.

On the other hand, inspecting the critical line where $V_{LRXY}[\theta]$ is marginal, i.e. where Eq. (4.35) has a coefficient identically zero, we find for the transition into a long-range XY (LRXY) phase with a broken continuous symmetry (CSB) the condition,

$$K'_c(\Delta, \alpha) = \frac{1}{2(3 - \alpha)}, \quad (4.37)$$

defining the phase transition line in the parameter space (Δ, α) of the LRXXZ model. Note that the transition into the CSB phase can only occur for finite values of $\alpha \leq 3$ since the Luttinger parameter is $K > 0$. Noteworthy to discuss are two points in the parameter plane (Δ, α) . Firstly, consider $\alpha \rightarrow 3$ in which case $K'_c \rightarrow +\infty$ which is the same behaviour of the Luttinger parameter when approaching the XY-FM transition at $\Delta = +1$ in the short-range case, cf. Eq. (4.30). As discussed in

Appendix 4.A, long-range interactions neither alter the position $\Delta_c^{\text{FM}} = +1$ of this phase transition nor do they change the ground state itself. This suggests the Luttinger parameter K does not change on the XY–FM phase boundary either but is diverging $K \rightarrow \infty$ on the whole line which would imply the SRXY–LRXY phase transition line defined by $K'_c(\Delta, \alpha)$ meets the XY–FM phase boundary at $(\Delta = -1, \alpha = 3)$ in the LRXXZ parameter plane. Indeed, we confirm this behaviour through numerical simulations, cf. Section 4.4.3. Secondly, consider $\alpha = 2$ in which case $K'_c = 1/2 = K_c$. Thus, we expect the SRXY–LRXY phase boundary meets the AFM–XY phase boundary at $\alpha = 2$. Figure 4.3.2 shows a projection of the RG-flow diagram of the effective bosonic field theory, defined by the first-order flow equations (4.34) and (4.35). Here, we chose to visualise the flow in terms of the two parameters K and α^{-1} and not as usual in terms of the couplings g_{ZZ} and g_{LR} . The vector field plots the derivatives g'_{ZZ} and g'_{LR} as the x - and y -components respective vector at the corresponding point. We see for $K > 1/2$ and rather short-ranged interactions ($\alpha^{-1} \rightarrow 0$), the ground state flows towards the Luttinger liquid fixed point and exhibits conformal symmetry. For $K > 1/2$ and long-ranged interactions ($\alpha^{-1} > 1/3$), the ground state spontaneously breaks the symmetry $K \rightarrow 1/K$ and $\phi(x) \rightarrow \theta(x)$ as V_{LRXY} becomes relevant. This reflects the spontaneous breaking of the $U(1)$ symmetry in the microscopic spin model. At $K < 1/2$, the Hamiltonian renormalises to the antiferromagnetic Néel phase when V_{ZZ} becomes relevant. There, the cosine term of V_{ZZ} breaks the chiral symmetry, opens a gap in the spectrum, and the system is not well-approximated by the linearisation of the lattice dispersion and Luttinger liquid theory breaks down. We thus consider the emergent phase between the red critical curve and the green critical curve for $\alpha^{-1} > 0.5$ an artefact of the effective linearisation of the lattice dispersion and the linearisation of the RG-flow equations, therefore not reflecting a phase of the microscopic spin chain.

Last but not least, long-range interactions must increase the frustration in the ground state when the coupling is not ferromagnetic, i.e. it is antiferromagnetic following our definition of J . Thus, they alter the AFM–XY phase boundary compared to the well-known point $\Delta = -1, \alpha = \infty$ in the short-range limit of the LRXXZ model. In the following, we determine this shift by numerical simulation of several observables and verify the predictions obtained through RG.

4.4 Results

4.4.1 Geometric entanglement

We first consider the ground-state geometric entanglement (GE), defined as,

$$E_g(\psi) = -\log_2\left(\max_{\phi:\text{prod}} |\langle\phi|\psi\rangle|^2\right), \quad (4.38)$$

where $|\psi\rangle$ is the exact ground state of the model and the set $\{|\phi\rangle\}$ span the submanifold of product states [199]. It has been previously shown to be instrumental for identifying quantum phase transitions, including infinite order ones, in a variety of models, for instance short-range spin models [153], and two-dimensional classical models [224], and is related to other geometric measures of the entanglement [205]. Here we compute the GE for the LRXXZ model on the MPS ground state using a two-step approach as detailed in Section 2.A.1: We first compute the exact MPS ground

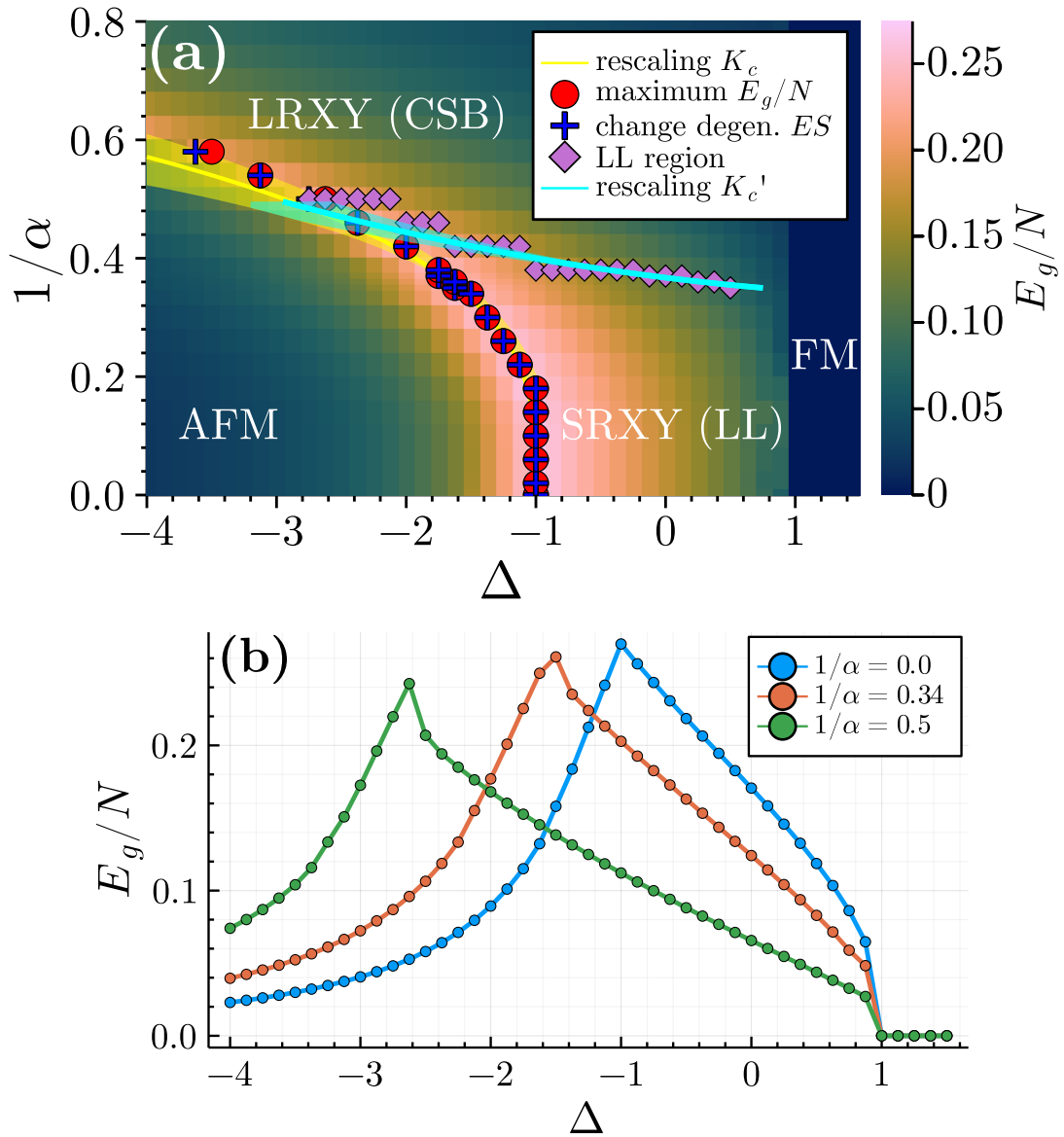


Figure 4.4.1: (a) Quantum phase diagram of the LRXXZ model, Eq. (4.2), versus the anisotropy (Δ) and long-range (α^{-1}) parameters. The colour scale indicates the GE density E_g/N , Eq. (4.38). It shows a cusp at the AFM-XY phase transition (indicated by the red points) and a non-analytic step at the XY-FM phase transition (see Inset). Also shown are numerical results for the AFM-XY phase transition found from degeneracy lift of the entanglement spectrum (blue crosses), and for the upper bound in α^{-1} for LL behaviour (purple diamonds). The yellow solid line shows the AFM-XY phase transition as found from renormalisation group analysis combined with inverse rescaling of Eq. (4.41) at the critical Luttinger parameter $K_c = 1/2$, see Section 4.3.3. The cyan solid line shows the critical line for breaking of LL behaviour obtained similarly at $K'_c = 1/[2(3 - \alpha)]$. The transparent yellow and cyan ribbons as well as the size of the markers correspond to the uncertainty. (b) GE versus Δ for $\alpha^{-1} = 0$ (blue), 0.34 (orange), and 0.5 (green). For all calculations, the system size is $N = 192$. Figure adapted from [185].

state $|\psi\rangle$ using DMRG calculations with high bond dimension, perform a singular value decomposition (SVD), and truncate it down to a single dominating singular value, to reduce the MPS to a product state $|\phi_0\rangle$. Subsequently, we submit the obtained state $|\phi_0\rangle$ to several variational optimization sweeps, keeping the bond dimension fixed at unity, until convergence of the overlap $|\langle\phi|\psi\rangle|^2$. More precisely, the optimization procedure is stopped when the difference of the overlaps $|\langle\phi|\psi\rangle|^2$ before and after the optimization sweeps becomes negligible (in practice smaller than 10^{-9}). This algorithm yields the state $|\phi\rangle$ closest to the exact ground state $|\psi\rangle$ within the product-state manifold.

In Figure 4.4.1, the GE of the LRXXZ model is represented in colour scale versus the anisotropy parameter Δ and the long-range parameter α . The XY to FM phase transition is signalled by a sharp step from $E_g(\Delta \leq 1) > 0$ to $E_g(\Delta > 1) = 0$, see Fig. 4.4.1(b). This transition occurs at $\Delta = 1$, irrespective to the value of the long-range parameter α^{-1} being consistent with the expected transition to the trivial, fully z-polarized ground state of the FM phase, see Appendix 4.A. On the other hand, the AFM to XY phase transition is signalled with a marked cusp of the GE, see Fig. 4.4.1(b). Paralleling its behaviour in the short-range case [153], the GE's ability to signal the AFM–XY phase transition persists in the long-range case for all considered values of α^{-1} . Furthermore, we have checked that the position of the local maximum signalling the phase transition is well converged in system size, see Appendix 4.C. Consequently, the pronounced peak in the GE allows us to locate the XY–FM phase transition versus the long-range parameter, see red disks in Fig. 4.4.1. While long-range interactions do not affect the XY–FM transition, they significantly shift the AFM–XY transition towards higher values of the antiferromagnetic anisotropy parameter $|\Delta|$. This is to be expected since z-oriented AFM order is frustrated by long-range interactions, which hence favour the XY phase. The two phase boundaries, the AFM–XY as well as the XY–FM as obtained from the GE are in excellent quantitative agreement with that found using the central charge in the conformally symmetric XY phase [223]. This shows that the GE provides a robust probe of both quantum phase transitions also in the long-range case. Nevertheless, RG predicts a phase transition away from the Luttinger liquid into a continuous symmetry broken phase following the condition Eq. (4.37). The geometric entanglement evidently fails to signalling this transition.

4.4.2 Entanglement spectrum

To gain more insight into the entanglement properties of the LRXXZ model, we now study the entanglement spectrum (ES) [112]. Its properties have been shown to signal quantum phase transitions in a variety of models, including the infinite order BKT phase transition of the XXZ model in the short-range case [118]. This contrasts with standard entanglement witnesses, such as Rényi entropies, which show a smooth behaviour at the AFM–XY transition [153, 187]. As defined in Appendix 2.A.2, the ES is defined in terms of the Schmidt decomposition of the ground state $|\psi\rangle$,

$$|\psi\rangle = \sum_j \sqrt{\lambda_j} |\psi_j^A\rangle \otimes |\psi_j^B\rangle, \quad (4.39)$$

where λ_j is the j -th Schmidt coefficient, and $|\psi_j^A\rangle$ and $|\psi_j^B\rangle$ are orthonormal bases of each subsystem. The reduced density matrix of a partition, $\rho_A = \text{tr}_B(|\psi\rangle\langle\psi|)$, is then cast in thermal-like form,

$$\rho_A = \sum_j e^{-\xi_j} |\psi_j^A\rangle\langle\psi_j^A|, \quad (4.40)$$

where the coefficients $\xi_j = -\ln(\lambda_j)$ are the entanglement energies and the effective temperature equals unity.

4.4.2.1 Entanglement spectrum of the LRXXZ chain

The ground-state ES of the LRXXZ is shown in Fig. 4.4.2 versus the anisotropy parameter Δ in the short-range case [(a) $\alpha^{-1} = 0$] and in the long-range case for two values of the long-range parameter [(b) $\alpha^{-1} = 0.3$ and (c) $\alpha^{-1} = 0.54$]. In all cases, the XY to FM phase transition is marked by the sharp divergence of all entanglement energies but ξ_1 , which vanishes for $\Delta = 1$. This is consistent with the onset of a fully polarized, exact product state in the FM phase, irrespective of the long-range parameter α^{-1} . The ground state deep in the AFM phase also tends towards a product state but only smoothly in the limit of infinite anisotropy, $\Delta \rightarrow -\infty$, as indicated by the monotonous increase of all ξ_j but ξ_1 . In the short-range case, Fig. 4.4.2(a), the AFM to XY phase transition at $\Delta = -1$ is marked by the sudden lift in the degeneracy of entanglement energies, see also Ref. [118]. More precisely, the entanglement energies ξ_2 and ξ_3 are degenerate in the XY phase while they are distinct in the AFM phase. The degeneracy lift, found exactly at $\Delta = -1$, marks the AFM–XY phase transition. A similarly sharp degeneracy lift is found for the entanglement energies ξ_5 and ξ_6 . Qualitatively similar features are found in the long-range case, for all considered values of long-range parameter α^{-1} . The degeneracy lift point is, however, found for a critical anisotropy parameter Δ that significantly depends on the long-range parameter α^{-1} , Figs. 4.4.2(b) and (c). It allows us to locate the AFM to XY phase transition in the LRXXZ model for all values of the long-range parameter. The result, shown as blue crosses in the phase diagram of Fig. 4.4.1, is in excellent agreement with the transition previously inferred from the cusp of the GE.

Note that the ES shows an apparent crossover regime in a narrow region of the AFM phase close to the AFM–XY phase transition, even for the relatively large system size used in our calculations ($N = 192$). It is marked by apparent degeneracies (e.g. $\xi_3 = \xi_4$) and a cusp of the lowest two entanglement energies in this crossover regime, see behaviour in the interval $-1.5 < \Delta < -1$ for the short-range case, and lower values for long-range cases. However, we find that this interval slowly shrinks towards the true AFM–XY critical point, see Appendix 4.C. This is consistent with the slow finite-size scaling of the local maximum of the entanglement entropy reported in earlier works [203, 204]. For a more detailed discussion of the finite-size effects on the ES, see Appendix 4.C. We hence consider the cusps of ξ_1 and ξ_2 , i.e. the local minimum of the Schmidt gap, as well as the apparent degeneracies in the crossover regime observed in Fig. 4.4.2 as finite-size artefacts. Note that in striking contrast the degeneracy lift point is nearly independent of the system size for $N \gtrsim 100$, see Appendix 4.C.

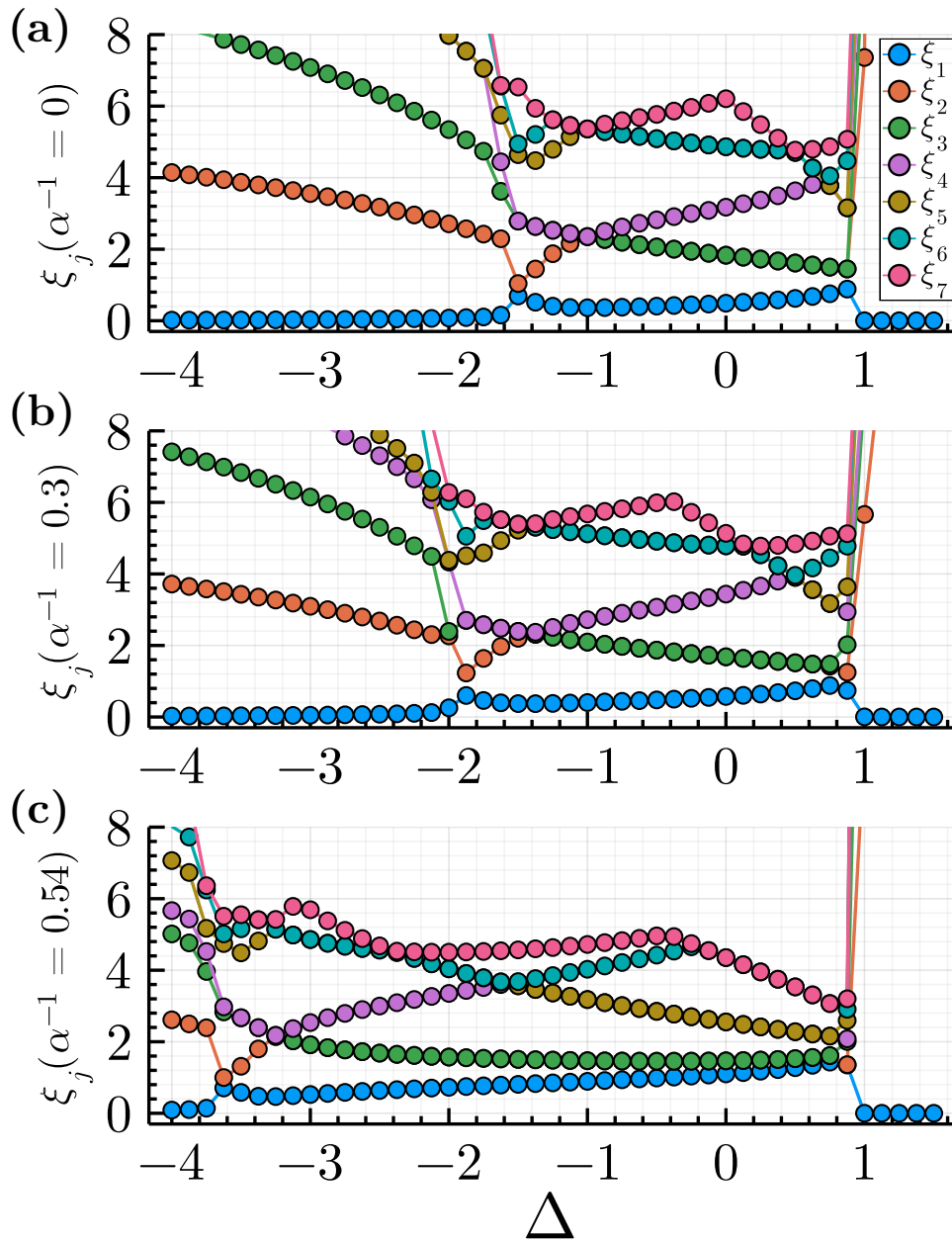


Figure 4.4.2: Entanglement spectrum of the ground state of (a) the short-range XXZ model, $\alpha^{-1} = 0$, and (b)-(c) the LRXXZ model for $\alpha^{-1} = 0.3$ and $\alpha^{-1} = 0.54$, respectively. Shown are the first seven entanglement energies (ξ_1 blue, ξ_2 orange, ξ_3 green, ξ_4 purple, ξ_5 brown, ξ_6 teal, and ξ_7 pink). The phase transition from XY to FM is marked by the divergence of all but the first entanglement energies at $\Delta = 1$. In the XY phase, the entanglement energies ξ_2 (orange) and ξ_3 (green) are degenerate ($\xi_2 = \xi_3$) while they are distinct deep in the AFM phase ($\xi_2 \neq \xi_3$), and the degeneracy lift marks the AFM–XY phase transition. Note the ES is in a crossover regime between the AFM–XY critical point and the cusps of ξ_1 and ξ_2 , see text. The system size is $N = 192$ for all calculations. The error bars are smaller than the size of the markers. Figure from [185]. See <https://jtschneider.github.io/es-rescaling> for an interactive version online.

4.4.2.2 Self-similarity

Inspection of the ES for a variable interaction range in the various panels of Fig. 4.4.1 shows a remarkable similarity, in particular in the low-entanglement-energy sector of the XY phase. Note that the entanglement spectrum ‘stretches’ in the direction $-\Delta$, starting from $\Delta = +1$, for ever-increasing interaction range, cf. Fig. 4.4.2 and follow <https://jtschneider.github.io/es-rescaling> to an interactive plot online. More precisely, we can find a nonlinear rescaling of the anisotropy parameter of the form

$$\Delta \rightarrow \tilde{\Delta}(\Delta, \alpha) = -\gamma(\alpha)|\Delta - 1|^{\nu(\alpha)} + 1, \quad (4.41)$$

such that all spectral lines (approximately) collapse onto the ES of the short-range model, see Fig. 4.4.3. The rescaling (4.41) is consistent with the exact fixed point $\Delta^* = 1$ corresponding to the XY–FM transition. The parameters $\gamma(\alpha)$ and $\nu(\alpha)$ are then found by minimizing a weight function constructed over a wide interval containing the AFM–XY phase transition. For more details, see Appendix 4.D. Figure 4.4.4 shows the rescaling parameters γ and ν versus the long-range parameter α^{-1} . Both start to significantly differ from unity at $\alpha^{-1} \simeq 0.2$, consistently with Fig. 4.4.1.

More precisely, we distinguish two regimes. For roughly $\alpha^{-1} \lesssim 0.3$, all spectral lines almost perfectly collapse onto the short-range ES upon rescaling in the XY phase, see Fig. 4.4.3(a). On the other hand, for $\alpha^{-1} \gtrsim 0.3$, only the lowest three spectral lines ξ_1, ξ_2, ξ_3 are congruent with the short-range ones upon rescaling, see Fig. 4.4.3(b). In contrast, the rescaled spectrum shows a worse match for higher entanglement energies (ξ_4 and higher). For instance, while ξ_4 (purple) is rescaled to greater values of $\tilde{\Delta}$, ξ_7 (pink) is rescaled to lower ones, pointing towards an irreconcilable mismatch following a global rescaling of the ES. Nevertheless, the good match of the lowest entanglement energies renders the scaling (4.41) sufficient to determine the AFM to XY transition found from the degeneracy lift of ξ_2 and ξ_3 . Similarly, the rescaling parameters $\gamma(\alpha)$, $\nu(\alpha)$ start to significantly deviate from close to unity around $\alpha^{-1} \simeq 0.2$ reflecting an onset of a stronger expansion of the ES to more negative values of Δ with longer ranged interactions. See also Fig. 4.4.2 for a direct observation of the degeneracy lift position expanding faster than linear towards more negative Δ with longer ranged interactions.

Note that the self-similarity applies in particular to the congruent rescaling of the degeneracy lift point indicating the AFM–XY phase transition. This implies the critical AFM–XY point characterised by $K_c = 1/2$ follows the same rescaling property as the ES, i.e. $K(\Delta = -1, \alpha = \infty) = 1/2 = K(\tilde{\Delta}(\Delta = -1, \alpha), \alpha)$. However, the self-similarity applies more importantly at least to the low-entanglement-energy spectrum over the entire XY phase. It is therefore reasonable to assume that not only the critical AFM–XY point at $K = 1/2$ can be rescaled to its long-range counterpart, but rather can K be rescaled over a wider region of the XY phase. With this assumption, we inspect the critical line where $V_{\text{LRXY}}[\theta]$, Eq. (4.28), turns relevant, corresponding to the condition $K'_c = 1/[2(3 - \alpha)]$, see Eq. (4.35). Replacing K'_c by the Bethe ansatz formula (4.30) and Δ by $\tilde{\Delta}(\Delta'_c, \alpha)$, Eq. (4.41), we then solve for $\Delta'_c(\alpha)$. It yields the cyan solid line in Fig. 4.4.1. Above this line, the physics is governed by the long-range XY model (LRXY phase in the Fig. 4.4.1), while below the

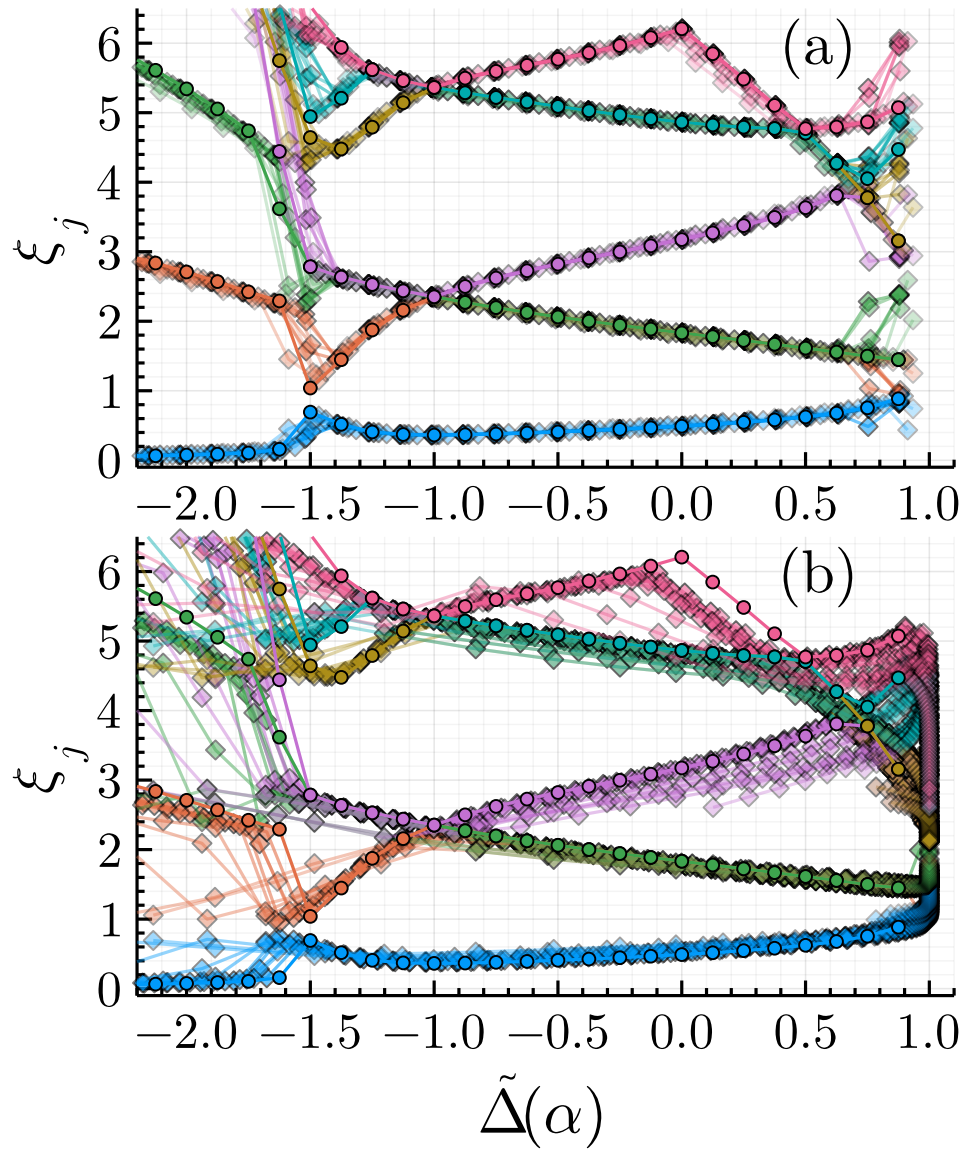


Figure 4.4.3: Entanglement spectra plotted versus the rescaled anisotropy parameter $\tilde{\Delta}$ for various long-range parameters α^{-1} . The short-range case $\alpha^{-1} = 0$ is shown as coloured circles while long-range cases are shown as coloured diamonds. (a): Values of α^{-1} from 0.02 to 0.3 with an increment of 0.04 corresponding to progressively fainter colour. (b): Same for values of α^{-1} from 0.34 to 0.78. Figure from [185].

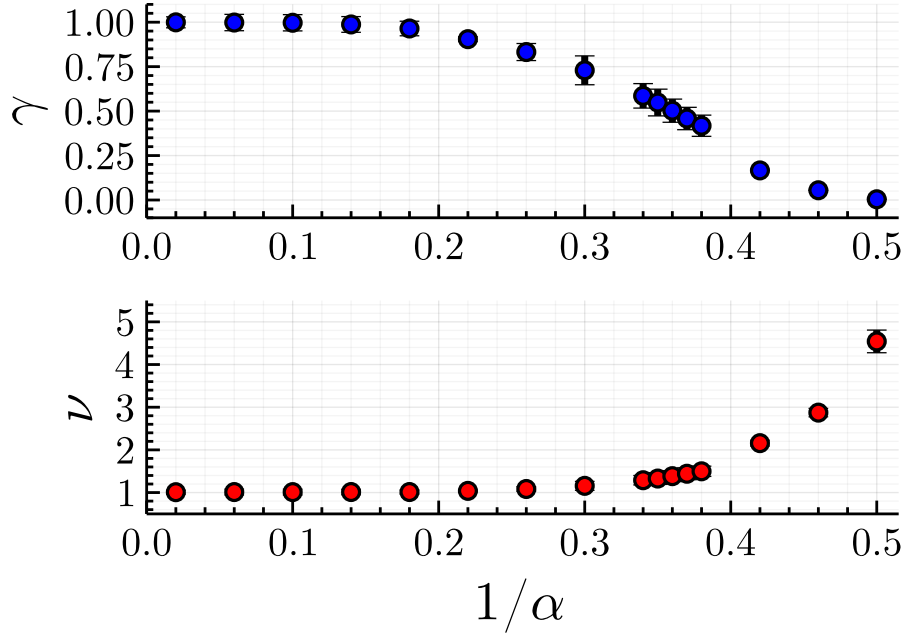


Figure 4.4.4: Rescaling parameters γ and ν of Eq. (4.41) versus the long-range parameter α^{-1} . The error bars are indicated by capped black lines (see method in Appendix 4.D). Figure from [185].

long-range XY term is irrelevant (SRXY phase). Numerical calculations confirm that the transition is characterised by the critical Luttinger parameter $K'_c = 1/[2(3 - \alpha)]$, see Sec. 4.4.3. Note that for $\alpha = 2$, the critical line for long-range behaviour yields $K'_c = 1/2$, at which point also $V_{ZZ}[\phi]$ becomes relevant ($K_c = 1/2$). We thus expect that the two critical lines approximately meet around $\alpha_c = 2$ within first order perturbative RG.

Likewise, we have checked that the same rescaling also applies to the geometric entanglement curves. Applying the rescaling of Eq. (4.41) with the scaling parameters $\gamma(\alpha)$ and $\nu(\alpha)$ found from the ES (Fig. 4.4.4), we find very good data collapse of the rescaled GE curves onto the corresponding short-range curve for $\alpha^{-1} \lesssim 0.3$, see Fig. 4.4.5(a). It is worth noting that this holds over both the AFM and XY phases. In contrast, for $\alpha^{-1} \gtrsim 0.3$, the rescaling gets increasingly worse for longer range interactions (increasing values of α^{-1}), although the cusp is still consistent with $\tilde{\Delta} \simeq -1$, see Fig. 4.4.5(b).

4.4.3 Luttinger liquid parameters in XY phase

This section is dedicated to the numerical verification of Luttinger liquid behaviour. The results above in Section 4.4.2.2 indicate that the entanglement properties (ES and GE) of the LRXXZ model can be deduced from their short-range counterpart upon the rescaling of Eq. (4.41). Furthermore, our RG analysis is consistent with the existence of an effective Luttinger parameter K fulfilling the same rescaling over the entire SRXY phase. In this section, we check Luttinger liquid behaviour as well as the self-similar features of K over the critical phase by inspecting a number of universal behaviours characteristic of LL.

We first consider the behaviour of the Rényi entropies, $\mathcal{S}_n = \ln[\text{tr}(\rho_A^n)]/(1 - n)$ with Rényi order $n \in \mathbb{R}^+$. Measuring Rényi entropies allows us on the one hand to verify that the central charge is

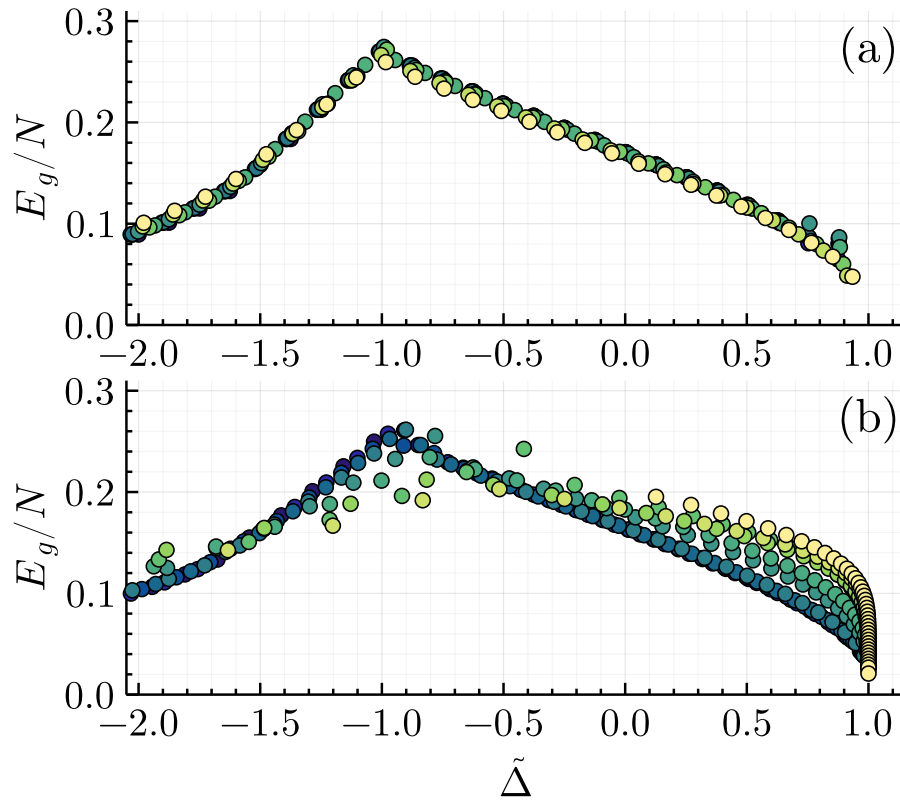


Figure 4.4.5: Rescaling of the ground-state GE density, Eq. (4.38), with Eq. (4.41) versus $\tilde{\Delta}$. (a) Data for $\alpha^{-1} \leq 0.3$, colour coding from dark blue to bright yellow for $\alpha^{-1} = [0.0, 0.02, 0.06, \dots, 0.3]$. (b) Data for $\alpha^{-1} > 0.3$, colour coding from dark blue to bright yellow for $\alpha^{-1} = [0.34, 0.38, \dots, 0.62]$. Figure from [185].

close to unity, a necessary condition for LL behaviour, and on the other hand to estimate the LL parameter K . The Rényi entropies of the short-range XXZ model in the critical XY phase may be written as [225, 226]

$$\mathcal{S}_n(N, l) = \mathcal{S}_n^{\text{CFT}}(N, l) + \mathcal{S}_n^{\text{osc}}(N, l), \quad (4.42)$$

with N the system size and a bipartition into two sub-systems A and B of respective sizes l and $N-l$. The first term is the conformal field theory (CFT) prediction. For a finite one-dimensional gapless system of size N with open boundary conditions, it reads as

$$\mathcal{S}_n^{\text{CFT}} = \frac{c(1+n^{-1})}{12} \ln \left[\frac{4(N+1)}{\pi} \sin \left(\frac{\pi(2l+1)}{2(N+1)} \right) \right] + c_1, \quad (4.43)$$

where c is the central charge, and c_1 is a nonuniversal constant [225, 226]. Note that the open boundary conditions (OBC) alter the chord distance $D_{\text{OBC}}(l, N) = 4(N+1) \sin[\pi(2l+1)/(2(N+1))]/\pi$ with respect to periodic boundary conditions (PBC) $D_{\text{PBC}}(l, N) = N \sin(\pi l/N)/\pi$ [226, 227]. The second term accounts for oscillatory corrections to the CFT prediction due to significant antiferromagnetic correlations in the critical XY phase of the XXZ model [226, 228]. It takes the universal form [225–229]

$$\mathcal{S}_n^{\text{osc}} = \frac{g_n}{N^{p_n}} \sin[(2l+1)k'_F] \left| \sin \left(\frac{\pi(2l+1)}{2(N+1)} \right) \right|^{-p_n}, \quad (4.44)$$

where g_n is a nonuniversal constant, the exponents of the oscillation amplitude, p_n , are related to the Luttinger parameter K as $p_n = 2K/n$ for OBC, and $k'_F = \frac{N}{N+1}k_F + \frac{\pi}{2(N+1)}$ is an effective Fermi momentum, including OBC finite-size corrections with respect to its counterpart in the thermodynamic limit, $k_F = \pi/2$.

To determine the effective central charge c and Luttinger parameter K of the LRXXZ, we fit Eq. (4.42) with Eqs. (4.43) and (4.44) to the Rényi entropy obtained from the ground state MPS in the range $l \in [10, \dots, N-10]$ at fixed system size N and fixed Rényi order n . It yields estimates of the four fitting parameters c , c_1 , g_n , p_n , and consequently of the Luttinger parameter, $K = np_n/2$. We focus on the critical XY phase ($-1 < \tilde{\Delta} < 1$) as previously identified from the GE and ES. We consider that the Rényi entropies are consistent with LL behaviour when the residual sum of squares (RSS) is below 2%. Typical fits of Eq. (4.42) to the MPS data are displayed in Fig. 4.4.6(a). Note that for clarity the various curves are shifted by an amount indicated on the right-hand-side of each curve. Judging from the fit quality check above, we find that the results are consistent with LL behaviour in a region of the critical phase bounded from above in direction of α^{-1} . The boundary is displayed as purple diamonds in Fig. 4.4.1. The breakdown of the LL behaviour is in excellent agreement with the critical line found from our RG analysis (solid cyan line). Consistently, we find that in the region so identified, the central charge—as extracted from the fits—does not significantly deviate from unity $c \approx 1$. This property was used in Ref. [223] as a criterion to identify the LL phase and yields a similar boundary. Moreover, we find that the various estimates of the Luttinger parameter from Rényi entropies of different orders n , $K = np_n/2$, consistently yield a value of K approximately independent of n with a tolerance of less than 7.5%.

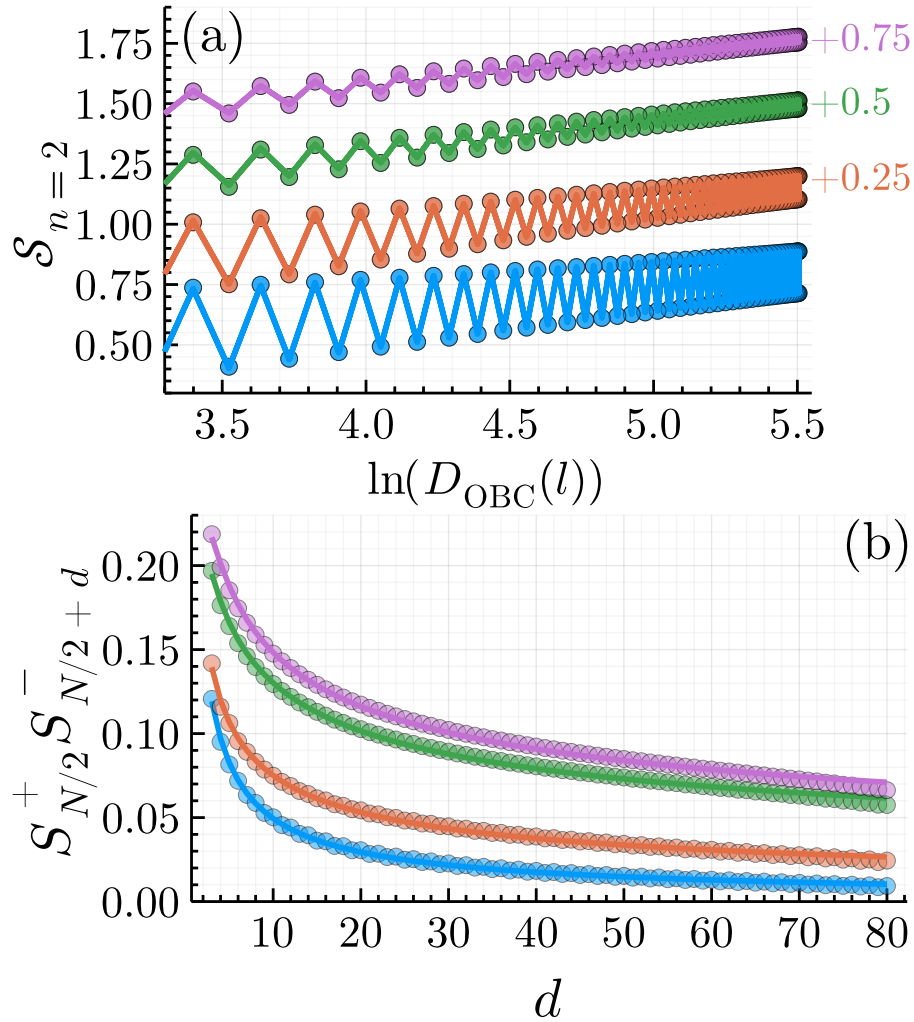


Figure 4.4.6: Typical MPS data for entanglement entropies and correlation functions for $\Delta = -0.875$, $\alpha^{-1} = 0.06$ (blue), $\Delta = -1.5$, $\alpha^{-1} = 0.42$ (orange), $\Delta = -0.125$, $\alpha^{-1} = 0.34$ (green), $\Delta = 0.5$, $\alpha^{-1} = 0.14$ (purple), and the system size $N = 192$. The error bars are smaller than the size of the marker. (a) Rényi entanglement entropies $S_{n=2}(N, l)$ (coloured circles) and corresponding fit of Eq. (4.42) (solid line) plotted versus the logarithm of the chord distance. Fits performed over $l \in [10, \dots, N - 10]$ yield $c_{\text{eff}} = 0.9$, $K = 0.6$ (blue), $c_{\text{eff}} = 1$, $K = 1.1$ (orange), $c_{\text{eff}} = 1$, $K = 1.5$ (green), and $c_{\text{eff}} = 1$, $K = 1.5$ (purple). For clarity, the curves are shifted by a constant offset indicated on the right-hand-side of each curve. (b) Correlation function $\langle S_{N/2}^+ S_{N/2+d}^- \rangle$ (points) and corresponding fit of Eq. (4.45) (solid line) plotted versus distance d . The fits yield $K = 0.6$ (blue), $K = 1.1$ (orange), $K = 1.4$ (green), and $K = 1.4$ (purple). Figure from [185].

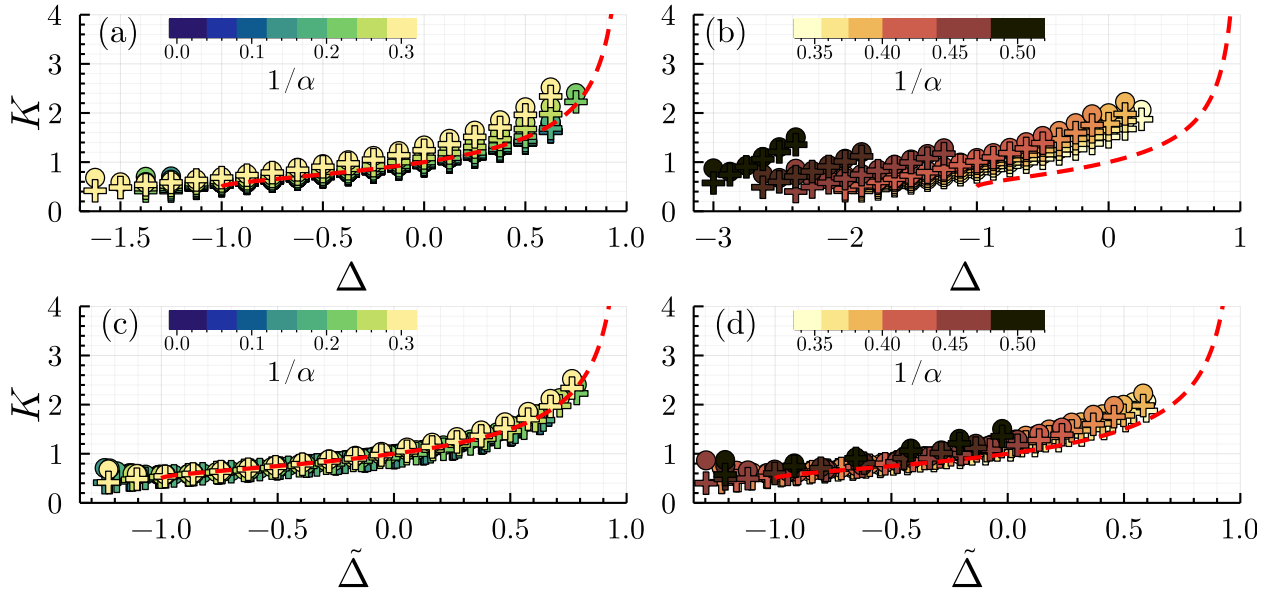


Figure 4.4.7: Luttinger parameter K versus the anisotropy parameter for various values of the long-range parameter α^{-1} . Coloured disks correspond to the Rényi-entropy estimates K^S , Eq. (4.42) with Rényi order $n = 2$, and coloured crosses to correlation-function estimates K^G , Eq. (4.45). Colour codings for α^{-1} are indicated in colour bars. The dashed red line is the short-range Bethe ansatz formula (4.30). The upper panels (a) and (b) show the data versus the bare anisotropy parameter Δ , separating the cases $0 \leq \alpha^{-1} \leq 0.3$ and $\alpha^{-1} > 0.3$ for clarity. The lower panels (c) and (d) show, respectively, the same data versus the rescaled parameter $\tilde{\Delta}$. The breakdown of LL theory is signalled by deviations between the two estimates at $\tilde{\Delta} \lesssim -1$. The size of the error bars is smaller than the size of the marker. Figure from [185].

To verify the validity of the LL behaviour within the SRXY phase, we now turn to a second, independent measurement of the effective Luttinger parameter K . To this end, we consider the $\langle S_R^+ S_{R'}^- \rangle$ correlation functions. For the short-range XXZ model they read as,

$$G(R, R') = \langle S_R^+ S_{R'}^- \rangle \approx \frac{C_1}{|R - R'|^{2K + \frac{1}{2K}}} + \frac{C_2}{|R - R'|^{\frac{1}{2K}}}, \quad (4.45)$$

where C_1 and C_2 are nonuniversal constants¹. We compute the correlation function $\langle S_{N/2}^+ S_{N/2+d}^- \rangle$ in the LL regime identified above. Typical MPS results (points) together with fits of Eq. (4.45) to the data (solid lines) are shown in Fig. 4.4.6(b), showing excellent agreement over the full LL regime. These fits confirm the LL behaviour and yield a second, independent, estimate of the Luttinger parameter K .

To compare the two estimates of the Luttinger parameter, from fits to the Rényi entropies (K^S) and to the correlation functions (K^G) respectively, first note that the same congruent rescaling as discussed above also applies to both K estimates. Figures 4.4.7(a) and (b) show the fitted values of K^S (coloured dots) and K^G (coloured stars) plotted against the anisotropy parameter Δ for different values of the long-range parameter α^{-1} . Data for $0 < \alpha^{-1} \leq 0.3$ and $0.3 < \alpha^{-1}$, respectively, are

¹The Hamiltonian of the short-range model obeys the symmetry $H(-J, -\Delta, h, \alpha = \infty) = U_2 H(J, \Delta, h, \alpha = \infty) U_2^{-1}$ with $U_2 = \prod_{l=\text{even}} \sigma_l^z = U_2^{-1}$. This maps S_l^x, S_l^y, S_l^z to $-S_l^x, -S_l^y, S_l^z$ for even l [217]. Using this transformation, Eq. (4.45) is consistent with its counterpart for antiferromagnetic coupling ($J < 0$), see Refs. [6, 217].

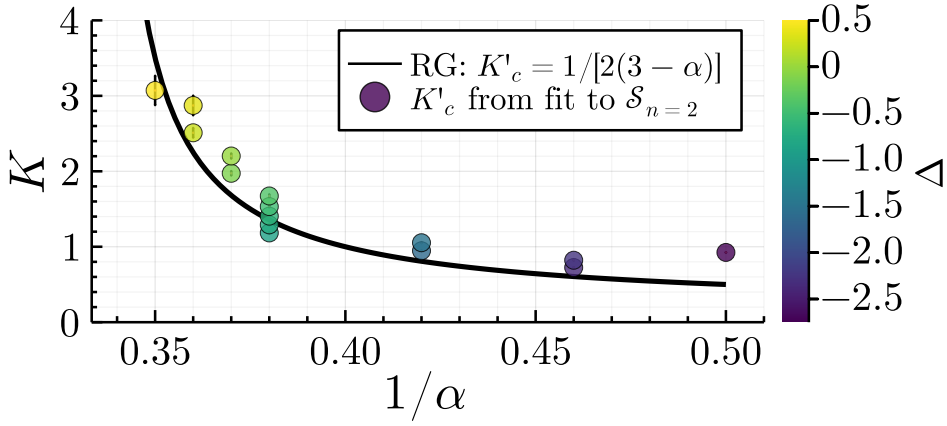


Figure 4.4.8: Critical Luttinger parameter along the SRXY-LRXY transition versus the long-range parameter α^{-1} . The solid black line is the RG prediction $K'_c = 1/[2(3 - \alpha_c)]$. The coloured disks show the numerically measured K^S through fits to Eq. (4.42) with Rényi order $n = 2$ at points in the phase diagram Fig. 4.4.1 closest to the RG critical boundary line (cyan solid line). The colour code correspond to values of Δ from $\Delta = 0.5$ (yellow) to $\Delta = -2.75$ (blue). Figure from [185].

separated in Figs. 4.4.7(a) and (b) for clarity. The dashed red line shows the analytic short-range result from Bethe ansatz, Eq. (4.30). Figures 4.4.7(c) and (d) show, respectively, the same data versus the rescaled anisotropy parameter $\tilde{\Delta}$. For $0 \leq \alpha^{-1} \leq 0.3$, we observe an almost perfect collapse of all long-range values of K^S and K^G onto the short-range curve upon the rescaling (4.41) with parameters as in Fig. 4.4.4, see Fig. 4.4.7(c). In contrast, the data for K^S and K^G for $\tilde{\Delta} < -1$ do not agree with each other, consistently with the breakdown of LL theory. Similarly, Fig. 4.4.7(d) displays K^S and K^G for $0.3 < \alpha^{-1}$ (colour coding from blue to yellow) and shows a good self-similar rescaling, albeit with few singular deviations inside $-1 < \tilde{\Delta} < 1$ for the largest values of α^{-1} . Here also the breakdown of LL theory is found for $\tilde{\Delta} < -1$ where K^S and K^G deviate from each other.

These results confirm the LL behaviour in the SRXY phase identified in the diagram of Fig. 4.4.1. They furthermore confirm the self-similarity features of the Luttinger parameter K that was assumed in the derivation of the critical lines in the self-similarity analysis in Section 4.4.2.2. The latter matches well our independent numerical analysis in this section, as well as the numerical results of Ref. [223]. The critical line we obtain from RG analysis constitutes a substantial improvement over the perturbatively computed analytic line *ibidem*.

Moreover, we find that the point where the two numerically estimated Luttinger parameters start to deviate, hence marking the breakdown of LL behaviour and found at $\tilde{\Delta} \simeq -1$, is consistent with the RG prediction for the AFM-XY phase transition, $K_c = 1/2$, for all values of α inspected, see Fig. 4.4.7(c). Similarly, we find that the Luttinger parameter computed from Rényi entropies, K^S , along the phase boundary estimated by K'_c (solid cyan line in Fig. 4.4.1) is consistent with the RG prediction for the SRXY-LRXY transition, see Fig. 4.4.8.

We finally consider the behaviour of the speed of sound u in the LL regime. To find it, we rely on the LL formula for the magnetic susceptibility $\chi = \partial M / \partial h|_{h=0} = K/(u\pi)$, where h is the magnetic field amplitude and $M = 2 \sum_n \langle S_n^z \rangle$ is the total magnetization. In the MPS simulations, we add the magnetic coupling term $-h \sum_n S_n^z$ to Hamiltonian (4.2) and compute M for various magnetic field amplitudes in the range $0.01 < h < 0.1$. The magnetic susceptibility χ is then found from a linear fit to the MPS data for the total magnetisation. The speed of sound is then given by

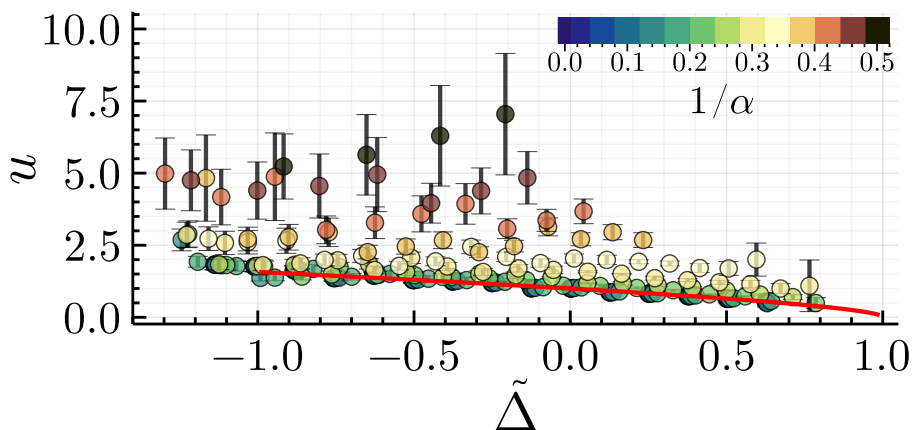


Figure 4.4.9: Speed of sound u versus the rescaled anisotropy parameter $\tilde{\Delta}$ for various values of the long-range parameter α^{-1} . The data are found from calculations of the magnetic susceptibility and estimates of the Luttinger parameter K from fits to the Rényi entropy, see text. The solid red line indicates the short-range analytic result. Data for $\alpha^{-1} \leq 0.3$, colour coded from dark blue to bright yellow while data for $\alpha^{-1} > 0.3$ is colour coded from bright yellow to dark brown. The uncertainty on each data point is marked by vertical capped error bars. Figure from [185].

$u = K^{\mathcal{S}}/(\pi\chi)$, where $K^{\mathcal{S}}$ is the estimate of the Luttinger parameter found from the entanglement entropy as discussed above. The results (coloured disks), together with the Bethe ansatz prediction $u(\Delta) = \pi\sqrt{1 - \Delta^2}/(2 \arccos(-\Delta))$ [6, 217, 218] are shown in Fig. 4.4.9. In striking contrast with the Luttinger parameter K , the speed of sound u does not follow the rescaling of Eq. (4.41). It rather increases in value upon increasing the long-range parameter α^{-1} . Quantitatively, the increase goes from a few percent for $\alpha^{-1} = 0$ to $\simeq 30\%$ for $\alpha^{-1} \simeq 0.2$ marking a small yet appreciable mismatch with the analytic short-range prediction, see Fig. 4.4.9 data coloured from dark blue to bright green. In contrast, for longer range interactions, $\alpha^{-1} \gtrsim 0.2$, we find a dramatic increase of u with respect to the short-range value, see Fig. 4.4.9 data coloured coding from bright yellow to black.

Note that the fact that u does not fulfil the same rescaling as K does not call into question the validity of the mapping to the effective short-range LL model identified above. It, however, indicates that the long-range XXZ Hamiltonian in the LL phase cannot be mapped into its short-range equivalent solely by the rescaling (4.41). In fact, it is necessary to add a rescaling in energy, determined by the results of Fig. 4.4.9. Since the latter only affects the energy scale, it does not affect the entanglement Hamiltonian.

4.4.4 Entanglement Hamiltonian

This section is presenting yet unpublished results on the structure of the entanglement Hamiltonian (EH) \tilde{H}_A introduced in Section 1.7 as the Hermitian operator who shares its eigenbasis with the reduced density matrix and whose spectrum is the entanglement spectrum. Recall that the EH is defined in terms of the reduced density matrix (RDM) $\rho_A = \exp(-\tilde{H}_A) = \sum_j \exp(-\xi_j) |\psi_j^A\rangle\langle\psi_j^A|$ where $|\psi_j^A\rangle$ is an (orthonormal) eigenbasis of the RDM. In the following, we will establish that the bipartite ground state of the LRXXZ admits an EH having an operator form inspired by the BW theorem (cf. Eq. (1.21)). Here, we follow the lines of Qi and Ranard in Ref. [230] to recon-

struct the EH given a single eigenstate². Note that an eigenstate of the reduced density matrix is necessarily also an eigenstate of the entanglement Hamiltonian. Following a real-space Schmidt decomposition (bipartition) of the ground state in complementary subsystems $A = [1, \dots, L]$ and $B = [L + 1, \dots, N]$,

$$|\psi^{\text{GS}}\rangle = \sum_{l=1}^r \lambda_l |\psi_l^A\rangle \otimes |\psi_l^B\rangle, \quad (4.46)$$

we thus start with the input state $|\psi_0^A\rangle$ corresponding to the state in A with the largest Schmidt value, i.e. the smallest entanglement energy. See also Eq. (2.26) for a graphical representation of the Schmidt decomposition. We now embark to reconstruct the entanglement Hamiltonian \tilde{H}_A given one of its eigenstates $|\psi_0^A\rangle$. To this end, we must minimise the energy variance,

$$\sigma_E^2 = \langle \psi_0^A | \tilde{H}_A^2 | \psi_0^A \rangle - \langle \psi_0^A | \tilde{H}_A | \psi_0^A \rangle^2, \quad (4.47)$$

because $|\psi_0^A\rangle$ can have vanishing energy variance $\sigma_E^2 = 0$ if and only if it is a true eigenstate of \tilde{H}_A . Following Qi and Ranard [230], we shift our perspective and keep $|\psi_0^A\rangle$ fixed by the Schmidt decomposition and minimise in the variable couplings of \tilde{H}_A given that we choose an operator ansatz inspired by the BW theorem. Our ansatz for the EH is therefore,

$$\tilde{H}_A = \sum_{n=1}^{L-1} J_n \sum_{m=n+1}^{n+M} \frac{1}{|n-m|^\alpha} (S_n^x S_m^x + S_n^y S_m^y + \Delta S_n^z S_m^z), \quad (4.48)$$

$$= \sum_{n=1}^{L-1} J_n^{XY} \sum_{m=n+1}^{n+M} \frac{1}{|n-m|^\alpha} (S_n^x S_m^x + S_n^y S_m^y) + \sum_{n=1}^{L-1} J_n^{ZZ} \sum_{m=n+1}^{n+M} \frac{1}{|n-m|^\alpha} S_n^z S_m^z \quad (4.49)$$

where L is the size of subsystem A , $J_n^{XY} = J_n$ and $J_n^{ZZ} = J_n \cdot \Delta$, and M is an upper limit to the long-range coupling we have to introduce to tame the computational complexity. The couplings J_n^{XY} and J_n^{ZZ} are unspecified variables which remain to be determined. Note that J_n forms an $L - 1$ dimensional vector $\mathbf{J} = (J_0, J_1, \dots, J_{L-1})^T$ containing all variables in the ansatz (4.49). We may simplify the notation with the definitions,

$$\tilde{H}_A = \sum_{n=1}^{L-1} J_n h_n \quad (4.50)$$

$$h_n := \sum_{m=n+1}^{n+M} \frac{1}{|n-m|^\alpha} (S_n^x S_m^x + S_n^y S_m^y + \Delta S_n^z S_m^z), \quad (4.51)$$

and note that the minimisation problem may be written as a simple linear algebra equation,

$$\sigma_E^2 = \sigma_E^2(\mathbf{J}) = \sum_{n=1}^{L-1} \sum_{m=1}^{L-1} J_n J_m \langle \psi_0^A | h_n h_m | \psi_0^A \rangle - \sum_{n=1}^{L-1} \sum_{m=1}^{L-1} J_n J_m \langle \psi_0^A | h_n | \psi_0^A \rangle \langle \psi_0^A | h_m | \psi_0^A \rangle \quad (4.52)$$

$$=: \sum_{n=1}^{L-1} \sum_{m=1}^{L-1} J_n C_{n,m} J_m = \mathbf{J}^T \cdot \mathbf{C} \cdot \mathbf{J}, \quad (4.53)$$

²The reconstruction of the Hamiltonian given one of its eigenstates is sometimes called the quantum inverse problem.

where we define the *correlation matrix* C as

$$C_{n,m} := \langle \psi_0^A | h_n h_m | \psi_0^A \rangle - \langle \psi_0^A | h_n | \psi_0^A \rangle \langle \psi_0^A | h_m | \psi_0^A \rangle. \quad (4.54)$$

Let us denote the eigenvalues of C in ascending order as $e_1 \leq e_2 \leq \dots$ and so on. From Eq. (4.53) it is evident if \mathbf{J} is an eigenvector of the correlation matrix C with eigenvalue 0 then the couplings in \mathbf{J} define an entanglement Hamiltonian through our ansatz (4.49) to which our input state $|\psi_0^A\rangle$ is a true eigenvector. Furthermore, if there is more than one vanishing eigenvalue, each eigenvector $\{\mathbf{J}\}$ in the kernel of C defines a Hamiltonian through the ansatz (4.49) and our approach cannot determine the entanglement Hamiltonian uniquely. We can uniquely determine the EH from the input state $|\psi_0^A\rangle$, should we find a single eigenvector in $\ker(C)$. Lastly, if there is no eigenvector in $\ker(C)$, we conclude that we cannot determine the EH of the form in Eq. (4.49) given the input state $|\psi_0^A\rangle$. Although this approach formally only ensures the EH defined by \mathbf{J} through Eq. (4.49) shares a single eigenstate, namely the input state $|\psi_0^A\rangle$, with the true entanglement Hamiltonian $\tilde{H}_A = -\log(\rho_A)$, it has recently been argued that all other eigenvectors of the EH defined by \mathbf{J} and the true EH match well whenever the lowest eigenvalue e_1 is vanishingly small [135].

Consequently, we measure all matrix elements of $C_{n,m}$ defined by Eq. (4.54) and numerically diagonalise it to obtain its lowest eigenvalue e_1 and the corresponding eigenvector v_1 . Note that $C_{n,m}$ is by definition a positive semi-definite Hermitian matrix implying J_n are real-valued and allowing us to resort to more efficient numerical diagonalisation algorithms than generic ones. Furthermore, note we have to measure all $\sim (L-1)^2 \cdot M$ connected 4-point correlation functions³ with respect to the input state $|\psi_0^A\rangle$ from the bipartition since our ansatz includes long-range couplings up to M -nearest neighbours. To tame the computational complexity, we restrict ourselves in practice to $M = M(\alpha)$ neighbours defined by $M^{-\alpha} \leq 0.02$. However, we also define a lower bound of no less than five nearest neighbours, $M_{\min} = 5$, being incorporated in the correlation matrix element⁴.

We proceed to measure the correlation matrix C (4.54) in the state with the lowest entanglement energy following a half-chain bipartition of the ground state of the LRXXZ model. We consider the BW inspired ansatz Eq. (4.49) to approximate the EH of the bipartite ground state if the lowest eigenvalue e_1 is numerically vanishing. Figure 4.4.10 displays the phase diagram obtained from the lowest eigenvalue of the correlation matrix C whereas the colour bar, indicating the value of e_1 , is logarithmically scaled. We note that e_1 is vanishingly small ($e_1 \ll 10^{-7}$ colour-coded as light blue) well into the phases above inferred to be the SRXY phase, i.e. Luttinger liquid, and the AFM phase. The smallest eigenvalue rises however appreciably beyond numerically small values before approaching the phase transition into the LRXY phase. Interestingly, we again encounter an artefact we attribute to the slow convergence of the entanglement entropy with system size, cf. Section 4.C, at $\Delta = -1.625$ and from $1/\alpha \geq 0$. Contrarily, e_1 increases when approaching the above determined phase transitions which is perceivable by the changing colour from very light blue to darker shades of blue. We conclude that in the regions shaded from dark red to light red in Fig. 4.4.10, the diagonalisation does not yield any eigenvector in the kernel of the correlation

³Note that each h_n contains two-body interaction terms rendering any matrix element $C_{n,m}$ a 4-point function.

⁴Note that we respect open boundary conditions meaning one encounters at most couplings up to the boundary and implying exceptions to $M_{\min} = 5$ when approaching the boundary closer than five sites.

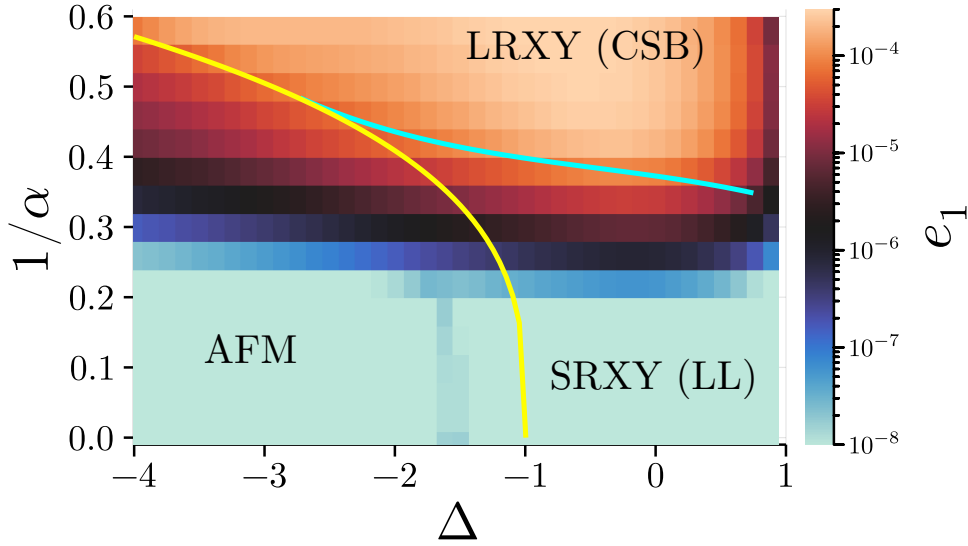


Figure 4.4.10: Phase diagram of the smallest eigenvalue e_1 of the correlation matrix Eq. (4.54). Note the logarithmic scale of the colour bar corresponding to the value of e_1 . The solid yellow line marks the transition between AFM and XY phases and the cyan line the transition between SRXY and LRXY phases. Both lines are the same as in Fig. 4.4.1. The for all data in this plot, DMRG simulation ran in system size is $N = 200$ with maximum link dimension $\chi_m = 450$.

matrix C . Therefore, there cannot be any EH in that region which follows our ansatz in Eq. (4.49). Furthermore, we note the second-smallest eigenvalue e_2 is consistently larger than e_1 by up to three orders of magnitude, as can be inspected in Fig. 4.4.11. We observe that the region where $e_2/e_1 \gg 1$ follows the region where $e_1 \ll 10^{-7}$, cf. Fig. 4.4.10 and Fig. 4.4.11. Hence, we also consider the eigenvector to e_1 to be the only vector in $\ker(C)$ therefore uniquely defining the EH through the ansatz of Eq. (4.49).

We proceed by checking the consistency of our estimated region where we reconstructed the EH. To this end, we compare the reconstructed couplings to the prediction from the short-range case via conformal field theory (CFT) in the SRXY phase, and via the corner transfer matrix (CTM) in the AFM phase, respectively. Considering the CFT prediction for a finite chain in open boundary conditions from Eq. (1.22), we expect the lattice couplings in the critical SRXY phase to follow,

$$J_n^{XY} \propto \sin\left(\frac{\pi n}{2L}\right), \quad J_n^{ZZ} \propto \Delta \sin\left(\frac{\pi n}{2L}\right), \quad (4.55)$$

while on the other hand the CTM prediction of Eq. (1.23) indicates a linear increase of the lattice couplings close to the bipartition position $n = 1$ in the gapped AFM phase,

$$J_n^{XY} \propto n, \quad J_n^{ZZ} \propto \Delta n, \quad (4.56)$$

with n being much smaller than the subsystem size L , $n \ll L$. Figure 4.4.12 shows some exemplary cases of inferred couplings of the EH. The analytical prediction from the short-range case is applying to Figs. 4.4.12(a)–(d). Figures 4.4.12(a) and (b) are located in the AFM phase where we find the CTM prediction of Eq. (4.56) to be a good fit (fitted curve drawn as dashed line) to the couplings (plotted as solid lines) close to the bipartition position $n = 1$ up to $L/2$. Furthermore, the CFT prediction of Eq. (4.55) is also a good fit (shown as dash-dotted lines) for the inferred couplings

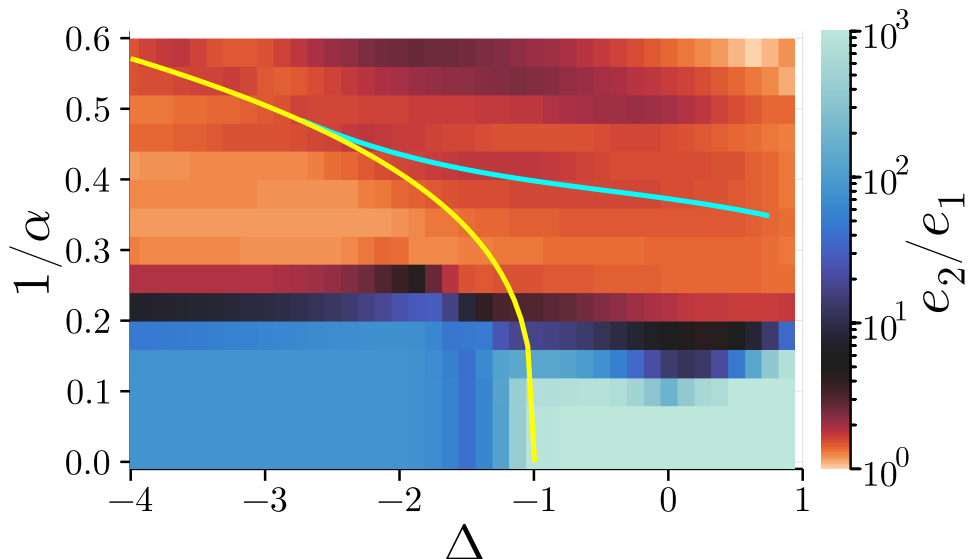


Figure 4.4.11: Phase diagram of the ratios of e_2/e_1 . Note the colour bar's perception is changing logarithmically with the magnitude of e_2/e_1 indicating ratios of $e_2/e_1 > 1$ from bright blue to dark blue while values of $e_2/e_1 \leq 1$ are coloured in black to red to bright red. The solid yellow line marks the transition between AFM and XY phases and the cyan line the transition between SRXY and LRXY phases. Both lines are the same as in Fig. 4.4.1.

(plotted as solid lines), as can be seen in Figs. 4.4.12(c) and (d) which are in the SRXY phase. Last, Figs. 4.4.12(e) and (f) are located in the darker blue region of Fig. 4.4.10 where the BW-inspired ansatz cannot be confirmed. We find the couplings to be obviously not well described by neither the CFT nor the CTM prediction. This corroborates our above conclusion that the BW-form of the EH as in the ansatz Eq. (4.49) does not apply to the bipartite ground state in the regions of Fig. 4.4.10 where $e_1 \gtrsim 10^{-7}$. Note that Figs. 4.4.12(c) and (f) are neighbouring data in Fig. 4.4.10 with the resolution of $\delta(1/\alpha) = 0.04$ we have chosen here. Hence, the reconstruction of the EH from the lowest-entanglement-energy state appears to be very sensitive to long-ranged interactions, although we have made sure the low-entanglement-energy spectral lines of the ground state are well-converged by utilising a maximum link dimension of up to $\chi_m = 450$ in the DMRG simulations for Figs. 4.4.10 and 4.4.11.

Finally, we wish to remark that the EH with an ansatz as a *local* operator, i.e. the ansatz of Eq. (4.49) with a long-range coupling limit of $M = 1$, consistently yields a phase diagram of the smallest eigenvalue e_1 of the corresponding correlation matrix C that is only reliably close to zero in a much smaller region confined to the line $1/\alpha \simeq 0$ than the ansatz Eq. (4.49) with at least $M \geq 5$ as was done for Fig. 4.4.10.

4.5 Discussion

In this chapter, we have shown that the entanglement properties, and more precisely the entanglement spectrum, are instrumental in determining both first-order and infinite-order phase transitions in a long-range quantum spin model. Specifically, we have shown that the entanglement spectrum combined with the RG analysis of the Luttinger liquid model contains sufficient inform-

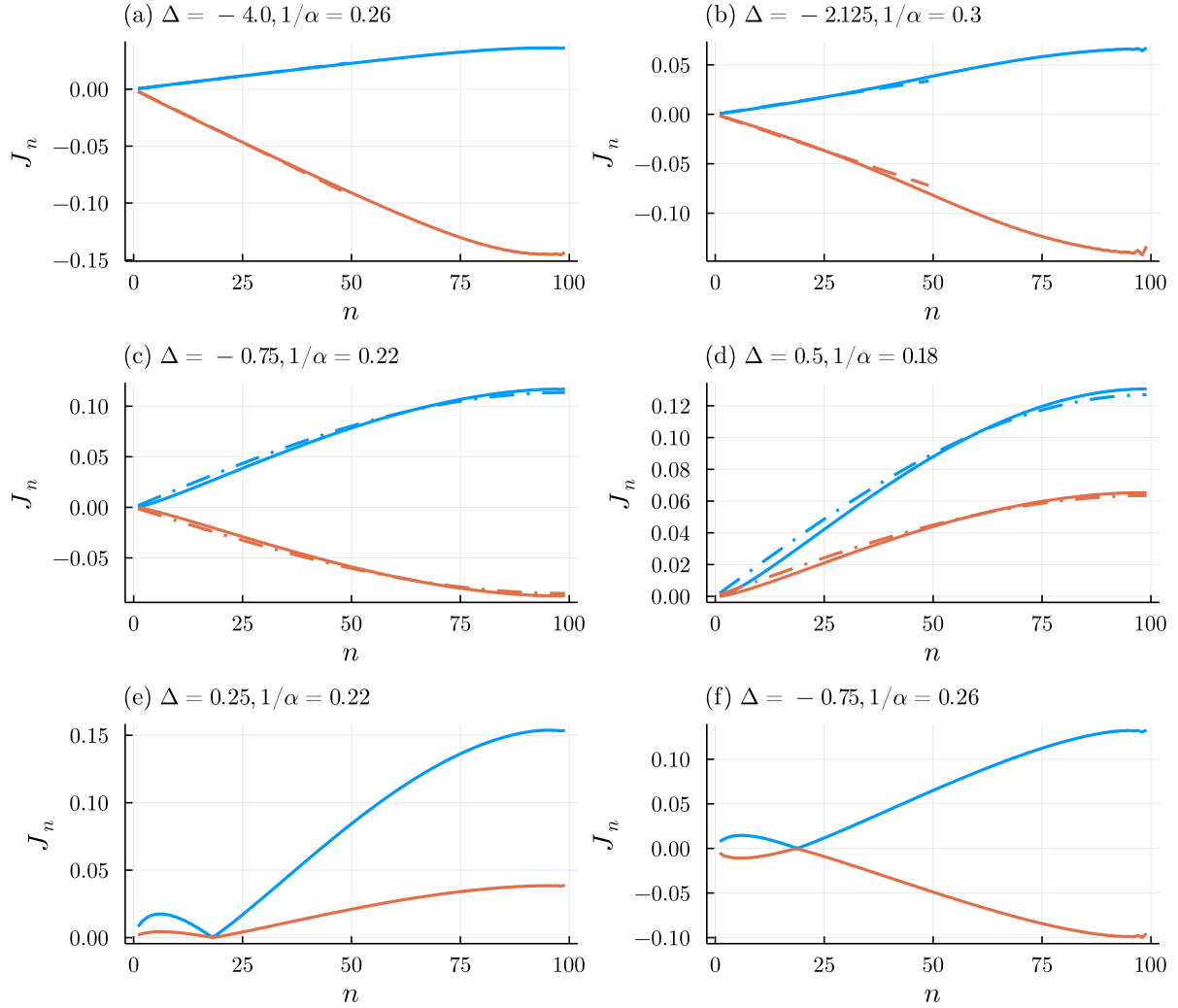


Figure 4.4.12: Collection of inferred couplings J_n defining the EH in Eq. (4.49). In all plots, the blue solid line represents J_n^{XY} while the solid orange line is J_n^{ZZ} . (a)–(d) are located in the bright blue region of Fig. 4.4.10 with $e_1 \ll 10^{-7}$. A dashed line marks a fitted CTM prediction in the AFM phase (Eq. (4.56)), and the fit to the CFT prediction in the SRXY phase (Eq. (4.55)) is shown as a dash-dotted line. (e) and (f) are in the dark blue region of Fig. 4.4.10 where $e_1 \gtrsim 10^{-7}$.

ation to fully determine the quantum phase diagram of the LRXXZ model, and locate the corresponding phase transitions in terms of the anisotropy and long-range parameters. In contrast, geometrical entanglement signals the AFM–SRXY and SRXY–FM transitions, reminiscent of the short-range XXZ model, but shows a smooth behaviour at the onset of genuine long-range effects, namely across the SRXY–LRXY transition. We have found that, within the XY phase, the entanglement spectrum exhibits a remarkable self-similarity, which allows us to map the long-range model onto its short-range counterpart. The latter can be exploited in combination with RG theory to locate the AFM–SRXY and SRXY–LRXY phase transitions from the breakdown of LL theory. The AFM, SRXY, and FM phases hence obtained are reminiscent of the short-range XXZ model, while the LRXY phase is characterised by emerging long-range effects and continuous symmetry breaking. The obtained phase diagram is in good agreement with our numerical calculations using tensor-network approaches, as well as with previous results.

We have further shown that the self-similarity identified in the entanglement properties extends to both the geometrical entanglement and the Luttinger parameter in the SRXY phase. In contrast, the speed of sound, which defines the energy scale of LL theory exhibits a different rescaling with the long-range parameter. Finally, we have checked the validity of LL theory by comparing estimates of the Luttinger parameter from various Rényi entropies and correlation functions, which all agree within the SRXY phase.

Lastly, we have shown the EH can be uniquely determined in large regions into the SRXY and AFM phase for significantly long-ranged interactions. In those regions, the EH follows the form of paradigm of the BW theorem—namely, near the bipartition site, it is given by a linear weighting of the system Hamiltonian density. On the other hand, the BW form of the entanglement Hamiltonian can be ruled out in the LRXY phase. Nevertheless, we found a departure of the BW-form of the EH when increasing the long-range interaction range before the above determined phase transition lines.

These results call for further studies of the entanglement properties of long-range quantum systems. A particularly important question would be to understand the origin of the self-similar rescaling found here from a microscopic point of view including effects beyond perturbation theory, and extend it to other quantum models as well as thermal equilibrium states. Similarly, whether the triple point, where SRXY, LRXY and AFM phase meet, is a robust feature beyond first order perturbation theory in RG remains to be understood. Furthermore, it remains an open question whether the early departure of the EH from a BW form is due to the DMRG ground state being ill-converged in entanglement entropy. Due to the rather large maximum link dimension employed here, we rather believe in a slow finite-size convergence of the entanglement properties, including the convergence of the smallest-entanglement-energy state, which possibly shifts the departure of the EH from the BW form closer to the determined phase transitions, similarly as is the case in the direction of the anisotropic coupling, cf. Appendix 4.C. Increasing the long-range coupling limit M in Eq. (4.51) may improve the inferred EH and move the apparent departure of the BW form closer to the phase transition into the LRXY phase. However, studying this was regrettably outside the scope of this thesis. We expect that the approach we use here can be straightforwardly extended to other short-range and long-range models. In this respect, we stress that the analysis of the entanglement spectrum is self-contained and does not rely on any previous knowledge of the

phase diagram. Degeneracy lifts are the primary signals of phase transitions and appear to be robust against finite-size effects. Other features, such as the Schmidt gap, may be more sensitive to finite-size effects but can be excluded using proper finite-scaling analysis. The approach developed here may also constitute a useful tool in studying out-of-equilibrium dynamics of many-body quantum systems with long-range interactions, which attracts significant attention [21, 31–34, 45, 48–50, 56, 99, 100, 172, 231].

Appendix

4.A FM-phase ground state analysis

In this appendix, we provide a simple argument showing that the ground state of the LRXXZ model in the FM phase ($\Delta \geq 1$) is a trivial, fully polarized, product state. Proofs at the spin-wave level are discussed in previous work, see for instance Refs. [223, 232]. Contrarily, we stay within the full spin description not linearising the Hamiltonian in bosonic form. Here we write the Hamiltonian (4.2) as

$$H_{\text{LRXXZ}} = \sum_{n \neq m} \frac{-J/2}{|n-m|^\alpha} (\vec{T}_{nm}^2 + (\Delta - 1)(T_{n,m}^z)^2) + \text{const}, \quad (4.57)$$

where we have introduced the two-site spin operator $\vec{T}_{nm} = \vec{S}_n + \vec{S}_m$, $T_{nm}^z = S_n^z + S_m^z$, and we have used the identities $\vec{S}_n^2 = S(S+1) = 3/4$ and $(S_n^z)^2 = 1$. Consider first the minimisation of the energy of each two-site term independently. Due to the ferromagnetic coupling, this corresponds to the maximization of the expectation value,

$$\langle \psi_{n,m} | \vec{T}_{nm}^2 + (\Delta - 1)(T_{nm}^z)^2 | \psi_{n,m} \rangle \longrightarrow \max_{\psi_{n,m}}. \quad (4.58)$$

The operator \vec{T}_{nm} represents a spin 0 or spin 1, and the quantity $\langle \vec{T}_{nm}^2 \rangle$ is maximized for spin 1. The expectation value $\langle (T_{nm}^z)^2 \rangle$ is also maximized for spin 1 states. Either of the product states $|T = 1, T_z = +1\rangle_{n,m} = |\uparrow\rangle_n \otimes |\uparrow\rangle_m$ or $|T = 1, T_z = -1\rangle_{n,m} = |\downarrow\rangle_n \otimes |\downarrow\rangle_m$ represent spin 1 with respect to \vec{T}_{nm} and maximize the pair term of Eq. (4.58) for $\Delta \geq 1$. It follows that either of the fully polarized states,

$$|\psi\rangle = \bigotimes_n |\uparrow\rangle_n, \quad (4.59)$$

$$\text{or } |\psi\rangle = \bigotimes_n |\downarrow\rangle_n, \quad (4.60)$$

jointly maximizes *all the pair terms* constituting the entire Hamiltonian, and consequently minimize H_{LRXXZ} . Note that for $\Delta < 1$, each pair is optimized by the antiferromagnetic state

$$|T = 1, T_z = 0\rangle_{n,m} = \frac{1}{\sqrt{2}} (|\uparrow\rangle_n \otimes |\downarrow\rangle_m + |\downarrow\rangle_n \otimes |\uparrow\rangle_m). \quad (4.61)$$

This yields to frustration when including all two-site terms and pairwise optimization for the entire Hamiltonian breaks down.

4.B Derivation of the Renormalisation group flow equations

In this appendix, we detail the derivation of the renormalisation group flow equations for the two interaction terms considered for the bosonic field description of the LRXXZ model. To this end, we consider the microscopic generating functional $Z = \exp(-S[\phi, \theta])$ with action $S[\phi, \theta] = S_0[\phi] - V_{ZZ}[\phi] - V_{LRXY}[\theta]$. Integrating out the fast moving modes in the momentum shell $d\ell$, we inspect how the coupling constants change under such an RG step. Firstly, we split the spacetime Fourier modes of both fields in slow and fast moving ones according to,

$$\phi(k) = \begin{cases} \phi_s(k) & \text{if } 0 \leq k \leq \Lambda(1 - d\ell) \\ \phi_f(k) & \text{if } \Lambda(1 - d\ell) < k \leq \Lambda \end{cases}, \quad (4.62)$$

$$\phi(k) = \phi_s(k) + \phi_f(k), \quad (4.63)$$

with k being the norm of the Fourier spacetime vector, and $d\ell$ the width of the spacetime momentum shell being integrated out. The analogous splitting applies to the field $\theta(k) = \theta_s(k) + \theta_f(k)$. Integrating out the fast moving modes $\phi_f(k)$, $\theta_f(k)$ yields,

$$\begin{aligned} Z = & \int \int D\phi_s D\phi_f D\theta_s D\theta_f \exp\left(-\int \left[\frac{1}{2}(\partial_\mu \phi_s)^2 + \frac{1}{2}(\partial_\mu \phi_f)^2\right] dt dx\right) \\ & \cdot \exp\left(-\frac{g_{ZZ}\Lambda^2}{2} \int \cos(\sqrt{16\pi}(\phi_s + \phi_f)) d\tau dx\right) \\ & \cdot \exp\left(-\frac{g_{LR}\Lambda}{2} \int \frac{(-1)^{(x-y)/a}}{|x-y|^\alpha} \cos(\sqrt{\pi}[\theta_s(t, x) - \theta_s(t, y) + \theta_f(t, x) - \theta_f(t, y)]) dt dx dy\right), \end{aligned} \quad (4.64)$$

where we identified $\Lambda = 1/(\pi a_c)$. Note that under the path integral the fields are only \mathbb{C} -numbers and thus commute. Next we expand $\cos(a + b) = \cos(a)\cos(b) - \sin(a)\sin(b)$ and ignore the terms proportional to $\sin(\phi_f)$ or $\sin(\theta_f)$ because they average to zero over the even path integral measure. Next, we recognize the expectation value with respect to the ground state of ϕ_f defined as

$$\langle A[\phi_f] \rangle = \int D\phi_f A[\phi_f] \exp(-S_0^f[\phi_f]) = \int D\phi_f A[\phi_f] \exp\left(-\frac{1}{(2\pi)^2} \int_{\Lambda(1-d\ell)}^\Lambda (p^\mu \phi_f)^2 d\mathbf{p}\right), \quad (4.65)$$

where the spacetime integral over the action only contains modes in the momentum shell of width $d\ell$. This allows us to write,

$$\begin{aligned} Z = & \int D\phi_s \exp\left(-\int \frac{1}{2}(\partial_\mu \phi_s)^2 d\tau dx\right) \times \left\langle \exp\left[-\frac{g_{ZZ}\Lambda^2}{2} \int \cos(\sqrt{16\pi}\phi_s) \cos(\sqrt{16\pi}\phi_f) d\tau dx\right] \right. \\ & \left. \times \exp\left[-\frac{g_{LR}\Lambda}{2} \int \frac{(-1)^{(x-y)/a}}{|x-y|^\alpha} \cos(\sqrt{\pi}[\theta_s(t, x) - \theta_s(t, y)]) \cos(\sqrt{\pi}[\theta_f(t, x) - \theta_f(t, y)]) dt dx dy\right] \right\rangle_f. \end{aligned} \quad (4.66)$$

The expression above is exact and would yield the full, non-perturbative picture of a renormalisation step. However, it is often unfeasible to compute $\langle e^A \rangle$ nonperturbatively. Instead, we take the

approach to introduce an approximation in the form of a first-order cumulant expansion, $\langle e^A \rangle \approx e^{\langle A \rangle}$, thereby ignoring higher order cross-terms of the interaction operators,

$$Z \approx \int D\phi_s \exp\left(-\int \frac{1}{2}(p^\mu \phi_s)^2 \frac{d^2 p}{(2\pi)^2}\right) \times \exp\left(-\frac{g_{ZZ}\Lambda^2}{2} \int \cos(\sqrt{16\pi}\phi_s) \langle \cos(\sqrt{16\pi}\phi_f) \rangle_f \frac{d^2 p}{(2\pi)^2}\right) \\ \times \exp\left(-\frac{g_{LR}\Lambda}{2} \int \frac{(-1)^{(x-y)/a}}{|x-y|^\alpha} \cos(\sqrt{\pi}[\theta_s(t,x) - \theta_s(t,y)]) \langle \cos(\sqrt{\pi}[\theta_f(t,x) - \theta_f(t,y)]) \rangle_f dt dx dy\right). \quad (4.67)$$

To evaluate the expectation value of a trigonometric function of the fields, we use below identity [216],

$$e^A \cdot e^B = :e^{A+B}: e^{\langle AB \rangle + \frac{1}{2}\langle A^2 + B^2 \rangle}, \quad (4.68)$$

where $:A:$ is the normal ordering of A . It follows as a corollary from the Baker–Campbell–Hausdorff formula when $[A, B]$ commutes with A and B . Note that we have by definition $:A:|0\rangle = 0$ implying $\langle : \exp(A) : \rangle = 1$. Using Eq. (4.68) and setting $B = 0$ and $A = i\beta X$, we find

$$\langle e^{i\beta X} \rangle = e^{-\frac{1}{2}\beta^2 \langle X^2 \rangle}, \quad \text{implying} \quad \langle \cos(\beta X) \rangle = e^{-\frac{1}{2}\beta^2 \langle X^2 \rangle}. \quad (4.69)$$

We thus find

$$\langle \cos(\sqrt{16\pi}\phi_f) \rangle_f = \exp\left[-8\pi \langle \phi_f^2 \rangle_f\right] \quad (4.70)$$

and

$$\langle \cos(\sqrt{\pi}[\theta_f(t,x) - \theta_f(t,y)]) \rangle_f = \exp\left[-\frac{\pi}{2} \langle [\theta_f(t,x) - \theta_f(t,y)]^2 \rangle_f\right]. \quad (4.71)$$

Equation (4.70) is readily evaluated as [216]

$$\langle \cos(\sqrt{16\pi}\phi_f) \rangle_f = \exp\left[-8\pi \langle \phi_f^2 \rangle_f\right] = \exp\left[-8\pi \frac{1}{(2\pi)^2} \int_{\Lambda(1-d\ell)}^\Lambda D_\phi(\mathbf{p}) d^2\mathbf{p}\right] \\ = \exp\left[-8\pi \frac{1}{(2\pi)^2} \int_{\Lambda(1-d\ell)}^\Lambda \frac{K}{p^2} p dp \int_0^{2\pi} d\varphi\right] = \exp\left[-4K \ln\left(\frac{\Lambda}{\Lambda(1-d\ell)}\right)\right] = 1 - 4K d\ell. \quad (4.72)$$

Upon rescaling with $s = \Lambda/\Lambda'$ and $\Lambda' = (1 - d\ell)\Lambda$, the spacetime integral measure reads $d^2\mathbf{x} = s^2 d^2\mathbf{x}' = (1 + 2d\ell) d^2\mathbf{x}'$. With this result, we conclude that one RG step yields the RG flow equation for g_{ZZ} up to first order perturbation theory (omitting to prime new variables),

$$\frac{g_{ZZ}\Lambda^2}{2} \int d^2\mathbf{x} \cos(\sqrt{16\pi}\phi(\mathbf{x})) \rightarrow \frac{g_{ZZ}\Lambda^2}{2} (1 + (2 - 4K) d\ell) \int d^2\mathbf{x} \cos(\sqrt{16\pi}\phi(\mathbf{x})). \quad (4.73)$$

Hence, we find

$$\frac{dg_{ZZ}}{dl} = (2 - 4K)g_{ZZ}, \quad (4.74)$$

which is Eq. (4.34) in the main text.

Equation (4.71) is similarly evaluated as the connected two-point equal-time correlation function. With the use of the symmetry of S_0 under the duality transformation $\phi \rightarrow \theta$, $K \rightarrow 1/K$, $D_\phi(p) \rightarrow D_\theta(p) = K^{-1}p^{-2}$, Eq. (4.71) yields [6, 216, 218],

$$\langle \cos(\sqrt{\pi}[\theta_f(t, x) - \theta_f(t, y)]) \rangle_f = \exp\left[-\frac{\pi}{2} \langle [\theta_f(t, x) - \theta_f(t, y)]^2 \rangle_f\right] \quad (4.75)$$

$$= \exp\left[-\frac{\pi}{2} \int_{|x-y| \gg a} \langle \theta_f(\mathbf{p})\theta_f(\mathbf{q}) \rangle_f (e^{i\mathbf{p}\mathbf{x}} - e^{i\mathbf{p}\mathbf{y}})(e^{i\mathbf{q}\mathbf{x}} - e^{i\mathbf{q}\mathbf{y}}) d^2\mathbf{p} d^2\mathbf{q}\right] \quad (4.76)$$

$$= \exp\left[-\frac{\pi}{2} \frac{1}{(2\pi)^2} \int_{\Lambda(1-d\ell)}^\Lambda D_\theta(p)\delta(\mathbf{p} + \mathbf{q})(e^{i\mathbf{p}\mathbf{x}} - e^{i\mathbf{p}\mathbf{y}})(e^{i\mathbf{q}\mathbf{x}} - e^{i\mathbf{q}\mathbf{y}}) d^2\mathbf{p} d^2\mathbf{q}\right] \quad (4.77)$$

$$= \exp\left[-\frac{\pi}{2} \frac{1}{2\pi} \int_{\Lambda(1-d\ell)}^\Lambda 2D_\theta(p)[1 - \cos(p\|\mathbf{x} - \mathbf{y}\|)]p dp\right] \quad (4.78)$$

$$= \exp\left[-\frac{1}{2K} \ln\left(\frac{\Lambda}{\Lambda(1-d\ell)}\right)\right] = 1 - \frac{d\ell}{2K}. \quad (4.79)$$

Here above we ignored the integral over the cosine since its frequency oscillations are large $\|\mathbf{x} - \mathbf{y}\| \gg a$ compared to the modes considered for $p \simeq \Lambda = 1/a$, and it thus averages out under the integral. In the case of g_{LRXY} , the spacetime integral measure transforms as $dt dy dx = s^3 dt' dy' dx' = (1 + 3d\ell) dt' dy' dx'$ while the long-range interaction potential scales as $|x - y|^{-\alpha} = s^{-\alpha}|x' - y'|^{-\alpha} = (1 - \alpha d\ell)|x' - y'|^{-\alpha}$. Therefore, the RG step and RG flow equation for the long-range XY operator yield (omitting to prime new variables),

$$-\frac{g_{LR}\Lambda}{2} \int \frac{\cos(\sqrt{\pi}[\theta(t, x) - \theta(t, y)])}{|x - y|^\alpha} \rightarrow -\frac{g_{LR}\Lambda}{2} \left(1 + \left(3 - \alpha - \frac{1}{2K}\right)d\ell\right) \int \frac{\cos(\sqrt{\pi}[\theta(t, x) - \theta(t, y)])}{|x - y|^\alpha}, \quad (4.80)$$

and

$$\frac{dg_{LRXY}}{dl} = \left(3 - \alpha - \frac{1}{2K}\right)g_{LRXY}, \quad (4.81)$$

which is Eq. (4.35) in the main text.

4.C Finite-size scaling

In this appendix, we examine the finite-size scaling of the bare observables on the MPS ground state. To this end, we showcase the explicit finite-size scaling of the short-range ($\alpha^{-1} = 0$) and a long-range ($\alpha^{-1} = 0.5$) case for the geometric entanglement as well as the entanglement spectrum. The

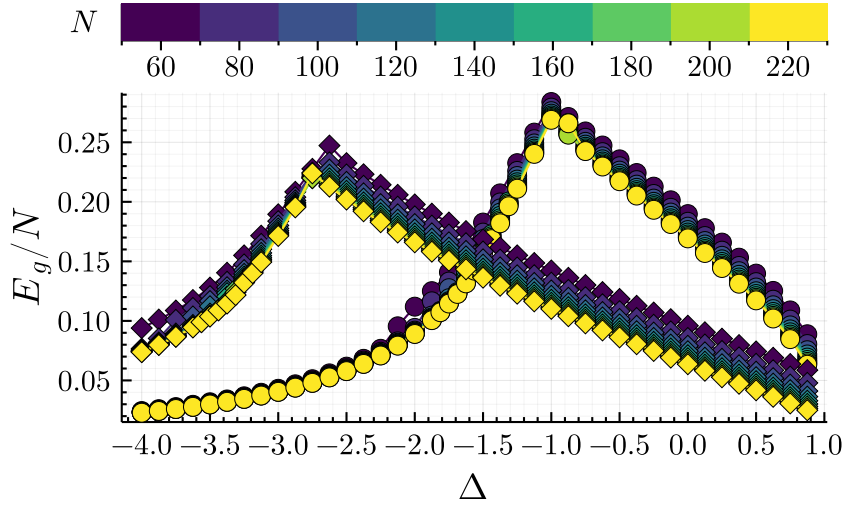


Figure 4.C.1: Geometric entanglement density E_g/N over the anisotropic parameter Δ for $\alpha^{-1} = 0$ (coloured circles) and $\alpha^{-1} = 0.5$ (coloured diamonds) whereas the colour corresponds to system size indicated in colour bar above.

same qualitative behaviour and convergence are found for all other α^{-1} considered in the main text too. Here, we inspect system sizes $N = [60, 80, \dots, 220]$. As illustrated in Figure 4.C.1, the GE is well converged in system size for $N \geq 160$ for all considered values of α^{-1} . The finite-size scaling of the entanglement spectrum is showcased in Fig. 4.C.2. Although we observe the ES being moderately well converged for the largest system sizes and large entanglement energies, the degeneracy lift signalling the AFM-XY phase transition is very well converged as are the low entanglement energy lines, cf. red diamonds in Fig. 4.C.2. The Schmidt gap, defined as the difference $\xi_2 - \xi_1$, has a local minimum which is marked by the green diamonds in Fig. 4.C.2, which directly corresponds to a local maximum in the entanglement entropy. Furthermore, this local minimum coincides with a second lift of the apparent degeneracy of $\xi_3 = \xi_4$. We refer to this region between the local minimum of the Schmidt gap and the lift of the degeneracy $\xi_2 = \xi_3$ as the crossover regime in the main text. Figure 4.C.3 shows the finite-size convergence of these independent signals and the size of the crossover regime. In the short-range case, the two signals locate the QPT at the same position for all system sizes considered (blue data in Fig. 4.C.3). Contrarily, we find the degeneracy lift being converged much earlier in system size compared to the local maximum of E_g/N when considering longer ranged interactions, cf. orange data in Fig. 4.C.3. Furthermore, we observe a very slow convergence of the crossover regime in system size, cf. crosses in Fig. 4.C.3, consistently with previous studies of slow finite-size convergence of the entanglement entropy convergence of the (short-range) XXZ model [203, 204].

4.D Optimization of self-similar rescaling parameters

To obtain the optimal self-similar rescaling parameters for the ES, we proceed as follows. We first consider each spectral line as a function of the anisotropy parameter, $\xi_j = \xi_j(\Delta)$ and rescale the argument as $\Delta \rightarrow \tilde{\Delta}(\gamma, \nu)$ following Eq. (4.41). The rescaling parameters $\gamma(\alpha)$ and $\nu(\alpha)$ depend on the anisotropy parameter α , and we have the fixed point $\tilde{\Delta}(\alpha = \infty) = \Delta$. We compute the ES of the

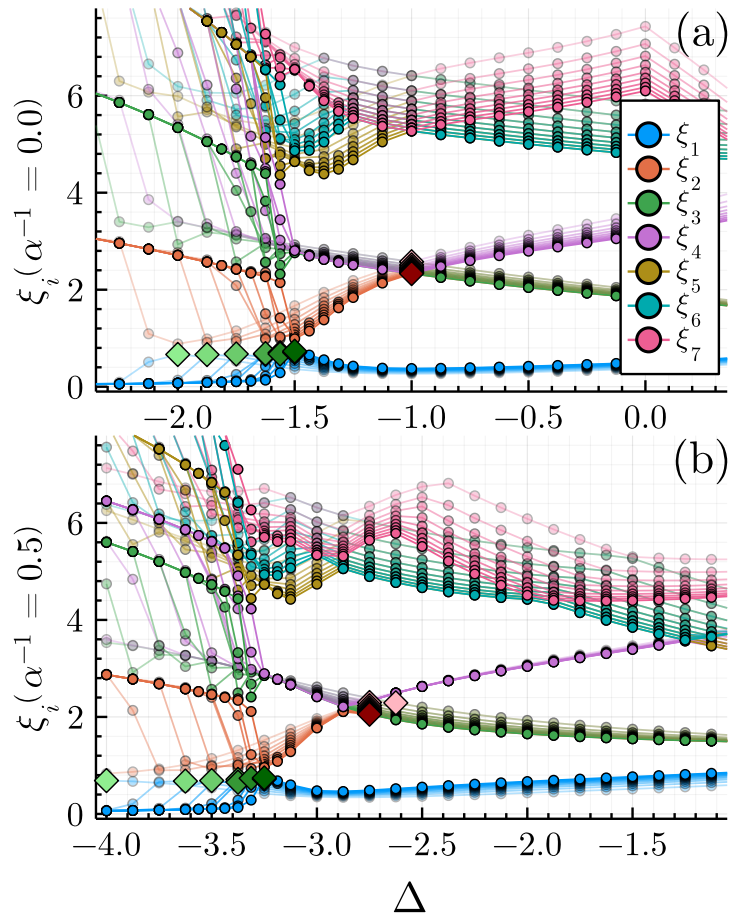


Figure 4.C.2: Finite-size scaling of the first seven entanglement energies $\{\xi_j\}$ for (a) $\alpha^{-1} = 0$ and (b) $\alpha^{-1} = 0.5$. The transparency of each line decreases with the system size from $N = 60$ (70% transparency) to $N = 220$ (0% transparency). The size step is $\Delta N = 20$. The degeneracy lift is marked by the red diamonds for each system size (light red $N = 60$, dark red $N = 220$), and the minimum of the Schmidt gap ($\xi_2 - \xi_1$) is marked by green diamonds for the corresponding system size (light green $N = 60$, dark green $N = 220$).

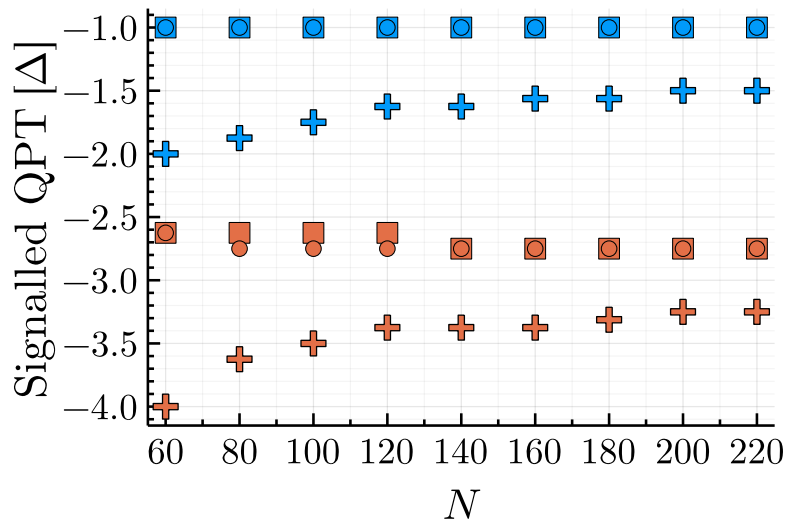


Figure 4.C.3: Position of AFM-XY quantum phase transition (QPT) in values of the anisotropy coupling Δ versus system sizes N as found from the degeneracy lift in the ES (circles), from the maximum of the GE (squares), and from the local minimum of the Schmidt gap ($\xi_2 - \xi_1$, crosses). Blue and orange markers correspond to $\alpha^{-1} = 0$ and $\alpha^{-1} = 0.5$, respectively.

MPS ground state for a discrete set of values of the anisotropy parameter, $\Delta_d = -4, -3.875, \dots 1.5$ and interpolate linearly each spectral line. The scaling parameters $\gamma(\alpha)$ and $\nu(\alpha)$ are then fitted in order to minimize the quadratic weight function over a few (here 4) low-lying spectral lines,

$$W(\gamma, \nu) = \sum_{1 \leq j \leq 4} \int_{\tilde{\Delta}_i}^{\tilde{\Delta}_f} d\tilde{\Delta} [\xi_j(\tilde{\Delta}(\gamma, \nu), \alpha) - \xi_j(\Delta, \alpha = \infty)]^2, \quad (4.82)$$

where we vary the integral boundaries $\tilde{\Delta}_i, \tilde{\Delta}_f$ over a set of four different pairs of lower and upper integral boundaries $(\tilde{\Delta}_i, \tilde{\Delta}_f) = [(-1.5, 0.0), (-1.25, -0.5), (-1.25, 0.5), (-2, 0.5)]$ such as to optimize the rescaling over a broad region including the AFM-XY transition, at $\tilde{\Delta} = -1$. We then infer the value of the rescaling parameters γ and ν from the average over the four samples of different integration intervals and estimate its error from the standard deviation. The result is shown in Fig. 4.4.4 The numerical optimization is performed with the Julia package `Optim.jl` [233].

5 *Conclusions and outlook*

In this thesis, we have studied the effects of long-range interactions that fall off with the relative distance R between two constituents as $1/R^\alpha$ on both in-equilibrium and out-of-equilibrium features of spin chains through complementary analytical and numerical methods. The two main works are focused on the emergence of causality during out-of-equilibrium dynamics in the long-range interacting transverse-field Ising (LRTI) chain, and the entanglement properties of and its role in the ground state of the long-range interacting XXZ (LRXXZ) model. Specifically, we have investigated the emergence of causality through studying the spreading of correlations and information in the LRTI chain. The out-of-equilibrium dynamics were induced by homogeneous global quenches after which we inspected correlation spreading, as well as inhomogeneous local quenches after which we inspected local magnetisation and entanglement entropy spreading. We showed the theoretical framework of the quasiparticle picture is matching the twofold nature of correlation and local magnetisation spreading in state-of-the-art tensor-network simulations. In the former, we employed a linear spin wave approximation applicable to both short- and long-range interacting D -dimensional lattice models. In the latter, the two characteristic features close to the signal front, the signal's edge and the signal's local maxima, are excellently explained by the quasiparticle picture. Furthermore, these two edges follow a generic algebraic power-law relation in a spacetime diagram, i.e. $t \propto R^\beta$, whereas the analytical prediction of the dynamical exponent's functional behaviour with the long-range interaction exponent, $\beta(\alpha)$, is very well matching the data from our tensor-network simulations. While entanglement spreading following an inhomogeneous local quench does not display a twofold nature, the unique signal front and the constant ballistic behaviour of the corresponding dynamical exponent, $\beta(\alpha) = 1$, irrespective of the interaction range are predicted by our extensions of the quasiparticle picture and very well match the simulations.

In particular, we investigated the emergence of causality in the local as well as the intermediate quasi-local regime. First, in the quasi-local regime, long-range interactions fall off slowly enough such that the quasiparticle group velocity acquires a non-analyticity in the Brillouin zone. There, the quasiparticle picture, together with stationary phase approximations, allows for predictions of all dynamical exponents of correlations, local magnetisation, and entanglement entropies as a function of the long-range exponent, $\beta(\alpha)$, which are well-matched by our tensor-network simulations. The emergent causal edges of corrections and local magnetisation propagate with the same sub-ballistic dynamical exponent, $\beta_{\text{CE}} = \beta_{\text{SE}} > 1$. However, local maxima in the vicinity of the causal edge propagate ballistically in the case of corrections, $\beta_m < 1$, while those of the local magnetisation propagate super-ballistically, $\beta_m < 1$. Second, in the local regime, long-range interactions fall off fast enough such that the quasiparticles' group velocity is analytic over the entire Brillouin zone. There, a qualitative difference to the short-range limit is neither predicted by the quasiparticle picture nor found in our tensor-network simulation. We observe an emergent form of

causality analogous to the short-range interacting limit where the maximum group velocity determines the signal edge, while the inner extrema close to the edge propagate with the phase velocity corresponding to the quasi-momentum where the group velocity is maximum.

The distinction of the two signals—the enclosing signal edge and local maxima—is not only crucial regarding the emergence of a causal cone but also provides a unique fingerprint of the distinct dynamical regimes of the LRTI model. This suggests the emergence of a *dynamical phase diagram* where in the intermediate quasi-local regime a weak form of causality emerges characterised by algebraic power-laws $t \propto R^\beta$ with dynamical exponents β depending on the observable and the range of interaction.

Contrarily, the causal edge of all Rényi entropies propagates ballistically in both the local regime and the quasi-local regime where it is notably faster than the sub-ballistic local magnetisation. The interior of the causal region being without marked features, and the saturation of all entanglement entropies to $\log(2)$ is both excellently predicted by the quasi-particle picture. For the latter, the two orthogonal elementary states describing the initial state after the inhomogeneous local quench become maximally entangled.

We furthermore investigated in this thesis the entanglement properties of and its role in the long-range interacting XXZ (LRXXZ) model. We have shown that through studying the entanglement spectrum one can determine both first-order and infinite-order quantum phase transitions in the phase diagram of the long-range XXZ model. In the XY phase, we have found the entanglement spectrum to exhibit a remarkable self-similarity which allows us to map the long-range model onto its short-range counterpart. This self-similarity together with the renormalisation group analysis of the corresponding effective field theory, a Luttinger liquid, can be exploited to form a synergetic prediction locating the phase transition from the Luttinger liquid (SRXY) phase into the antiferromagnetic (AFM) phase as well as the transition into the long-range XY (LRXY) phase which marks the onset of genuine long-range effects. Crucially, the self-similarity extends to the Luttinger parameter, and also applies to the geometric entanglement. However, while the geometric entanglement signals the AFM–SRXY and the SRXY–FM transitions, thereby paralleling its behaviour in the short-range limit, its signal is smooth across the SRXY–LRXY transition. Furthermore, we have shown the entanglement Hamiltonian in large parts of the AFM and SRXY phases is uniquely identified to follow the form of the Bisognano–Wichmann theorem while such a form can be ruled out in the LRXY phase.

The obtained AFM, FM, and SRXY phases are analogous to the three phases of the short-range XXZ model. Through our observed self-similarity, the SRXY phase in the long-range case is indeed identical to its short-range limit with respect to entanglement features in form of the entanglement spectrum and the geometric entanglement. On the other hand, the LRXY phase is characterised by the onset of long-range effects and continuous symmetry breaking. Moreover, the predicted phase diagram is in good agreement with our data simulated through DMRG.

Outlook Our results concerning the out-of-equilibrium dynamics of the long-range transverse-field Ising model prompt several perspectives of research, both experimentally and theoretically. The verification of our results on experimental quantum simulators would be timely as new larger scale platforms with more qubits of the order of the system size inspected in our simulations are nowadays accessible, in particular trapped ions in optical lattices [96], and Rényi entropies have now been measured in those platform [180, 181] and other noisy intermediate-scale quantum devices [182]. Among the theoretical perspectives, an interesting direction constitutes the extension of the generic quasiparticle picture for out-of-equilibrium dynamics to fermionic lattice models. The use of mean-field approximations and Bogolyubov theory to generically describe the out-of-equilibrium dynamics of a fermionic lattice model up to quadratic terms is fundamentally similar to the existing approach through bosonic Holstein–Primakoff approximations such that it could be readily studied in the (possibly long-range) XXZ model, and the Hubbard model. As another perspective serves the study of open quantum systems being coupled to an environment and the investigation how these behave differently compared to its closed counterpart. Further perspectives are offered through the lens of quantum information and the study of entanglement entropy and its role on the early- and late-time dynamics towards thermal equilibration particularly in the context of long-range interacting systems. As we have shown in the context of the long-range Ising model, entanglement entropies are propagating faster than local magnetisations in the quasi-local regime. It remains an debated question how long-range interactions influence the equilibration towards thermal equilibrium.

The results of our study of the long-range XXZ model suggest several future directions. Of particular importance to us would be to understand the origin of the self-similar rescaling of the entanglement properties and the Luttinger parameter from a microscopic point of view. This calls for further theoretical studies including effects beyond perturbation theory which could possibly be inspired by functional renormalisation group techniques as well as similar techniques applicable to the integrable Haldane–Shastry model [234–236], which is the special case of the LRXXZ Hamiltonian (4.2) at $\Delta = -1, \alpha = 2$. Similarly, it remains to be understood whether the triple point where SRXY, LRXY and AFM phase meet within the approximation of our analysis and the accuracy of our numerical calculations, is a robust feature both beyond first-order perturbation theory in the RG analysis, and more detailed numerical studies in this neighbourhood. Furthermore, it remains an open question whether the entanglement Hamiltonian follows the Bisognano–Wichmann theorem’s form of a linear weighting of the system Hamiltonian’s density over the entire phases which are reminiscent of their short-range counterpart, namely the AFM phase and the SRXY phase. Additional numerical investigations could verify this author’s hypothesis that the entanglement properties of the LRXXZ model converge slowly with system size and finite-size effects shift their deceptive signal not only in the direction of anisotropic coupling as was shown in Appendix 4.C, but also in the direction of the long-range interaction exponent. Moreover, we expect the study of the entanglement spectrum and its signals of phase transitions, namely degeneracy lifts and divergence of the Schmidt gap, can be transferred to other lattice models, both short-range and long-range interacting. Lastly and to link to the perspectives following our out-of-equilibrium results, studying the dynamical features

of the LRXXZ model with the approach taken here may prove fruitful. The operator form of the EH may shed new light onto the behaviour and features of the subsystem. Similarly, the operator form may allow for a physically intuitive interpretation of entanglement features through a thermodynamic picture considering the general form $\rho_A = \exp(-\tilde{H}_A)$. Specifically, the investigation of the entanglement spectrum and more generally the entanglement Hamiltonian following out-of-equilibrium dynamics may yield a novel window into the mechanism of thermal equilibration, or the lack thereof in integrable models and non-ergodic phases of disordered systems.

Bibliography

- 1.J. I. Cirac and P. Zoller, ‘Goals and opportunities in quantum simulation’, [Nature Physics](#) **8**:4, 264–266 (2012) (cit. on pp. 6, 15).
- 2.L. Sanchez-Palencia, ‘Quantum simulation: From basic principles to applications: Foreword’, [Comptes Rendus Physique, Quantum Simulation / Simulation Quantique](#) **19**:6, 357–364 (2018) (cit. on pp. 6, 15).
- 3.J. Preskill, ‘Quantum Computing in the NISQ era and beyond’, [Quantum](#) **2**, 79 (2018) (cit. on p. 6).
- 4.B. Zeng, X. Chen, D.-L. Zhou, and X.-G. Wen, *Quantum Information Meets Quantum Matter: From Quantum Entanglement to Topological Phases of Many-Body Systems*, Quantum Science and Technology, Springer New York, New York, NY, 2019 (cit. on pp. 6, 18).
- 5.J. I. Cirac, D. Pérez-García, N. Schuch, and F. Verstraete, ‘Matrix product states and projected entangled pair states: Concepts, symmetries, theorems’, [Reviews of Modern Physics](#) **93**:4, 045003 (2021), [arXiv:2011.12127](#) (cit. on pp. 6, 7, 18, 19, 23, 25, 34, 45, 57).
- 6.T. Giamarchi, *Quantum Physics in One Dimension*, Oxford University Press, 18th2003 (cit. on pp. 6, 89–91, 93–96, 108, 110, 122).
- 7.F. D. M. Haldane, ‘‘Luttinger liquid theory’’ of one-dimensional quantum fluids. I. Properties of the Luttinger model and their extension to the general 1D interacting spinless Fermi gas’, [Journal of Physics C: Solid State Physics](#) **14**:19, 2585–2609 (1981) (cit. on p. 6).
- 8.F. D. M. Haldane, ‘Effective Harmonic-Fluid Approach to Low-Energy Properties of One-Dimensional Quantum Fluids’, [Physical Review Letters](#) **47**:25, 1840–1843 (1981) (cit. on p. 6).
- 9.S. Coleman, ‘Quantum sine-Gordon equation as the massive Thirring model’, [Physical Review D](#) **11**:8, 2088–2097 (1975) (cit. on p. 6).
- 10.H. Bethe, ‘Zur theorie der metalle’, [Zeitschrift für Physik](#) **71**:3, 205–226 (1931) (cit. on p. 7).
- 11.V. E. Korepin, N. M. Bogoliubov, and A. G. Izergin, *Quantum inverse scattering method and correlation functions*, Vol. 3, Cambridge University Press, 1997 (cit. on p. 7).
- 12.M. Troyer and U.-J. Wiese, ‘Computational Complexity and Fundamental Limitations to Fermionic Quantum Monte Carlo Simulations’, [Physical Review Letters](#) **94**:17, 170201 (2005) (cit. on p. 7).
- 13.J. W. Gibbs, *Elementary principles of statistical mechanics developed with especial reference to the rational foundation of thermodynamics*, C. Scribner’s sons, 1902 (cit. on p. 8).
- 14.L. D. Landau, ‘Zur theorie der phasenumwandlungen ii’, [Phys. Z. Sowjetunion](#) **11**:545, 26–35 (1937) (cit. on p. 9).

15. V. L. Ginzburg and L. D. Landau, ‘On the Theory of Superconductivity’, in *On Superconductivity and Superfluidity: A Scientific Autobiography*, edited by V. L. Ginzburg, Springer, Berlin, Heidelberg, 2009, pp. 113–137 (cit. on p. 9).
16. S. Sachdev, *Quantum Phase Transitions*, 2nd ed., Cambridge University Press, Cambridge, 2011 (cit. on pp. 10, 87, 89, 91).
17. J. Eisert, M. Friesdorf, and C. Gogolin, ‘Quantum many-body systems out of equilibrium’, *Nature Physics* **11**:2, 124–130 (2015) (cit. on p. 12).
18. P. Calabrese and J. Cardy, ‘Time Dependence of Correlation Functions Following a Quantum Quench’, *Physical Review Letters* **96**:13, 136801 (2006) (cit. on pp. 12, 13, 77).
19. M. A. Cazalilla, ‘Effect of Suddenly Turning on Interactions in the Luttinger Model’, *Physical Review Letters* **97**:15, 156403 (2006) (cit. on p. 12).
20. A. Iucci and M. A. Cazalilla, ‘Quantum quench dynamics of the Luttinger model’, *Physical Review A* **80**:6, 063619 (2009) (cit. on p. 12).
21. D. V. Else, F. Machado, C. Nayak, and N. Y. Yao, ‘Improved Lieb-Robinson bound for many-body Hamiltonians with power-law interactions’, *Physical Review A* **101**:2, 022333 (2020) (cit. on pp. 12, 14, 61, 117).
22. E. H. Lieb and D. W. Robinson, ‘The finite group velocity of quantum spin systems’, *Communications in Mathematical Physics* **28**:3, 251–257 (1972) (cit. on pp. 12, 64).
23. M. B. Hastings and T. Koma, ‘Spectral Gap and Exponential Decay of Correlations’, *Communications in Mathematical Physics* **265**:3, 781–804 (2006) (cit. on pp. 13, 14, 61, 64).
24. A. M. Läuchli and C. Kollath, ‘Spreading of correlations and entanglement after a quench in the one-dimensional Bose–Hubbard model’, *Journal of Statistical Mechanics: Theory and Experiment* **2008**:05, P05018 (2008) (cit. on pp. 13, 14).
25. M. Cheneau, P. Barmettler, D. Poletti, M. Endres, P. Schauß, T. Fukuhara, C. Gross, I. Bloch, C. Kollath, and S. Kuhr, ‘Light-cone-like spreading of correlations in a quantum many-body system’, *Nature* **481**:7382, 484–487 (2012) (cit. on pp. 13, 14).
26. T. Fukuhara, P. Schauß, M. Endres, S. Hild, M. Cheneau, I. Bloch, and C. Gross, ‘Microscopic observation of magnon bound states and their dynamics’, *Nature* **502**:7469, 76–79 (2013) (cit. on pp. 13, 14).
27. R. Geiger, T. Langen, I. E. Mazets, and J. Schmiedmayer, ‘Local relaxation and light-cone-like propagation of correlations in a trapped one-dimensional Bose gas’, *New Journal of Physics* **16**:5, 053034 (2014) (cit. on pp. 13, 14).
28. S. R. Manmana, S. Wessel, R. M. Noack, and A. Muramatsu, ‘Time evolution of correlations in strongly interacting fermions after a quantum quench’, *Physical Review B* **79**:15, 155104 (2009) (cit. on pp. 13, 14, 79).
29. P. Barmettler, D. Poletti, M. Cheneau, and C. Kollath, ‘Propagation front of correlations in an interacting Bose gas’, *Physical Review A* **85**:5, 053625 (2012) (cit. on pp. 13, 14).

- 30.G. Carleo, F. Becca, L. Sanchez-Palencia, S. Sorella, and M. Fabrizio, ‘Light-cone effect and supersonic correlations in one- and two-dimensional bosonic superfluids’, *Physical Review A* **89**:3, 031602 (2014) (cit. on pp. 13, 14).
- 31.J. Despres, L. Villa, and L. Sanchez-Palencia, ‘Twofold correlation spreading in a strongly correlated lattice Bose gas’, *Scientific Reports* **9**:1, 4135 (2019) (cit. on pp. 13, 14, 60, 62, 63, 117).
- 32.L. Cevolani, G. Carleo, and L. Sanchez-Palencia, ‘Protected quasilocality in quantum systems with long-range interactions’, *Physical Review A* **92**:4, 041603 (2015) (cit. on pp. 13, 14, 61, 63, 79, 117).
- 33.L. Cevolani, G. Carleo, and L. Sanchez-Palencia, ‘Spreading of correlations in exactly solvable quantum models with long-range interactions in arbitrary dimensions’, *New Journal of Physics* **18**:9, 093002 (2016) (cit. on pp. 13, 14, 63–65, 117).
- 34.L. Cevolani, J. Despres, G. Carleo, L. Tagliacozzo, and L. Sanchez-Palencia, ‘Universal scaling laws for correlation spreading in quantum systems with short- and long-range interactions’, *Physical Review B* **98**:2, 024302 (2018) (cit. on pp. 13, 59–64, 66, 76, 79, 82, 85, 117).
- 35.T. Dauxois, S. Ruffo, E. Arimondo, and M. Wilkens, ‘Dynamics and Thermodynamics of Systems with Long-Range Interactions: An Introduction’, in *Dynamics and Thermodynamics of Systems with Long-Range Interactions*, edited by T. Dauxois, S. Ruffo, E. Arimondo, and M. Wilkens, Springer, Berlin, Heidelberg, 2002, pp. 1–19 (cit. on p. 14).
- 36.M. Kastner, ‘Nonequivalence of ensembles in the Curie–Weiss anisotropic quantum Heisenberg model’, *Journal of Statistical Mechanics: Theory and Experiment* **2010**:07, P07006 (2010) (cit. on p. 14).
- 37.M. Kastner, ‘Nonequivalence of Ensembles for Long-Range Quantum Spin Systems in Optical Lattices’, *Physical Review Letters* **104**:24, 240403 (2010) (cit. on p. 14).
- 38.W. Thirring, ‘Systems with negative specific heat’, *Zeitschrift für Physik A Hadrons and nuclei* **235**:4, 339–352 (1970) (cit. on p. 14).
- 39.N. D. Mermin and H. Wagner, ‘Absence of Ferromagnetism or Antiferromagnetism in One- or Two-Dimensional Isotropic Heisenberg Models’, *Physical Review Letters* **17**:22, 1133–1136 (1966) (cit. on p. 14).
- 40.P. C. Hohenberg, ‘Existence of Long-Range Order in One and Two Dimensions’, *Physical Review* **158**:2, 383–386 (1967) (cit. on p. 14).
- 41.D. Peter, S. Müller, S. Wessel, and H. P. Büchler, ‘Anomalous behaviour of Spin Systems with Dipolar Interactions’, *Physical Review Letters* **109**:2, 025303 (2012) (cit. on p. 14).
- 42.J. Eisert, M. Cramer, and M. B. Plenio, ‘Colloquium: Area laws for the entanglement entropy’, *Reviews of Modern Physics* **82**:1, 277–306 (2010) (cit. on pp. 14, 19, 24, 25).
- 43.T. Koffel, M. Lewenstein, and L. Tagliacozzo, ‘Entanglement Entropy for the Long-Range Ising Chain in a Transverse Field’, *Physical Review Letters* **109**:26, 267203 (2012) (cit. on pp. 14, 63).
- 44.A. Cadarso, M. Sanz, M. M. Wolf, J. I. Cirac, and D. Pérez-García, ‘Entanglement, fractional magnetization, and long-range interactions’, *Physical Review B* **87**:3, 035114 (2013) (cit. on p. 14).

45. J. Schachenmayer, B. P. Lanyon, C. F. Roos, and A. J. Daley, 'Entanglement Growth in Quench Dynamics with Variable Range Interactions', *Physical Review X* **3**:3, 031015 (2013) (cit. on pp. 14, 61, 79, 117).
46. T. Kuwahara and K. Saito, 'Area law of noncritical ground states in 1D long-range interacting systems', *Nature Communications* **11**:1, 1–7 (2020) (cit. on pp. 14, 25).
47. L. Villa, J. Despres, S. J. Thomson, and L. Sanchez-Palencia, 'Local quench spectroscopy of many-body quantum systems', *Physical Review A* **102**:3, 033337 (2020) (cit. on pp. 14, 63).
48. L. Villa, J. Despres, and L. Sanchez-Palencia, 'Unraveling the excitation spectrum of many-body systems from quantum quenches', *Physical Review A* **100**:6, 063632 (2019) (cit. on pp. 14, 63, 117).
49. P. Hauke and L. Tagliacozzo, 'Spread of Correlations in Long-Range Interacting Quantum Systems', *Physical Review Letters* **111**:20, 207202 (2013) (cit. on pp. 14, 61, 63, 65, 117).
50. J. Eisert, M. van den Worm, S. R. Manmana, and M. Kastner, 'Breakdown of Quasilocality in Long-Range Quantum Lattice Models', *Physical Review Letters* **111**:26, 260401 (2013) (cit. on pp. 14, 61, 117).
51. M. Foss-Feig, Z.-X. Gong, C. W. Clark, and A. V. Gorshkov, 'Nearly Linear Light Cones in Long-Range Interacting Quantum Systems', *Physical Review Letters* **114**:15, 157201 (2015) (cit. on pp. 14, 61).
52. C.-F. Chen and A. Lucas, 'Finite Speed of Quantum Scrambling with Long Range Interactions', *Physical Review Letters* **123**:25, 250605 (2019) (cit. on pp. 14, 61).
53. M. C. Tran, C.-F. Chen, A. Ehrenberg, A. Y. Guo, A. Deshpande, Y. Hong, Z.-X. Gong, A. V. Gorshkov, and A. Lucas, 'Hierarchy of Linear Light Cones with Long-Range Interactions', *Physical Review X* **10**:3, 031009 (2020) (cit. on pp. 14, 61).
54. T. Kuwahara and K. Saito, 'Strictly Linear Light Cones in Long-Range Interacting Systems of Arbitrary Dimensions', *Physical Review X* **10**:3, 031010 (2020) (cit. on pp. 14, 61).
55. J. Schachenmayer, A. Pikovski, and A. M. Rey, 'Dynamics of correlations in two-dimensional quantum spin models with long-range interactions: a phase-space Monte-Carlo study', *New Journal of Physics* **17**:6, 065009 (2015) (cit. on pp. 14, 61).
56. A. S. Buyskikh, M. Fagotti, J. Schachenmayer, F. Essler, and A. J. Daley, 'Entanglement growth and correlation spreading with variable-range interactions in spin and fermionic tunneling models', *Physical Review A* **93**:5, 053620 (2016) (cit. on pp. 14, 61, 117).
57. D. J. Luitz and Y. Bar Lev, 'Emergent locality in systems with power-law interactions', *Physical Review A* **99**:1, 010105 (2019) (cit. on pp. 14, 61).
58. L. Colmenarez and D. J. Luitz, 'Lieb-Robinson bounds and out-of-time order correlators in a long-range spin chain', *Physical Review Research* **2**:4, 043047 (2020) (cit. on pp. 14, 61).
59. X.-L. Deng, D. Porras, and J. I. Cirac, 'Effective spin quantum phases in systems of trapped ions', *Physical Review A* **72**:6, 063407 (2005) (cit. on pp. 14, 15).

- 60.R. Islam, E. E. Edwards, K. Kim, S. Korenblit, C. Noh, H. Carmichael, G.-D. Lin, L.-M. Duan, C.-C. Joseph Wang, J. K. Freericks, and C. Monroe, ‘Onset of a quantum phase transition with a trapped ion quantum simulator’, *Nature Communications* **2**:1, 377 (2011) (cit. on p. 14).
- 61.B. P. Lanyon, C. Hempel, D. Nigg, M. Müller, R. Gerritsma, F. Zähringer, P. Schindler, J. T. Barreiro, M. Rambach, G. Kirchmair, M. Hennrich, P. Zoller, R. Blatt, and C. F. Roos, ‘Universal Digital Quantum Simulation with Trapped Ions’, *Science* **334**:6052, 57–61 (2011) (cit. on p. 14).
- 62.C. Schneider, D. Porras, and T. Schaetz, ‘Experimental quantum simulations of many-body physics with trapped ions’, *Reports on Progress in Physics* **75**:2, 024401 (2012) (cit. on p. 14).
- 63.R. Blatt and C. F. Roos, ‘Quantum simulations with trapped ions’, *Nature Physics* **8**:4, 277–284 (2012) (cit. on pp. 14, 15).
- 64.A. Bermudez, L. Tagliacozzo, G. Sierra, and P. Richerme, ‘Long-range Heisenberg models in quasiperiodically driven crystals of trapped ions’, *Physical Review B* **95**:2, 024431 (2017) (cit. on p. 14).
- 65.V. Bendkowsky, B. Butscher, J. Nipper, J. P. Shaffer, R. Löw, and T. Pfau, ‘Observation of ultralong-range Rydberg molecules’, *Nature* **458**:7241, 1005–1008 (2009) (cit. on p. 14).
- 66.H. Weimer, M. Müller, I. Lesanovsky, P. Zoller, and H. P. Büchler, ‘A Rydberg quantum simulator’, *Nature Physics* **6**:5, 382–388 (2010) (cit. on p. 14).
- 67.P. Schauß, M. Cheneau, M. Endres, T. Fukuhara, S. Hild, A. Omran, T. Pohl, C. Gross, S. Kuhr, and I. Bloch, ‘Observation of spatially ordered structures in a two-dimensional Rydberg gas’, *Nature* **491**:7422, 87–91 (2012) (cit. on p. 14).
- 68.A. Browaeys, D. Barredo, and T. Lahaye, ‘Experimental investigations of dipole–dipole interactions between a few Rydberg atoms’, *Journal of Physics B: Atomic, Molecular and Optical Physics* **49**:15, 152001 (2016) (cit. on pp. 14, 15).
- 69.A. Griesmaier, J. Werner, S. Hensler, J. Stuhler, and T. Pfau, ‘Bose-Einstein Condensation of Chromium’, *Physical Review Letters* **94**:16, 160401 (2005) (cit. on p. 14).
- 70.Q. Beaufils, R. Chicireanu, T. Zanon, B. Laburthe-Tolra, E. Maréchal, L. Vernac, J.-C. Keller, and O. Gorceix, ‘All-optical production of chromium Bose-Einstein condensates’, *Physical Review A* **77**:6, 061601 (2008) (cit. on p. 14).
- 71.M. Lu, N. Q. Burdick, S. H. Youn, and B. L. Lev, ‘Strongly Dipolar Bose-Einstein Condensate of Dysprosium’, *Physical Review Letters* **107**:19, 190401 (2011) (cit. on p. 14).
- 72.S. Baier, M. J. Mark, D. Petter, K. Aikawa, L. Chomaz, Z. Cai, M. Baranov, P. Zoller, and F. Ferlaino, ‘Extended Bose-Hubbard models with ultracold magnetic atoms’, *Science* **352**:6282, 201–205 (2016) (cit. on p. 14).
- 73.T. Lahaye, C. Menotti, L. Santos, M. Lewenstein, and T. Pfau, ‘The physics of dipolar bosonic quantum gases’, *Reports on Progress in Physics* **72**:12, 126401 (2009) (cit. on p. 14).
- 74.A. Micheli, G. K. Brennen, and P. Zoller, ‘A toolbox for lattice-spin models with polar molecules’, *Nature Physics* **2**:5, 341–347 (2006) (cit. on p. 14).

75. B. Yan, S. A. Moses, B. Gadway, J. P. Covey, K. R. A. Hazzard, A. M. Rey, D. S. Jin, and J. Ye, ‘Observation of dipolar spin-exchange interactions with lattice-confined polar molecules’, *Nature* **501**:7468, 521–525 (2013) (cit. on p. 14).
76. S. A. Moses, J. P. Covey, M. T. Miecniowski, D. S. Jin, and J. Ye, ‘New frontiers for quantum gases of polar molecules’, *Nature Physics* **13**:1, 13–20 (2017) (cit. on p. 14).
77. O. Firstenberg, T. Peyronel, Q.-Y. Liang, A. V. Gorshkov, M. D. Lukin, and V. Vuletić, ‘Attractive photons in a quantum nonlinear medium’, *Nature* **502**:7469, 71–75 (2013) (cit. on p. 14).
78. L. Childress, M. V. Gurudev Dutt, J. M. Taylor, A. S. Zibrov, F. Jelezko, J. Wrachtrup, P. R. Hemmer, and M. D. Lukin, ‘Coherent Dynamics of Coupled Electron and Nuclear Spin Qubits in Diamond’, *Science* **314**:5797, 281–285 (2006) (cit. on p. 14).
79. G. Balasubramanian, P. Neumann, D. Twitchen, M. Markham, R. Kolesov, N. Mizuochi, J. Isoya, J. Achard, J. Beck, J. Tissler, V. Jacques, P. R. Hemmer, F. Jelezko, and J. Wrachtrup, ‘Ultralong spin coherence time in isotopically engineered diamond’, *Nature Materials* **8**:5, 383–387 (2009) (cit. on p. 14).
80. F. Dolde, I. Jakobi, B. Naydenov, N. Zhao, S. Pezzagna, C. Trautmann, J. Meijer, P. Neumann, F. Jelezko, and J. Wrachtrup, ‘Room-temperature entanglement between single defect spins in diamond’, *Nature Physics* **9**:3, 139–143 (2013) (cit. on p. 14).
81. I. Buluta and F. Nori, ‘Quantum Simulators’, *Science* **326**:5949, 108–111 (2009) (cit. on p. 15).
82. I. M. Georgescu, S. Ashhab, and F. Nori, ‘Quantum simulation’, *Reviews of Modern Physics* **86**:1, 153–185 (2014) (cit. on p. 15).
83. I. Bloch, J. Dalibard, and S. Nascimbène, ‘Quantum simulations with ultracold quantum gases’, *Nature Physics* **8**:4, 267–276 (2012) (cit. on p. 15).
84. A. Aspuru-Guzik and P. Walther, ‘Photonic quantum simulators’, *Nature Physics* **8**:4, 285–291 (2012) (cit. on p. 15).
85. A. A. Houck, H. E. Türeci, and J. Koch, ‘On-chip quantum simulation with superconducting circuits’, *Nature Physics* **8**:4, 292–299 (2012) (cit. on p. 15).
86. C. Gross and I. Bloch, ‘Quantum simulations with ultracold atoms in optical lattices’, *Science* **357**:6355, 995–1001 (2017) (cit. on p. 15).
87. L. Tarruell and L. Sanchez-Palencia, ‘Quantum simulation of the Hubbard model with ultracold fermions in optical lattices’, *Comptes Rendus Physique, Quantum Simulation / Simulation Quantique* **19**:6, 365–393 (2018) (cit. on p. 15).
88. M. Aidelsburger, S. Nascimbene, and N. Goldman, ‘Artificial gauge fields in materials and engineered systems’, *Comptes Rendus Physique, Quantum Simulation / Simulation Quantique* **19**:6, 394–432 (2018) (cit. on p. 15).
89. J. Lebreuilly and I. Carusotto, ‘Quantum simulation of zero-temperature quantum phases and incompressible states of light via non-Markovian reservoir engineering techniques’, *Comptes Rendus Physique, Quantum Simulation / Simulation Quantique* **19**:6, 433–450 (2018) (cit. on p. 15).

- 90.K. Le Hur, L. Henriot, L. Herviou, K. Plekhanov, A. Petrescu, T. Goren, M. Schiro, C. Mora, and P. P. Orth, ‘Driven dissipative dynamics and topology of quantum impurity systems’, *Comptes Rendus Physique, Quantum Simulation / Simulation Quantique* **19**:6, 451–483 (2018) (cit. on p. 15).
- 91.M. T. Bell, B. Douçot, M. E. Gershenson, L. B. Ioffe, and A. Petković, ‘Josephson ladders as a model system for 1D quantum phase transitions’, *Comptes Rendus Physique, Quantum Simulation / Simulation Quantique* **19**:6, 484–497 (2018) (cit. on p. 15).
- 92.F. Alet and N. Laflorencie, ‘Many-body localization: An introduction and selected topics’, *Comptes Rendus Physique, Quantum Simulation / Simulation Quantique* **19**:6, 498–525 (2018) (cit. on p. 15).
- 93.M. Lewenstein, A. Sanpera, and V. Ahufinger, *Ultracold Atoms in Optical Lattices: Simulating quantum many-body systems*, Oxford University Press, 8th2012 (cit. on p. 15).
- 94.S. Lloyd, ‘Universal Quantum Simulators’, *Science* **273**:5278, 1073–1078 (1996) (cit. on p. 15).
- 95.H. Haffner, C. Roos, and R. Blatt, ‘Quantum computing with trapped ions’, *Physics Reports* **469**:4, 155–203 (2008) (cit. on pp. 15, 16).
- 96.J. Zhang, G. Pagano, P. W. Hess, A. Kyprianidis, P. Becker, H. Kaplan, A. V. Gorshkov, Z.-X. Gong, and C. Monroe, ‘Observation of a many-body dynamical phase transition with a 53-qubit quantum simulator’, *Nature* **551**:7682, 601–604 (2017) (cit. on pp. 15, 79, 129).
- 97.A. Sørensen and K. Mølmer, ‘Quantum Computation with Ions in Thermal Motion’, *Physical Review Letters* **82**:9, 1971–1974 (1999) (cit. on pp. 15, 16).
- 98.M. Müller, K. Hammerer, Y. L. Zhou, C. F. Roos, and P. Zoller, ‘Simulating open quantum systems: from many-body interactions to stabilizer pumping’, *New Journal of Physics* **13**:8, 085007 (2011) (cit. on p. 16).
- 99.P. Jurcevic, B. P. Lanyon, P. Hauke, C. Hempel, P. Zoller, R. Blatt, and C. F. Roos, ‘Quasiparticle engineering and entanglement propagation in a quantum many-body system’, *Nature* **511**:7508, 202–205 (2014) (cit. on pp. 17, 18, 61, 78, 117).
- 100.P. Richerme, Z.-X. Gong, A. Lee, C. Senko, J. Smith, M. Foss-Feig, S. Michalakis, A. V. Gorshkov, and C. Monroe, ‘Non-local propagation of correlations in quantum systems with long-range interactions’, *Nature* **511**:7508, 198–201 (2014) (cit. on pp. 17, 18, 61, 78, 117).
- 101.A. Browaeys and T. Lahaye, ‘Many-body physics with individually controlled Rydberg atoms’, *Nature Physics* **16**:2, 132–142 (2020) (cit. on p. 18).
- 102.P. Scholl, M. Schuler, H. J. Williams, A. A. Eberharter, D. Barredo, K.-N. Schymik, V. Lienhard, L.-P. Henry, T. C. Lang, T. Lahaye, A. M. Läuchli, and A. Browaeys, ‘Quantum simulation of 2D antiferromagnets with hundreds of Rydberg atoms’, *Nature* **595**:7866, 233–238 (2021) (cit. on p. 18).
- 103.K.-N. Schymik, S. Pancaldi, F. Nogrette, D. Barredo, J. Paris, A. Browaeys, and T. Lahaye, ‘Single Atoms with 6000-Second Trapping Lifetimes in Optical-Tweezer Arrays at Cryogenic Temperatures’, *Physical Review Applied* **16**:3, 034013 (2021) (cit. on p. 18).

- 104.N. Laflorencie, ‘Quantum entanglement in condensed matter systems’, *Physics Reports, Quantum Entanglement in Condensed Matter Systems* **646**, 1–59 (2016) (cit. on pp. 18, 19, 21, 22, 49, 50, 87, 88).
- 105.N. Regnault, ‘Entanglement spectroscopy and its application to the quantum Hall effects’, in *Topological Aspects of Condensed Matter Physics: École de Physique Des Houches, Session CIII, 4-29 August 2014*, edited by C. Chamon, M. O. Goerbig, R. Moessner, and L. F. Cugliandolo, Oxford University Press, 26th2017, pp. 165–216 (cit. on pp. 18, 21, 87, 88).
- 106.H. Casini and M. Huerta, ‘Renormalization group running of the entanglement entropy of a circle’, *Physical Review D* **85**:12, 125016 (2012) (cit. on p. 19).
- 107.I. Frérot and T. Roscilde, ‘Entanglement Entropy across the Superfluid-Insulator Transition: A Signature of Bosonic Criticality’, *Physical Review Letters* **116**:19, 190401 (2016) (cit. on p. 19).
- 108.J. Helmes and S. Wessel, ‘Entanglement entropy scaling in the bilayer Heisenberg spin system’, *Physical Review B* **89**:24, 245120 (2014) (cit. on p. 19).
- 109.A. B. Kallin, K. Hyatt, R. R. P. Singh, and R. G. Melko, ‘Entanglement at a Two-Dimensional Quantum Critical Point: A Numerical Linked-Cluster Expansion Study’, *Physical Review Letters* **110**:13, 135702 (2013) (cit. on p. 19).
- 110.M. A. Metlitski, C. A. Fuertes, and S. Sachdev, ‘Entanglement entropy in the $O(N)$ model’, *Physical Review B* **80**:11, 115122 (2009) (cit. on p. 19).
- 111.E. Fradkin and J. E. Moore, ‘Entanglement Entropy of 2D Conformal Quantum Critical Points: Hearing the Shape of a Quantum Drum’, *Physical Review Letters* **97**:5, 050404 (2006) (cit. on p. 19).
- 112.H. Li and F. D. M. Haldane, ‘Entanglement Spectrum as a Generalization of Entanglement Entropy: Identification of Topological Order in Non-Abelian Fractional Quantum Hall Effect States’, *Physical Review Letters* **101**:1, 010504 (2008) (cit. on pp. 19, 49, 50, 88, 99).
- 113.A. Kitaev and J. Preskill, ‘Topological Entanglement Entropy’, *Physical Review Letters* **96**:11, 110404 (2006) (cit. on p. 19).
- 114.M. Levin and X.-G. Wen, ‘Detecting Topological Order in a Ground State Wave Function’, *Physical Review Letters* **96**:11, 110405 (2006) (cit. on p. 19).
- 115.G. De Chiara, L. Lepori, M. Lewenstein, and A. Sanpera, ‘Entanglement Spectrum, Critical Exponents, and Order Parameters in Quantum Spin Chains’, *Physical Review Letters* **109**:23, 237208 (2012) (cit. on pp. 19, 88).
- 116.L. Lepori, G. De Chiara, and A. Sanpera, ‘Scaling of the entanglement spectrum near quantum phase transitions’, *Physical Review B* **87**:23, 235107 (2013) (cit. on pp. 19, 88).
- 117.R. Thomale, D. P. Arovas, and B. A. Bernevig, ‘Nonlocal Order in Gapless Systems: Entanglement Spectrum in Spin Chains’, *Physical Review Letters* **105**:11, 116805 (2010) (cit. on p. 19).
- 118.X. Plat and C. Hotta, ‘Entanglement spectrum as a marker for phase transitions in the density embedding theory for interacting spinless fermionic models’, *Physical Review B* **102**:14, 140410 (2020) (cit. on pp. 19, 88, 99, 100).

- 119.X. Deng and L. Santos, ‘Entanglement spectrum of one-dimensional extended Bose-Hubbard models’, *Physical Review B* **84**:8, 085138 (2011) (cit. on p. 19).
- 120.N. Laflorencie and S. Rachel, ‘Spin-resolved entanglement spectroscopy of critical spin chains and Luttinger liquids’, *Journal of Statistical Mechanics: Theory and Experiment* **2014**:11, P11013 (2014) (cit. on p. 19).
- 121.A. M. Läuchli, ‘Operator content of real-space entanglement spectra at conformal critical points’, 4th2013, [arXiv:1303.0741](https://arxiv.org/abs/1303.0741) [cond-mat, physics:hep-th, physics:quant-ph] (cit. on pp. 19, 88).
- 122.J. J. Bisognano and E. H. Wichmann, ‘On the duality condition for a Hermitian scalar field’, *Journal of Mathematical Physics* **16**:4, 985–1007 (1975) (cit. on p. 20).
- 123.J. J. Bisognano and E. H. Wichmann, ‘On the duality condition for quantum fields’, *Journal of Mathematical Physics* **17**:3, 303–321 (1976) (cit. on p. 20).
- 124.M. Dalmonte, V. Eisler, M. Falconi, and B. Vermersch, ‘Entanglement Hamiltonians: from field theory, to lattice models and experiments’, 10th2022, [arXiv:2202.05045](https://arxiv.org/abs/2202.05045) [cond-mat, physics:hep-th, physics:math-ph, physics:quant-ph] (cit. on pp. 20, 21, 49, 50).
- 125.J. Cardy and E. Tonni, ‘Entanglement Hamiltonians in two-dimensional conformal field theory’, *Journal of Statistical Mechanics: Theory and Experiment* **2016**:12, 123103 (2016) (cit. on p. 20).
- 126.P. D. Hislop and R. Longo, ‘Modular structure of the local algebras associated with the free massless scalar field theory’, *Communications in Mathematical Physics* **84**:1, 71–85 (1982) (cit. on p. 20).
- 127.R. J. Baxter, ‘Exactly Solved Models in Statistical Mechanics’, in G. D’Ariano, A. Montorsi, and M. Rasetti, *Integrable Systems in Statistical Mechanics*, Vol. 1, Series on Advances in Statistical Mechanics, WORLD SCIENTIFIC, 1985, pp. 5–63 (cit. on p. 20).
- 128.B. Davies, ‘On the spectrum of six-vertex corner transfer matrices’, *Physica A: Statistical Mechanics and its Applications* **159**:2, 171–187 (1989) (cit. on p. 20).
- 129.H. Frahm and H. B. Thacker, ‘Corner transfer matrix eigenstates for the six-vertex model’, *Journal of Physics A: Mathematical and General* **24**:23, 5587–5603 (1991) (cit. on p. 20).
- 130.M. Dalmonte, B. Vermersch, and P. Zoller, ‘Quantum simulation and spectroscopy of entanglement Hamiltonians’, *Nature Physics* **14**:8, 827–831 (2018) (cit. on p. 21).
- 131.F. Parisen Toldin and F. F. Assaad, ‘Entanglement Hamiltonian of Interacting Fermionic Models’, *Physical Review Letters* **121**:20, 200602 (2018) (cit. on p. 21).
- 132.G. Giudici, T. Mendes-Santos, P. Calabrese, and M. Dalmonte, ‘Entanglement Hamiltonians of lattice models via the Bisognano-Wichmann theorem’, *Physical Review B* **98**:13, 134403 (2018) (cit. on p. 21).
- 133.V. Eisler, G. D. Giulio, E. Tonni, and I. Peschel, ‘Entanglement Hamiltonians for non-critical quantum chains’, *Journal of Statistical Mechanics: Theory and Experiment* **2020**:10, 103102 (2020) (cit. on p. 21).

134. J. Zhang, P. Calabrese, M. Dalmonte, and M. A. Rajabpour, ‘Lattice Bisognano-Wichmann modular Hamiltonian in critical quantum spin chains’, *SciPost Physics Core* **2:2**, 007 (2020) (cit. on p. 21).
135. W. Zhu, Z. Huang, and Y.-C. He, ‘Reconstructing entanglement Hamiltonian via entanglement eigenstates’, *Physical Review B* **99:23**, 235109 (2019) (cit. on pp. 21, 112).
136. C. Gogolin and J. Eisert, ‘Equilibration, thermalisation, and the emergence of statistical mechanics in closed quantum systems’, *Reports on Progress in Physics* **79:5**, 056001 (2016) (cit. on p. 21).
137. D. J. Luitz, N. Laflorencie, and F. Alet, ‘Many-body localization edge in the random-field Heisenberg chain’, *Physical Review B* **91:8**, 081103 (2015) (cit. on p. 22).
138. U. Schollwöck, ‘The density-matrix renormalization group in the age of matrix product states’, *Annals of Physics* **326:1**, 96–192 (2011), arXiv:1008.3477 (cit. on pp. 23, 35, 43, 45, 46, 54, 89).
139. R. Orús, ‘A practical introduction to tensor networks: Matrix product states and projected entangled pair states’, *Annals of Physics* **349**, 117–158 (2014) (cit. on pp. 23, 25, 30, 35, 40, 45).
140. L. Vanderstraeten, J. Haegeman, and F. Verstraete, ‘Tangent-space methods for uniform matrix product states’, *SciPost Physics Lecture Notes*, 007 (2019) (cit. on pp. 23, 47, 54, 57).
141. *Observable universe*, in *Wikipedia*, 1st2022 (cit. on p. 23).
142. D. Poulin, A. Qarry, R. Somma, and F. Verstraete, ‘Quantum Simulation of Time-Dependent Hamiltonians and the Convenient Illusion of Hilbert Space’, *Physical Review Letters* **106:17**, 170501 (2011) (cit. on p. 23).
143. M. B. Hastings, ‘An area law for one-dimensional quantum systems’, *Journal of Statistical Mechanics: Theory and Experiment* **2007:08**, P08024–P08024 (2007) (cit. on pp. 25, 30, 87).
144. J. D. Bekenstein, ‘Black Holes and Entropy’, *Physical Review D* **7:8**, 2333–2346 (1973) (cit. on p. 25).
145. S. W. Hawking, ‘Black hole explosions?’, *Nature* **248:5443**, 30–31 (1974) (cit. on p. 25).
146. R. Bousso, ‘The holographic principle’, *Reviews of Modern Physics* **74:3**, 825–874 (2002) (cit. on p. 25).
147. R. Penrose, ‘Applications of negative dimensional tensors’, *Combinatorial mathematics and its applications* **1**, 221–244 (1971) (cit. on p. 25).
148. R. Orús, ‘Tensor networks for complex quantum systems’, *Nature Reviews Physics* **1:9**, 538–550 (2019) (cit. on pp. 30–32).
149. M. B. Hastings, ‘Solving gapped Hamiltonians locally’, *Physical Review B* **73:8**, 085115 (2006) (cit. on p. 30).
150. B. Swingle, ‘Entanglement renormalization and holography’, *Physical Review D* **86:6**, 065007 (2012) (cit. on p. 32).
151. C. Cao, S. M. Carroll, and S. Michalakis, ‘Space from Hilbert space: Recovering geometry from bulk entanglement’, *Physical Review D* **95:2**, 024031 (2017) (cit. on p. 32).

- 152.T.-C. Wei and P. M. Goldbart, ‘Geometric measure of entanglement and applications to bipartite and multipartite quantum states’, *Physical Review A* **68**:4, 042307 (2003) (cit. on pp. 35, 49, 87).
- 153.R. Orús and T.-C. Wei, ‘Visualizing elusive phase transitions with geometric entanglement’, *Physical Review B* **82**:15, 155120 (2010) (cit. on pp. 35, 49, 87, 97, 99).
- 154.I. P. McCulloch, ‘From density-matrix renormalization group to matrix product states’, *Journal of Statistical Mechanics: Theory and Experiment* **2007**:10, P10014–P10014 (2007) (cit. on p. 41).
- 155.G. Beylkin and L. Monzón, ‘Approximation by exponential sums revisited’, *Applied and Computational Harmonic Analysis, Special Issue on Continuous Wavelet Transform in Memory of Jean Morlet, Part I* **28**:2, 131–149 (2010) (cit. on p. 43).
- 156.B. Pirvu, V. Murg, J. I. Cirac, and F. Verstraete, ‘Matrix product operator representations’, *New Journal of Physics* **12**:2, 025012 (2010) (cit. on p. 43).
- 157.G. Beylkin and L. Monzón, ‘On approximation of functions by exponential sums’, *Applied and Computational Harmonic Analysis* **19**:1, 17–48 (2005) (cit. on p. 43).
- 158.M. Fishman, S. White, and E. Stoudenmire, ‘The ITensor Software Library for Tensor Network Calculations’, *SciPost Physics Codebases*, 004 (2022) (cit. on p. 45).
- 159.J. Bezanson, A. Edelman, S. Karpinski, and V. B. Shah, ‘Julia: A Fresh Approach to Numerical Computing’, *SIAM Review* **59**:1, 65–98 (2017) (cit. on p. 45).
- 160.S. R. White, ‘Density matrix formulation for quantum renormalization groups’, *Physical Review Letters* **69**:19, 2863–2866 (1992) (cit. on p. 45).
- 161.S. R. White, ‘Density-matrix algorithms for quantum renormalization groups’, *Physical Review B* **48**:14, 10345–10356 (1993) (cit. on p. 45).
- 162.U. Schollwöck, ‘The density-matrix renormalization group’, *Reviews of Modern Physics* **77**:1, 259–315 (2005) (cit. on pp. 45, 46).
- 163.K. A. Hallberg, ‘New trends in density matrix renormalization’, *Advances in Physics* **55**:5-6, 477–526 (2006) (cit. on p. 45).
- 164.S. Paeckel, T. Köhler, A. Swoboda, S. R. Manmana, U. Schollwöck, and C. Hubig, ‘Time-evolution methods for matrix-product states’, *Annals of Physics* **411**, 167998 (2019) (cit. on pp. 46, 48, 54, 57).
- 165.J. Haegeman, J. I. Cirac, T. J. Osborne, I. Pižorn, H. Verschelde, and F. Verstraete, ‘Time-Dependent Variational Principle for Quantum Lattices’, *Physical Review Letters* **107**:7, 070601 (2011) (cit. on pp. 46, 54).
- 166.J. Haegeman, C. Lubich, I. Oseledets, B. Vandereycken, and F. Verstraete, ‘Unifying time evolution and optimization with matrix product states’, *Physical Review B* **94**:16, DOI: 10.1103/PhysRevB.94.165116 (2016) (cit. on pp. 46, 54, 57).
- 167.J. Haegeman, T. J. Osborne, and F. Verstraete, ‘Post-matrix product state methods: To tangent space and beyond’, *Physical Review B* **88**:7, 075133 (2013) (cit. on p. 47).

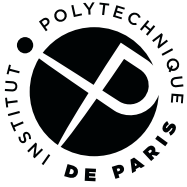
- 168.M. P. Zaletel, R. S. K. Mong, C. Karrasch, J. E. Moore, and F. Pollmann, ‘Time-evolving a matrix product state with long-ranged interactions’, *Physical Review B* **91**:16, 165112 (2015) (cit. on p. 48).
- 169.A. Chandran, M. Hermanns, N. Regnault, and B. A. Bernevig, ‘Bulk-edge correspondence in entanglement spectra’, *Physical Review B* **84**:20, 205136 (2011) (cit. on p. 50).
- 170.X.-L. Qi, H. Katsura, and A. W. W. Ludwig, ‘General Relationship between the Entanglement Spectrum and the Edge State Spectrum of Topological Quantum States’, *Physical Review Letters* **108**:19, 196402 (2012) (cit. on p. 50).
- 171.S. R. White, ‘Density matrix renormalization group algorithms with a single center site’, *Physical Review B* **72**:18, DOI: 10.1103/PhysRevB.72.180403 (2005) (cit. on p. 54).
- 172.J. T. Schneider, J. Despres, S. J. Thomson, L. Tagliacozzo, and L. Sanchez-Palencia, ‘Spreading of correlations and entanglement in the long-range transverse Ising chain’, *Physical Review Research* **3**:1, L012022 (2021) (cit. on pp. 59, 64, 74–76, 81, 83, 117).
- 173.T. Holstein and H. Primakoff, ‘Field Dependence of the Intrinsic Domain Magnetization of a Ferromagnet’, *Physical Review* **58**:12, 1098–1113 (1940) (cit. on p. 65).
- 174.N. M. Bogoliubov, ‘On the theory of superfluidity’, *Journal of Physics* **11**:1 (1947) (cit. on p. 65).
- 175.A. Hurwitz, ‘Einige eigenschaften der dirichletschen functionen $F(s) = \sum \frac{D}{n} \cdot \frac{1}{n^2}$, die bei der bestimmung der klassenanzahlen binärer quadratischer formen auftreten’, *Zeitschrift für Math. u. Physik* **27**, 86–101 (1882) (cit. on p. 72).
- 176.W. Magnus, F. Oberhettinger, and R. P. Soni, ‘The gamma function and related functions’, in *Formulas and Theorems for the Special Functions of Mathematical Physics*, edited by W. Magnus, F. Oberhettinger, and R. P. Soni, Die Grundlehren Der Mathematischen Wissenschaften, Springer, Berlin, Heidelberg, 1966, pp. 1–37 (cit. on p. 72).
- 177.V. Alba and P. Calabrese, ‘Entanglement and thermodynamics after a quantum quench in integrable systems’, *Proceedings of the National Academy of Sciences* **114**:30, 7947–7951 (2017) (cit. on p. 77).
- 178.A. Bastianello and P. Calabrese, ‘Spreading of entanglement and correlations after a quench with intertwined quasiparticles’, *SciPost Physics* **5**:4, 033 (2018) (cit. on p. 77).
- 179.P. Calabrese, ‘Entanglement spreading in non-equilibrium integrable systems’, *SciPost Physics Lecture Notes*, 020 (2020) (cit. on p. 77).
- 180.N. M. Linke, S. Johri, C. Figgatt, K. A. Landsman, A. Y. Matsuura, and C. Monroe, ‘Measuring the Rényi entropy of a two-site Fermi-Hubbard model on a trapped ion quantum computer’, *Physical Review A* **98**:5, 052334 (2018) (cit. on pp. 79, 129).
- 181.T. Brydges, A. Elben, P. Jurcevic, B. Vermersch, C. Maier, B. P. Lanyon, P. Zoller, R. Blatt, and C. F. Roos, ‘Probing Rényi entanglement entropy via randomized measurements’, *Science* **364**:6437, 260–263 (2019) (cit. on pp. 79, 129).
- 182.J. Vovrosh and J. Knolle, ‘Confinement and entanglement dynamics on a digital quantum computer’, *Scientific Reports* **11**:1, 11577 (2021) (cit. on pp. 79, 129).

- 183.L. Yang and A. Feiguin, ‘From deconfined spinons to coherent magnons in an antiferromagnetic Heisenberg chain with long range interactions’, *SciPost Physics* **10:5**, 110 (2021) (cit. on p. 79).
- 184.L. Yang, P. Weinberg, and A. E. Feiguin, ‘Topological to magnetically ordered quantum phase transition in antiferromagnetic spin ladders with long-range interactions’, 24th2021, [arXiv:2111.09798 \[cond-mat\]](https://arxiv.org/abs/2111.09798) (cit. on p. 79).
- 185.J. T. Schneider, S. J. Thomson, and L. Sanchez-Palencia, ‘Entanglement spectrum and quantum phase diagram of the long-range XXZ chain’, *Physical Review B* **106:1**, 014306 (2022) (cit. on pp. 87, 98, 101, 103–105, 107–110).
- 186.X.-G. Wen, ‘Colloquium: Zoo of quantum-topological phases of matter’, *Reviews of Modern Physics* **89:4**, 041004 (2017) (cit. on p. 87).
- 187.G. De Chiara and A. Sanpera, ‘Genuine quantum correlations in quantum many-body systems: a review of recent progress’, *Reports on Progress in Physics* **81:7**, 074002 (2018), [arXiv:1711.07824](https://arxiv.org/abs/1711.07824) (cit. on pp. 87–89, 99).
- 188.V. L. Berezinskii, ‘Destruction of Long-range Order in One-dimensional and Two-dimensional Systems having a Continuous Symmetry Group I. Classical Systems’, *Soviet Journal of Experimental and Theoretical Physics* **32**, 493 (1971) (cit. on p. 87).
- 189.V. L. Berezinskii, ‘Destruction of Long-range Order in One-dimensional and Two-dimensional Systems Possessing a Continuous Symmetry Group. II. Quantum Systems’, *Soviet Journal of Experimental and Theoretical Physics* **34**, 610 (1972) (cit. on p. 87).
- 190.J. M. Kosterlitz and D. J. Thouless, ‘Ordering, metastability and phase transitions in two-dimensional systems’, *Journal of Physics C: Solid State Physics* **6:7**, 1181–1203 (1973) (cit. on p. 87).
- 191.A. Osterloh, L. Amico, G. Falci, and R. Fazio, ‘Scaling of entanglement close to a quantum phase transition’, *Nature* **416:6881**, 608–610 (2002) (cit. on p. 87).
- 192.T. J. Osborne and M. A. Nielsen, ‘Entanglement in a simple quantum phase transition’, *Physical Review A* **66:3**, 032110 (2002) (cit. on p. 87).
- 193.G. Vidal, J. I. Latorre, E. Rico, and A. Kitaev, ‘Entanglement in Quantum Critical Phenomena’, *Physical Review Letters* **90:22**, 227902 (2003) (cit. on p. 87).
- 194.P. Calabrese and J. Cardy, ‘Entanglement entropy and quantum field theory’, *Journal of Statistical Mechanics: Theory and Experiment* **2004:06**, P06002 (2004) (cit. on p. 87).
- 195.C. Holzhey, F. Larsen, and F. Wilczek, ‘Geometric and renormalized entropy in conformal field theory’, *Nuclear Physics B* **424:3**, 443–467 (1994) (cit. on p. 87).
- 196.V. E. Korepin, ‘Universality of Entropy Scaling in One Dimensional Gapless Models’, *Physical Review Letters* **92:9**, 096402 (2004) (cit. on p. 87).
- 197.H. Barnum and N. Linden, ‘Monotones and invariants for multi-particle quantum states’, *Journal of Physics A: Mathematical and General* **34:35**, 6787–6805 (2001) (cit. on p. 87).
- 198.A. Shimony, ‘Degree of Entanglement’, *Annals of the New York Academy of Sciences* **755:1**, 675–679 (1995) (cit. on p. 87).

- 199.T.-C. Wei, D. Das, S. Mukhopadhyay, S. Vishveshwara, and P. M. Goldbart, ‘Global entanglement and quantum criticality in spin chains’, *Physical Review A* **71**:6, 060305 (2005) (cit. on pp. 87, 97).
- 200.R. Orús, ‘Universal Geometric Entanglement Close to Quantum Phase Transitions’, *Physical Review Letters* **100**:13, DOI: 10.1103/PhysRevLett.100.130502 (2008) (cit. on p. 87).
- 201.Q.-Q. Shi, R. Orús, J. O. Fjærestad, and H.-Q. Zhou, ‘Finite-size geometric entanglement from tensor network algorithms’, *New Journal of Physics* **12**:2, 025008 (2010) (cit. on p. 87).
- 202.J.-M. Stéphan, G. Misguich, and F. Alet, ‘Geometric entanglement and Affleck-Ludwig boundary entropies in critical XXZ and Ising chains’, *Physical Review B* **82**:18, 180406 (2010) (cit. on p. 87).
- 203.B. Wang, M. Feng, and Z.-Q. Chen, ‘Berezinskii-Kosterlitz-Thouless transition uncovered by the fidelity susceptibility in the XXZ model’, *Physical Review A* **81**:6, 064301 (2010) (cit. on pp. 87, 100, 123).
- 204.Z.-H. Li, ‘Ground states of long-range interacting fermions in one spatial dimension’, *Journal of Physics: Condensed Matter* **31**:25, 255601 (2019) (cit. on pp. 87, 100, 123).
- 205.P. Schmoll, A. Kshetrimayum, J. Eisert, R. Orús, and M. Rizzi, ‘The classical two-dimensional Heisenberg model revisited: An SU(2)-symmetric tensor network study’, *SciPost Physics* **11**:5, 098 (2021) (cit. on pp. 87, 97).
- 206.V. Alba, M. Haque, and A. M. Läuchli, ‘Boundary-Locality and Perturbative Structure of Entanglement Spectra in Gapped Systems’, *Physical Review Letters* **108**:22, 227201 (2012) (cit. on p. 88).
- 207.P. Calabrese and A. Lefevre, ‘Entanglement spectrum in one-dimensional systems’, *Physical Review A* **78**:3, 032329 (2008) (cit. on p. 88).
- 208.J. I. Cirac, D. Poilblanc, N. Schuch, and F. Verstraete, ‘Entanglement spectrum and boundary theories with projected entangled-pair states’, *Physical Review B* **83**:24, 245134 (2011) (cit. on p. 88).
- 209.F. Pollmann, A. M. Turner, E. Berg, and M. Oshikawa, ‘Entanglement spectrum of a topological phase in one dimension’, *Physical Review B* **81**:6, 064439 (2010) (cit. on p. 88).
- 210.L. Fidkowski, ‘Entanglement Spectrum of Topological Insulators and Superconductors’, *Physical Review Letters* **104**:13, 130502 (2010) (cit. on p. 88).
- 211.I. Peschel, ‘On the entanglement entropy for an XY spin chain’, *Journal of Statistical Mechanics: Theory and Experiment* **2004**:12, P12005 (2004) (cit. on p. 88).
- 212.F. Franchini, A. R. Its, and V. E. Korepin, ‘Renyi entropy of the XY spin chain’, *Journal of Physics A: Mathematical and Theoretical* **41**:2, 025302 (2007) (cit. on p. 88).
- 213.F. Franchini, A. R. Its, B.-Q. Jin, and V. E. Korepin, ‘Ellipses of constant entropy in the XY spin chain’, *Journal of Physics A: Mathematical and Theoretical* **40**:29, 8467–8478 (2007) (cit. on p. 88).

- 214.E. Ercolessi, S. Evangelisti, and F. Ravanini, ‘Exact entanglement entropy of the XYZ model and its sine-Gordon limit’, *Physics Letters A* **374**:21, 2101–2105 (2010) (cit. on p. 88).
- 215.J. Gray, S. Bose, and A. Bayat, ‘Many-body localization transition: Schmidt gap, entanglement length, and scaling’, *Physical Review B* **97**:20, 201105 (2018) (cit. on p. 88).
- 216.R. Shankar, *Quantum Field Theory and Condensed Matter: An Introduction*, Cambridge University Press, Cambridge, 2017 (cit. on pp. 89, 91, 93, 95, 96, 121, 122).
- 217.M. Takahashi, *Thermodynamics of one-dimensional solvable models*, Cambridge University Press, 1999, 266 pp. (cit. on pp. 89, 95, 108, 110).
- 218.F. Franchini, *An Introduction to Integrable Techniques for One-Dimensional Quantum Systems*, Vol. 940, Lecture Notes in Physics, Springer International Publishing, 2017, [arXiv:1609.02100](https://arxiv.org/abs/1609.02100) (cit. on pp. 89, 91, 93–95, 110, 122).
- 219.M. Žnidarič, T. Prosen, and P. Prelovšek, ‘Many-body localization in the Heisenberg XXZ magnet in a random field’, *Physical Review B* **77**:6, 064426 (2008) (cit. on p. 89).
- 220.F. H. L. Essler and M. Fagotti, ‘Quench dynamics and relaxation in isolated integrable quantum spin chains’, *Journal of Statistical Mechanics: Theory and Experiment* **2016**:6, 064002 (2016) (cit. on p. 89).
- 221.P. Calabrese, F. H. L. Essler, and G. Mussardo, ‘Introduction to ‘Quantum Integrability in Out of Equilibrium Systems’’, *Journal of Statistical Mechanics: Theory and Experiment* **2016**:6, 064001 (2016) (cit. on p. 89).
- 222.H. Inoue and K. Nomura, ‘Conformal field theory in the Tomonaga–Luttinger model with the $1/R^\beta$ -long-range interaction’, *Journal of Physics A: Mathematical and General* **39**:9, 2161–2175 (2006) (cit. on p. 94).
- 223.M. F. Maghrebi, Z.-X. Gong, and A. V. Gorshkov, ‘Continuous Symmetry Breaking in 1D Long-Range Interacting Quantum Systems’, *Physical Review Letters* **119**:2, 023001 (2017) (cit. on pp. 95, 96, 99, 106, 109, 119).
- 224.J. Goold, C. Gogolin, S. R. Clark, J. Eisert, A. Scardicchio, and A. Silva, ‘Total correlations of the diagonal ensemble herald the many-body localization transition’, *Physical Review B* **92**:18, 180202 (2015) (cit. on p. 97).
- 225.P. Calabrese, M. Campostrini, F. Essler, and B. Nienhuis, ‘Parity Effects in the Scaling of Block Entanglement in Gapless Spin Chains’, *Physical Review Letters* **104**:9, 095701 (2010) (cit. on p. 106).
- 226.J. C. Xavier and F. C. Alcaraz, ‘Rényi entropy and parity oscillations of anisotropic spin- s Heisenberg chains in a magnetic field’, *Physical Review B* **83**:21, 214425 (2011) (cit. on p. 106).
- 227.J. C. Xavier and F. C. Alcaraz, ‘Finite-size corrections of the entanglement entropy of critical quantum chains’, *Physical Review B* **85**:2, 024418 (2012) (cit. on p. 106).
- 228.P. Calabrese and F. H. L. Essler, ‘Universal corrections to scaling for block entanglement in spin- $1/2$ XX chains’, *Journal of Statistical Mechanics: Theory and Experiment* **2010**:08, P08029 (2010) (cit. on p. 106).

- 229.M. Fagotti and P. Calabrese, ‘Universal parity effects in the entanglement entropy of XX chains with open boundary conditions’, *Journal of Statistical Mechanics: Theory and Experiment* **2011:01**, P01017 (2011) (cit. on p. 106).
- 230.X.-L. Qi and D. Ranard, ‘Determining a local Hamiltonian from a single eigenstate’, *Quantum* **3**, 159 (2019), [arXiv:1712.01850](https://arxiv.org/abs/1712.01850) (cit. on pp. 110, 111).
- 231.M. Foss-Feig, Z.-X. Gong, C. W. Clark, and A. V. Gorshkov, ‘Nearly Linear Light Cones in Long-Range Interacting Quantum Systems’, *Physical Review Letters* **114:15**, 157201 (2015) (cit. on p. 117).
- 232.I. Frérot, P. Naldesi, and T. Roscilde, ‘Entanglement and fluctuations in the XXZ model with power-law interactions’, *Physical Review B* **95:24**, 245111 (2017) (cit. on p. 119).
- 233.P. K. Mogensen and A. N. Riseth, ‘Optim: A mathematical optimization package for Julia’, *Journal of Open Source Software* **3:24**, 615 (2018) (cit. on p. 125).
- 234.F. D. M. Haldane, ‘Exact Jastrow-Gutzwiller resonating-valence-bond ground state of the spin- $\frac{1}{2}$ antiferromagnetic Heisenberg chain with $1/r^2$ exchange’, *Physical Review Letters* **60:7**, 635–638 (1988) (cit. on p. 129).
- 235.B. S. Shastry, ‘Exact solution of an S=1/2 Heisenberg antiferromagnetic chain with long-ranged interactions’, *Physical Review Letters* **60:7**, 639–642 (1988) (cit. on p. 129).
- 236.J. C. Talstra and F. D. M. Haldane, ‘Integrals of motion of the Haldane-Shastry model’, *Journal of Physics A: Mathematical and General* **28:8**, 2369–2377 (1995) (cit. on p. 129).



DOCTORAL SCHOOL

Titre : Dynamique loin de l'équilibre et intrication de systèmes quantiques longues portées

Mots clés : dynamique loin de l'équilibre; intrication quantiques; interactions de longues portées; tensor network simulations

Résumé : Les systèmes quantiques avec interaction à longue portée ont attiré une attention considérable ces dernières années, tant d'un point de vue expérimental que théorique. Dans cette thèse, nous étudions les effets des interactions à longue portée sur les propriétés hors équilibre et à l'équilibre des modèles de spin sur réseau en utilisant des calculs analytiques complémentaires utilisant des simulations de réseaux tensoriels de pointe, tout en nous concentrant particulièrement sur la caractéristique quantique centrale et unique de l'intrication. Premièrement, dans le modèle d'Ising en champ transverse de longue portée, nous montrons l'émergence d'une forme faible de causalité caractérisée par des exposants dynamiques non universels. D'une part, la magnétisation et les corrélations locales présentent un cône causal émergent sub-balistique tandis que les caractéristiques marquées à l'intérieur de celui-ci se propagent de manière super-balistique ou balistique, respectivement. Alors que l'aimantation et les corrélations locales présentent un cône causal sub-balistique émergent, celui qui émerge pour toutes les entropies d'intrication s'avère être balistique indépendamment de la por-

tée des interactions. Deuxièmement, nous déterminons le diagramme de phase quantique d'équilibre du modèle XXZ à longue portée en termes de couplage anisotrope et d'exposant d'interaction de longue portée en étudiant une représentation du spectre de la matrice de densité réduite suivant une bipartition en demi-chaîne, appelée spectre d'intrication. Nous montrons qu'il présente une autosimilarité remarquable dans la phase critique où le système est décrit par un liquide de Luttinger. La transition hors du liquide de Luttinger est cohérente avec la rupture de l'autosimilarité et une analyse par groupe de renormalisation. La combinaison synergique de ces deux dernières nous permet de déterminer les transitions de phase correspondantes que nous corroborons à l'aide de simulations numériques. De plus, nous montrons que le Hamiltonien d'intrication, l'opérateur hermitien dont le spectre est le spectre d'intrication, suit la forme du théorème de Bisognano–Wichmann dans les grandes régions des phases incluant la limite à courte portée, tandis qu'une telle forme peut être exclue dans la phase où les effets à longue portée sont véritablement pertinents.

Title: Far-from-equilibrium dynamics and entanglement in long-range quantum systems

Keywords: far-from-equilibrium dynamics; quantum entanglement; long-range interactions; tensor network simulations

Abstract: Long-range interacting quantum systems have attracted considerable attention in recent years both from an experimental and theoretical perspective. In this thesis, we study the effects of long-range interactions on out-of-equilibrium and equilibrium features of lattice spin models by employing complementary analytical calculations and state-of-the-art tensor-network simulations while particularly focusing on the central and unique quantum feature of entanglement. First, in the long-range transverse-field Ising model, we show the emergence of a weak form of causality characterised by non-universal dynamical exponents. While local magnetisation and correlations have an emergent sub-ballistic causal cone, the one emerging for all entanglement entropies is shown to be ballistic irrespective of the interaction range. Second, we determine the equilibrium quantum phase diagram of the long-range XXZ model in terms of the anisotropic coupling and the

long-range interaction exponent through studying a representation of the spectrum of the reduced density matrix following a half-chain bipartition, the so-called entanglement spectrum. We show it exhibits a remarkable self-similarity within the critical phase where the system is described by a Luttinger liquid. The transition away from a Luttinger liquid is consistent with the breakdown of self-similarity and a renormalisation group analysis. The synergistic combination of the two latter allows us to locate the corresponding phase transitions which we corroborate by numerical simulations. Furthermore, we show the entanglement Hamiltonian, the Hermitian operator whose spectrum is the entanglement spectrum, follows the form of the Bisognano–Wichmann theorem in large regions of the phases which include the short-range limit, while such a form can be excluded in the phase where genuinely long-ranged effects are relevant.

